RUSSIAN JOURNAL of EARTH SCIENCES

Vol. 25
Issue 2

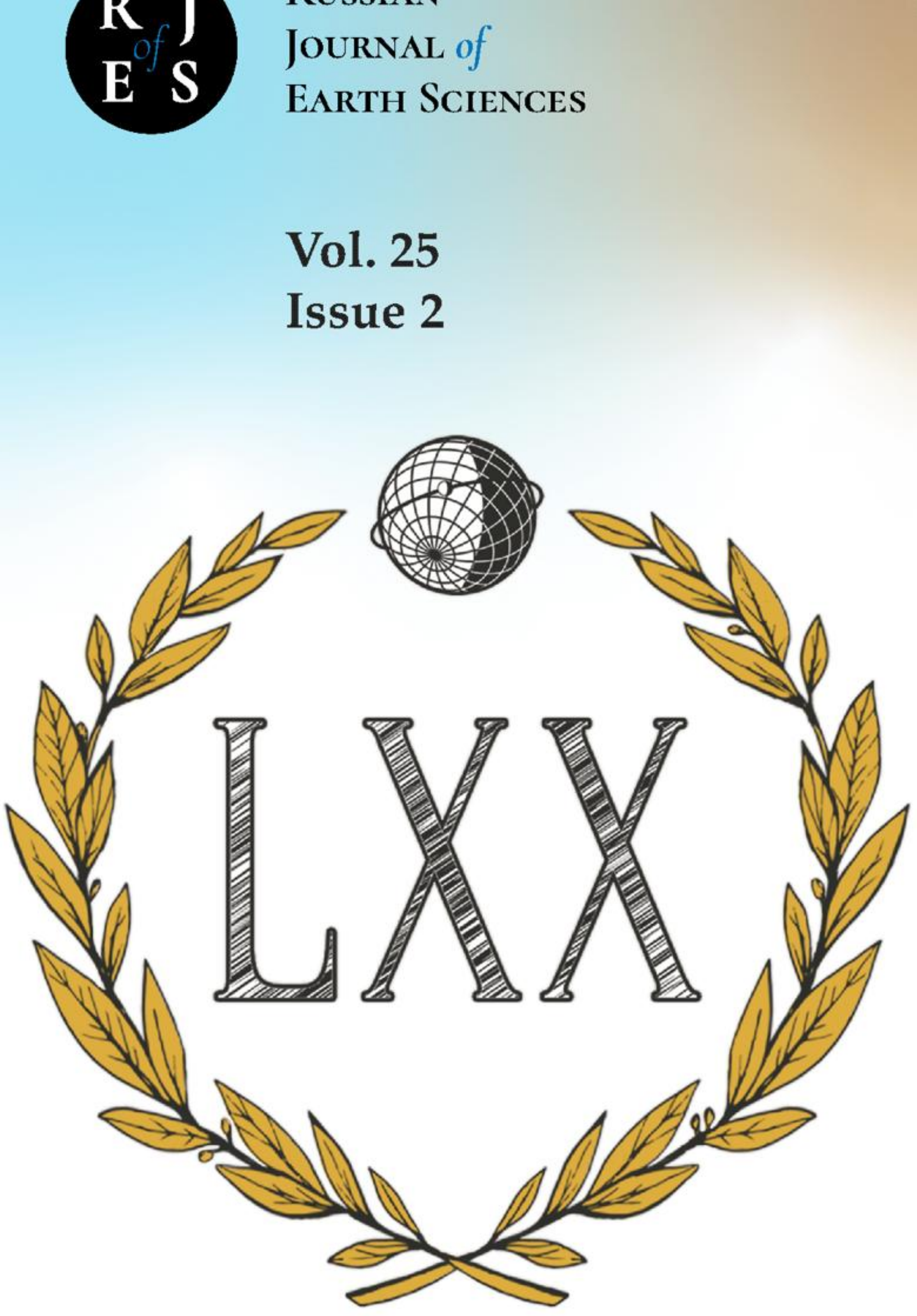

Russian Journal of Earth Sciences

Special Issue: "Data Science, Geoinformatics and Systems Analysis in Geosciences"

Density Model Creation Based on Separating Gravity Field by Depth

P. S. Martyshko[1], **D. D. Byzov**[1]

[1]Institute of Geophysics named after Yu. P. Bulashevich, UB RAS, Ekaterinburg, Russia
* **Correspondence to:** Martyshko Petr Sergeevich, pmart3@mail.ru

Abstract: As a rule, it is known from a priori data that the studied field anomalies are caused by geological structures located at a certain depth below the day surface. Separation of anomalies of the observed potential field by depth and their connection with deep objects can form the basis of interpretation schemes for modeling problems. The classical method of field separation includes spectral filtering with subsequent analytical continuation of the separated anomalies. We propose an original method of height-based transformations of potential fields based on solving the inverse problem of analytical continuation of harmonic functions from a plane to the "inner" half-space. This problem is reduced to solving the Fredholm integral equation of the first kind for the Poisson integral, which can be used to represent a harmonic function in the "outer" half-space by its boundary values on the plane. The parallel algorithm for solving the integral equation is implemented on graphics accelerators using the NVidia CUDA and AMD ROCm libraries in the application software. The results of the method application are shown on the example of separation of the vertical component of the gravity field in the Bouguer reduction for the Sarginskaya area (Urals, Russia). For this territory, a detailed 3D density model was created by solving the linear inverse problem of gravimetry.

Keywords: analytical continuation of potential fields, linear inverse problem of gravimetry, 3D density model.

Citation: Martyshko, P. S., and D. D. Byzov (2025), Density Model Creation Based on Separating Gravity Field by Depth, *Russian Journal of Earth Sciences*, 25, ES2001, EDN: EKYBST, https://doi.org/10.2205/2025ES000960

1. Introduction

Volumetric seismic density models of the Earth's crust provide new information about the internal structure of the Earth and significantly expand the possibilities of forecasting and prospecting for mineral deposits, especially hydrocarbon deposits. Various methods for constructing density models are considered in a number of works. The article [*Nurmukhamedov et al.*, 2020] presents a geological and geophysical model of the structure of the Earth's crust and upper mantle along the regional profile of the settlement of Apacha — Mutnaya Bay in the south of Kamchatka. The two-dimensional model was created based on a comprehensive interpretation of materials from the method of converted waves from remote earthquakes, gravity exploration and magnetotelluric sounding. The work [*Sidorov et al.*, 2022] presents a methodology for creating a density volumetric model of the Earth's crust and upper mantle for the southern part of the Kamchatka Peninsula. The model was created based on the results of interpreting Bouguer anomalies and deep soundings using seismic exploration and electrical exploration methods. In the article [*Sharov et al.*, 2020], a model of the structure of the crystalline part of the Earth's crust of the White Sea region is compiled based on the analysis of geological and geophysical data. Data on deep seismic sounding (DSS) profiles are used, and an analysis of petrophysical, geothermal, and gravimetric data is performed.

Research Article

Received: 15 November 2024
Accepted: 15 April 2025
Published: 23 May 2025

Note that, unlike the works of other researchers, the method of constructing three-dimensional models of the Earth's crust used by us is based on the author's algorithms for solving direct and inverse gravimetry problems and is implemented in automated computer technology using graphic accelerators, which allows a thousandfold reduction in the time of calculating the density values in the grid nodes. For the Ural region and adjacent territories of the East European platform and the West Siberian plate, a volumetric model of density distribution (with a discretization step of 500 m) in the layers of the Earth's crust and upper mantle to a depth of 80 km was previously created [*Byzov et al.*, 2024]. In this paper, the regional model will be refined and detailed (up to 50 m) within the Sarginskaya area to a depth of 5 km. An important preliminary stage for this is the separation of local gravity field anomalies by depth.

Method of separating fields by depth

To separate the gravity field anomalies by depth, the idea of height-based transformations is used, first proposed in the work [*Martyshko et al.*, 2003], but significantly improved by the Authors in terms of the application methodology and implementation in the form of an effective numerical algorithm [*Martyshko et al.*, 2021]. We will describe the recalculation methodology. We assume that the initial separable field $g(x, y, 0)$ is specified on the plane $z = 0$. The general scheme of the method for isolating the effect of sources in the layer from the Earth's surface to a certain depth $z = -H$ consists of three stages:

1. The field is analytically continued upward to the level $z = H$: $g(x, y, 0) \overset{\text{up}(H)}{\Rightarrow} g(x, y, H)$, while we assume that the influence of local near-surface sources (to a depth $z = -H$), if not completely eliminated, then significantly weakens.
2. In order to "get rid" of the influence of local sources located in the horizontal layer from the daytime surface $z = 0$ to the depth $z = -H$, the field $g(x, y, H)$ recalculated upwards is then analytically continued downwards to the depth $z = -H$: $g(x, y, H) \overset{\text{down}(2H,\kappa)}{\Rightarrow} u(x, y, -H \mid (-\infty, -H])$. The resulting field can be considered as a field from sources located below the boundary $z = -H$, defined on the plane $z = -H$.
3. At the last step, the field $u(x, y, -H \mid (-\infty, -H])$ is recalculated again upwards to the level of the daytime surface $z = 0$: $u(x, y, -H \mid (-\infty, -H]) \overset{up(H)}{\Rightarrow} u(x, y, 0 \mid (-\infty, -H])$.

The resulting field can be considered as a field from sources located below the boundary $z = -H$, defined on the plane $z = 0$. Next, we subtract this field from the original one and obtain the field from the layer $z \in (-H, 0]$: $u(x, y, 0 \mid (-H, 0]) = g(x, y, 0) - u(x, y, 0 \mid (-\infty, -H])$.

Let us assume that the gravitating masses are located in a layer below the horizontal plane with the applicate z. On this plane, we denote the gravitational field by $u(\cdot, \cdot, z)$ and take it as the boundary function of the Dirichlet problem for the Laplace equation over a semi-infinite domain. From the values on the boundary, the solution $u(\cdot, \cdot, \zeta)$ of this problem restores the harmonic function of the field everywhere above z. Thus, for points of the upper half-space $\zeta \geq z$, the solution $u(\cdot, \cdot, \zeta)$ of the problem can be written in terms of the Poisson integral [*Blakely*, 1995]:

$$u(\xi, \eta, \zeta) = \frac{\zeta - z}{2\pi} \iint_{-\infty}^{+\infty} \frac{u(x, y, z)dxdy}{((x - \xi)^2 + (y - \eta)^2 + (z - \zeta)^2)^{\frac{3}{2}}}. \quad (1)$$

The operation $u(\cdot, \cdot, z) \overset{\text{up}(H)}{\Rightarrow} u(\cdot, \cdot, \zeta)$ of recalculation upwards by the difference in heights (depths) $H = \zeta - z \geq 0$ is a direct taking of the integral in formula (1). The operation $u(\cdot, \cdot, \zeta) \overset{\text{down}(H,\kappa)}{\Rightarrow} u(\cdot, \cdot, z)$ of recalculation downwards by the difference in heights (depths) $H = \zeta - z \geq 0$ is a solution to the Fredholm integral equation of the first kind (1), where the values of the field $u(\cdot, \cdot, \zeta)$ are considered given, and it is necessary to find the values of $u(\cdot, \cdot, z)$ under the integral sign. In the general case, finding a solution to this equation is an ill-posed problem requiring regularization. Since the kernel of integral (1) is symmetric

and positive definite, we can apply M. M. Lavrentiev's regularization [*Lavrentiev*, 1967]. The regularized equation has the form

$$u(\xi,\eta,\zeta) = \kappa u(\xi,\eta,z) + \frac{\zeta - z}{2\pi} \iint_{-\infty}^{+\infty} \frac{u(x,y,z)dxdy}{((x-\xi)^2 + (y-\eta)^2 + (z-\zeta)^2)^{\frac{3}{2}}},$$

where ζ and z are fixed, $\kappa > 0$ is the regularization parameter. This equation, for any left-hand side from L_2, necessarily has exactly one solution from L_2 and it depends continuously on κ [*Lavrentiev*, 1967].

Let us consider the proposed method for extracting from the general observed field $g(x,y,0)$ the gravitational effect $u(x,y,0 \mid (-\infty,-H])$ of sources in the half-space below some depth $z = -H < 0$: $g(x,y,0) \overset{\text{up}(H)}{\Rightarrow} g(x,y,H) \overset{\text{down}(2H,\kappa)}{\Rightarrow} u(x,y,-H \mid (-\infty,-H]) \overset{\text{up}(H)}{\Rightarrow} u(x,y,0 \mid (-\infty,-H])$. We assume that $g(x,y,0)$ is specified exactly by its piecewise constant representation. If the operations up(H) and down$(H,0)$ were performed analytically exactly, then, of course, in As a result, we would get $u(x,y,0 \mid (-\infty,-H]) \equiv g(x,y,0)$. If we strive for the greatest accuracy in implementing the recalculation scheme using the analytical continuation of harmonic functions, then no separation of fields will be obtained. In fact, formal regularization was introduced into the down(H,κ) operation for the purposes of separation.

The result $u(x,y,0 \mid (-\infty,-H])$ of the three-stage recalculation scheme continuously depends on the regularization parameter κ, in addition, the larger κ, the smoother it is. Let us divide the observed field $g(x,y,0)$ into L horizontal layers with depth intervals $((-H_{i+1},-H_i])_{i=0}^{L-1}$ and take as the field of this layer $u(x,y,0 \mid (-H_{i+1},-H_i]) = u(x,y,0 \mid (-\infty,-H_i]) - u(x,y,0 \mid (-\infty,-H_{i+1}])$, while fields $u(x,y,0 \mid (-\infty,-H_i])$ are obtained using the regularizers κ_i, with the exception of $u(x,y,0 \mid (-\infty,-H_0]) = g(x,y,0)$, $H_0 = 0$, $\kappa_0 = 0$. It turns out that to fulfill the condition of "continuous" joining of separated fields $u(x,y,0 \mid (-H_{i+1},-H_i])$ of adjacent layers, we need to choose κ_i in ascending order between $\kappa_0 = 0$ and κ_L without sharp transitions from κ_{i-1} to κ_i. Of course, there are infinitely many variants of "continuous" increasing sequences of κ_i, and these variants can give significantly different recalculations and, accordingly, density models, but this is where the non-uniqueness of the solution of the linear inverse problem of gravimetry is manifested. The choice of one of the variants falls on the shoulders of the interpreter, this is an element of subjectivity. The big plus is that small changes in the sequence κ_i will lead to small changes in the separated fields and the resulting density model.

Thus, κ is used in the recalculations not for regularization, but as a continuous filtering factor (the larger κ, the larger the band of "high frequencies" we filter). For the purposes of separating fields, filters operating in the "frequency" region [*Serbulenko*, 1967] can also be used, but, in the opinion of the Authors, they are less clear in terms of binding to specific depths.

2. Creation of a density model of Sarginskaya area

As a practical example of the application of the method of separating fields by depth, we will consider the construction of a 3D density model of the Sarginskaya area. The digital model of the gravity field in the Bouguer reduction for the specified territory (within the boundaries of sheets O-40-XXIII, XXVIII, XXIX, XXXIV, XXXV) was taken from the electronic version of the report of the Bazhenov Geophysical Expedition [*Sokolova et al.*, 2010]. The grid step along the X and Y coordinates is 50 m, the total area is 3750 km^2, the declared root-mean-square error of the digital model is 60 μGal. As an initial approximation model for interpreting the field, a regional 3D density model with a discretization step of 500 m for the territory of sheets O-40, O-41, previously constructed by the Authors [*Byzov et al.*, 2024], was taken. The field of the initial approximation model was subtracted from the interpreted field. The range of variations of the resulting difference field is ±1.9 mGal, the standard deviation is 0.45 mGal. Then the difference field was divided according to our method into 100 terms corresponding to sources in layers limited by horizontal planes

at successive depths from 0 km to 5 km with a step of 50 m. In this case, a restriction was imposed during the division process: for each layer, the 1st and 99th percentiles of the corresponding field should deviate from 0 by approximately 18 μGal. Due to the continuous dependence of the field-result of the division method on the parameter κ, a field satisfying these restrictions can be found for each layer using a simple binary search for κ. Naturally, each layer will have its own κ. Figure 1 (on the left) shows the statistical indicators of a set of fields divided for each layer. The ordinate axis shows the depth to the upper boundary of the layer, the abscissa axis shows the minimum, maximum, 1st and 99th percentiles, and standard deviation corresponding to its field. The limitation of 18 μGal was chosen so that when performing the separation procedure, the difference field would "end" at a depth of up to 5 km. If we take the limitation of 17 μGal, then the difference field will "end" after a depth of 5 km.

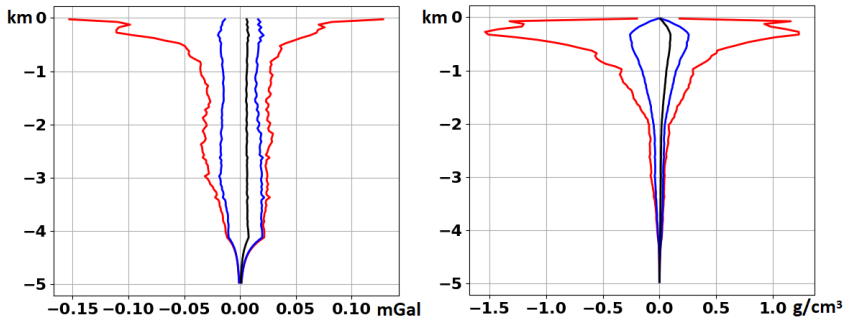

Figure 1. Statistical indicators for horizontal layers at depths plotted along the ordinate axis: on the left – separated fields, on the right – corresponding density distributions. Red lines – minimum and maximum, blue – 1st and 99th percentiles, black – standard deviation.

After the separation procedure, a lateral density distribution was selected independently in each horizontal layer by the corresponding field by solving the linear inverse problem of gravity exploration. As is known [*Novoselitskii*, 1965], the problem of finding a laterally variable density in a horizontal layer has a unique solution that continuously depends on the input field. Figure 1 (on the right) shows the statistical indicators of the found density distributions for all layers. It can be seen that the 1st and 99th percentiles at all depths "fit" into 0.2 g/cm^3, but the minimum and maximum in the upper layers reach values of −1.5 g/cm^3 and 1.1 g/cm^3, respectively. For a difference field, these are fairly large density values, and we will adjust the initial model by these values. Note that there are less than 1% of such "bad" points, and almost all additional masses are concentrated at depths of up to 2 km. It has already been indicated above that the densities in the layer continuously depend on the layer field, and therefore on the parameter κ. Therefore, the restrictions on the 1st and 99th percentiles could be imposed not on the divided field, but directly on the density distribution in the layer, then it would be possible to achieve a more uniform (or even arbitrary, at the interpreter's discretion) distribution of masses by depth. However, this is a task for future research.

After calculating the density distribution by the difference field, it was added to the regional model. And thus, the final 3D density model of the Sarginskaya area was obtained with a discretization step of 50 m to a depth of 5 km (Figure 2). The profile along which vertical sections of the regional and final models were made for comparison is marked with a red line above (Figure 3).

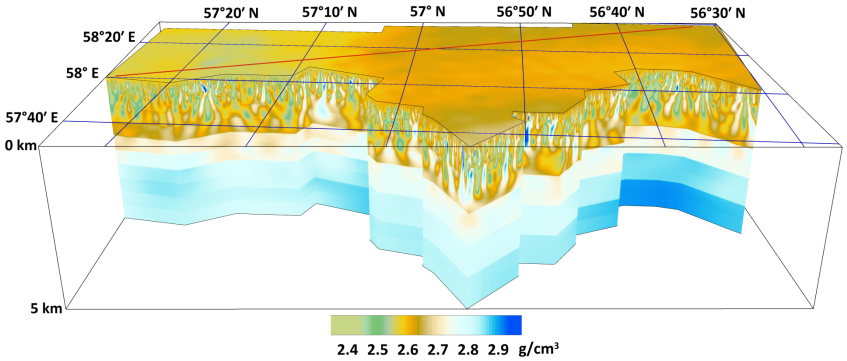

Figure 2. General view of the final 3D density model of Sarginskaya area.

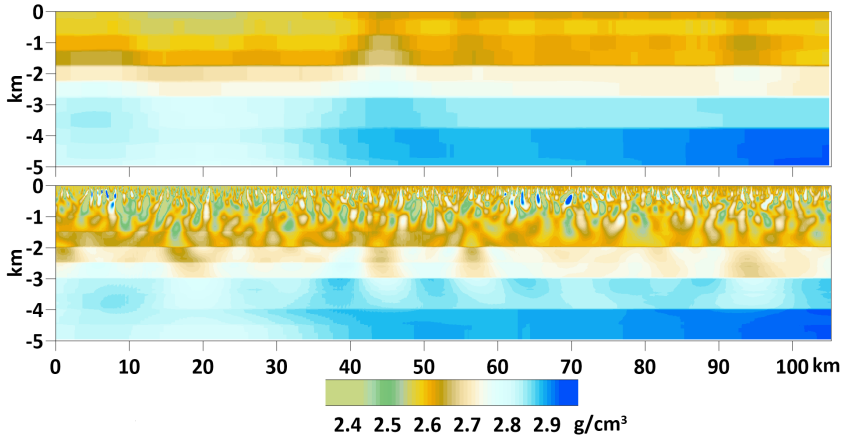

Figure 3. Vertical sections of the regional (top) and final (bottom) 3D density models.

3. Conclusion

A grid density model of the Earth's crust of the Sarginskaya area of the eastern part of the Volga-Ural oil and gas province was constructed to a depth of 5 km with a grid step of 50 m, on which local heterogeneities are clearly visible. The method is based on parallel algorithms for solving the equation of the first kind. A regional density model, previously constructed by the authors based on seismic-gravity modeling, was used as the initial model for solving the inverse gravimetry problem.

Acknowledgments. This research was funded by Russian Science Foundation, grant number 20-17-00058.

References

Blakely R. J. Potential Theory in Gravity and Magnetic Applications. — Cambridge University Press, 1995. — DOI: 10.1017/cbo9780511549816.

Byzov D. D., Martyshko P. S., Ladovskii I. V., et al. 3D Seismic Density Models of the Earth's Crust and Structural Diagrams of Tectonic Zoning of the Middle Urals // Russian Geology and Geophysics. — 2024. — Vol. 65, no. 10. — P. 1240–1251. — DOI: 10.2113/rgg20244731.

Lavrentiev M. M. Some Improperly Posed Problems of Mathematical Physics. — Springer Berlin Heidelberg, 1967. — DOI: 10.1007/978-3-642-88210-4.

Martyshko P. S., Prutkin I. L. Technology for separating gravitational field sources by depth // Geophysical Journal. — 2003. — Vol. 25, no. 3. — P. 159–168. — (In Russian).

Martyshko P. S., Ladovskii I., Byzov D. Parallel Algorithms for Solving Inverse Gravimetry Problems: Application for Earth's Crust Density Models Creation // Mathematics. — 2021. — Vol. 9, no. 22. — P. 2966. — DOI: 10.3390/math9222966.

Novoselitskii V. M. On the theory of determining density changes in a horizontal formation by gravity anomalies // Izv. AN SSSR, Fizika Zemli. — 1965. — No. 5. — P. 25–32. — (In Russian).

Nurmukhamedov A. G., *Sidorov M. D.*, *Moroz Y. F.* A model of the deep structure of the Earth's crust and upper mantle in the area of the Karymshinsky gold-ore cluster according to geophysical data (South Kamchatka) // Georesources. — 2020. — Vol. 22(1). — P. 63–72. — DOI: 10.18599/grs.2020.1.63-72. — (In Russian).

Serbulenko M. G. Linear methods of potential fields separation // Application of some mathematical methods to the interpretation of geophysical data / ed. by E. E. Fotiadi, M. M. Lavrentiev. — Novosibirsk : Nauka, 1967. — P. 5–75. — (In Russian).

Sharov N. V., *Bakunovich L. I.*, *Belashev B. Z.*, *et al.* Geological-geophysical models of the crust for the White Sea region // Geodynamics & Tectonophysics. — 2020. — Vol. 11, no. 3. — P. 566–582. — DOI: 10.5800/GT-2020-11-3-0491.

Sidorov M. D., *Nurmukhamedov A. G.* Three-dimensional image of crustal density model: a case study in South Kamchatka // Russian Geology and Geophysics. — 2022. — Vol. 63, no. 10. — P. 1189–1206. — DOI: 10.2113/rgg20204328.

Sokolova E. V., *Bliznetsov M. T.*, *Desyatnichenko L. I.* Report on object No. 70-01/10 "Completion of zonal-regional geophysical studies (seismic exploration in combination with gravimetric survey) in the eastern part of the Volga-Ural oil and gas province (Sverdlovsk region, Sarginskaya area)" / Rosnedra. — 2010. — (In Russian).

Russian Journal of Earth Sciences

Special Issue: "Data Science, Geoinformatics and Systems Analysis in Geosciences"

Evaluation of Hydrocarbon Potential at a Regional Scale Using Morphometric and Lineament Analysis of DEMs

I. Yu. Chernova[1], **D. K. Nurgaliev**[1], **F. N. Garaev**[1], **O. V. Luneva**[1]

[1]Kazan (Volga region) Federal University, Kazan, Russia
* **Correspondence to:** Chernova Inna Yu., inna.chernova@kpfu.ru

Abstract: This study presents the results of morphometric and lineament analysis conducted on a DEM of a study area in the southwestern Siberian Platform, encompassing several petroleum provinces. The research highlights the informative value of the difference between 6th and 7th order base surfaces, revealing that known deposits are predominantly located in areas with low amplitudes of neotectonic movements. This correlation was used as a prospectivity indicator. Additionally, the relationship between macrofracturing in the sedimentary cover, expressed through lineament density, and the location of known deposits was examined. Known petroleum deposits are mainly situated in areas with low to medium macrofracturing, suggesting this characteristic can be considered a factor in petroleum trap integrity. A comprehensive prospectivity map was generated based on these two exploration criteria, and its reliability was validated. The study demonstrates the effectiveness of using geographic information systems in petroleum exploration.

Keywords: petroleum exploration, neotectonics, morphometric analysis, lineament density, geographic information system, Siberian Platform.

Citation: Chernova, I. Yu., D. K. Nurgaliev, F. N. Garaev, and O. V. Luneva (2025), Evaluation of Hydrocarbon Potential at a Regional Scale Using Morphometric and Lineament Analysis of DEMs, *Russian Journal of Earth Sciences*, 25, ES2002, EDN: POXKPA, https://doi.org/10.2205/2025ES000961

1. Introduction

Modern hydrocarbon exploration approaches emphasize the crucial role of geodynamic processes in the formation and reformation of petroleum deposits. This approach, first proposed by geomorphologists, neotectonics specialists, and petroleum geologists as far back as 50 years ago [*Lastochkin*, 1974], implies that petroleum deposits are relatively young, with their age comparable to the formation time of the modern-day landscape in petroleum provinces [*Nurgaliev et al.*, 2009].

Neotectonic activity affects the integrity of hydrocarbon deposits in various ways. Generally, higher activity increases the likelihood of discovering hydrocarbon accumulations, but excessively high tectonic activity can lead to deposit destruction [*Chernova et al.*, 2021; *Lastochkin*, 1974]. Therefore, petroleum forecasting should analyze two interrelated processes: deposit formation under neotectonic influences (particularly the intensity of vertical movements) and their degradation due to geodynamic factors (specifically, the macroscopic fracturing of the sedimentary cover).

The task of determining quantitative characteristics of neotectonic processes (direction and amplitude of vertical movements, fracture density) in the areas with hydrocarbon deposits or accumulations can be effectively accomplished through morphometric and lineament analysis of a DEM. It can be performed automatically using GIS tools [*Chernova et al.*, 2021] along with ranking the territories based on said characteristics.

This study aims to discuss the informative value and effectiveness of the proposed method for assessing hydrocarbon potential, focusing on regional-scale petroleum exploration in an area that is promising for new petroleum discoveries, but poorly explored.

Research Article

Received: 15 November 2024
Accepted: 15 April 2025
Published: 23 May 2025

2. Study area

The study area covers 270,969 km^2 in the southern part of Eastern Siberia, extending from 94°30′ to 102°40′ E and from 56°0′ to 61°30′ N (Figure 1a). The topography is characterized by a substantial elevation gradient, ranging from 80 to 980 meters, with a mean elevation between 300 and 400 meters. This type of terrain is conducive to effective morphometric analysis [*Filosofov*, 1975; *Lastochkin*, 1974].

The sedimentary cover of the Siberian Platform underwent multiple restructurings throughout the Phanerozoic [*Seregin et al.*, 1985; *Sokolov et al.*, 1985; *Varlamov*, 1985], leading to repeated re-formations of large dome-shaped deposits. Recent tectonic activity amplified the structural expression of pre-existing anticlines while promoting their fragmentation into discrete blocks [*Sokolov et al.*, 1985]. Late Cenozoic tectogenesis is considered a factor controlling the degree of preservation or destruction of petroleum deposits [*Seregin et al.*, 1985; *Varlamov*, 1985], underscoring the value of neotectonic analysis in petroleum exploration strategies.

3. Methodology and input data

The DEM was generated using 1:100000 scale topographic maps (339 map sheets in .gdb format, from which terrain and hydrography were extracted). Data processing and visualization were performed using ESRI's ArcGIS Pro 3.0 and WinLessa, a specialized lineament analysis software [*Zlatopolsky*, 1992; 2024].

3.1. Morphometric Analysis

The analysis was based on V. P. Filosofov's concepts [*Filosofov*, 1975] with modifications through the application of ArcGIS hydrological modeling tools [*Chernova et al.*, 2021]. The analysis focused on base surfaces (surfaces that connect local erosion base levels) and differences between them, as these can be generated almost entirely automatically. The hydrological modeling resulted in a stream order map, with the lower reaches of the Angara and Podkamennaya Tunguska rivers attaining 9th to 10th order status (Figure 1b).

Base surfaces and the differences between them illuminate long-term terrain evolution patterns. Like watercourses, base surfaces are classified by order [*Filosofov*, 1975]. Differences between base surfaces reveal the magnitudes of vertical crustal movements during specific time frames. For instance, the differences between first and second-order surfaces, as well as between second and third-order surfaces, correspond to the most recent periods of neotectonic activity. Meanwhile, the differences between fifth and sixth-order surfaces, sixth and seventh-order surfaces, and those of even higher orders represent earlier stages of neotectonic activity.

Neotectonic activity is believed to influence hydrocarbon deposit distribution, but the specific stages causing large-scale hydrocarbon migration are unknown. To investigate this, spatial correlations between neotectonic movement amplitudes and known deposit locations were analyzed by overlaying deposit outlines onto calculated differences between base surfaces of consecutive orders.

The most revealing result came from the difference between 6th and 7th order base surfaces, showing that known deposits are predominantly located in regions of neotectonic quiescence (Figure 1d).

3.2. Lineament Analysis

The WinLESSA software [*Zlatopolsky*, 2024] was employed to generate a map of lineament traces — linear elements identified in the DEM. A macro-fracturing raster was then created by calculating the density of lineament traces (using Zlatopolsky's method [*Zlatopolsky*, 1992]). Each cell in this raster represents the ratio of the total length of all lineament traces to the area of a defined neighborhood around that cell (Figure 1c). The values are expressed in arbitrary units on an 8-bit scale (0–255). Known hydrocarbon deposits are predominantly located in areas with low macro-fracturing (Figure 1c), suggesting that structural integrity plays a significant role in deposit preservation.

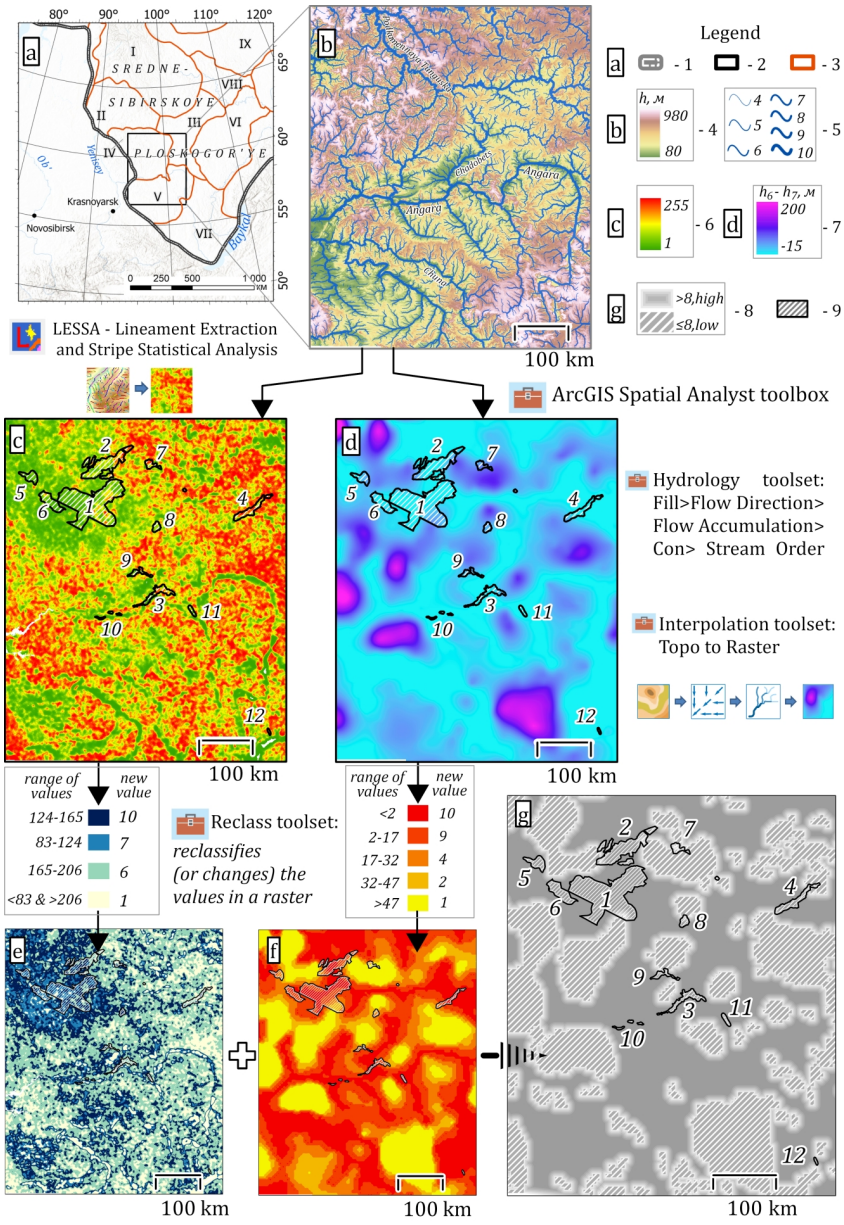

Figure 1. Creation of a prospectivity map using GIS tools: a) overview map; b) DEM of the study area and the stream order map created from it; c) macrofracturing of the sedimentary cover; d) difference between the base surfaces of the 6th and 7th orders; e) reclassification of the macrofracturing raster; f) reclassification of displacement amplitudes; g) comprehensive solution based on two factors.

Legend:

a: 1 — Siberian Platform; 2 — study area; 3 — petroleum province (I — North-Tungusskaya, II — South-Tungusskaya, III — Katangskaya, IV — Baikitskaya, V — Prisayano-Eniseiskaya, VI — Nepsko-Botuobinskaya, VII — Angaro-Lenskaya, VIII — Syugdzherskaya, IX — Anabarskaya);

b: 4 — DEM, scale 1:100 000; 5 — stream order map (the map does not show streams of less than 4th order because of their large number);

c: 6 — macrofracturing (standard units);

d: 7 — difference between the base surfaces of 6th and 7th orders (m);

g: 8 — likelihood of petroleum occurrence (high, low); 9 — hydrocarbon fields (1 — Yurubcheno-Tohomskoye, 2 — Kuyumbinskoye, 3 — Agaleyevskoye, 4 — Sobinskoye, 5 — Borshchevskoye, 6 — Omorinskoye, 7 — Shushukskoye, 8 — Ischuhskoye, 9 — Ilbokichskoye, 10 — Imbinskoye, 11 — Beryambinskoye, 12 — Bratskoye).

3.3. Creating a Prospectivity Map

ArcGIS geoprocessing tools were used to determine specific ranges of neotectonic indicators for a more precise and quantitative description of observed spatial correlations. First, all cells within the boundaries of known deposits were extracted from the macro-fracturing raster (Figure 1c) and the base surface difference raster (Figure 1d). Frequency distribution diagrams were then constructed for extracted cell values representing macro-fracturing intensity and neotectonic movement amplitudes.

The frequency distribution of macro-fracturing values approximates a normal distribution, with most deposits falling within a range of 124 to 165. In terms of deposit preservation potential, this range offers optimal conditions for undiscovered deposits. While visual analysis suggested deposits were mainly in low macro-fracturing areas, statistical analysis showed correlation with both low and moderate macro-fracturing. For neotectonic movement amplitudes, the distribution exhibits a positive skew, with peak frequencies occurring at low amplitude values. Most petroleum fields are associated with neotectonic movement amplitudes falling within two distinct ranges: −15 to 2 meters and 2 to 17 meters. These intervals are likely most favorable for new petroleum discoveries when considering neotectonic activity intensity.

The next step in creating a prospectivity map involves reclassifying the rasters of base surface differences and macro-fracturing using a unified scale (from 1 to 10), where 1 indicates areas least likely to contain deposits, and 10 represents the most promising locations. The final prospectivity map was generated through arithmetic addition of the two reclassified rasters (Figure 1f, e), producing a comprehensive solution ranking the study area according to its potential for new discoveries (Figure 1g).

4. Discussion

The prospectivity map illustrates areas of high potential, indicating locations with the most favorable conditions based on neotectonic movement intensity and sedimentary cover macrofracturing. The validity of this map is reinforced by the close alignment between known deposit boundaries and high-ranking areas in the proposed classification scheme.

In assessing the accuracy of the prediction, it's important to note that results were most significantly influenced by the cluster of deposits in the Yurubcheno-Tokhomskaya petroleum province, particularly the Yurubcheno-Tokhomskoye and Kuyumbinskoye petroleum fields. These large fields are predominantly situated in zones of low neotectonic activity and minimal macrofracturing. Smaller fields with different characteristics received lower weights in the reclassification process.

The Shushukskoye field appears to be in the least favorable position, situated in a region characterized by high-amplitude neotectonic movements and extensive macrofracturing. It is highly probable that this field is currently experiencing rapid deterioration.

The neotectonic phase in the Siberian Platform's evolution is critical for understanding the distribution of modern deposits, as the platform's structural layout reached its final form during the Late Cenozoic. Some active structures in the region may still be in the process of formation.

Conclusion

The proposed method is recommended for regional and preliminary exploration in poorly studied platform areas due to its high efficiency and cost-effectiveness. This method:

- requires no field;
- identifies important stages in the neotectonic history that critically influenced hydrocarbon deposits formation and destruction in the study area;
- enhances the reliability and value of DEM data interpretation by automating all stages of data processing, thus reducing time to results.

However, the significance of the macrofracturing factor is still poorly understood and requires additional studies.

Acknowledgments. This work was supported by the Ministry of Science and Higher Education of the Russian Federation under the agreement No. 075-15-2020-931 within the framework of the development program for the world-class Research Center "Efficient development of the global liquid hydrocarbon reserves".

References

Chernova I. Y., *Nourgaliev D. K.*, *Chernova O. S.*, *et al.* Applying the combination of GIS tools with upgraded structural and morphological methods for studying neotectonics // SOCAR Proceedings. — 2021. — P. 93–103. — DOI: 10.5510/OGP2021SI200560.

Filosofov V. P. Fundamentals of the morphometric method of searching for tectonic structures. — Saratov : Saratov State University named after N.G. Chernyshevsky, 1975. — P. 232. — (In Russian).

Lastochkin A. N. Neotectonic movements and the location of oil and gas deposits. — Leningrad : Nedra, 1974. — P. 68. — (In Russian).

Nurgaliev D. K., *Chernova I. Y.*, *Nugmanov I. I.*, *et al.* Scientific Foundations of Modern Technology for Forecasting Oil and Gas Potential of Territories // Scientific Notes of Kazan University, Natural Sciences Series. — 2009. — Vol. 151, no. 4. — P. 192–202. — (In Russian).

Seregin A. M., *Ferdman L. I.* Late Cenozoic tectonics of sedimentary basins of the Siberian Platform and hydrocarbon generation processes // Recent Tectonics of the Siberian Platform and Its Influence on Hydrocarbon Potential. — Moscow : Nauka, 1985. — P. 33–38. — (In Russian).

Sokolov B. A., *Egorov V. A.*, *Syagaeva E. N.* Influence of fault-block neotectonics on the distribution of petroleum fields across the Siberian Platform // Recent Tectonics of the Siberian Platform and Its Influence on Hydrocarbon Potential. — Moscow : Nauka, 1985. — P. 26–32. — (In Russian).

Varlamov I. P. Recent tectonics of petroleum-bearing regions of Siberia // Recent Tectonics of the Siberian Platform and Its Influence on Hydrocarbon Potential. — Moscow : Nauka, 1985. — P. 3–14. — (In Russian).

Zlatopolsky A. A. Program LESSA (Lineament Extraction and Stripe Statistical Analysis) automated linear image features analysis-experimental results // Computers & Geosciences. — 1992. — Vol. 18, no. 9. — P. 1121–1126. — DOI: 10.1016/0098-3004(92)90036-Q.

Zlatopolsky A. A. LESSA — Lineament Extraction and Stripe Statistical Analysis. — URL: https://www.lineament.ru (visited on 09/27/2024).

Russian Journal of Earth Sciences

Special Issue: "Data Science, Geoinformatics and Systems Analysis in Geosciences"

Forecast of the Distribution of Hydrocarbon Accumulations by Size. Status and Issues

L. M. Burshtein[1], **V. R. Livshits**[1,2]

[1]IPGG SB RAS, Novosibirsk, Russia
[2]NSU, Novosibirsk, Russia
* **Correspondence to:** Burshtein Lev M., levi@ipgg.sbras.ru

Abstract: The most important element of the structure of hydrocarbon resources is their distribution by accumulations of different sizes. The formalism of this direction is developed in detail. Estimates of the resource structure of the largest oil and gas provinces of Russia are carried out. However, the lack of a substantiated theoretical model for the formation of the distribution of accumulations by size gives rise to a number of problems, including practical ones. This concerns the forecast of the number of small accumulations and hydrocarbon resources concentrated in them in well-studied oil and gas systems, the forecast of distribution for poorly studied systems, and the identification of the relationship between distribution parameters and the geological characteristics of the oil and gas system. The explanation of some empirically established regularities, in particular, the stable nature of the value of the distribution parameter $\lambda \sim 2$, is of independent theoretical interest. The paper presents the current state of this complex of problems and some possible directions for their solution.

Keywords: oil and gas system, structure of hydrocarbon resources, distribution by size of deposits, truncated Pareto distribution.

Citation: Burshtein, L. M., and V. R. Livshits (2025), Forecast of the Distribution of Hydrocarbon Accumulations by Size. Status and Issues, *Russian Journal of Earth Sciences*, 25, ES2003, EDN: OUYFAZ, https://doi.org/10.2205/2025ES000962

1. Introduction

The most important element of the structure of hydrocarbon resources is their distribution by accumulations of different sizes. Research in this area emerged in the sixties and seventies of the twentieth century [*Arps et al.*, 1958; *Kaufman*, 1963]. The distribution of the sizes of the identified deposits in most cases was satisfactorily approximated by a logarithmically normal law. Analysis of changes in the sets of identified hydrocarbon accumulations with increasing exploration of the study area led to the assumption that the distribution of accumulations in nature is described by the Pareto power law with the value of the parameter λ close to 2 [*Shpilman*, 1972]:

$$\varphi(\theta) = \frac{C}{\theta^{\lambda}},\ \theta_0 \le \theta \tag{1}$$

Here $\varphi(\theta)$ is the distribution density function, θ is the size of the accumulation, λ, θ_0 are the distribution parameters, C is the normalizing factor.

Based on data from well-studied basins of the world, A. E. Kontorovich and V. I. Demin established that the distribution of hydrocarbon accumulations by the size of reserves is described by the truncated Pareto distribution they proposed [*Kontorovich et al.*, 1977; 1979]:

$$\varphi(\theta) = C \cdot \left(\frac{1}{\theta^{\lambda}} - \frac{1}{\theta_{\max}^{\lambda}}\right),\ \theta_0 \le \theta \le \theta_{\max}, \tag{2}$$

Research Article

Received: 15 November 2024
Accepted: 15 April 2025
Published: 23 May 2025

where θ_0, θ_{max} are respectively the minimum and maximum sizes of the cluster taken into account, C is the normalizing factor.

The results of V. I. Shpilman, A. E. Kontorovich, V. I. Demin were confirmed by the works of N. A. Krylov, Yu. A. Arsiriy and others.

The development of this direction led to a detailed development of the formal aspects of the application of the truncated Pareto distribution and an assessment of the structure of resources of the largest oil and gas provinces of Russia [*Kontorovich et al.*, 2017; 2021].

Nevertheless, a number of questions have not found convincing answers. Among them are:

1. To what extent are the type and parameters of the distribution established empirically for the right "tail" of the distribution of the studied large oil and gas systems (OGS) adequate for the left, understudied interval of the natural set of accumulations?
2. For poorly studied OGS, the problem of substantiating the type, parameters of the approximating distribution and their connection with the characteristics of the OGS is even stronger.
3. The empirical fact of the stable gravitation of the parameter λ in (2) to the value ~ 2 cannot be explained.

All these questions cannot be resolved without developing a sufficiently clear and meaningful model of the formation of distributions of hydrocarbon accumulations by size.

2. Methods and Results

Attempts to theoretically substantiate the type of accumulations' distribution and establish the relationship between its parameters and the characteristics of the host geological objects can be found in [*Kontorovich et al.*, 1988] and etc. These works show that the power-law nature of the distribution of accumulations is probably determined by the relationship between the processes of accumulation and dissipation of hydrocarbons in the deposit. Examples of the implementation of this approach are given below.

I. It is natural to consider the size θ of an individual hydrocarbon accumulation in the OGS as a consequence of accumulation and dissipation processes. As a first approximation, the changes in θ over time can be represented as [*Burshtein*, 2004]:

$$\frac{d\theta}{dt} = a - b \cdot \theta. \tag{3}$$

Here t is the time, a is the rate of hydrocarbon entry into the trap, b is the relative rate of destruction of the accumulation.

The parameters a and b can be interpreted as random variables, independent of time for long stages of OGS development. Then θ reaches a stationary value:

$$\frac{d\theta}{dt} = 0, \ \theta = \frac{a}{b}.$$

For statistically independent a and b, the density of the distribution of hydrocarbon accumulation $\varphi(\theta)$ has the form:

$$(\theta) = \frac{1}{\theta^2} \int_{\Omega_a} \varphi_1(a) \cdot \varphi_2\left(\frac{a}{\theta}\right) \cdot a \cdot da. \tag{4}$$

Here Ω_a is the integration domain depending on θ; φ_1 and φ_2 are the probability densities for the distributions of hydrocarbon accumulations in the OGS by a and b.

In the particular case where the parameters a and b are distributed uniformly, the explicit form of the density $\varphi(\theta)$ for sufficiently large θ is identical to the truncated Pareto distribution (2) with the exponent $\lambda = 2$.

It is difficult to expect a uniform distribution of the parameters a and b in real OGS. In the general case, the behavior of distribution (4) on the left tail (i.e. in the area of small accumulations) differs to the direction of decreasing the proportion of accumulations compared to the truncated Pareto distribution (2). Naturally, this circumstance is significant only for values $\theta > \theta_0$. On the right tail, distribution (4) retains a power-law character, with exponents λ depending on the type of φ_1 and φ_2.

Model (3) allows us to identify the qualitative influence of the age of the OGS on the shape of the distribution density $\varphi(\theta)$ and the value of the parameter λ [*Burshtein*, 2006].

The model considered above does not take into account the spatially distributed nature of the migration process, which precedes the process of hydrocarbon accumulation and should influence the type of distribution of accumulations.

II. It is accepted that secondary migration of oil occurs in the form of movement of primary accumulations. The pore medium is defined by a random field with an exponential correlation function. The speed of movement of the primary accumulation (globules) is determined by the forces of gravitational ascent. Multiple modeling of migration is performed at different values of the parameters of porosity distribution, permeability, and formation inclination angle, taking into account random fluctuations [*Livshits*, 2017]. The sought characteristics and their fluctuations were statistically estimated from a set of such realizations. This allowed us to identify the conditions under which the lateral migration of accumulations leads to the formation of their mass distribution corresponding to the Pareto distribution.

1. The main factor determining the occurrence of a power-law distribution is the distance from the centers of generation to the traps: a power-law distribution does not occur if the traps are located too close to the centers; a large distance from the traps also reduces the probability of occurrence of a power-law distribution, since in this case the globules suffer significant migration losses. Thus, for the occurrence of a power-law distribution, the process of globule migration is necessary, but without significant migration losses.
2. The influence of the filtration-capacitive and geometric parameters of the globule migration paths on the occurrence of a power-law distribution is small, and with an increase in the dispersion of these values it weakens.
3. The latter circumstance explains the fundamental nature of the power-law distribution of hydrocarbon accumulations by mass: it has a high probability of occurrence in a wide range of changes in the parameters of migration routes, i.e. it does not depend on the individual characteristics of the basin.

III. Among the approaches that justify the emergence of distributions with a "heavy", power-law tail, a large group consists of models based on the presence of a random component ("noise") in the system.

Let us assume that the change in the size of a single accumulation θ is described by an analogue of the equation (3):

$$\frac{d\theta}{dt} = f(\theta) + g(\theta) \cdot \xi(t). \tag{5}$$

Here t is the time; $f(\theta)$ is a deterministic function that describes the dynamics of a system; $g(\theta)$ is the amplitude of the dynamic stochastic component; $\xi(t)$ is the stochastic component.

Equation (5), under certain assumptions, corresponds to the Fokker-Planck equation for the distribution density $\varphi(\theta)$:

$$\frac{\partial \varphi(\theta)}{dt} = \frac{\partial}{\partial \theta}(f(\theta) \cdot \varphi(\theta)) + \frac{1}{2}\frac{\partial^2}{\partial \theta^2}(g^2(\theta) \cdot \varphi(\theta)).$$

For the stationary case, by specifying the functions $f(\theta)$ and $g(\theta)$, we can obtain:

$$f(\theta) = a;\ g(\theta) = -b \cdot \theta;\ \varphi(\theta) = \varphi_0 \cdot e^{\frac{-2a}{b^2 \cdot \theta}} \cdot \frac{1}{\theta^2}. \quad (6)$$

Asymptotically ($\theta \to \infty$) $\varphi(\theta)$ from (6) tends to the form (1) with an exponent of ~ 2.

Within the framework of the proposed approach, it is possible to estimate the parameters a and b for real OGS, but a number of substantive points and questions remains unclear:

1. It is easy to propose other types of functions $f(\theta)$ and $g(\theta)$, leading to a distribution of type (1);
2. It is not obvious that the stationarity condition is sufficiently satisfied for real OGS;
3. The nature and type of the stochastic component ξ raises questions;
4. It is clear that in a specific OGS the functions $f(\theta)$ and $g(\theta)$ must be individual for each accumulation and the size distribution for the entire set of accumulations must take this circumstance into account.

The list of such questions can be expanded and should be considered with further research.

3. Conclusion

The success of the application of the methodology for forecasting the most important element of the resource structure of large oil and gas systems — the distribution of hydrocarbon accumulations — created by the efforts of domestic researchers is beyond doubt. The existing approach is based on the empirically established power-law nature of this distribution, at least in the area of sufficiently large accumulations. The absence of a clear, well-founded theoretical model for the formation of hydrocarbon accumulations gives rise to a number of problems, including practical ones. First of all, this concerns the forecast of the number of small accumulations and hydrocarbon resources concentrated in them in well-studied OGS. There are grounds to assume that extrapolation of the type of distribution established by the set of identified large accumulations is not always adequate. Another problem is related to the forecast of the distribution of accumulations of hydrocarbons for poorly studied oil and gas systems. The validity of the forecast will be strengthened if the nature of the relationship between the distribution parameters and the geological characteristics of the oil and gas system is established. The explanation of some empirically established regularities, in particular the stable nature of the value of the parameter $\lambda \sim 2$, is of independent theoretical interest.

Acknowledgments. The work was carried out within the framework of the state program FSR FWZZ-2022-0007.

References

Arps J. J., *Roberts T. G.* Economics of Drilling for Cretaceous Oil on East Flank of Denver-Julesburg Basin // AAPG Bulletin. — 1958. — Vol. 42, no. 11. — P. 2549–2566. — DOI: 10.1306/0BDA5BF7-16BD-11D7-8645000102C1865D.

Burshtein L. M. Possible control of size distribution of oil and gas fields // Geology and geophysics. — 2004. — No. 7. — P. 815–825. — (In Russian).

Burshtein L. M. Statistical estimation of parameters of size distribution of oil accumulations in poorly studied sedimentaru basins // Geology and geophysics. — 2006. — No. 9. — P. 1013–1023. — (In Russian).

Kaufman G. M. Statistical Decision and Related Techniques in Oil and Gas Exploration. — Prentice-Hall, 1963.

Kontorovich A. E., *Demin V. I.* Method for assessing the quantity and distribution of oil and gas deposits in large oil and gas basins // Oil and gas geology. — 1977. — No. 12. — P. 18–26. — (In Russian).

Kontorovich A. E., *Demin V. I.* Prognosis of the number and distribution of the oil and gas fields in respect to their rezerves // Geologiya i geofizika. — 1979. — Vol. 20, no. 3. — P. 26–46. — (In Russian).

Kontorovich A. E., *Burshtein L. M.*, *Gurevich G. C.*, *et al.* Quantitative assessment of the prospects of oil and gas content of poorly detected regions. — Moscow : Nedra, 1988. — 223 p. — (In Russian).

Kontorovich A. E., *Livshits V. R.* New methods of assessment, structure, and development of oil and gas resources of mature petroleum provinces (Volga-Ural province) // Russian Geology and Geophysics. — 2017. — Vol. 58, no. 12. — P. 1453–1467. — DOI: 10.1016/j.rgg.2017.11.010.

Kontorovich A. E., *Livshits V. R.*, *Burshtein L. M.*, *et al.* Assessment of the Initial, Promising, and Predicted Geologic and Recoverable Oil Resources of the West Siberian Petroleum Province and Their Structure // Russian Geology and Geophysics. — 2021. — Vol. 62, no. 5. — P. 576–588. — DOI: 10.2113/rgg20204302.

Livshits V. R. Lateral migration of hydrocarbons as a possible mechanism of origin of their power-law distribution by mass // Russian Geology and Geophysics. — 2017. — Vol. 58, no. 3/4. — P. 299–309. — DOI: 10.1016/j.rgg.2016.09.006.

Shpilman V. I. Methods for predicting the size of deposits // Proceedings of the Institute of Zap-SibNIGNI. — 1972. — Vol. 53. — P. 118–126. — (In Russian).

Russian Journal of Earth Sciences

Special Issue: "Data Science, Geoinformatics and Systems Analysis in Geosciences"

Retrospective Analysis of the Spectral Properties of a Bog Changed by Road Construction

A. A. Kaverin[1], **D. V. Ilyasov**[1], **I. V. Filippov**[1]

[1]Yugra State University, Khanty-Mansiysk, Russia
* **Correspondence to:** Danil Ilyasov, d_ilyasov@ugrasu.ru

Abstract: Peatland ecosystems ecosystems in mineral extraction areas experience anthropogenic impacts because of the construction of seismic survey lines, power lines, temporary and permanent roads, as well as pipelines. Accurately assessing the impact of construction projects such as roads on ecosystems can provide scientific basis for ecosystem protection. The assessment of the impact of roads on moisture and vegetation properties could be based on information about these properties before and after construction. This study proposes an algorithm for delineating the road influence zone on a bog by analyzing retrospective changes in spectral properties before and after road construction. Using archival Landsat images (2000–2021), we quantified statistically significant changes in spectral indices (NDWI, NDMI, MNDWI, GVMI, EVI, and CVI) around a road built in 2007 on an oligotrophic bog in Western Siberia. It was found that over the time interval from 2007 to 2021, the MNDWI index significantly decreased by 125% on a specific area of 96,280 m^2 km^{-1}. Statistically significant increases in the spectral indices NDWI, NDMI, GVMI, EVI, and CVI were observed only sporadically (in space). The results presented will serve as the basis for calculating changes in the specific emissions of CO_2 and CH_4 in the studied area. In addition, the obtained data can be used for a preliminary assessment of the area and magnitude of possible changes in the properties of the wetlands before the construction of permanent and temporary roads and can also be scaled to a larger area.

Keywords: road construction, oligotrophic bog, wetland vegetation cover, moisture of the underlying surface, Western Siberia.

Citation: Kaverin, A. A., D. V. Ilyasov, and I. V. Filippov (2025), Retrospective Analysis of the Spectral Properties of a Bog Changed by Road Construction, *Russian Journal of Earth Sciences*, 25, ES2004, EDN: NHBCVQ, https://doi.org/10.2205/2025ES000963

1. Introduction

Peatland ecosystems are natural long-term sink of atmospheric CO_2, stored in the peat, and they are a source of CH_4. This makes them one of the key components of the carbon cycle of the land-atmosphere system [*IPCC Climate Change…*, 2013; *Joosten et al.*, 2016]. Throughout the Holocene, wetlands have accumulated 500 Gt of carbon in peat deposits, which is comparable to the phytomass of forests, assuming they occupy an order of magnitude smaller area [*Assessment on Peatlands...*, 2008; *Dise*, 2009; *Xu et al.*, 2018]. Given increasing anthropogenic pressures and climate change, preserving these carbon stocks and maintaining the sink function of peatlands is critically important [*IPCC Climate Change…*, 2013; *Joosten*, 2024].

Wetland ecosystems, especially those located in mining areas, experience anthropogenic impact from the development of seismic survey lines, power lines, temporary and permanent roads, and pipeline installations [*Pasher et al.*, 2013; *Saraswati et al.*, 2019]. These interventions have direct and indirect effects on the carbon absorption capacity of wetlands.

Research Article

Received: 15 November 2024
Accepted: 15 April 2025
Published: 23 May 2025

Roads are the most extensive infrastructure and one of the most significant in terms of their impact on the natural hydrological conditions and vegetation cover of peatlands [*Bocking et al.*, 2017; *Campbell et al.*, 2012; *Partington et al.*, 2016; *Plach et al.*, 2017; *Saraswati et al.*, 2023; *Strack et al.*, 2017]. The construction of roads can lead to localized flooding and/or drainage of wetland areas over a stretch of several tens or hundreds of meters [*Saraswati et al.*, 2019; *Strack et al.*, 2017]. Directly under the roadbed, peat is compacted, which disrupts its hydrological conductivity and slows down lateral soil water flow. Changes in hydrological regime, moisture of the underlying surface, and water table levels are particularly severe in areas where roads are constructed across water flow lines. Several years after road construction, the altered hydrological regime can lead to changes in wetland vegetation [*Saraswati et al.*, 2023; *Strack et al.*, 2017], which may collectively increase CH_4 emissions and/or reduce CO_2 assimilation.

To assess the impact of roads on the hydrology and vegetation properties of wetlands, it is necessary to have information about these properties before and after road construction. Remote sensing (RS) data provide a valuable tool for such analyses, enabling the evaluation of spectral characteristics of wetland surfaces over time. Moreover, the use of RS data allows for accounting for the spatio-temporal heterogeneity of the underlying surface properties, which is extremely high in peatland ecosystems.

The aim of our study was to localize the zone of road influence on the peatland by analyzing the retrospective dynamics of the spectral properties of the underlying surface in the period before and after road construction.

2. Methodology

The study area is located at a boreal patterned bog (60°50′41″N and 70°6′20″E), which is situated 58 km east-southeast from Khanty-Mansiysk, Khanty-Mansi Autonomous Okrug (KhMAO), Russia. The road to the study area at the boreal patterned bog was constructed in 2007: it is an earthen embankment up to 2 meters high without asphalt paving. The road is positioned across the natural bog water flows directed from southwest to northeast: thus, one part of the bog complex (upon visual inspection) was presumably flooded, while the other was drained.

The impact of road construction (for a section 3.0 km long) on soil moisture and the vegetation cover of the bog complex was assessed using a retrospective analysis of the spatiotemporal variability of the spectral indices NDWI, NDMI, MNDWI, GVMI, EVI, and CVI. Median cloud-free summer (June–September) composites were generated using Google Earth Engine with Landsat-7 (2000–2005), Landsat-5 (2007–2011), and Landsat-8 (2013–2021) imagery.

Then, in MATLAB (MathWorks, USA), using the "ranksum" function, a pixel-by-pixel Mann-Whitney test ($p = 0.05$; grouping variable: "before" or "after" road construction) was conducted on a time series from 2000 to 2021. The aim was to create a sample of only those pixels where statistically significant differences in spectral index values by grouping variable were observed. Thus, the spatial localization of the road impact zone on the bog was performed. Then, a quantitative assessment of the relative magnitude of spectral index changes for the localized impact zone was carried out. For this, the median values of the spectral indices for significantly differing pixels (by space, for each year) were calculated using the "median" function. Finally, the difference in the averaged (from 2000 to 2005 and from 2007 to 2021) medians of the spectral index values before and after road construction were calculated.

3. Results and discussion

The retrospective analysis of the spectral characteristics of the underlying surface showed that: 1) the majority (71–84%) of pixels showing statistically significant differences (Mann-Whitney test, $p < 0.05$) between pre- and post-construction periods were concentrated along a 250-meter zone along the road (71–84% of them are within a 125-meter zone) 2) the largest share among them (from 81% in the case of MNDWI to 100% in the

case of CVI) consists of areas with a decrease of spectral indices (Figure 1, brown) and they are mainly located northeast of the road, that is, on the drained part of the bog 3) contrary to expectations, a statistically significant increase in the spectral indices was not detected southwest of the road in the supposedly "waterlogged" part of the bog and is generally sporadic within the 250-meter zone from the road (Figure 1, turquoise). The decrease in median values (when comparing periods before and after road construction) of NDWI, NDMI, MNDWI, and GVMI ranged from −14 to −125%, which indicates: 1) the reduction of water content in the vegetation 2) the formation of drier soil conditions 3) the development of water stress in plants 4) the deterioration of their condition or replacement by more drought-resistant species.

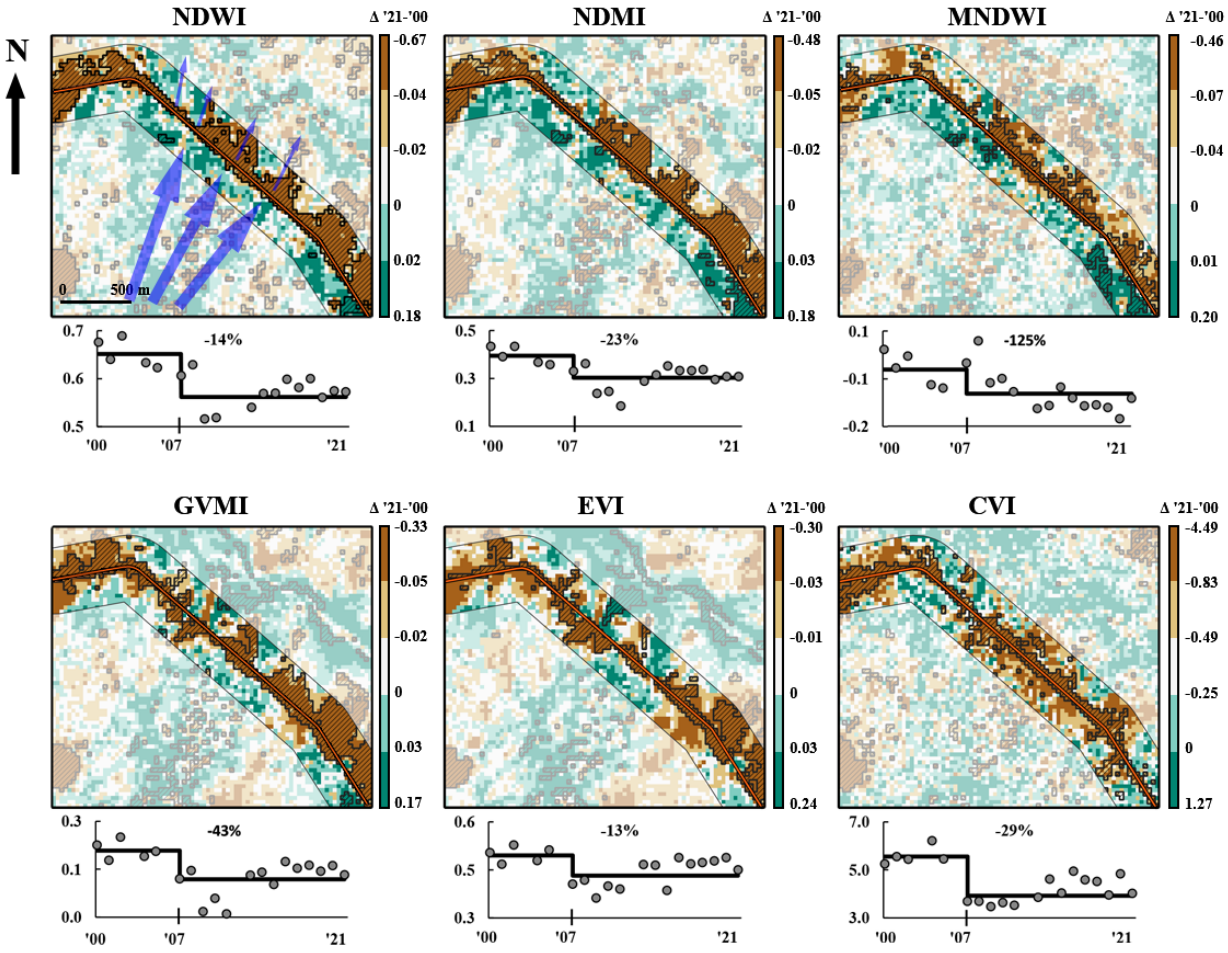

Figure 1. Schemes of the differences in median spectral index values in the bog area intersected by the road for the period before (2000–2005) and after (2007–2021) its construction. Pixels that significantly differed according to the Mann-Whitney test ($p \leq 0.05$, grouping variable: "before" or "after" road construction for the entire period under consideration) are shown with black outlines and hatching. Below the maps, the difference in median spectral index values (in groups before and after road construction) for pixels with $p \leq 0.05$ and their values by years are shown. Blue arrows indicate the direction of bog water flows.

The decrease in average EVI and CVI values was −13% and −29% respectively, which is usually associated with: 1) a reduction in the density of green vegetation 2) a decrease in chlorophyll content in leaves 3) a decline in productivity and photosynthetic activity of the vegetation cover. The decrease in EVI and CVI was more evenly distributed to the northeast and southwest of the road than NDWI, NDMI, MNDWI, and GVMI.

Conservatively evaluating the changes in the properties of the underlying surface of the bog because of road construction, we present the smallest impacted area: it was obtained using the MNDWI index and amounted to 288,839 m^2 (or 96,280 m^2 per km of road). In this zone, only the part that was subjected to statistically significant drying was considered.

Compared to earlier studies conducted on bog areas intersected by roads along bog water flow lines [*Saraswati et al.*, 2019; 2023; *Strack et al.*, 2017], we show a significantly larger (reaching up to 250 meters in some places) zone of road impact on bog moisture. The main consequence of road construction was the drainage of the bog portion downstream (to the northeast) from the road, whereas flooding upstream (to the southwest) was not detected. We hypothesize that the excess moisture in the bog area did not lead to terrain flooding due to drainage through one of two paths: 1) lateral drainage through roadside ditches leading outside our study area 2) engineered drainage via subsurface pipes directing water northeastward to adjacent river systems.

Undoubtedly, the vegetation indices are a relative indicator of changes in the properties of the underlying surface, and in our case, they are more qualitative (due to the lack of ground data on phytomass, surface moisture, and plant properties in previous years). However, they allowed us to localize the area of road impact on the vegetation and soil cover, as well as confirm the presence of long-term changes related not to random factors but specifically to road construction.

4. Conclusion

By implementing an algorithm to analyze retrospective spectral dynamics before and after road construction, we successfully localized the zone of hydrological and ecological impact on the studied bog. Key findings include that during the time interval from 2007 to 2021 (directly after the road was built), the MNDWI index value significantly decreased over a specific area of 96,280 m^2 km^{-1} by 125%. Also, statistically significant growth in the spectral indices NDWI, NDMI, GVMI, EVI, and CVI was observed only sporadically. The results presented will serve as a basis for calculating changes in the specific emissions of CO_2 and CH_4 in the area studied. Additionally, the obtained data can be used for a preliminary assessment of the area and magnitude of possible changes in the properties of the underlying surface of bogs before the construction of permanent and temporary roads and can also be scaled to a larger territory.

Acknowledgments. The research was supported by the state assignment of Ministry of Science and Higher Education of the Russian Federation to organize a new young researcher Laboratory in Yugra State University (Research number 1022031100003-5-1.5.1) as a part of the implementation of the National Project “Science and Universities”.

References

Assessment on Peatlands, Biodiversity and Climate Changee: Main Report / ed. by F. Parish, A. Sirin, D. Charman, *et al.* — Wageningen, The Netherlands : Global Environment Centre, Kuala Lumpur, Wetlands International, 2008.

Bocking E., *Cooper D. J.*, *Price J.* Using tree ring analysis to determine impacts of a road on a boreal peatland // Forest Ecology and Management. — 2017. — Vol. 404. — P. 24–30. — DOI: 10.1016/j.foreco.2017.08.007.

Campbell D., *Bergeron J.* Natural Revegetation of Winter Roads on Peatlands in the Hudson Bay Lowland, Canada // Arctic, Antarctic, and Alpine Research. — 2012. — Vol. 44, no. 2. — P. 155–163.

Dise N. B. Peatland Response to Global Change // Science. — 2009. — Vol. 326, no. 5954. — P. 810–811. — DOI: 10.1126/science.1174268.

IPCC. Climate Change 2013: The Physical Science Basis. Contribution of Working Group I to the Fifth Assessment Report of the Intergovernmental Panel on Climate Change / ed. by T. F. Stocker, D. Qin, G.-K. Plattner, *et al.* — Cambridge, UK, New York, USA, 2013.

Joosten H., *Sirin A.*, *Couwenberg J.*, *et al.* The role of peatlands in climate regulation // Peatland Restoration and Ecosystem Services. — Cambridge University Press, 2016. — P. 63–76. — DOI: 10.1017/cbo9781139177788.005.

Joosten H. Peatland Must Be Wet: Advance Rewetting, Stop Peat Extraction // 3 Degrees More. — Springer Nature Switzerland, 2024. — P. 179–203. — DOI: 10.1007/978-3-031-58144-1_9.

Partington M., Gillies C., Gingras B., et al. Resource roads and wetlands: A guide for planning, construction and maintenance. — Canada : FPInnovations, 2016.

Pasher J., Seed E., Duffe J. Development of boreal ecosystem anthropogenic disturbance layers for Canada based on 2008 to 2010 Landsat imagery // Canadian Journal of Remote Sensing. — 2013. — Vol. 39, no. 1. — P. 42–58. — DOI: 10.5589/m13-007.

Plach J. M., Wood M. E., Macrae M. L., et al. Effect of a semi-permanent road on N, P, and CO2 dynamics in a poor fen on the Western Boreal Plain, Canada // Ecohydrology. — 2017. — Vol. 10, no. 7. — DOI: 10.1002/eco.1874.

Saraswati S., Strack M. Road Crossings Increase Methane Emissions From Adjacent Peatland // Journal of Geophysical Research: Biogeosciences. — 2019. — Vol. 124, no. 11. — P. 3588–3599. — DOI: 10.1029/2019jg005246.

Saraswati S., Xu B., Strack M. Presence of Access Roads Results in Reduced Growing Season Carbon Uptake in Adjacent Boreal Peatlands // Journal of Geophysical Research: Biogeosciences. — 2023. — Vol. 128, no. 1. — DOI: 10.1029/2022jg007206.

Strack M., Softa D., Bird M., et al. Impact of winter roads on boreal peatland carbon exchange // Global Change Biology. — 2017. — Vol. 24, no. 1. — DOI: 10.1111/gcb.13844.

Xu J., Morris P. J., Liu J., et al. PEATMAP: Refining estimates of global peatland distribution based on a meta-analysis // CATENA. — 2018. — Vol. 160. — P. 134–140. — DOI: 10.1016/j.catena.2017.09.010.

Russian Journal of Earth Sciences

Special Issue: "Data Science, Geoinformatics and Systems Analysis in Geosciences"

Curie Point Depths of the Amur Tectonic Plate

A. N. Didenko[1,2], **M. Yu. Nosyrev**[2], **G. Z. Gilmanova**[2]

[1]Geological Institute RAS, Moscow, Russia
[2]Institute of Tectonics & Geophysics FEB RAS, Khabarovsk, Russia
* **Correspondence to:** Didenko Alexei N., alexei_didenko@mail.ru

Abstract: Based on the analysis of the anomaly magnetic field for the Amur Plate and adjacent territories, a Curie Point Depth (CPD) map has been constructed, which we identify with the isotherm 578°C — the temperature of the Curie point of magnetite. Within the Amur plate, the CPD values range from 13.4 to 38.0 km. Three large areas are clearly visible on the map: 1) NE-trending zone with CPD values of 25–20 km — Yellow Sea-Korean Peninsula-Sea of Japan; 2) ENE-trending central zone with CPD values of 30–38 km. Large depth values are due to the presence of the late Paleozoic and Mesozoic sedimentary basins of Erlyan, Songliao and Sredneamursky; 3) ENE-trending central zone with CPD values of 30-38 km. Large depth values are due to the presence of the late Paleozoic and Mesozoic sedimentary basins of Erlyan, Songliao and Sredneamursky. The fourth area of decrease in CPD values spatially coincides with volcanic structures of Pliocene-Pleistocene age in the area of the Toko Stanovik. Comparison of the generated CPD map with the Amur plate boundaries determined mainly from seismic data shows that the surface boundaries of the plate coincide mainly with the zones of the largest gradients of the 578°C isotherm distribution in depth.

Keywords: Amur plate, anomaly magnetic field, spectral analysis, Curie point depth.

Citation: Didenko, A. N., M. Yu. Nosyrev, and G. Z. Gilmanova (2025), Curie Point Depths of the Amur Tectonic Plate, *Russian Journal of Earth Sciences*, 25, ES2005, EDN: NUVKQI, https://doi.org/10.2205/2025ES000964

1. Introduction

The structural study of the upper shell of the solid Earth based on spectral analysis of magnetic anomalies is one of the components of deep investigations using a multidisciplinary approach. And while in the vast majority of cases the magnetized layer on the continents is located within the earth's crust, in the case of the oceanic lithosphere, secondary magnetic rocks (serpentinized ultrabasites) belong to the upper mantle according to petrological criteria. The main task here is to determine the depth to the bottom of the magnetized layer or, as it is often called, the Curie Point Depth (CPD). The presence of this boundary is due to an increase in temperature with depth and a transition of accessory magnetic minerals found in rocks from a ferrimagnetic state to a paramagnetic one. For continental regions, this is the Curie temperature for magnetite which is the main carrier of magnetism in the continental lithosphere.

Within continental areas, the distribution of surface heat flow and deep thermal structures may differ due to the long-term evolution of the latter and thermal disturbances at late stages through filtration and rise of fluids to the surface. In continental lithosphere, delays may be observed between changes in temperature of the underlying asthenospheric and surface heat flow measurements. The heat generated by the radioactive decay of K, U, and Th isotopes also contributes to the total surface heat flow of the continents. Therefore, the CPD estimation and interpretation is important both in connection with the study of deep mantle heat flow, and from the point of view of structural, tectonic and geodynamic reconstructions.

Research Article

Received: 15 November 2024
Accepted: 15 April 2025
Published: 23 May 2025

Large tectonic units of the southern Far East are characterized by CPD values only within limited areas [*Didenko et al.*, 2017; *Gao et al.*, 2015; *Wang et al.*, 2018; *Xiong et al.*, 2016], which makes it difficult to obtain a complete picture of the deep structure of the eastern Central Asian fold belt and its junction with the Pacific belt. To fill this gap, we chose the Amur plate (Figure 1), which is one of the main tectonic megastructures in the southeast of the Eurasian continent at the Mesozoic-Cenozoic geodynamic stage, as an object of CPD estimations. The following tasks were defined for the study: 1) estimation of the depth to the bottom of magnetic sources using the centroid method based on spectral analysis of magnetic anomalies [*Tanaka et al.*, 1999] of CPD for window squares of 200×200 km covering the entire Amur plate and adjacent territories; and 2) construction of a CPD model of the Amur plate and adjacent territories using the ArcGis geospatial platform [*ArcGIS…*, 2011].

(**a**) Amur plate is highlighted by white hatching. Orthographic projection, central meridian is 120°.

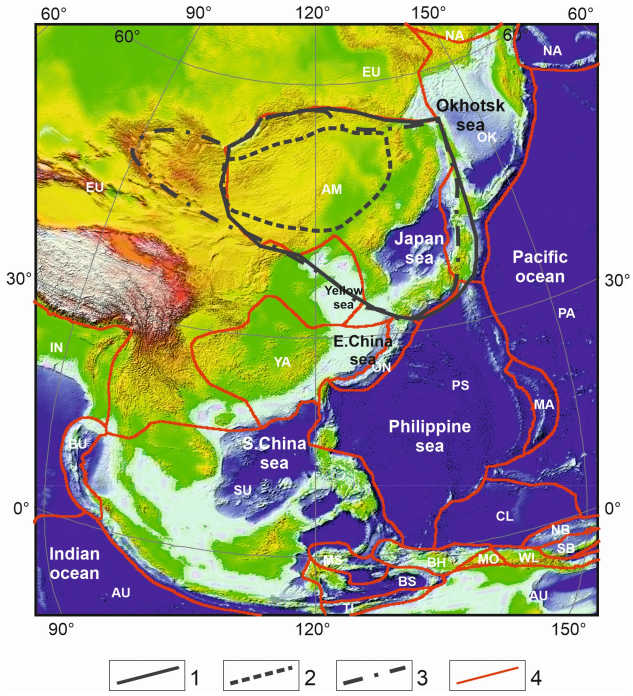

(**b**) 1–4 — boundaries of the Amur lithospheric plate after: 1 — [*Yarmolyuk et al.*, 2019], 2 — [*Imaev et al.*, 2003], 3 — [*Petit et al.*, 2004], 4 — [*Argus et al.*, 2011]. The plates are indicated by abbreviations: AM — Amur, AU — Australian, BH — Birds Head, BS — Banda Sea, BU — Burma, CL — Caroline, EU — Eurasia, IN — India, MA — Mariana, MO — Maoke, MS — Molucca Sea, NA — North America, NB — North Bismarck, OK — Okhotsk, ON — Okinawa, PA — Pacific, PS — Philippine Sea, SB — South Bismarck, SA — Sunda, TI — Timor, WL — Woodlark (Woodlark), YA — Yangtze. Orthographic projection, central meridian is 120°.

Figure 1. Position of the Amur plate: a on the world map and b in the system of lithospheric tectonic plates of Southeast Asia after [*Argus et al.*, 2011] with amendments and additions.

It should be mentioned that the CPD value was calculated for the entire Earth, except for the polar regions [*Li et al.*, 2017], using the fractal method based on the analysis of the EMAG2 Earth Magnetic Anomaly Model [*Maus et al.*, 2009]. Firstly, in our study, we used the latest EMAG2 version 3 [*Meyer et al.*, 2017] grid, and secondly, CPD estimations were performed using the classical centroid method [*Tanaka et al.*, 1999].

2. Boundaries of the Amur lithospheric plate

Continental and subcontinental lithospheric plates are complex in geological structure and composition, which is, to a large extent, characteristic of plate boundaries represented as extended banded zones of hummocking and fragmentation, the identification of which is often controversial [*Deep Structure…*, 2010]. This fully applies to the Amur lithospheric plate.

Since the identification of the Amur lithospheric plate as a self-dependent geodynamic unit [*Yarmolyuk et al.*, 2019] its boundaries have been the subject of debate. There are at least 10 variants of the Amur plate boundaries; for more details see [*Ashurkov et al.*, 2011; *Li et al.*, 2019]. Figure 1b, in addition to the first model of plate boundaries after [*Yarmolyuk et al.*, 2019], shows three more models. The first two are models of extreme values in terms of area covered: the minimum area model of [*Imaev et al.*, 2003] and the maximum area model of [*Petit et al.*, 2004]. And the third is the Global Plate Model [*Argus et al.*, 2011], which is most often used in present-day geodynamic reconstructions and is in good agreement with the model developed by [*Yarmolyuk et al.*, 2019], with the exception of the southern part of Sakhalin, Hokkaido, the northern part of Honshu Island and the Yellow Sea. The most recent model of the Amur plate boundary is used in this study.

3. The data used and methodology of estimations

The anomalous magnetic field of the Amur plate area (Figure 2) is heterogeneous and reflects the large tectonic units of the region according to the magnetic properties of the rocks that compose them. The field strength varies from −637 to +1366 nT at an amplitude of about 700 nT, without taking into account local positive magnetic anomalies in iron ore deposits. Sedimentary terranes of orogenic belts, Mesozoic-Cenozoic superimposed troughs and depressions filled with non-magnetic sediments are distinguished by a reduced and weakly differentiated magnetic field. The marginal parts of cratons and ancient blocks in the Central Asian belt are characterized by an alternating magnetic field, where positive magnetic anomalies are associated with both ancient metamorphosed basic and ultrabasic igneous rocks, and late basic intrusions. Northeast-oriented anomalous zones are dominant in the magnetic field, with two main strike azimuths of approximately 30 and 60 degrees. Zones of positive magnetic anomalies of this orientation are hundreds to thousands of kilometers long with a width of 100–200 km. The calculations were carried out using the centroid method under the assumption of a random distribution of magnetic sources [*Tanaka et al.*, 1999] with the determination of their top and bottom. This method was chosen, first of all, for the absence of any requirements for preliminary knowledge of the magnetization of the medium.

At the initial stage, taking into account the large extent of the study area from north to south, the magnetic field was transformed to the pole. Then, considering the range of CPD values in the interval between 13 and 48 km based on the data from previous studies in discrete regions of Southeast Asia [*Didenko et al.*, 2017; *Gao et al.*, 2015; *Wang et al.*, 2018; *Xiong et al.*, 2016], the entire study area was divided into square windows of 200×200 km, for which depths to the bottom of the magnetized layer were calculated. The window step in longitude was 100 km (i.e. with 50% overlap), in latitude — 200 km. The calculation results were related to the window center. As a result, the calculations were performed in 940 windows, with the network of window central points of 100×200 km.

The subsequent steps for each sheet included the same operations.

1. Calculation of the average circular energy spectrum for each sheet based on the implementation of the fast Fourier transform.
2. Calculation of spectra to estimate the depths to the centroid and top of the magnetic body after [*Tanaka et al.*, 1999] using the following formulas:

$$\ln\left[\frac{P^{1/2}}{|S|}\right] = \ln A - 2\pi|S|Z_0$$

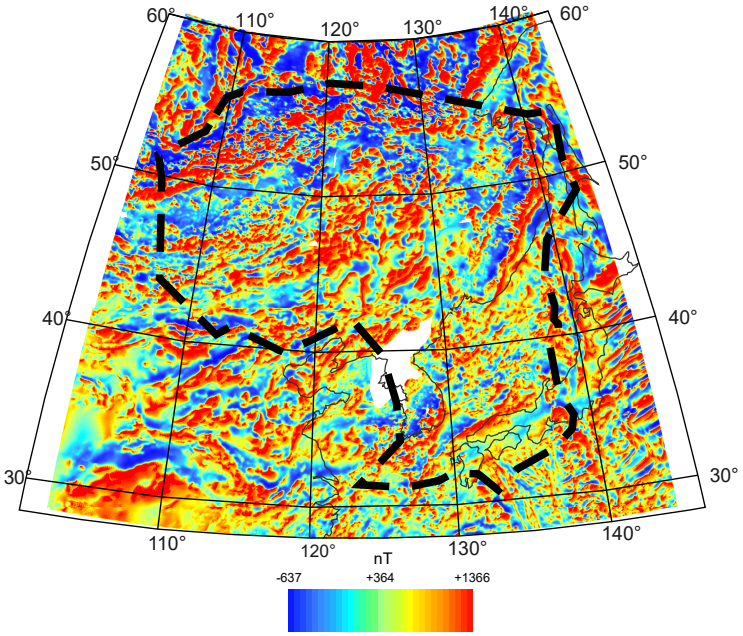

Figure 2. Maps of the anomalous magnetic field. Observed anomalous field based on the EMAG2v3 model [*Meyer et al.*, 2017]. Amur plate boundaries are shown by a black dashed line. The Gauss-Kruger projection is used, the central meridian is 123°.

and

$$\ln P^{1/2} = \ln B - 2\pi|S|Z_t$$

where Z_0, Z_t — centroid and top bound of the magnetic source, respectively, P — power spectrum, S — cyclic frequency, A and B — magnetization-dependent constants.

3. Since P and S are known from the previously calculated spectrum, Z_0 and Z_t are estimated, and then the depth to the bottom of the magnetic body: $Z_b = 2Z_0 - Z_t$. Since the magnetic field model [*Meyer et al.*, 2017] is computed for an altitude of 4 km above the geoid surface, a correction is introduced in Z_b to bring it to the true depth.

Another important aspect of the calculation method is the choice of frequency intervals for determining the center (Z_0) and the upper edge of the centroid (Z_t). Based on the analysis of the above mentioned works, the interval 0–0.025 cycles/km (0–0.157 rad×km^{-1}) was chosen for calculating Z_0, and the interval 0.042–0.075 cycles/km (0.26–0.47 rad×km^{-1}) was chosen for calculating Z_t. The calculation intervals were fixed for all spectra.

3.1. A brief introduction to the CPD map and some conclusions

Depth calculations in ArcGis, using the Natural Neighbor algorithm, culminated in CPD map construction (Figure 3a), which we identified with the 578 °C isotherm, that is, the Curie temperature for magnetite.

Within the Amur plate, the CPD values range from 13.4 to 38.0 km; and although the geometric mean (23.8), median (24.3), and mode (25.3) are close to the arithmetic mean (24.5±5.7), the Shapiro-Wilk test showed a significant deviation from the normal distribution ($p = 0.0008, W = 0.9793$) with right-sided asymmetry (0.26) and negative excess (−0.7062).

The computed map (Figure 3a) is differentiated, with three distinct domains:

- NE-trending zone with CPD values of 25–20 km — Yellow Sea-Korean Peninsula-Sea of Japan (Figure 3a). The basement area of the Korean Peninsula is composed of Precambrian rocks and belongs to the North China Platform (Figure 3b), whereas the opening of the Sea of Japan began in the Middle Miocene by breaking off and rotating counterclockwise (roll-back mechanism) of the northeastern segment of the Japanese Island Arc;

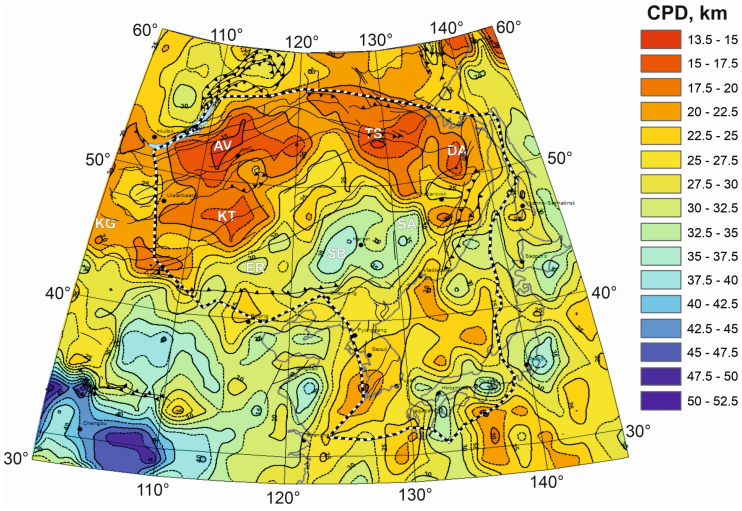

(**a**) Map CPD of the Amur plate and adjacent areas and tectonic scheme.

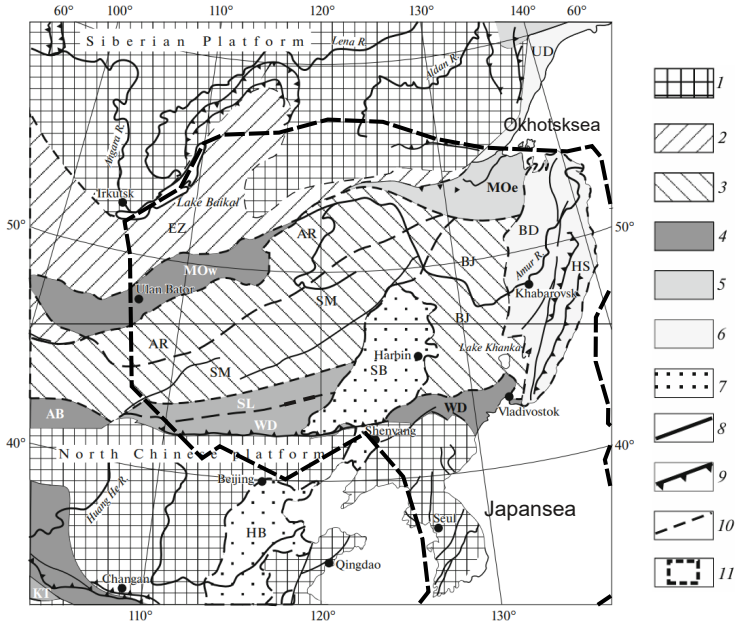

(**b**) Map CPD of of the eastern Central Asian fold belt.

Figure 3. a. CPD map (this study). Letter designations indicate distribution areas of: 1) giant and large granitoid batholiths (AV – Angara-Vitim, DA – Dusse-Alin, KG – Khangai, KT – Khantei); 2) mantle feeder structures (TS – Toka, Verkhne-Zeya, Zeya); 3) sedimentary basins (ER -Erlian), SA – Sredneamursky, SB – Songliao). Position and type of faults are copied from (b).
b. Tectonic scheme compiled after [*Didenko et al.*, 2016] with additions. (1) undivided Precambrian crust; (2–6) orogenic belts: (2) Caledonian, (3) Variscan (Hercynian); (4) Early Cimmerian, (5) Late Cimmerian, (6) Pacific (Yan Shan); (7) Mesozoic sedimentary basins; (8) faults, (9) thrust faults; (10) boundaries of terranes; (11) boundary of the Amur Plate. Letters show orogenic belts (terranes): (AB) Atas-Bogdo, (AR) Argun–Mamyn, (BD) Badzhal, (BJ) Bureya-Jiamusi, (EZ) Yenisei-Transbaikalia, (HS) Sikhote Alin, (KT) Kun Lun–Tsilin, (MOw) Mongol–Okhtsk (western), (MOe) Mongol–Okhotsk (eastern), (SL) Solonker, (SM) South Mongol–Khingan, (UD) Uda volcanic belt, (WD) Wundurmiao (Shara-Muren); Sedimentary basins: (HB) Hubei, (SB) Songliao.
In (a) and (b) the Gauss-Kruger projection is used, the central meridian is 123°.

- ENE-trending central zone with CPD values of 30–38 km. Large depth values are due to the presence of the late Paleozoic and Mesozoic sedimentary basins of Erlyan, Songliao and Sredneamursky (Figure 3a). The generalized tectonic diagram also clearly

shows the northeast strike zone formed by sedimentary basins — Hubei in the south and Songliao in the north (Figure 3b);

- northern zone of sublatitudinal strike with CPD values between 13.4 and 22 km. Figure 3a shows four areas of reducing the CPD. In the west and east, three areas spatially coincide with the late Paleozoic Angara-Vitim and Mesozoic Khentei and Dusse-Alin giant granitoid batholiths [*Yarmolyuk et al.*, 2019]. The formation of gigantic masses of granitoids in these three areas is probably associated with the closure of the Mongol-Okhotsk Paleocean. This can be confirmed by the spatial coincidence of the minimum CPD depths in the northern zone (Figure 3a) with the Early Cimmerian in the west and Late Cimmerian in the east orogenic belts (Figure 3b), marking the closure of the western and eastern parts of the Mongol-Okhotsk paleoocean, respectively. In the center of the zone of reducing the CPD, in the area of the Toko-Stanovik, Yu. F. Malyshev recognized the so-called mantle feeder structures identified with a mantle plume (quoted from [*Sakhno*, 2008]). This is supported by numerous volcanic structures in the area of the Toko-Stanovik filled with alkaline basaltoids with an age of 0.28–7.9 Ma [*Sakhno*, 2008].

It can be argued that the features of drawing the CPD map of the Amur Plate (Figure 3a), performed in this work, find a completely acceptable explanation when compared with the tectonic structure of the region (Figure 3b).

Comparison of the generated CPD map with the Amur plate boundaries determined mainly from seismic data [*Argus et al.*, 2011] and shown in Figure 1, (shows that the surface boundaries of the plate coincide mainly with the zones of the largest gradients of the 578 °C isotherm distribution in depth.

Acknowledgments. The authors express their gratitude to the anonymous reviewer of the manuscript, most of whose comments were taken into account when preparing the final version of the work. The study was supported by the Russian Science Foundation Grant (Project No. 25-17-68001 (extended from No. 22-17-00023)). Basic funding came through the implementation of state assignments of the Geological Institute of the Russian Academy of Sciences (research topic No. FMMG-2023-0010) and the Institute of Tectonics and Geophysics, Far Eastern Branch, Russian Academy of Sciences (research topics No. 121021000095-1).

References

ArcGIS Desktop: Release 10. — Redlands, CA : ESRI, 2011.

Argus D. F., *Gordon R. G.*, *DeMets C.* Geologically current motion of 56 plates relative to the no-net-rotation reference frame // Geochemistry, Geophysics, Geosystems. — 2011. — Vol. 12, no. 11. — DOI: 10.1029/2011gc003751.

Ashurkov S. V., *Sankov V. A.*, *Miroshnichenko A. I.*, *et al.* GPS geodetic constraints on the kinematics of the Amurian Plate // Russian Geology and Geophysics. — 2011. — Vol. 52, no. 2. — P. 239–249. — DOI: 10.1016/j.rgg.2010.12.017.

Deep Structure and Metallogeny of East Asia / ed. by A. N. Didenko, Y. F. Malyshev, B. G. Saksin. — Vladivostok : Dalnauka, 2010. — 332 p. — (In Russian).

Didenko A. N., *Li Y.-F.*, *Peskov A. Y.*, *et al.* Closure of the Solonker basin: Paleomagnetism of the Linxi and Xingfuzhilu formations (Inner Mongolia, China) // Russian Journal of Pacific Geology. — 2016. — Vol. 10, no. 5. — P. 317–336. — DOI: 10.1134/s181971401605002x.

Didenko A. N., *Nosyrev M. Y.*, *Shevchenko B. F.*, *et al.* Thermal structure of Sikhote Alin and adjacent areas based on spectral analysis of the anomalous magnetic field // Doklady Earth Sciences. — 2017. — Vol. 477, no. 1. — P. 1368–1372. — DOI: 10.1134/s1028334x17110198.

Gao G., *Kang G.*, *Li G.*, *et al.* Crustal magnetic anomaly and Curie surface beneath Tarim Basin, China, and its adjacent area // Canadian Journal of Earth Sciences. — 2015. — Vol. 52, no. 6. — P. 357–367. — DOI: 10.1139/cjes-2014-0204.

Imaev V. S., *Imaeva L. P.*, *Kozmin B. M.* Buffer seismogenic structures between the Eurasian and Amur lithospheric plates in southern Siberia // Tikhookeanskaya Geologiya. — 2003. — Vol. 22. — P. 55–61. — (In Russian).

Li C.-F., *Lu Y.*, *Wang J.* A global reference model of Curie-point depths based on EMAG2 // Scientific Reports. — 2017. — Vol. 7, no. 1. — DOI: 10.1038/srep45129.

Li S. H., *Li C.*, *Wang C. X.* Boundaries of the Amurian Plate identified using multiple geophysical methods // Geosciences Journal. — 2019. — Vol. 24, no. 1. — P. 49–59. — DOI: 10.1007/s12303-019-0011-1.

Maus S., *Barckhausen U.*, *Berkenbosch H.*, *et al.* EMAG2: A 2–arc min resolution Earth Magnetic Anomaly Grid compiled from satellite, airborne, and marine magnetic measurements // Geochemistry, Geophysics, Geosystems. — 2009. — Vol. 10, no. 8. — DOI: 10.1029/2009gc002471.

Meyer B., *Saltus R.*, *Chulliat A.* EMAG2v3: Earth Magnetic Anomaly Grid (2-arc-minute resolution) / NOAA National Centers for Environmental Information. — 2017. — DOI: 10.7289/V5H70CVX.

Petit C., *Fournier M.* Present-day velocity and stress fields of the Amurian Plate from thin-shell finite-element modelling: Modelling Amurian Plate tectonics // Geophysical Journal International. — 2004. — Vol. 160, no. 1. — P. 358–370. — DOI: 10.1111/j.1365-246x.2004.02486.x.

Sakhno V. G. Most recent and present-day volcanism of the southern Far East. — Vladivostok : Dalnauka, 2008. — 128 p. — (In Russian).

Tanaka A., *Okubo Y.*, *Matsubayashi O.* Curie point depth based on spectrum analysis of the magnetic anomaly data in East and Southeast Asia // Tectonophysics. — 1999. — Vol. 306, no. 3/4. — P. 461–470. — DOI: 10.1016/s0040-1951(99)00072-4.

Wang J., *Li C.-F.* Curie point depths in Northeast China and their geothermal implications for the Songliao Basin // Journal of Asian Earth Sciences. — 2018. — Vol. 163. — P. 177–193. — DOI: 10.1016/j.jseaes.2018.05.026.

Xiong S.-Q., *Yang H.*, *Ding Y.-Y.*, *et al.* Characteristics of Chinese continent Curie point isotherm // Chinese Journal of Geophysics. — 2016. — Vol. 59, no. 6. — P. 643–657. — DOI: 10.6038/cjg20161008.

Yarmolyuk V. V., *Kozlovsky A. M.*, *Travin A. V.*, *et al.* Duration and Geodynamic Nature of Giant Central Asian Batholiths: Geological and Geochronological Studies of the Khangai Batholith // Stratigraphy and Geological Correlation. — 2019. — Vol. 27, no. 1. — P. 73–94. — DOI: 10.1134/s0869593819010088.

Zonenshain L. P., *Savostin L. A.* Introduction to Geodynamics. — Moscow : Nedra, 1979. — 311 p. — (In Russian).

Russian Journal of Earth Sciences

Special Issue: "Data Science, Geoinformatics and Systems Analysis in Geosciences"

Representative Catalogue of the Neva Floods. Construction Principles

A. A. Rodionov[1], **A. A. Lobanov**[1], **T. I. Malova**[1]

[1]Shirshov Institute of Oceanology, RAS, Moscow, Russia
* **Correspondence to:** Rodionov A. A., malova.ti@yandex.ru

Abstract: The Neva floods should be studied as a phenomenon, the origin and characteristics of which are the result of direct and indirect manifestations of natural factors that differ significantly in their spatiotemporal scales. The problem should be approached interdisciplinary. In the process of studying historical the Neva floods scientific principles were formulated for constructing a representative flood catalogue, which has not yet been created, which creates additional difficulties in studying the evolution of the hydrodynamic system that includes Ladoga Lake, the Neva and the Gulf of Finland: a comprehensive methodological approach to solving the problem; unconditional priority of primary sources; refusal to "correct" historical series *post factum*; cataloguing typos and discrepancies in versions for the entire period of observations; development and implementation into practice of a unified program for assessing the representativeness of series; search for new information on water level observations.

Keywords: Neva floods, representative catalogue, historical series of floods, evolution of natural processes on secular intervals, database of the Neva floods of 18th century.

Citation: Rodionov, A. A., A. A. Lobanov, and T. I. Malova (2025), Representative Catalogue of the Neva Floods. Construction Principles, *Russian Journal of Earth Sciences*, 25, ES2006, EDN: XYZZPA, https://doi.org/10.2205/2025ES000965

1. Introduction

The current year, 2024, is very important in the history of St. Petersburg in terms of the floods that have occurred there. The city was founded at the mouth of the Neva, an obviously unsafe place, and Peter I faced the problem of flooding just three months after the founding. Among floods of varying levels of danger, it is customary to single out catastrophic ones. In the history of the Neva floods, catastrophic events are those of 1777, 1824, and 1924. It is noteworthy that the assessment of destructiveness in the 18th and 20th–21st centuries is different: in the first half of the 18th century there were no embankments, and floods with non-catastrophic maximum marks by modern standards could have led to fatal consequences. A number of publications in 2010 proved the legitimacy of including the floods of 1721, 1726, and 1752 in the list of catastrophic ones. A three-hundred-year series of catastrophic floods is emerging, occurring with a period of approximately 100 years: 1721, 1726, 1824, and 1924. Hence, we can consider the current year 2024 as a tragic anniversary of all catastrophic Neva floods [*Bogdanov et al.*, 2009a,b; 2012; *Malova et al.*, 2021; *Malova*, 2008].

Information about floods is of fundamental scientific and great practical interest. When studying the evolution of the hydrodynamic system, including Ladoga Lake, the Neva, and the Gulf of Finland, when studying secular changes in the region, and when refining the flood protection strategy in St. Petersburg and adjacent territories.

Today, the problem of systematization of information about historical Neva floods seems extremely urgent. The fact is that the construction of prognostic models, planning

Research Article

Received: 15 November 2024
Accepted: 15 April 2025
Published: 23 May 2025

of hydrotechnical, engineering, social and cultural activities are difficult without analyzing information about floods. The difficulty is that the official catalogs available to researchers, unfortunately, are full of distortions [*Malova*, 2022b; *Rumyantzev et al.*, 2024].

The situation is also complicated by the non-representativeness of the initial series of floods, which is critical given the extension of flood height measurement systems to all previous times. The non-representativeness is also because there have been several ordinaries (points where the level measurement took place) within St. Petersburg throughout the history of flood studies: on the Moika River, on the Neva near the Academy of Arts, near the Academy of Sciences, near the Main Admiralty, inside the Main Admiralty Canal, near the Peter and Paul Fortress, and near the supports of many St. Petersburg bridges. There are known cases when the same flood was measured from different ordinaries, and then the confusion in the height values went into the catalogs [*Malova*, 2022b].

What is the relevance of systematizing information about historical floods of the Neva? Three hundred years is a long period, we are talking about the evolution of natural processes at secular intervals and about instrumental support for observing the changes that occur. Three centuries of changes are significant for a single city.

2. Materials and methods

One of the reasons for the presence of distortions in official lists and catalogues presenting information on the heights of the Neva floods is the cloning of erroneous information, which turns a complex and confusing data system into the absence of any system at all.

The main obvious shortcomings of modern lists of the Neva floods can be summarized as follows:

1. the extension of flood height measurement systems (either from the Mining Institute's ordinar or from the beginning of the Baltic height system) to all previous times and the assignment of a single accuracy (±1 cm) to flood heights measured with different accuracy;
2. lack of information on the stability of the Kronstadt sea gauge;
3. the presence of a huge number of typos and distortions of information about the Neva floods, the maximum of which occurred in the years after the flood of 1924;
4. In addition, we must take into account the methodological and metrological imperfections of the established practice of forming centuries-old series of instrumental natural measurements [*Bogdanov et al.*, 2009a,b; 2012; *Malova*, 2008].

Let us clarify the flood of September 23, 1924. During the research it was revealed that it was during this period that a number of floods by I.G. Leitman over the period 1721–1729, a number by E. I. Shreter over the period 1749–1777 were completely destroyed and distorted. During this same period several more legends related to the Neva floods appeared. For example, the existence of the mythical Petropavlovsk tide gauge was "substantiated". Academician V. L. Kraft was accused of distorting the height of the catastrophic flood of 1777 [*Bogdanov et al.*, 2009b; 2012].

What happened in 1924? Why were the consequences of the flood so terrifying? Here we recall the monk of the Valamo Monastery Iuvian. On Valamo island there was a meteorological station and a water level measuring post, where regular observations had been conducted since 1861. Iuvian analyzed the data, compared them with the current meteorological situation. He concluded that the level in the Neva depends on the level of Lake Ladoga. The summer of 1924 was very rainy, the level of the lake was extremely high. In mid-September Iuvian sent a letter to Academician Sovetov and warned about the upcoming flood. But at that time, the opinion of a cleric meant little. The flood happened, the damage was enormous [*Bogdanov et al.*, 2009b].

3. Results and discussion

Work on systematization of information on historical floods of the Neva continues. A database of the Neva floods of the 18th century has been created in the St. Petersburg branch of the Institute of Oceanology. The database is open access. The main objective

of its creation is to provide information support for research related to the restoration of distorted series (or individual historical Neva floods) [*Malova*, 2022a,b].

From the point of view of the analysis of the subject area, the database provides systematization of data on floods, gives a comprehensive idea of each specific episode from a qualitative and quantitative point of view, and allows searching for information on:

- date (in different chronology systems),
- the height of water rise relative to different ordinaries,
- to the author of the flood description (if any),
- a link to a bibliographic source (published or archival).

In terms of functionality, the use of the database allows visually assessing the distorted series of historical Neva floods and verifying information about them.

The database covers historical floods of the Neva for the period 1703–1799. All events archived in currently existing catalogues, as well as in archival sources examined during the study, all events were analyzed [*Malova*, 2022a]. The database is publicly available on the website of the St. Petersburg branch of the Shirshov Institute of Oceanology, RAS [*Malova*, 2020].

The proposed database is not a full-fledged representative catalogue of the Neva floods. Its purpose is to systematize information about the Neva floods of the 18th century. The creation of a representative catalogue that would cover all events from the foundation of St. Petersburg to the present day is a matter for the future. The principles of constructing such a catalogue, tested on the materials of sea level observations at the Kronstadt tide gauge, can be reduced to the following:

I. an integrated methodological approach to solving the problem,
II. unconditional priority of primary sources,
III. refusal to "correct" time series and information *post factum*,
IV. cataloguing typos and discrepancies in versions over the entire period of observation,
V. publication of all surviving versions and materials without exception,
VI. development and implementation into practice of a unified program for assessing the homogeneity, long-term accuracy and representativeness of secular series,
VII. search for new information on water level observations.

However, it is necessary to take into account that the available materials and information:

1. fragmentary, incomplete and contradictory,
2. contain an abundance of emotional characteristics,
3. are obtained from observations at various points, sometimes several kilometers apart,
4. are represented by measurements in various non-uniform reference systems changing in time and space,
5. were assigned at different stages to different systems of counting heights (from a single ordinary level, in various geodetic coordinate systems, etc.),
6. are distorted by various kinds of "amendments" and "corrections", in particular, due to the "correction" of primary materials,
7. are deformed by extrapolating later or even modern Baltic height systems tens and hundreds of years ago.

The search for information on the Neva floods, their analysis and verification must certainly be continued from a modern scientific standpoint. Currently the proposed electronic database, which includes information on the Neva floods of the 18th century, can be considered a fundamentally new stage in the formation of a fundamental representative catalog of the Neva floods.

Acknowledgments. The article was prepared within the framework of the state assignment FMWE-2024-0028.

References

Bogdanov V. I., *Malova T. I.* On assessments of the height of the largest catastrophic flood that occurred in St. Petersburg in the Neva River mouth on November 7 (19), 1824 // Doklady Earth Sciences. — 2009a. — Vol. 424, no. 1. — P. 123–126. — DOI: 10.1134/s1028334x09010267.

Bogdanov V. I., *Malova T. I.* The catastrophic flood of the Neva River in 1924 // Doklady Earth Sciences. — 2009b. — Vol. 427, no. 2. — P. 985–987. — DOI: 10.1134/s1028334x0906021x.

Bogdanov V. I., *Malova T. I.* On the restoration of the heights of the historical Neva floods // Doklady Akademii nauk. — 2012. — Vol. 443, no. 1. — P. 108–111. — EDN: OWXJYR.

Malova T. I., *Rodionov A. A.* The catastrophic flood of the Neva in 1721 (on the 300th anniversary of the event) // Fundamentalnaya i prikladnaya gydrofizika. — 2021. — Vol. 14, no. 4. — P. 111–118. — DOI: 10.7868/S2073667321040109. — (In Russian).

Malova T. I. Height of the catastrophic flood of the Neva River on September 10(21), 1777 // Doklady Earth Sciences. — 2008. — Vol. 423, no. 1. — P. 1262–1264. — DOI: 10.1134/s1028334x08080175.

Malova T. I. Electronic database "Neva floods in the 18th century". — 2020. — URL: https://spb.ocean.ru/wp-content/uploads/2020/09/Baza-dannykh-navodneniy-Nevy-XVIII-v.xlsx (visited on 09/15/2020).

Malova T. I. "The floods of the Neva, XVIII century". Database // Fundamental and Applied Hydrophysics. — 2022a. — Vol. 15, no. 1. — P. 112–118. — DOI: 10.59887/fpg/g66z-rp28-gmr9. — (In Russian).

Malova T. I. Representative Catalog of the Neva Floods // Hydrometeorology and Ecology. — 2022b. — No. 67. — P. 305–323. — DOI: 10.33933/2713-3001-2022-67-305-323. — (In Russian).

Rumyantzev V. A., *Rodionov A. A.*, *Lobanov A. A.*, *et al.* The problem of Neva floods in the light of global climate change, adverse anthropogenic factors and the geopolitical situation in the region // Advanced Technologies of Hydroacoustics and Hydrophysics: Proceedings of All-Russian Conference. — Saint Petersburg : POLYTECH-PRESS, 2024. — P. 21–25. — EDN: MQKATY. — (In Russian).

Russian Journal of Earth Sciences

Special Issue: "Data Science, Geoinformatics and Systems Analysis in Geosciences"

Key Aspects of Information Technology for Maintaining of the Unified State Fund of Data on the State of the Environment, Its Pollution

E. V. Kolesnikov[1], **V. M. Shaimardanov**[1]

[1] All-Russia Research Institute of Hydrometeorological Information, World Data Center (RIHMI-WDC), Obninsk, Russia

* **Correspondence to:** Kolesnikov Evgeny Vladimirovich, ekolesnikov@meteo.ru

Abstract: Information from the Unified State Fund of Data on the State of the Environment and its Pollution (USFD), which consolidates large amounts of data from hydrometeorological observations and pollution monitoring, is one of the key factors affecting the life of modern world society and the stable economic development of every state on the planet Earth. This effect is due to the presence of particularly dangerous hydrometeorological phenomena and adverse weather conditions that can cause social and economic damage. In this regard, the tasks of collecting, accounting, long-term storage and timely provision of such information to consumers of various sectors of economic activity for use in decision-making remain relevant. This article discusses the key aspects of the information technology of the USFD, which is formed as a result of the activities of the Federal Service of Russia for Hydrometeorology and Pollution Monitoring (Roshydromet). As a result of the work, a description of the technological process of maintaining USFD, statistical data on the demand and use of USFD information and a new documentary information search system solving the problem of accounting and long-term storage of USFD information resources are presented. The system was developed using modern information technologies, international standards for describing information resources and taking into account the experience of foreign organizations engaged in activities similar to Roshydromet. The direction of further development of digital technologies for operational public service with information products created on the basis of verified USFD information resources is also outlined.

Keywords: Hydrometeorology, Environmental monitoring, Big data, Long-term storage, Information systems and technologies, Retrieval system, Databases, Metadata, Information resources.

Citation: Kolesnikov, E. V., and V. M. Shaimardanov (2025), Key Aspects of Information Technology for Maintaining of the Unified State Fund of Data on the State of the Environment, Its Pollution, *Russian Journal of Earth Sciences*, 25, ES2007, EDN: RCERJT, https://doi.org/10.2205/2025ES000966

Research Article

Received: 15 November 2024
Accepted: 15 April 2025
Published: 23 May 2025

1. Introduction

Regular monitoring of the state of the natural environment in Russia and the storage of collected information has been carried out for two centuries. At the beginning of the XIX century, many proposals were submitted for the creation of regular hydrometeorological observations in Russia, which formed the basis for the project of organizing the service, curated by a talented scientist and organizer, academician Adolf Yakovlevich Kupfer. In 1848, the activities of the organization headed by Kupfer led to the creation on its basis of the Main Physical Observatory (MPO), known today as the Main Geophysical Observatory named after A.I. Voeikov. It was from this moment that the creation of a network of meteorological observations, the replication of observation materials, the creation of meteorological instrumentation and an instrument verification system began. Today, this function is performed by Roshydromet, as a result of which the USFD is formed. This is

a unique data collection that contains an orderly, constantly updated set of documented information on environmental pollution monitoring, hydrometeorology and related fields (aerology, hydrology, meteorology, oceanology, heliogeophysics, etc.).

Information products created on the basis of USFD data are actively used in almost all major sectors of the economy, for example, in construction, architecture and design, energy, transport and communications, aviation, agriculture, as well as in scientific research and the activities of executive authorities. This once again confirms the relevance of the tasks of collecting, long-term storage and timely operational access to this kind of information. Figure 1 shows statistics on the number of requests and users over the past 13 years.

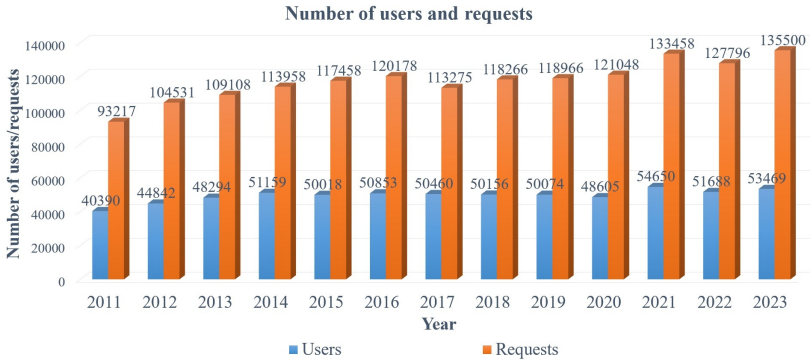

Figure 1. Number of requests and users.

A large proportion of requests, not counting individuals, falls on architecture, design and construction, which is reasonable. Today, no construction is possible without an important component - a set of engineering and survey works, which include engineering and hydrometeorological surveys.

Figure 2 shows the distribution of users by types of primary economic activity for 2023. Specialists engaged in survey work must study the components of the surrounding natural environment at the construction site: water bodies, natural and climatic conditions, land resources, atmospheric air, soil cover, etc. It is especially important to have information about particularly dangerous hydrometeorological processes and phenomena. Nature itself, due to constant changes in environmental conditions, regularly confirms the relevance of survey work and forces a person to conduct such research for the construction of objects of any level of complexity, be it a house, a bridge, a pipeline or a power transmission line pole.

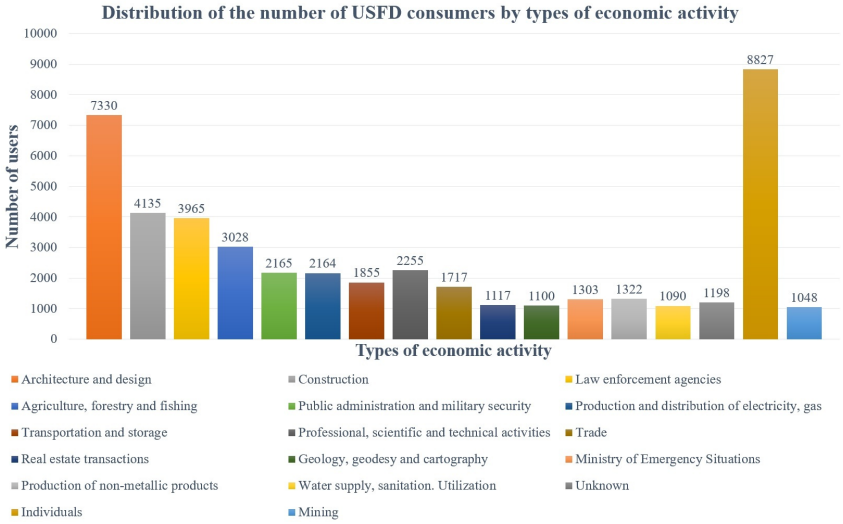

Figure 2. Distribution of users by types of primary economic activity for 2023.

The tasks of accounting and long-term storage of information resources are not new in the field of information systems and technologies. However, the application of a particular

technological solution largely depends on the subject area, namely, on the features of its information resources – storage objects, the management of which must be implemented. In the context of the USFD, not many works have been published on these tasks at the moment. This is due to the specificity of the subject area. Attempts to solve the problems of long-term storage and accounting of information resources of the USFD are presented in works [*Dolgih et al.*, 2014a,b]. However, the project was not fully implemented.

Thus, the aim of the work is to describe the information process of the technology of maintaining the USFD, to note the relevance of the tasks of collection and long-term storage, to present a new documentary information retrieval system of accounting and long-term storage, taking into account the experience of domestic and foreign colleagues in solving these problems.

2. Technology for maintaining USFD

Figure 3 shows the general structural diagram of the technological process of maintaining the Unified State Hydrometeorological Data. The structure of Roshydromet, which participates in the process of maintaining the Unified State Hydrometeorological Data, can be divided into several logical levels.

At the first level (local), there is the State Observation Network of Observation Units, which collects and processes primary observation data for the following types: meteorological, aerological, agrometeorological, synoptic, hydrological, marine hydrometeorological, geophysical, heliogeophysical, pollution monitoring, satellite.

At the second level (regional) are the Territorial Administration for Hydrometeorological and Environmental Monitoring (ROHEM), which perform tasks on processing and accumulating primary observation data and ensuring the functioning of their observation units. Scientific research institutions are also located at this level. The subject of the activities of the research institutions of Roshydromet is scientific research in the field of hydrometeorology, related areas and pollution monitoring. Each research institute is assigned specific types of observations in the context of which measurement methods and tools are being developed and improved, as well as methodological and software for processing and accumulating primary observational data.

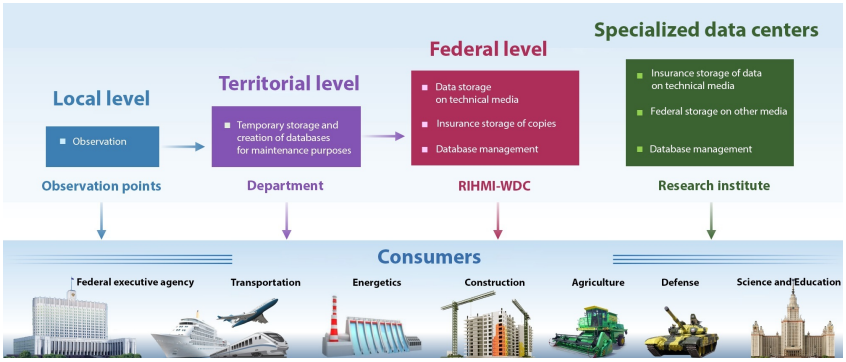

Figure 3. Structural diagram of maintaining the USFD.

To solve the urgent problems of centralized accounting and long-term storage of the USFD, the All-Russian Research Institute of Hydrometeorological Information – World Data Center (FSBI "RIHMI-WDC") was created in the city of Obninsk [*History…*, 2024].

3. Composition and structure of the USFD

Today, the USFD includes information resources included in the list of governance document (GD) 52.19.143 "List of documents of the archival data fund on the state of the environment, its pollution", which determines the terms and place of storage of each information resource. Figure 4 shows the distribution of the volume of information in the USFD by discipline on paper and electronic media. As of January 1, 2024, the USFD is located on the following types of media:

- Photo media (microfilms) – 857,653 storage units.
- Paper media – 2,840,289 storage units (of which 2,710,579 units are of permanent storage period, 129,710 units are of temporary storage period).
- Electronic media (optical disks, cartridges, magnetic tapes, tape libraries – with a total volume of information of 2.8 TB of verified series of primary observation data and 30 TB of primary observation data.

It is also worth noting that paper documents undergo a digitization stage using scanning. At the moment, about 500 thousand documents of the USFD have been scanned, with a total volume of about 150 TB. This solution is described in the work [*Kolesnikov et al.*, 2021; 2022].

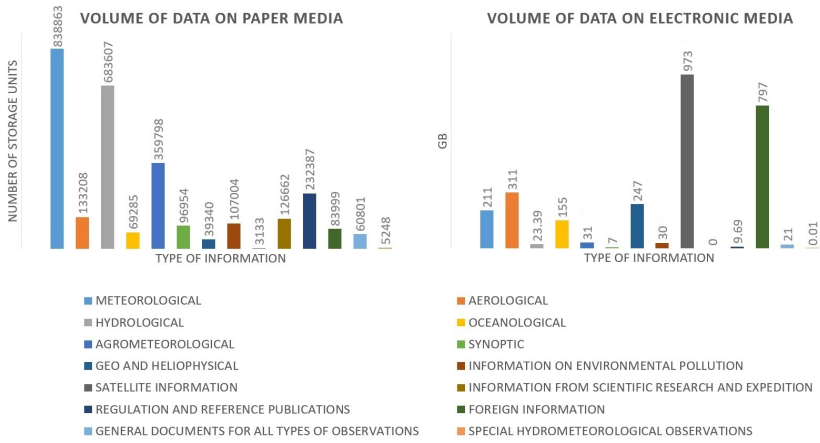

Figure 4. Distribution of the volume of information in the USFD by discipline on paper and electronic media.

The collection of USFD data consists of about 50 million files with observational data and is unique. Its information component meets the criteria of Big Data. We are talking about both the 3V and 5V criteria. The technological component of maintaining the USFD began to form in the early 1970s of the last century, long before the concept of Big Data appeared. The foundations of the "computer infrastructure" for meteorological and climate research using observation data were laid – from a modern perspective, it can be called "Seamless Technology". This largely anticipated those areas of development of RIHMI-WDC that we today attribute to Big Data. Figure 5 shows the corresponding IT infrastructure, which ensures a stable ability to perform the task of maintaining the USFD.

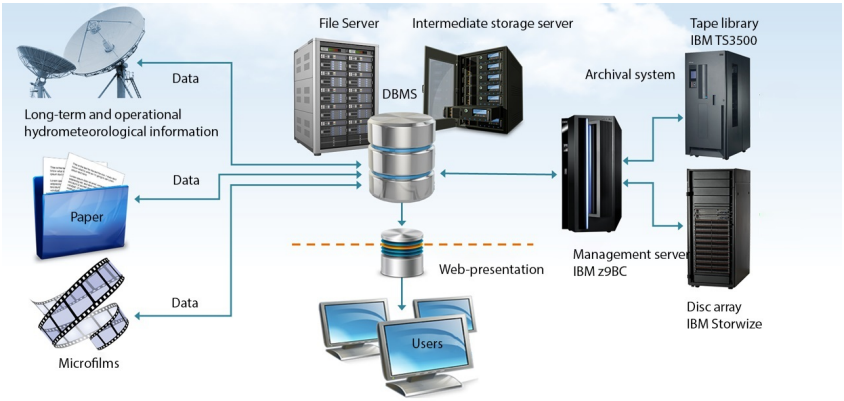

Figure 5. IT infrastructure for maintaining the USFD.

To store a large volume of information resources, the USFD uses a hardware and software complex based on tape libraries [*Shaimardanov et al.*, 2014]. Storage systems based on magnetic tape technology are currently the most reliable means for ensuring long-term storage of digital information.

4. The problem of accounting and long-term storage of the USFD

The main problem of accounting and searching for information resources of the USFD is that the USFD information resources are documents that contain factual information about the state of the environment. In this case, the search for the necessary information resource is reduced to a visual review of the catalog structure of documents. Having analyzed the works [*Dolgih et al.*, 2014a,b], in which attempts were made to solve the problems of accounting and searching, as well as the experience of foreign colleagues (public portals of foreign electronic archives [*Databases…*, 2024; *National Meteorological Library*, 2024; *Weather…*, 2024]), we can conclude that the solution to the problem is reduced to the creation of an information system based on an information model of metadata that allows describing each information resource as a unique storage object, similar to the accounting of books in a library.

The USFD information refers to geographic (spatial) information. However, the object of the study is not the data on the state of the environment itself, but the documents that contain them. Therefore, in order to create a metadata model, it is necessary to consider the standards of librarianship and publishing. Such materials include the Dublin Core specification (DC), which is widely used both in domestic and international practice. The corresponding international standards have been developed on its basis: ISO 15836-1:2017, ISO 15836-2:2019, GOST R 7.0.10-2019, GOST R ISO 15836-2-2022.

5. Results

The analysis of information systems of foreign organizations, similar to Roshydromet, showed that all systems belong to the class of documentary ones and in all systems for searching information resources there is a trend of using attribute search.

The key result of this work is the presentation of the metadata information model, which allows identifying each USFD information resource as a unique storage unit. This model is the basis for the information retrieval system for accounting of information resources of the USFD. Table 1 shows the attribute composition of the metadata model (47 elements), formed on the basis of the previously presented standards of the Dublin Core specification.

Table 1. Attributive composition of the model of metadata of information resources of the USFD.

GROUP OF IDENTIFICATION ELEMENTS		
No.	Field	Discription
1	Title	Document name
2	Alternative Title	Alternative document name
3	Subject	Subject (aerology, hydrology, meteorology, etc.)
4	View of observation	Type of observations
5	Collection	Article number in RD 52.19.143
6	Array	The array that contains the document
7	Inventory book	The inventory book in which the document is entered
8	Inventory number	Inventory number of the document
9	Identifier	Unique Composite Index: Subject_View of observation_Collection_ Array_ Inventory number
GROUP OF ELEMENTS OF MAIN PROPERTIES		
10	Volume	Document size
11	Resource type	The class or type to which the document belongs

Continued on next page

Table 1. Attributive composition of the model of metadata of information resources of the USFD. (Continued)

12	File format	Document file format
13	Access rights	Information about who can access the document
14	Frequency	Frequency with which the array is replenished with a document
15	Link	Link to the document in the file system
16	Media type	Physical medium of the document
17	Creator	Entity responsible for creating the document
18	Publisher	Entity responsible for providing the document
19	Co-executor	Entity responsible for contributing to the creation of the document
	PHYSICAL PLACEMENT OF THE DOCUMENT	
20	Location	Physical location of original document
21	Archival Repository Number	Archive storage number
22	Stack Number	Rack/cabinet number
23	Section Number	Section number
24	Shelf Number	Shelf number
	GROUP OF TIME CHARACTERISTICS ELEMENTS	
25	Date created	Document creation date
26	Date of publication	Document publication date
27	Date accepted	Document adoption date
28	Date copyrighted	Copyright date
29	Date submitted	Document submission date
30	Date modified	Modification date
31	Date available	Date the document was or will be available
32	Date valid	Date (often a range of dates) of the document's validity
	GROUP OF ELEMENTS OF CONNECTION WITH OTHER OBJECTS	
33	Has part	A related document that is physically or logically included in the document being described
34	Has version	A related document that is a version, revision, or adaptation of the document being described
35	Has format	A related document that is substantially the same as an existing document being described but is in a different format
36	Requires	A related document that is required by the document being described to support its operation, presentation, or coordination
37	Replaces	A related document that is superseded, replaced, or continued by the document being described
38	Is part of	A related document that is physically or logically included in the document being described
39	Is version of	A related document of which the document being described is a version, revision, or adaptation
40	Is format of	An existing related document that is substantially the same as the document being described but is in a different format

Continued on next page

Table 1. Attributive composition of the model of metadata of information resources of the USFD. (Continued)

41	Is required by	A related document that requires the document being described to support its operation, presentation, or coordination
42	Is replaced by	A related document that supersedes, replaces, or is a continuation of the document being described
	GROUP OF ELEMENTS OF THE CONTENT OF OBJECTS	
43	Start date of observations	Environmental monitoring start date
44	End date of observations	Environmental monitoring end date
45	Observation area	Observation area
46	Language	Document language
47	Annotation	Document description

6. Discussion

The information retrieval system, which has been implemented into trial operation, provides accounting, operational remote search and provision of information resources of the Unified State Register of Documents. However, for the class of users who are not familiar with the composition and structure of the Unified State Register of Documents, problems may arise in working with documents. In this case, the user needs to visually search for actual observation data in the provided information resource. This significantly slows down the process of obtaining data. Therefore, the further development of information technologies for operational customer service consists in the development of new digital services that will contain the actual data of the EGFD. In other words, each information resource of the Unified State Register of Documents will be transformed into a relational database structure that will allow creating search queries to the data. Work in this direction is already underway and at the first stage a prototype of specialized software has been developed [*Peretyatko*, 2022; 2023], which will form the basis of the new factographic information-retrieval system.

7. Conclusions

This paper presented the information process of the technology for maintaining the Unified State Register of Documents, its composition and structure, and noted the relevance of the tasks of collecting and long-term storage of Unified State Register of Documents information in view of its demand for decision-making in various sectors of economic activity. As a solution to these problems, a new documentary information retrieval system for accounting and long-term storage was presented, taking into account the features of the information resources of the Unified State Register of Documents. It was also announced that the technology of operational maintenance with actual observation data would be further developed.

References

Databases. Publication of various survey and observation data and so forth. — 2024. — URL: https://www.jamstec.go.jp/e/database (visited on 10/14/2024).

Dolgih S. G., Shaimardanov V. M. Creating a data management technology in automated archiving system // Proceedings of the Voeikov Main Geophysical Observatory. — 2014a. — No. 572. — P. 162–174. — EDN: SZXXSH. — (In Russian).

Dolgih S. G., Shaimardanov V. M. The development of technology of data management in an automated archival system // Proceedings of the Voeikov Main Geophysical Observatory. — 2014b. — No. 575. — P. 204–214. — EDN: TIQKSX. — (In Russian).

History of the Federal State Budgetary Institution "All-Russian Research Institute of Hydrometeorological Information - World Data Center". — 2024. — URL: http://meteo.ru/about/history (visited on 10/14/2024). — (In Russian).

Kolesnikov E. V., Shaimardanov V. M. Electronic fund of scanned hydrometeorological documents. Database RU 2021621423. — 2021. — EDN: CGZKFV. — (In Russian).

Kolesnikov E. V., Shaimardanov V. M. Development of an Automated Paper Documents Scanning Technology for the Russian Meteorological Service // Russian Journal of Cybernetics. — 2022. — 1(9). — P. 28–38. — DOI: 10.51790/2712-9942-2022-3-1-4. — (In Russian).

National Meteorological Library. — 2024. — URL: http://www.bom.gov.au/library (visited on 10/14/2024).

Peretyatko L. O. The National Hydrometeorological Archive as Big Data. Appropriate Technologies and Tools // Russian Journal of Cybernetics. — 2022. — Vol. 3, no. 4. — P. 98–101. — DOI: 10.51790/2712-9942-2022-3-4-11. — (In Russian).

Peretyatko L. O. The National Hydrometeorological Archive as Big Data. A Universal Parser of the Hydrometeorological Data Description Language // Russian Journal of Cybernetics. — 2023. — Vol. 4, no. 2. — P. 47–52. — DOI: 10.51790/2712-9942-2023-4-2-07. — (In Russian).

Shaimardanov V. M., Shaimardanov M. Z. Development of Roshydromet automated archived data system // Uchenye zapiski RGGMU. — 2014. — No. 36. — P. 60–66. — EDN: TQUBAD. — (In Russian).

Weather and climate change. — 2024. — URL: https://www.metoffice.gov.uk (visited on 10/14/2024).

Russian Journal of Earth Sciences

Special Issue: "Data Science, Geoinformatics and Systems Analysis in Geosciences"

Enhanced Wintertime Convergence of Atmospheric and Oceanic Heat Transports in the Barents Sea Region under Present Climate Warming

M. M. Latonin[1], **I. L. Bashmachnikov**[1,2], **V. A. Semenov**[3,4]

[1]Nansen International Environmental and Remote Sensing Centre, Saint Petersburg, Russia
[2]Saint Petersburg State University, Saint Petersburg, Russia
[3]A. M. Obukhov Institute of Atmospheric Physics RAS, Moscow, Russia
[4]Institute of Geography RAS, Moscow, Russia
* **Correspondence to:** Mikhail M. Latonin, mikhail.latonin@niersc.spb.ru

Abstract: A distinctive feature of the Barents Sea climate system is a suggested positive feedback in the ocean–sea ice–atmosphere system that can enhance regional climate variations. The objective of this study is to assess the effectiveness of this positive feedback for the advective heat fluxes in the winter season using the ORAS4 ocean reanalysis and ERA5 atmospheric reanalysis data for the period 1959–2017. Based on the signs of the linear trends of the oceanic heat transport, two periods were identified for the analysis: 1959–1987 and 1987–2017. Composite maps of surface wind fields indicate an increase in the effectiveness of the positive feedback in the Barents Sea region during the present period relative to the previous one. This is manifested in the strengthening of the southern winds over the southeastern part of the sea in years with the maximum oceanic heat transport and in the weakening of the northern winds over the northwestern part of the sea in years with the minimum oceanic heat transport. The convergence of the atmospheric sensible heat transport over the Barents Sea has a maximum in the lower troposphere, 1000–900 hPa. An increasing synchronization of the convergence of atmospheric and oceanic heat transports in the Barents Sea region, derived in this study, contributes to an acceleration of the local warming.

Keywords: Barents Sea, advective heat fluxes, atmospheric and oceanic circulation, convergence, Arctic warming, climate feedbacks, reanalysis datasets.

Citation: Latonin, M. M., I. L. Bashmachnikov, and V. A. Semenov (2025), Enhanced Wintertime Convergence of Atmospheric and Oceanic Heat Transports in the Barents Sea Region under Present Climate Warming, *Russian Journal of Earth Sciences*, 25, ES2008, EDN: DRHLZX, https://doi.org/10.2205/2025ES000967

Research Article

Received: 15 November 2024
Accepted: 15 April 2025
Published: 23 May 2025

1. Introduction

The Barents Sea plays a crucial role in functioning of the Arctic climate system [*Bengtsson et al.*, 2004; *Smedsrud et al.*, 2013]. A unique geographical position of the Sea creates favorable conditions for the intense ocean–atmosphere coupling [*Eisbrenner et al.*, 2024], and the regional processes may even impact a global climate [*Semenov et al.*, 2010]. A warming rate in the Barents Sea area is the highest for the Arctic region [*Isaksen et al.*, 2022], and both atmospheric and oceanographic conditions are strongly impacted by the climate warming in this region [*Ingvaldsen et al.*, 2021; *Lind et al.*, 2018; *Przybylak et al.*, 2019]. An essential component of the heat budget of the Arctic and the Barents Sea are advective heat fluxes controlled by the atmospheric and oceanic circulation patterns [*Bashmachnikov et al.*, 2018; *Trenberth et al.*, 2001].

One of the important features of the regional climate dynamics in the Barents Sea is a positive feedback in the ocean–sea ice–atmosphere system [*Bengtsson et al.*, 2004; *Kalavichchi*

et al., 2019; 2021]. The increased oceanic heat influx into the Barents Sea is thought to contribute to the retreat of the sea ice edge. This in turn leads to the increased turbulent sensible and latent heat fluxes from the ocean to the atmosphere, which contributes to local cyclonic atmospheric vorticity. Such atmospheric circulation contributes to further enhancement of the convergence of oceanic and atmospheric heat transports in the region. This relatively local mechanism may actually impact a larger territory. For example, one of the leading explanations of the reasons of the early 20th century Arctic warming is related to this positive feedback loop [*Bengtsson et al.*, 2004]. If the inflow of the oceanic heat into the Barents Sea is restricted, the positive feedback in the Barents Sea might be reversed to act as a cooling mechanism leading at some conditions even to a shutdown of the oceanic inflow to the Sea [*Semenov et al.*, 2009].

This study focuses on the assessment of the effectiveness of positive feedback during the winter season in the ocean–sea ice–atmosphere system of the Barents Sea based on the ORAS4 and ERA5 reanalysis datasets for the period 1959–2017.

2. Data and methods

For the calculation of the oceanic heat transport, the seawater potential temperature and zonal current velocity were obtained from the ORAS4 reanalysis dataset [*Balmaseda et al.*, 2012]. For the calculation of the atmospheric sensible heat transport at isobaric surfaces 1000–100 hPa, the following variables were obtained from the ERA5 reanalysis dataset [*Hersbach et al.*, 2020]: air temperature, specific humidity, geopotential, zonal and meridional wind velocities. In addition, for the composite analysis, the mean surface sensible and latent heat fluxes, sea level atmospheric pressure, zonal and meridional components of the wind speed at 10 m were downloaded from the ERA5 archive. The analysis was performed for the extended winter season December–March. Figure 1 shows the study area with the sections used for the estimates of the advective heat fluxes in the ocean and atmosphere.

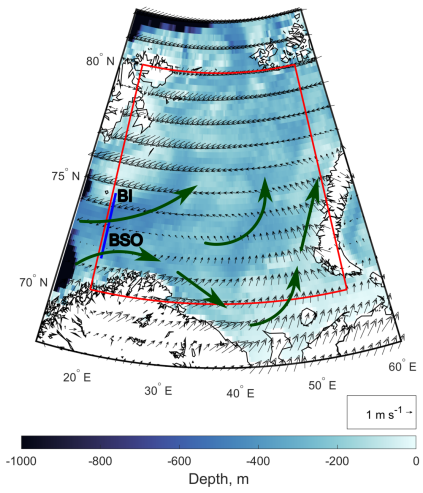

Figure 1. Study area with the sections for the calculation of the advective oceanic and atmospheric sensible heat fluxes. The blue line shows the section for the oceanic heat transport (20.5°E, 71.5°N–74.5°N), and the red lines show four sections for the atmospheric sensible heat transport (20°E, 70°N–80°N; 80°N, 20°E–55°E; 55°E, 70°N–80°N; 70°N, 20°E–55°E). Green arrows show schematic warm ocean currents from the North Atlantic entering the sea across the Barents Sea Opening (BSO); BI denotes Bear Island. Black arrows show mean wintertime surface wind directions at a height of 10 m over the period 1959–2017 based on the ERA5 reanalysis dataset. Bathymetry data are from the ETOPO 2022 15 Arc-Second Global Relief Model (https://www.ncei.noaa.gov/products/etopo-global-relief-model).

The oceanic heat flux (OHF) was calculated based on the monthly data as follows:

$$\mathrm{OHF}_{l,z,t(20.5°\mathrm{E})} = C_p\rho(\theta_{l,z,t} - \theta_{\mathrm{ref.}})U_{l,z,t},$$

where C_p is the typical specific heat capacity of seawater at constant pressure ($4000\,\mathrm{J\,kg^{-1}\,°C^{-1}}$), ρ is the typical seawater density ($1028\,\mathrm{kg\,m^{-3}}$), l is latitude, z is depth, t is time, θ is the monthly mean seawater potential temperature (°C), $\theta_{\mathrm{ref.}}$ is the reference temperature taken to be 0 °C, and U is the monthly mean eastward current velocity ($\mathrm{m\,s^{-1}}$). The reference temperature was set to 0 °C due to the established fact that it nearly corresponds to the outflow temperature of the cold waters leaving the Barents Sea [*Schauer et al.*, 2002].

The oceanic heat transport across the Barents Sea Opening was calculated as:

$$\mathrm{OHT} = \int_0^Z \int_{71.5°\mathrm{N}}^{74.5°\mathrm{N}} (\mathrm{OHF}_{l,z,t(20.5°\mathrm{E})})\mathrm{d}l\mathrm{d}z,$$

where integration over the latitude was carried out from 71.5°N to 74.5°N with a step $\mathrm{d}l = 1°$ (in meters), and over the depth, it was carried out from the surface to the bottom Z. Numerical integration was carried out by the trapezoidal method.

The atmospheric sensible heat fluxes (ASHF) were calculated based on the 6-hourly data as follows:

$$\begin{aligned}
\mathrm{ASHF}_{l,p,t(20°\mathrm{E})} &= C_p\rho T_{l,p,t(20°\mathrm{E})}U_{l,p,t(20°\mathrm{E})},\\
\mathrm{ASHF}_{l,p,t(80°\mathrm{N})} &= C_p\rho T_{l,p,t(80°\mathrm{N})}U_{l,p,t(80°\mathrm{N})},\\
\mathrm{ASHF}_{l,p,t(55°\mathrm{E})} &= C_p\rho T_{l,p,t(55°\mathrm{E})}U_{l,p,t(55°\mathrm{E})},\\
\mathrm{ASHF}_{l,p,t(70°\mathrm{N})} &= C_p\rho T_{l,p,t(70°\mathrm{N})}U_{l,p,t(70°\mathrm{N})},
\end{aligned}$$

where C_p is the typical specific heat capacity of air at constant pressure ($1005\,\mathrm{J\,kg^{-1}\,K^{-1}}$), ρ is the air density calculated according to (1), l is latitude or longitude, p is isobaric surface, t is time, T is the 6-hourly air temperature (K), Q is the 6-hourly specific humidity ($\mathrm{kg\,kg^{-1}}$), V is the 6-hourly northward wind velocity ($\mathrm{m\,s^{-1}}$) and U is the 6-hourly eastward wind velocity ($\mathrm{m\,s^{-1}}$).

$$\rho = \frac{P}{TR_d(1 + 0.61Q)}, \tag{1}$$

where P is atmospheric pressure (Pa), T is the 6-hourly air temperature (K), R_d is the specific gas constant for dry air ($287.04\,\mathrm{J\,kg^{-1}\,K^{-1}}$), Q is the 6-hourly specific humidity ($\mathrm{kg\,kg^{-1}}$). This method for the calculation of air density is taken from [*Brutsaert*, 1982].

The atmospheric sensible heat transports across the four sections displayed in Figure 1 were calculated as:

$$\begin{aligned}
\mathrm{ASHT}_{(20°\mathrm{E})} &= \int_{1000\mathrm{hPa}}^{900\mathrm{hPa}} \int_{70°\mathrm{N}}^{80°\mathrm{N}} (\mathrm{ASHF}_{l,p,t(20°\mathrm{E})})\mathrm{d}l\mathrm{d}p,\\
\mathrm{ASHT}_{(80°\mathrm{N})} &= \int_{1000\mathrm{hPa}}^{900\mathrm{hPa}} \int_{20°\mathrm{E}}^{55°\mathrm{E}} (\mathrm{ASHF}_{l,p,t(80°\mathrm{N})})\mathrm{d}l\mathrm{d}p,\\
\mathrm{ASHT}_{(55°\mathrm{E})} &= \int_{1000\mathrm{hPa}}^{900\mathrm{hPa}} \int_{70°\mathrm{N}}^{80°\mathrm{N}} (\mathrm{ASHF}_{l,p,t(55°\mathrm{E})})\mathrm{d}l\mathrm{d}p,\\
\mathrm{ASHT}_{(70°\mathrm{E})} &= \int_{1000\mathrm{hPa}}^{900\mathrm{hPa}} \int_{20°\mathrm{E}}^{55°\mathrm{E}} (\mathrm{ASHF}_{l,p,t(70°\mathrm{N})})\mathrm{d}l\mathrm{d}p,
\end{aligned}$$

where the horizonal integration step $\mathrm{d}l$ =0.25° expressed in meters, and the vertical integration step $\mathrm{d}p = 25\,\mathrm{hPa}$ expressed in meters according to the data on the geopotential heights (m) at each grid point corresponding to the isobaric surfaces. Numerical integration was carried out by the trapezoidal method. This method of estimation of the atmospheric heat

transport was used by [*Latonin et al.*, 2022]. The integration was performed for the layer 1000–900 hPa based on the results of the dominant directions of heat fluxes (see the section "Results").

The chosen sections for the calculation of the advective heat fluxes have been used in the previous studies [*Årthun et al.*, 2012; *Kalavichchi et al.*, 2021]. The oceanic section is also equivalent to the measure of the convergence of the oceanic heat transport into the Barents Sea [*Årthun et al.*, 2012]. For the atmospheric sections, as a measure of the convergence, the sum of the integral heat fluxes across four sections was used. Generally, the boundaries of the Barents Sea used in this study are commonplace [*Cai et al.*, 2022].

3. Results

Figure 2 shows the integral oceanic heat flux entering the Barents Sea. During 1959–2017, the mean wintertime oceanic heat transport across the Barents Sea Opening is 64 ± 4 TW. This quantity is in a good agreement with the simulated values of the oceanic heat transport across this section. For example, 59 TW was obtained in [*Årthun et al.*, 2012]. In another study, the oceanic heat transported by the North Cape Current across the western boundary of the Barents Sea to the south of the Bear Island was estimated to be 65 TW [*Bashmachnikov et al.*, 2018].

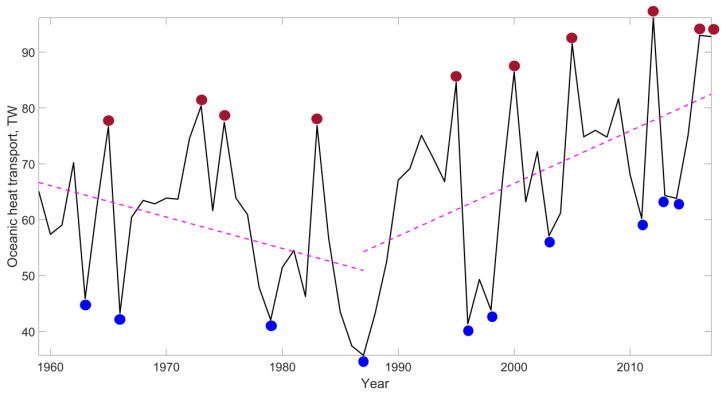

Figure 2. Wintertime oceanic heat transport across the western boundary of the Barents Sea. Dashed lines show linear trends for the periods 1959–1987 and 1987–2017. Red and blue circles mark the years with maxima and minima of the oceanic heat transport. The years with maxima and minima for the first period are: 1965, 1973, 1975, 1983 and 1963, 1966, 1979, 1987, respectively. The years with maxima and minima for the second period are: 1995, 2000, 2005, 2012, 2016, 2017 and 1996, 1998, 2003, 2011, 2013, 2014, respectively.

For further analysis, the time series was split into two parts: 1959–1987, when a statistically significant negative linear trend of −0.56 TW yr^{-1} was observed, and 1987–2017, when a statistically significant positive linear trend of 0.94 TW yr^{-1} was observed. Composite analysis was performed separately for the two periods, with averaging of four maxima and minima for the first period and of six extrema for the second period.

Figure 3 shows the mean ocean–atmosphere sensible and latent heat fluxes and their changes over two periods. The sum of two components was considered. It was reported in previous studies that the sensible heat flux strongly dominates over the latent heat flux, and the interannual variability of turbulent heat fluxes is the highest in the areas of strong sea ice reduction [*Årthun et al.*, 2010].

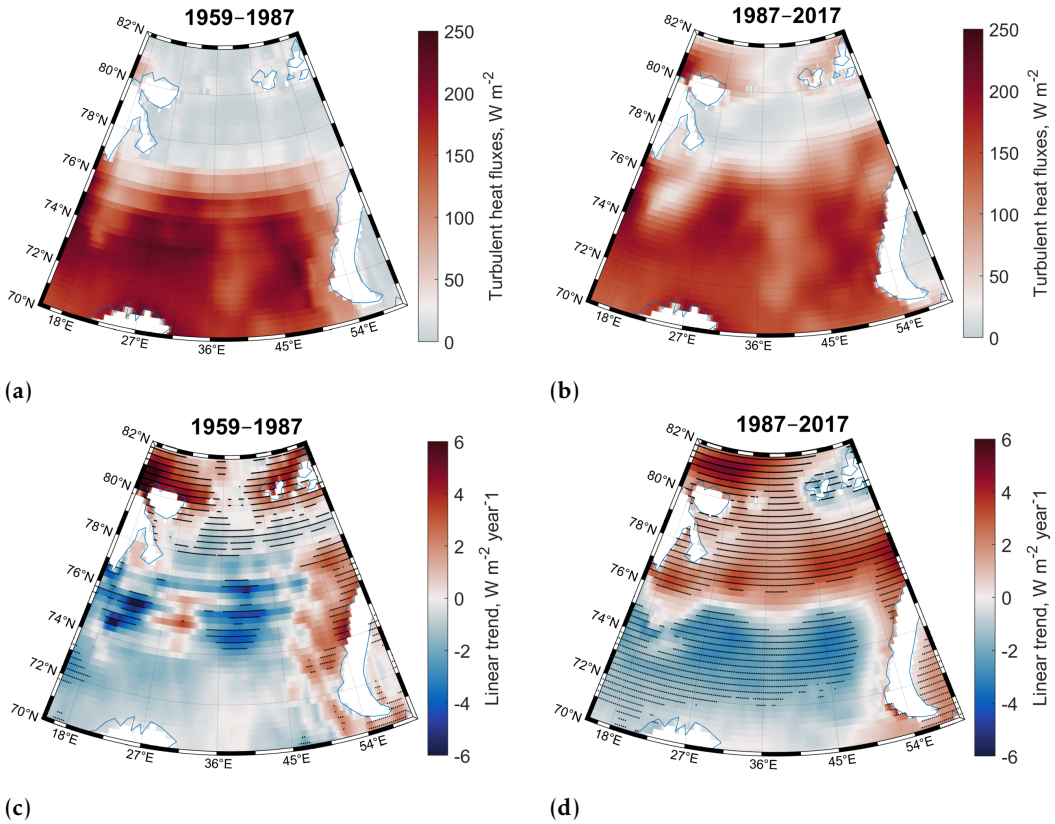

Figure 3. Mean values of total turbulent heat fluxes (a, b) for the first period (a) and for the second period (b) and linear trends of total turbulent heat fluxes (c, d) for the periods 1959–1987 (c) and 1987–2017 (d). Positive values on the maps (a) and (b) correspond to the direction of heat fluxes from the ocean to the atmosphere. Black dots on the maps (c) and (d) mark the areas of the statistically significant linear trends at the 5% significance level.

The structure of the obtained fields differs significantly between the two periods. These differences are related to the strong climate warming, which has begun in the 1980s. The area of the zones with the heat flux from the ocean to the atmosphere is higher for the modern period than for the previous one (Figure 3a, b). At the same time, the intensity of the heat flux ocean–atmosphere over the areas, where open water has always been observed, is lower in the modern period due to the increase in the air temperature and the decrease in the temperature difference between the ocean and the atmosphere. Figure 3d divides the sea practically into two parts: the northern part, in which the heat flux to the atmosphere increases due to the decrease in the concentration of sea ice, and the southern part, where the heat flux to the atmosphere decreases due to the decrease in the temperature contrast between water and air. It was found in [*Surkova et al.*, 2021] that anomalies in the turbulent heat fluxes and atmospheric pressure over the Barents Sea are coupled through changes in the North Atlantic Oscillation.

Composite maps of sea level atmospheric pressure anomalies for the maxima and minima in the oceanic heat transport are shown in Figure 4.

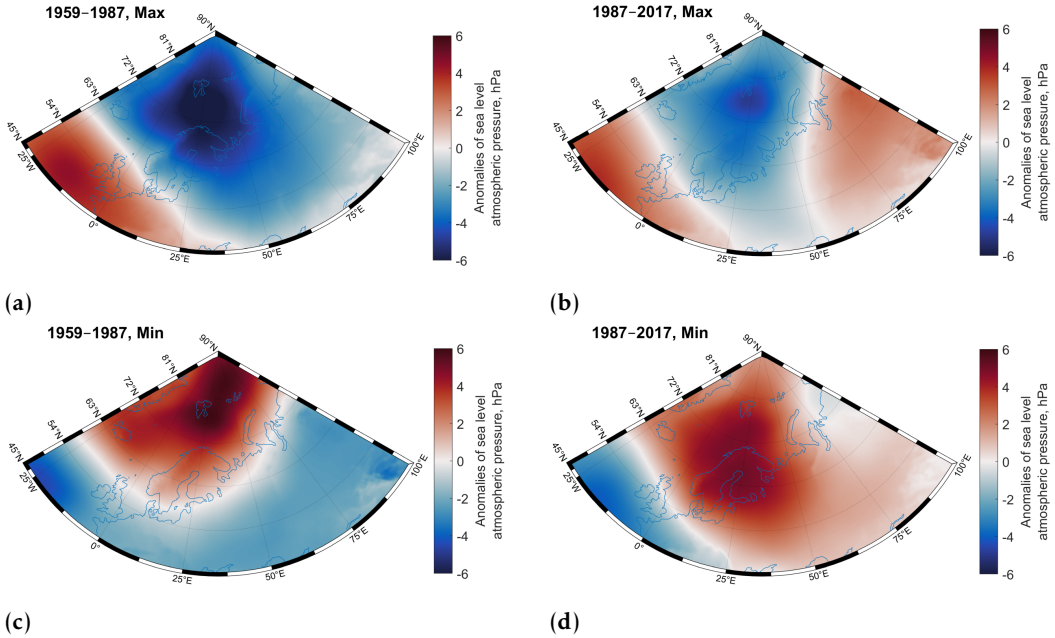

Figure 4. Anomalies of sea level atmospheric pressure relative to the periods 1959–1987 and 1987–2017 for the years with the maximum values of oceanic heat transport at the entrance to the Barents Sea (a, b) and for the years with the minimum values of oceanic heat transport at the entrance to the Barents Sea (c, d).

Negative pressure anomalies are observed over the Barents Sea and adjacent areas in the years with the maximum oceanic heat transport (Figure 4a, b), with the weaker anomaly for the modern period being compensated by a positive anomaly to the southeast of the sea (Figure 4b). The situation is opposite in the years with the minimum oceanic heat transport (Figure 4c, d). The negative pressure anomalies for the period 1987–2017 correspond to a more intense cyclonic atmospheric vorticity over the subpolar North Atlantic and the Barents Sea relative to the period 1959–1987 (Figure 5a, b). At the same time, the positive pressure anomalies for both periods correspond to the mostly cyclonic atmospheric vorticity over this region too; however, it is significantly weaker during 1959–1987 relative to 1987–2017 (Figure 5c, d). Thus, the cyclonic atmospheric vorticity over the Barents Sea has intensified in the present period. This pattern is consistent with the stronger oceanic heat release due to the sea ice reduction in the Barents Sea during 1987–2017 relative to 1959–1987 (Figure 3). It is known that generally, wind stress with cyclonic atmospheric vorticity contributes to an increase in the influx of oceanic heat into the Barents Sea.

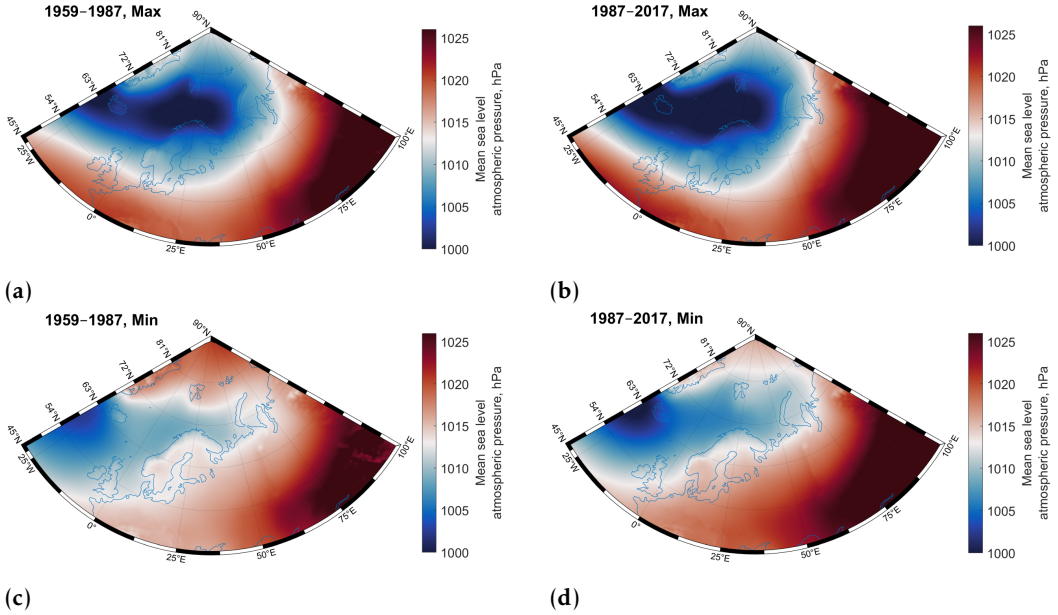

Figure 5. Mean sea level atmospheric pressure in the years with the maximum values of the oceanic heat transport at the entrance to the Barents Sea (a, b) and in the years with the minimum values of the oceanic heat transport at the entrance to the Barents Sea (c, d).

The mean wind fields corresponding to the maxima and minima of the oceanic heat transport are shown in Figure 6.

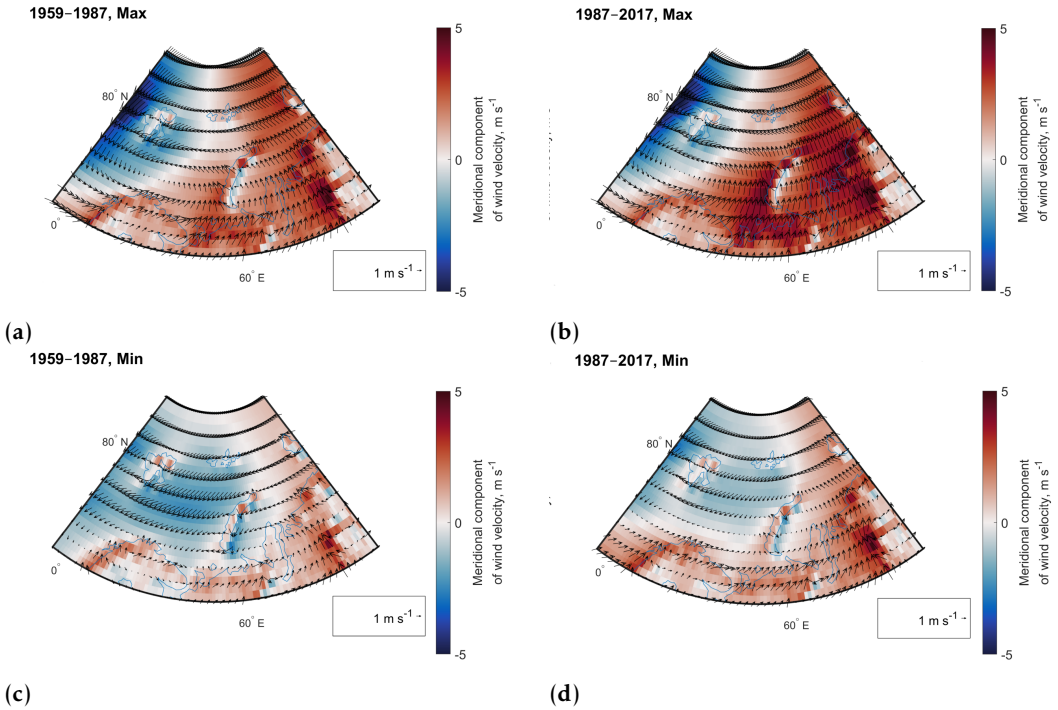

Figure 6. Mean wind velocity values (black arrows) at a height of 10 m in the years with the maximum values of the oceanic heat transport at the entrance to the Barents Sea (a, b) and in the years with the minimum values of the oceanic heat transport at the entrance to the Barents Sea (c, d). The colors show the values of the meridional component of the wind velocity; positive values correspond to the northward direction.

The composite maps in Figure 6 indicate an increase in the effectiveness of the positive feedback in the Barents Sea region in the modern period relative to the previous period. This is manifested in the strengthening of the southern winds over the southeastern part

of the sea in the years with the maximum oceanic heat transport (Figure 6a, b) and in the weakening of the northern winds over the northwestern part of the sea in the years with the minimum oceanic heat transport (Figure 6c, d). The relationship between the zonal oceanic heat transport and the meridional atmospheric heat transport is due to the fact that the cyclonic circulation is observed in the area of the western boundary of the Barents Sea (Figure 6a, b, d). These results are consistent with the previous findings by [*Kalavichchi et al.*, 2021], where an increase in the southern winds over the southeastern Barents Sea is accompanied by an increase of the oceanic heat transport across the Barents Sea Opening during the present period of climate warming.

Figure 7 shows the time-altitude diagrams for the atmospheric sensible heat fluxes.

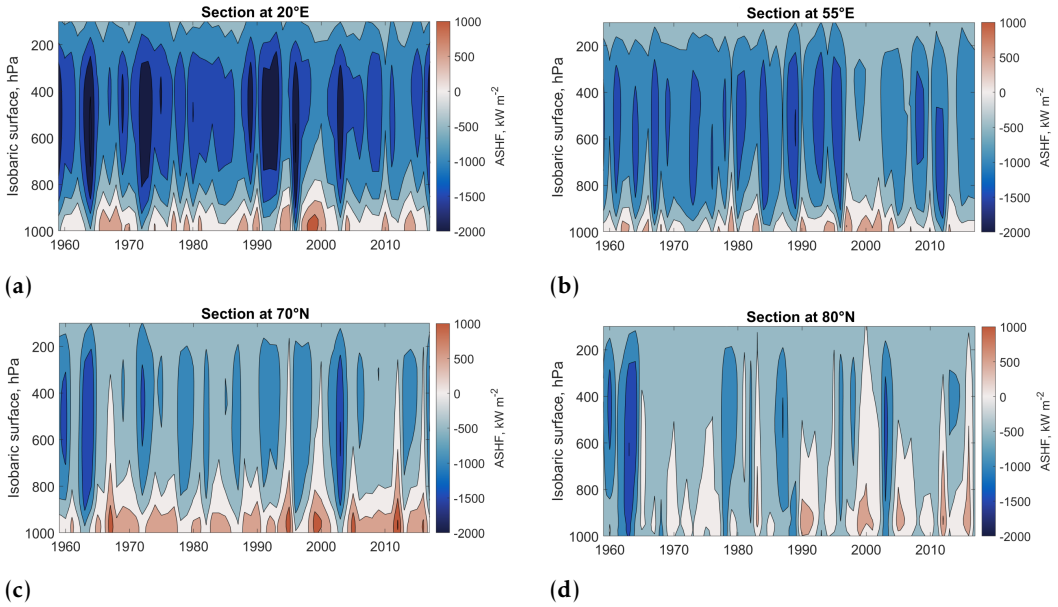

Figure 7. Vertical sections of atmospheric sensible heat flux (ASHF, kW m^{-2}). (a) Mean wintertime sensible heat flux across the section at 20°E, (b) Mean wintertime sensible heat flux across the section at 55°E, (c) Mean wintertime sensible heat flux across the section at 70°N, (d) Mean wintertime sensible heat flux across the section at 80°N. Positive values indicate heat flux to the west (a, b) and to the north (c, d).

According to the obtained vertical profiles, atmospheric sensible heat fluxes are directed predominantly to the west and north in the layer of the lower troposphere 1000–900 hPa, while in the higher levels, the direction changes to the opposite. At the same time, the intensity of fluxes is higher at the western and southern boundaries (Figure 7a, c) than at the eastern and northern boundaries (Figure 7b, d). Thus, only atmospheric circulation in the lower troposphere is directly involved in the emergence of the studied positive feedback. Therefore, integral heat fluxes in the 1000–900 hPa layer were then calculated for each atmospheric section.

The convergences of the oceanic and atmospheric heat transports are shown in Figure 8. The mean atmospheric heat convergence over the studied period is 401 ± 223 TW. The uncertainty is high due to very strong variability. The mean wintertime atmospheric heat transport convergence of 405 TW based on the ERA-Interim reanalysis dataset was reported in [*Kalavichchi et al.*, 2019]. This quantity is very close to 401 TW found in the present study. Thus, the atmospheric heat transport convergence strongly dominates over the oceanic heat transport convergence, which is only 64 TW.

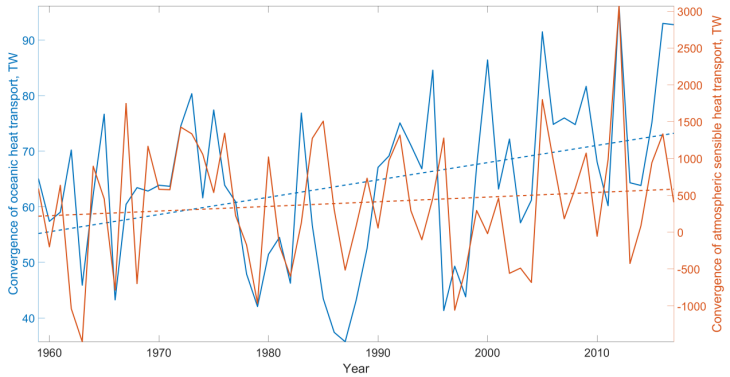

Figure 8. Convergence of oceanic and atmospheric heat transports in the Barents Sea region. 1 TW = 10^{12} W. Dashed lines show linear trends.

According to Figure 8, the correlation coefficient for the entire period 1959–2017 is 0.44. At the same time, for the period 1959–1987, the correlation is only 0.39, and for the period 1987–2017 it increases to 0.54. All correlations are statistically significant and reach a maximum with a zero time lag. The maximum correlation coefficient of 0.76 is achieved for the period 2003–2017. Therefore, one can conclude that over the modern period, the efficiency of positive feedback in the Barents Sea area has increased. This result indicates an increasing synchronization of the convergence of oceanic and atmospheric heat transports in the area of the Barents Sea, which contributes to an amplification of the local warming.

4. Conclusions

The results of the present study point out that climate warming contributes to the emergence of the effectiveness of the positive feedback in the Barents Sea region, which leads to a stronger warming in the area. The growing coherence of the atmospheric heat convergence with the growing oceanic heat transport into the sea contributes to the accelerated warming of the atmosphere over the Barents Sea compared to the rest of the Arctic Ocean.

The atmospheric circulation has become more meridional during the present period of climate warming, which is supported by the previous studies [*Francis et al.*, 2012]. This feature is related to the changes in the large-scale atmospheric circulation, with a growing role of the Siberian High [*Inoue et al.*, 2012; *Kalavichchi et al.*, 2021]. These processes affect the positive feedback in the Barents Sea area. Thus, although the Barents Sea has a unique climate system with the local feedback, the processes here are strongly coupled to the large-scale atmospheric circulation.

In turn, the accelerated sea ice retreat and corresponding wintertime increase of the sensible heat flux were suggested to lead to more frequent anticyclonic blocking events, which results in colder winters in Europe in the beginning of the 21th century [*Petoukhov et al.*, 2010; *Semenov et al.*, 2015].

Acknowledgments. This study was funded by the Russian Science Foundation (RSF), grant number 23-77-01046 (https://rscf.ru/en/project/23-77-01046/). M. M. L. would like to thank Alexander P. Makshtas for the valuable discussion on the methodology and advice.

References

Årthun M., Schrum C. Ocean surface heat flux variability in the Barents Sea // Journal of Marine Systems. — 2010. — Vol. 83, no. 1/2. — P. 88–98. — DOI: 10.1016/j.jmarsys.2010.07.003.

Årthun M., Eldevik T., Smedsrud L. H., et al. Quantifying the Influence of Atlantic Heat on Barents Sea Ice Variability and Retreat // Journal of Climate. — 2012. — Vol. 25, no. 13. — P. 4736–4743. — DOI: 10.1175/jcli-d-11-00466.1.

Balmaseda M. A., Mogensen K., Weaver A. T. Evaluation of the ECMWF ocean reanalysis system ORAS4 // Quarterly Journal of the Royal Meteorological Society. — 2012. — Vol. 139, no. 674. — P. 1132–1161. — DOI: 10.1002/qj.2063.

Bashmachnikov I. L., Yurova A. Y., Bobylev L. P., et al. Seasonal and Interannual Variations of Heat Fluxes in the Barents Sea Region // Izvestiya, Atmospheric and Oceanic Physics. — 2018. — Vol. 54, no. 2. — P. 213–222. — DOI: 10.1134/s0001433818020032.

Bengtsson L., Semenov V. A., Johannessen O. M. The Early Twentieth-Century Warming in the Arctic - A Possible Mechanism // Journal of Climate. — 2004. — Vol. 17, no. 20. — P. 4045–4057. — DOI: 10.1175/1520-0442(2004)017<4045:tetwit>2.0.co;2.

Brutsaert W. Evaporation into the Atmosphere. — Springer Netherlands, 1982. — DOI: 10.1007/978-94-017-1497-6.

Cai Z., You Q., Chen H. W., et al. Amplified wintertime Barents Sea warming linked to intensified Barents oscillation // Environmental Research Letters. — 2022. — Vol. 17, no. 4. — DOI: 10.1088/1748-9326/ac5bb3.

Eisbrenner E., Chafik L., Åslund O., et al. Interplay of atmosphere and ocean amplifies summer marine extremes in the Barents Sea at different timescales // Communications Earth & Environment. — 2024. — Vol. 5, no. 1. — DOI: 10.1038/s43247-024-01610-5.

Francis J. A., Vavrus S. J. Evidence linking Arctic amplification to extreme weather in mid-latitudes // Geophysical Research Letters. — 2012. — Vol. 39, no. 6. — DOI: 10.1029/2012gl051000.

Hersbach H., Bell B., Berrisford P., et al. The ERA5 global reanalysis // Quarterly Journal of the Royal Meteorological Society. — 2020. — Vol. 146, no. 730. — P. 1999–2049. — DOI: 10.1002/qj.3803.

Ingvaldsen R. B., Assmann K. M., Primicerio R., et al. Physical manifestations and ecological implications of Arctic Atlantification // Nature Reviews Earth & Environment. — 2021. — Vol. 2, no. 12. — P. 874–889. — DOI: 10.1038/s43017-021-00228-x.

Inoue J., Hori M. E., Takaya K. The Role of Barents Sea Ice in the Wintertime Cyclone Track and Emergence of a Warm-Arctic Cold-Siberian Anomaly // Journal of Climate. — 2012. — Vol. 25, no. 7. — P. 2561–2568. — DOI: 10.1175/jcli-d-11-00449.1.

Isaksen K., Nordli Ø., Ivanov B., et al. Exceptional warming over the Barents area // Scientific Reports. — 2022. — Vol. 12, no. 1. — DOI: 10.1038/s41598-022-13568-5.

Kalavichchi K. A., Bashmachnikov I. L. Mechanism of a Positive Feedback in Long-Term Variations of the Convergence of Oceanic and Atmospheric Heat Fluxes and of the Ice Cover in the Barents Sea // Izvestiya, Atmospheric and Oceanic Physics. — 2019. — Vol. 55, no. 6. — P. 640–649. — DOI: 10.1134/s0001433819060173.

Kalavichchi K. A., Bashmachnikov I. L. Ocean–Atmosphere Interactions in the Barents Sea from Reanalyses Data // Izvestiya, Atmospheric and Oceanic Physics. — 2021. — Vol. 57, no. 2. — P. 159–169. — DOI: 10.1134/s0001433821020067.

Latonin M. M., Bobylev L. P., Bashmachnikov I. L., et al. Dipole pattern of meridional atmospheric internal energy transport across the Arctic gate // Scientific Reports. — 2022. — Vol. 12, no. 1. — DOI: 10.1038/s41598-022-06371-9.

Lind S., Ingvaldsen R. B., Furevik T. Arctic warming hotspot in the northern Barents Sea linked to declining sea-ice import // Nature Climate Change. — 2018. — Vol. 8, no. 7. — P. 634–639. — DOI: 10.1038/s41558-018-0205-y.

Petoukhov V., Semenov V. A. A link between reduced Barents-Kara sea ice and cold winter extremes over northern continents // Journal of Geophysical Research: Atmospheres. — 2010. — Vol. 115, no. D21. — DOI: 10.1029/2009jd013568.

Przybylak R., Wyszyński P. Air temperature changes in the Arctic in the period 1951–2015 in the light of observational and reanalysis data // Theoretical and Applied Climatology. — 2019. — Vol. 139, no. 1/2. — P. 75–94. — DOI: 10.1007/s00704-019-02952-3.

Schauer U., Loeng H., Rudels B., et al. Atlantic Water flow through the Barents and Kara Seas // Deep Sea Research Part I: Oceanographic Research Papers. — 2002. — Vol. 49, no. 12. — P. 2281–2298. — DOI: 10.1016/s0967-0637(02)00125-5.

Semenov V. A., Park W., Latif M. Barents Sea inflow shutdown: A new mechanism for rapid climate changes // Geophysical Research Letters. — 2009. — Vol. 36, no. 14. — DOI: 10.1029/2009gl038911.

Semenov V. A., Latif M., Dommenget D., et al. The Impact of North Atlantic–Arctic Multidecadal Variability on Northern Hemisphere Surface Air Temperature // Journal of Climate. — 2010. — Vol. 23, no. 21. — P. 5668–5677. — DOI: 10.1175/2010jcli3347.1.

Semenov V. A., *Latif M.* Nonlinear winter atmospheric circulation response to Arctic sea ice concentration anomalies for different periods during 1966–2012 // Environmental Research Letters. — 2015. — Vol. 10, no. 5. — DOI: 10.1088/1748-9326/10/5/054020.

Smedsrud L. H., *Esau I.*, *Ingvaldsen R. B.*, *et al.* The Role of the Barents Sea in the Arctic Climate System // Reviews of Geophysics. — 2013. — Vol. 51, no. 3. — P. 415–449. — DOI: 10.1002/rog.20017.

Surkova G. V., *Romanenko V. A.* Climate change and heat exchange between atmosphere and ocean in the Arctic based on data from the Barents and the Kara sea // Arctic and Antarctic Research. — 2021. — Vol. 67, no. 3. — P. 280–292. — DOI: 10.30758/0555-2648-2021-67-3-280-292.

Trenberth K. E., *Caron J. M.* Estimates of Meridional Atmosphere and Ocean Heat Transports // Journal of Climate. — 2001. — Vol. 14, no. 16. — P. 3433–3443. — DOI: 10.1175/1520-0442(2001)014<3433:eomaao>2.0.co;2.

Russian Journal of Earth Sciences

Special Issue: "Data Science, Geoinformatics and Systems Analysis in Geosciences"

On the Methods of Constructing a Digital Regional Geological and Mathematical Model for the Western Siberia Region

A. A. Sidorov[1]

[1]V. I. Shpilman Research and Analytical Centre for the Rational Use of the Subsoil, Khanty-Mansiysk, Russia
* **Correspondence to:** Sidorov Andrei, darth@crru.ru

Abstract: The article presents an approach to creating a detailed regional digital geological model for the territory of Western Siberia. The non-standard nature of such tasks is noted, and a conclusion is made about the need to develop specialized software for these purposes. The variational grid mapping method as a tool for constructing digital structural models and property fields is considered. The object-hierarchical approach is proposed as a method of data space managing, algorithmization and automation of calculations. The "GST Agent" technology as an instrument of expanding the functionality of the software if proposed. The digital model of the region includes a structural framework consisting of more than 30 stratigraphic boundaries, as well as detailed submodels for the most studied areas. The approach ensures the possibility of automated recalculation of the model and full compliance of the modeling results with all the original data.

Keywords: regional model, mapping, variational grid method, object-hierarchical approach, structural framework.

Citation: Sidorov, A. A. (2025), On the Methods of Constructing a Digital Regional Geological and Mathematical Model for the Western Siberia Region, *Russian Journal of Earth Sciences*, 25, ES2009, EDN: RNQQGZ, https://doi.org/10.2205/2025ES000968

1. Introduction

Problem of constructing detailed regional digital models is non-standard. The level of study of the territory, the quality and structure of the initial data play an important role in it. However, the development of well-known specialized software (Petrel, IRAP RMS, T-Navigator, etc.) occurs primarily in commercially profitable directions. It is focused on building models for deposit areas for further volumetrics or hydrodynamic modeling. For this and other reasons, regional digital models are often built on the basis of the research teams' own developments [*Brekhuntsov et al.*, 2011; *Ershov et al.*, 2009; *Kontorovich et al.*, 2014; *Krasavchikov*, 2002; *Sidorov*, 2022c].

For over 20 years, the staff of the "V. I. Shpilman Scientific and Analytical Center for Rational Subsoil Use" have been systematically working to summarize a large volume of geological and geophysical information on the territory of Western Siberia. Methods and software tools are developed and implemented for solving problems of mathematical geology, in particular, regional modeling. As a result, a digital geological model is constructed, including a detailed structural framework and maps of the geological and physical properties of sedimentary cover rocks.

2. Methods

The modeling was made in the GST software, which was developed taking into account the specifics of regional problems. The main part of the mathematical kernel is the variational gridding method (VGM), based on the spline approximation approach [*Plavnik et al.*,

Research Article

Received: 15 November 2024
Accepted: 15 April 2025
Published: 23 May 2025

2021]. The article [*Plavnik et al.*, 2024] discusses the use of the VGM in the construction of a digital structural framework; [*Sidorov et al.*, 2004; *Sidorov*, 2022a] demonstrate its capabilities in solving problems of mathematical physics and modeling the sedimentation process; in [*Sidorov*, 2020] an adaptation of the approach for constructing maps with faults is discussed.

The functional of the variational problem is formed from two parts: the "measurement model" and the "knowledge model". The first one is a set of conditions for the gridding surface at given points. The second one determines the gridding surface in the entire modeling area. Both models are presented as a set of equations, the left and right parts of which are determined by linear differential operators with variable coefficients. The operator coefficients determine the physical meaning of the source data, and the weight coefficients indicate the quality of the measurements. These features make VGM a universal method for both structural gridding and mapping geological and physical parameters.

The module for algorithmization and automation of calculation processes, based on the object-hierarchical approach [*Sidorov*, 2022b], controls the mathematical kernel, export and import of information. The main semantic element of the theory is an object (Figure 1). It is described by a set of constant attributes, configuration parameters and a computational content. It is important that the computed content may not exist, i.e. the object may be "empty". Each object characterizes a certain part of the initial, intermediate data or final results of calculations. A set of objects connected by reference links (Figure 1 on the right) forms a hierarchy tree. The spectrum of discrete states of an object, indicating the "constructing stage", determines the dynamics of the hierarchy tree.

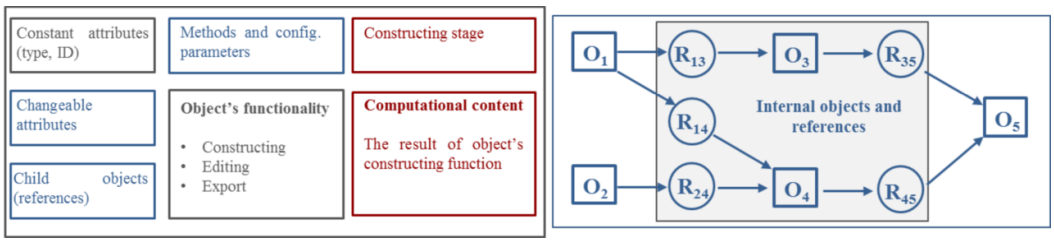

Figure 1. Schematic representation of an object and a hierarchy tree (Oi – objects containing initial, intermediate and final data, Rij – reference links).

This approach helps to build a problem solving algorithm, compose and modify the project graph through operations of copying objects groups, and perform automated calculations. It ensures that the modeling results correspond to the initial data and calculation parameters. Any source data modification is passed up the hierarchy and transfers objects to a stage that requires re-building.

Practical experience has shown that the optimal way to work with large tasks, such as building a regional model, is to break the task down into "algorithm blocks" (projects). The "GST Agent" technology, implemented in stand-alone module (in dll, as well), provides asynchronous data and commands exchange between applications that support this technology (Figure 2). The approach is based on the "request-response" scheme, where messages are a structured byte stream containing both the "body" of the request or response, and a block with source data and calculation results. The Agent module dispatches requests and responses between applications. This technology solves several problems: expanding functionality through writing calculation modules and implementing interaction with external software, as well as managing calculations in a group of projects.

3. Results

Figure 3 shows a scheme of a digital permanently operating geological model of the sedimentary cover of the Western Siberia. The model is most complete in the central part, which includes the territory of the Khanty-Mansiysk Autonomous Okrug; main seismic horizons and structural surfaces of Jurassic interval are mapped throughout the entire region of the oil and gas province. The basic detail structural framework, which includes

Figure 2. Scheme of interaction of GST instances and external applications.

maps of more than 30 stratigraphic surfaces, is built on grids with 500×500 meter cells. For areas with a complicated structural forms, provided with 3D seismic data, detailed sub-models with 250 or 125 meter cells are created. They are merged to the base model using the "smooth inserts" method [*Plavnik et al.*, 2024].

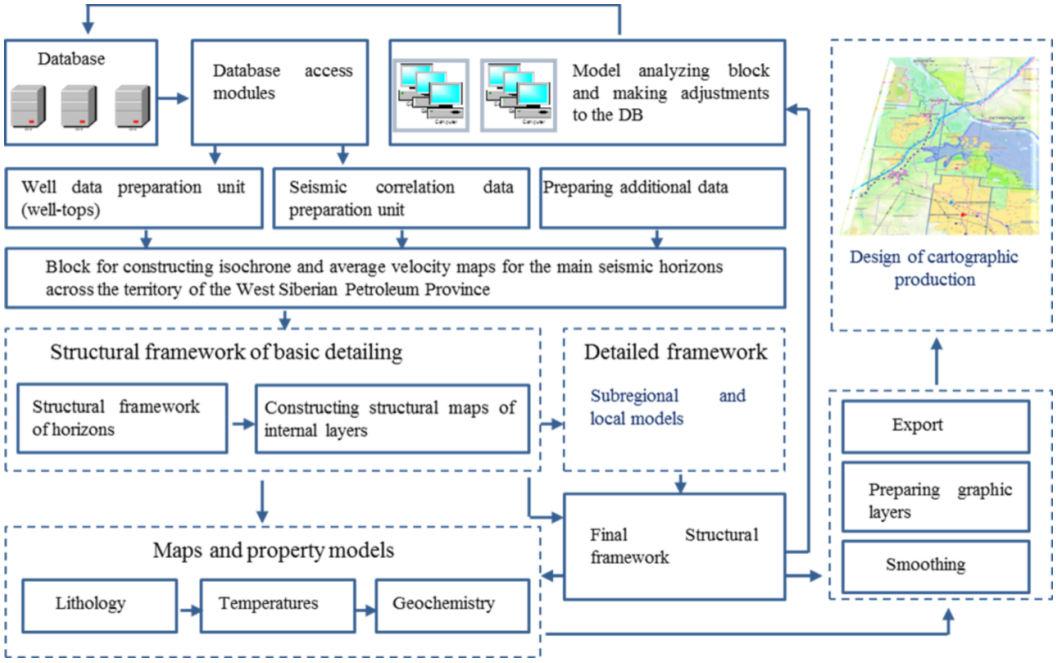

Figure 3. Scheme of the digital permanently operating geological model for the central part of Western Siberia.

Seismic correlation (more than 2000 surveys), "well-tops" and other source data are loaded into the model from the database using automated importing, filtering and categorizing procedures. The modeling results are analyzed using visualization projects that have direct access to the model based on the "linked projects" technology [*Sidorov*, 2022b,c].

As an example of the modeling results the basement structure regional map for the territory of Western Siberia is shown on Figure 4. The detailed fragment shows paleosurface (Lower Jurassic) of the basement in the area of Talin oilfield and the paleochannel. The level of detail, shown in the zoomed image, is typical for all surfaces of the digital structural framework.

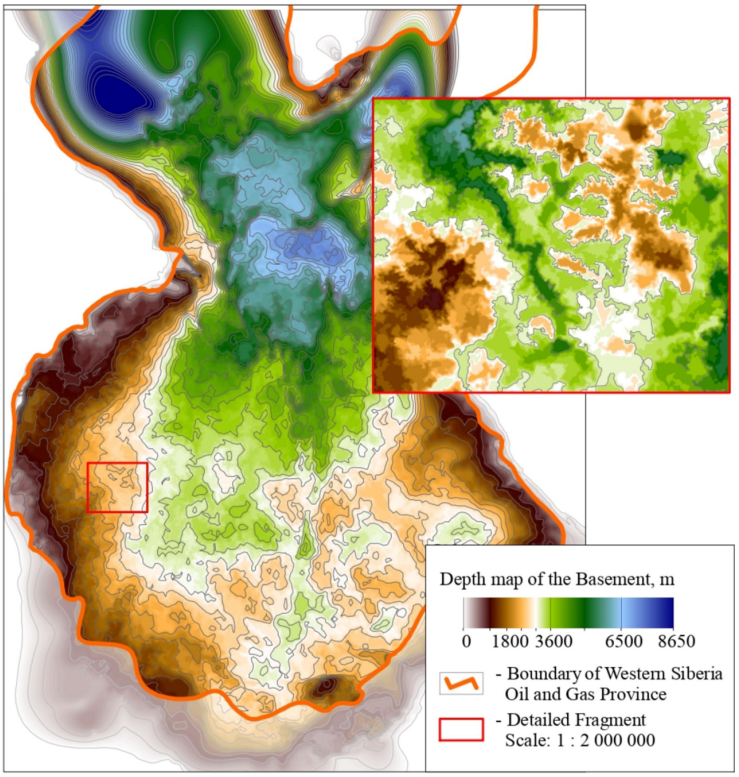

Figure 4. An element of the Digital structural framework: depth map of the Basement for the Western Siberia region and the detailed fragment with paleochannel.

The model consists of more than fifty projects, each of which describes the solution to the corresponding block of the problem. The entire calculation cycle from importing initial data from the database to obtaining the final result is performed automatically using a task script and "GST Agent" technology. The use of object-hierarchical approach ensures automated multi-threaded execution of the entire technological chain and full compliance of the calculation results with the initial data and modeling parameters.

4. Conclusion

The combined use of the object-hierarchical approach and "GST Agent" technology helps to solve regional modeling problems and handle large volumes of permanently changing initial geological and geophysical information. The hierarchical, object-oriented structure of projects significantly simplifies and accelerates the model's modification in case of updating the source data, changing the calculation methodology, or adjusting the very concept of the model.

Model evolution – detailing or adding new elements to the model is carried out by embedding new semantic blocks (projects) into the calculation scheme. Currently, the structural framework is being regularly refined by including detailed subregional and local submodels in the calculation scheme.

References

Brekhuntsov A. M., Monastyrev B. V., Nesterov I. I. Distribution patterns of oil and gas accumulations in West Siberia // Russian Geology and Geophysics. — 2011. — Vol. 52, no. 8. — P. 781–791. — DOI: 10.1016/j.rgg.2011.07.004. — EDN: NYJKCB.

Ershov S. V., Bukreeva G. F., Krasavchikov V. O. Computer simulation of Neocomian clinoform reservoirs in northern and arctic West Siberia // Russian Geology and Geophysics. — 2009. — Vol. 50, no. 9. — P. 797–807. — DOI: 10.1016/j.rgg.2009.08.005.

Kontorovich V. A., *Lapkovsky V. V.*, *Lunev B. V.* Model of forming neocomian clinoform complex of West-Siberian oil-and-gas bearing province with regard to isostasy // Russian oil & gas geology. — 2014. — Vol. 1. — P. 65–72. — EDN: RUMRDZ. — (In Russian).

Krasavchikov V. O. Synthetic interpretation of poorly correlated geological and geophysical data in regional structural mapping (sedimentary cover of the West-Siberian Plate) // Russian Geology and Geophysics. — 2002. — Vol. 43, no. 5. — P. 456–469.

Plavnik A. G., *Sidorov A. N.*, *Sidorov A. A.*, *et al.* Geomapping based on the spline approximation approach. — Tyumen' : TIU, 2021. — 189 p. — (In Russian).

Plavnik A. G., *Sidorov A. A.* Construction of compositional geological models using the variational grid method of geomapping and the object-hierarchical approach // Tyumen State University Herald. Physical and Mathematical Modeling. Oil, Gas, Energy. — 2024. — Vol. 10, no. 2. — P. 88–103. — DOI: 10.21684/2411-7978-2024-10-2-88-103. — (In Russian).

Sidorov A. N., *Plavnik A. G.* Solution of partial differential equations by spline approximation methods // Proceedings of the International Conference on Computational Mathematics ICCM-2004. — Novosibirsk : IVMiMG SO RAN, 2004. — P. 648–652.

Sidorov A. A. Using the method of boundary integral equations in solving of the geological mapping problems with faults // Tyumen State University Herald. Physical and Mathematical Modeling. Oil, Gas, Energy. — 2020. — Vol. 6, no. 2. — P. 110–126. — DOI: 10.21684/2411-7978-2020-6-2-110-126. — (In Russian).

Sidorov A. A. Variational gridding approach to the lithological modeling of clinoform-type deposits // Tyumen State University Herald. Physical and Mathematical Modeling. Oil, Gas, Energy. — 2022a. — Vol. 8, no. 1. — P. 109–125. — DOI: 10.21684/2411-7978-2022-8-1-109-125. — (In Russian).

Sidorov A. A. Object-Hierarchical approach for creating workflows in geo-modeling // Journal of Information Technologies and Computing Systems. — 2022b. — No. 4. — P. 103–114. — DOI: 10.14357/20718632210410. — (In Russian).

Sidorov A. A. On the Creation of a Digital Permanently Operating Structural Model for the Sedimentary Cover of the West Siberian Petroleum Province // Russian Geology and Geophysics. — 2022c. — Vol. 63, no. 8. — P. 955–965. — DOI: 10.2113/rgg20214342.

Russian Journal of Earth Sciences

Special Issue: "Data Science, Geoinformatics and Systems Analysis in Geosciences"

Field Geophysical Complex for Creating Maps of the Parameters of the Earth's Gravitational and Magnetic Fields

M. Murzabekov[1], P. Lopatin[1], D. Bobrov[1]

[1]FSUE "VNIIFTRI", Mendeleyevo, Solnechnogorsk, Moscow region, Russia
* **Correspondence to:** Murzabekov Murat, murzabekov@vniiftri.ru

Abstract: The article discusses a field geophysical complex that includes the Earth's gravity and magnetic fields parameters meters — an digital zenith camera (DZC), a relative gravimeter, onboard quantum magnetometer and ground magnetovariation station. This complex allows determining such parameters of the Earth's gravity field as acceleration and anomalies of gravity, plumb line deviations, horizontal components of the acceleration of gravity and gravitational gradients, and parameters of the Earth's magnetic field — absolute and anomalous values of induction. Maps of the Earth's gravity and magnetic fields can be used in various fields, in particular, in the creation and testing of integrated autonomous navigation systems using the parameters of these fields. The paper presents examples of parameter maps created using this complex. The measurement error of acceleration and gravity anomaly is 10 μGal, plumb line deviation is ≈ 0.2″, horizontal components of gravity acceleration are ≈ 1 mGal, gravitational gradients are 10 Eötvös at a distance between calculation points of ≈ 1.4 km, and the parameters of the Earth's magnetic field are 1 nT.

Keywords: Earth's gravity field, Earth's magnetic field, digital zenith camera, gravimeter, magnetometer, navigation charts.

Citation: Murzabekov, M., P. Lopatin, and D. Bobrov (2025), Field Geophysical Complex for Creating Maps of the Parameters of the Earth's Gravitational and Magnetic Fields, *Russian Journal of Earth Sciences*, 25, ES2010, EDN: SBATCM, https://doi.org/10.2205/2025ES000969

1. Introduction

Today, the highest navigation accuracy is achieved by systems based on the use of global satellite systems (GNSS) signals. However, to ensure "seamless" navigation in conditions of interference and unavailability of GNSS signals, it is necessary to develop an integrated navigation system. The integration of GNSS consumer navigation equipment and a strapdown inertial navigation system (SINS) has become widespread, which improves accuracy and noise immunity. However, as is known, in the case of a prolonged absence of GNSS signals, the error in determining the location using the SINS accumulates and its readings must be corrected. In such cases, it is possible to use the parameters of the Earth's gravity and magnetic fields (EGF and EMF) to correct SINS readings [*Canciani et al.*, 2017; *Denisenko et al.*, 2020; *Sazonova*, 2020; *Stepanov et al.*, 2020].

One of the components of such an integrated system is a reference navigation map of the parameters of the EGF and EMF, which is used to determine the current location based on the results of comparison with the measurement data of the onboard measuring device. It should be noted separately that, as noted in works [*Peshekhonov*, 2020; *Popadyev et al.*, 2015], EGF maps are also needed as a source of correction information for SINS. These works note that for promising SINS, the error in determining the EGF parameters will make a significant contribution to the accuracy of the navigation solution.

The paper presents a field geophysical complex that will allow the creation of EGF and EMF maps, with previously unattainable accuracy and discreteness, which can be used in the creation and testing of integrated navigation systems.

Research Article

Received: 15 November 2024
Accepted: 15 April 2025
Published: 23 May 2025

2. Field gravity complex

2.1. EGF measuring instruments

To measure the EGF parameters, it is proposed to use together the DZC to measure the deflection of vertical (DoV) developed by the FSUE "VNIIFTRI" [*Murzabekov et al.*, 2020] and the relative gravimeter of the Scintrex CG-5 (Figure 1).

Figure 1. DZC and relative gravimeter.

The combined use of these devices allows measuring the components ξ, η of the DoV and the acceleration of gravity g (AGG) at a single point. Both devices are field devices, relocatable and allow measurements to be taken with any specified discreteness. The measurement error of DoV is 0.2″, and of AGG is no more than 10 μGal.

With known values of DoV and AGG, the horizontal components of AGG g_x and g_y are calculated at the same point [*Ogorodova*, 2010]:

$$g_x \approx -g \cdot \xi;\ g_y \approx -g \cdot \eta.$$

With known g_x and g_y values between measurement points, the gravity gradients T_{ij} (second derivatives of the anomalous potential) are calculated as their change along the corresponding axis, divided by the distance between them. For example, the T_{xx} component of the gravity gradient between points 1 and 2, lying along the meridian (OX axis) at a distance of $\Delta x = x_2 - x_1$, is calculated as:

$$T_{xx} = \frac{g_{x_2} - g_{x_1}}{x_2 - x_1} = \frac{\Delta g_x}{\Delta x}.$$

Similarly, the expressions for calculating T_{yy} and T_{xy} are:

$$T_{yy} = \frac{\Delta g_y}{\Delta y};\ T_{xy} = \frac{\Delta g_x}{\Delta y},$$

where Δg_x and Δg_y are the changes in g_x and g_y between the measurement points along the meridian (OX axis) and parallel (OY axis); Δy is the distance between the points along the OY axis.

Figure 2a shows a graph of the dependence of the calculation error g_x on the latitude error of the DoV, and Figure 2b shows a graph of the dependence of the error T_{xx} on the distance between measurement points with an DoV error 0.1″÷0.3″.

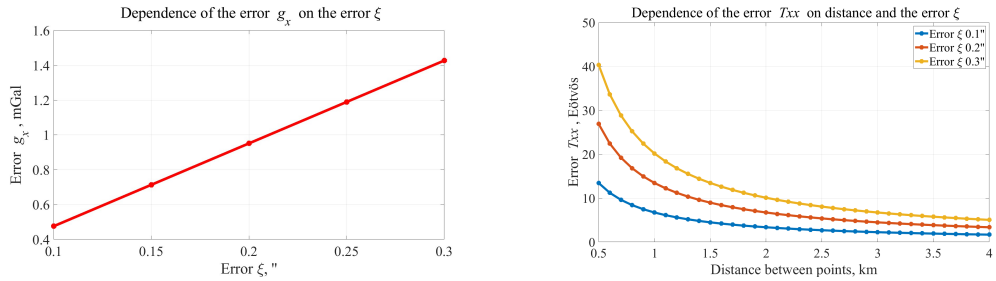

(a) **(b)**

Figure 2. g_x and T_{xx} calculation error.

2.2. Measuring instruments for EMF parameters

To measure the EMF parameters, the complex uses an onboard quantum magnetometer from *Geoscan* and a magnetovariation station from *Radar MMS Research and Production Enterprise* (Figure 3). In this case, to increase the efficiency of measurements, a quadcopter is used, to which an onboard magnetometer is attached on a 10 m long non-magnetic cable. A distance of 10 m is sufficient to completely eliminate the influence of interference from the quadcopter on the magnetometer readings.

(a) **(b)**

Figure 3. Measuring instruments for EMF parameters.

3. Map creation results

3.1. EGF maps

Joint measurements of the DoV and AGG components using an DZC and gravimeter were performed in the Moscow region at a test site with linear dimensions of approximately 20×20 km. The test site includes 32 measurement points with an average distance of approximately 4 km from each other. The measurement time at a single point using the complex does not exceed 1 hour.

To create DoV and AGG maps, a uniform grid with a step of 100 m was created, including measurement points. Interpolation DoV and AGG values into points of the uniform grid was performed using the well-known "remove-restore" method, which allows taking into account the influence of topographic masses and increases the accuracy of map creation [*Yang et al.*, 2020].

At each point of the uniform grid, first the calculation of g_x and g_y was performed, and then the gravity gradients were calculated at a distance of 1.4 km between the calculation points. Figure 4 shows examples of the created maps of some parameters of the EGF.

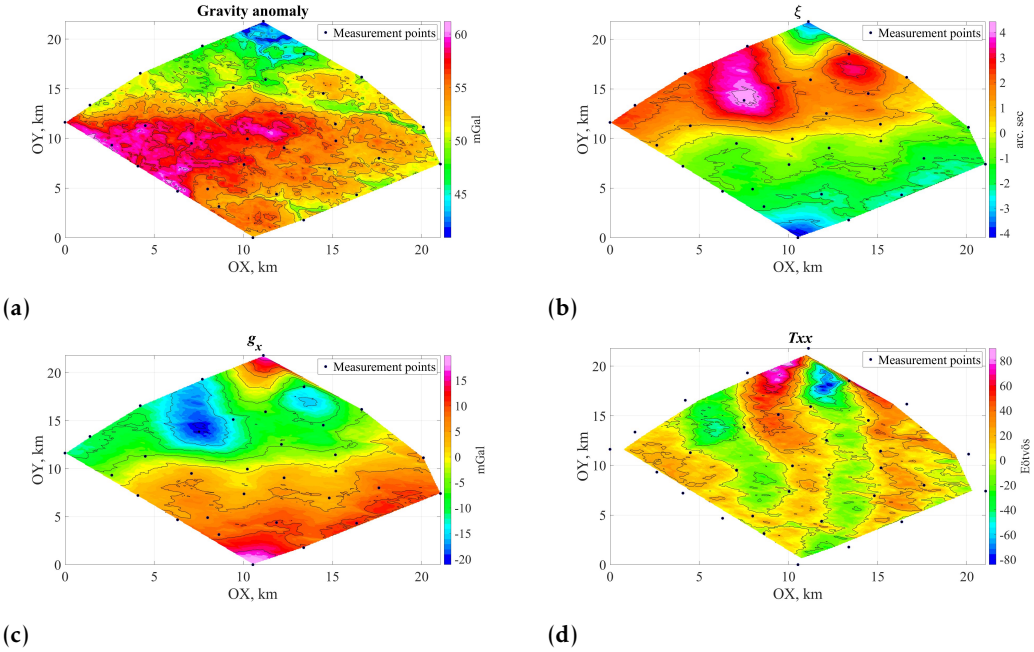

Figure 4. Examples of created EGF maps.

3.2. EMF maps

When creating the EMF maps, measurements were performed by tacks at a flight altitude of 150 m with a distance between tacks of 200 m. A magnetovariation station was located in the measurement area. The map of the EMF anomalous induction component, created based on the results of these measurements, is shown in Figure 5.

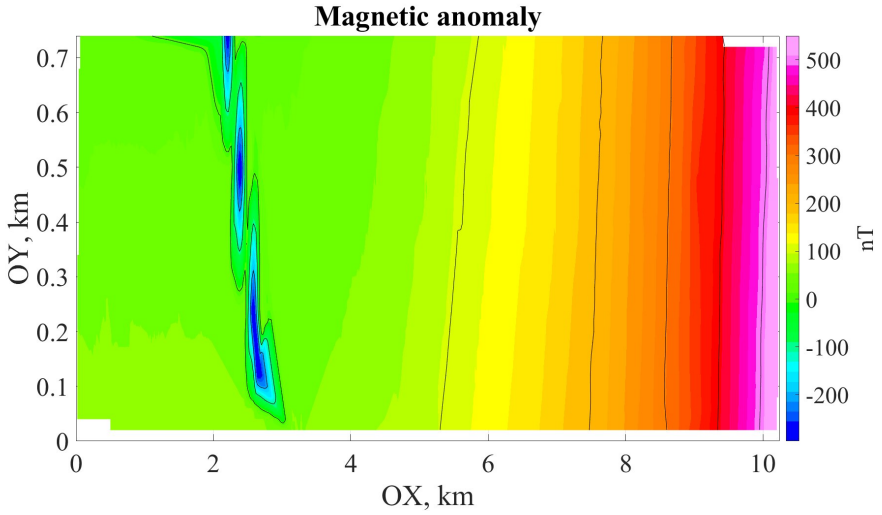

Figure 5. Anomalous EMF map.

The created anomalous EMF map is planned to be used in testing the experimental sample of the EMF navigation system, which is being created at the FSUE "VNIIFTRI". The experimental sample of the EMF navigation system will include the above-mentioned magnetometers and a quadcopter, as well as a SINS on MEMS sensors.

4. Conclusion

The paper presents a geophysical complex that includes meters for the parameters of the EGF and EMF. This complex allows creating maps of the AGG, DoV, gravity gradients, as well as a map of the anomalous EMF. These maps can be used, in particular, in the creation and testing of integrated navigation systems for the EGF and EMF.

Using the complex, examples of maps of the EGF and EMF parameters were created at a local test site. In this case, the measurement error of the AGG is 10 μGal, DoV ≈ 0.2″, horizontal components of the AGG ≈ 1 mGal, gravity gradients — 10 Eötvös at a distance between calculation points of ≈ 1.4 km, EMF parameters — 1 nT.

Acknowledgments. The study was supported by a grant from the Russian Science Foundation No. 23-67-10007, https://rscf.ru/project/23-67-10007/.

References

Canciani A., *Raquet J.* Airborne Magnetic Anomaly Navigation // IEEE Transactions on Aerospace and Electronic Systems. — 2017. — Vol. 53, no. 1. — P. 67–80. — DOI: 10.1109/taes.2017.2649238.

Denisenko O. V., *Pustovoit V. I.*, *Silvestrov I. S.*, *et al.* Problems of development of seamless assistive navigation technology in GNSS GLONASS based on measurements of parameters of geophysical fields // Almanac of modern metrology. — 2020. — 4 (24). — P. 127–160. — (In Russian).

Murzabekov M. M., *Fateev V. F.*, *Yuzefovich P. A.* Measuring Plumb-Line Deviations with a Digital Astrometer at the Moscow Gravitational Attraction // Astronomy Reports. — 2020. — Vol. 64, issue 10, no. 10. — P. 876–882. — DOI: 10.1134/s1063772920100042.

Ogorodova L. V. Normal field and definition of anomalous potential. — Moscow : MIIGAiK, 2010. — P. 105. — (In Russian).

Peshekhonov V. G. Problem of the Vertical Deflection in High-Precision Inertial Navigation // Giroskopiya i Navigatsiya. — 2020. — Vol. 28, no. 4. — P. 3–15. — DOI: 10.17285/0869-7035.0046. — (In Russian).

Popadyev V. V., *Soroka A. I.*, *Polubekhin A. I.* The possibilities of correction parameters of onboard inertial navigation systems for aircraft based on gravimetric maps of the Earth // Civil Aviation High Technologies. — 2015. — No. 222. — P. 90–97. — (In Russian).

Sazonova T. V. Experimental studies of the accuracy characteristics of correlation-extreme navigation systems based on the Earth's magnetic field // Almanac of modern metrology. — 2020. — 4(24). — P. 86–96. — (In Russian).

Stepanov O. A., *Nosov A. S.* A Map-Aided Navigation Algorithm without Preprocessing of Field Measurements // Giroskopiya i Navigatsiya. — 2020. — Vol. 28, no. 2. — P. 70–90. — DOI: 10.17285/0869-7035.0029. — (In Russian).

Yang M., *Hirt C.*, *Pail R.* TGF: A New MATLAB-based Software for Terrain-related Gravity Field Calculations // Remote Sensing. — 2020. — Vol. 12, no. 7. — P. 1063. — DOI: 10.3390/rs12071063.

Russian Journal of Earth Sciences

Special Issue: "Data Science, Geoinformatics and Systems Analysis in Geosciences"

Modelling of Mantle-Crust Migrant Systems: A New Approach to Systems Analysis of Seismic Events

V. I. Vasiliev[1], **E. V. Vasilieva**[1]

[1]Dobretsov Geological Institute of Siberian Branch of Russian Academy of Sciences, Ulan-Ude, Russia
* **Correspondence to:** Vasiliev Vladimir Igorievich, geovladi@yandex.ru

Abstract: Fluids have a significant impact on seismic processes in the lithosphere and the earth's crust. They can form systems of mantle-crust migrants that rise in a solid plastic medium due to fluid-fracturing. When migrants are formed, the energy accumulated earlier in the parent chambers under the strength barriers is released. The accumulating energy includes the potential energy of lithostatic pressure W_P and the energy of deformation of the strength barrier W_E. The released energy includes the energy of cavity formation W_C in the strength layer and the energy of fluid ascent into the cavity W_F. According to the condition $W_P + W_E - W_C - W_F > 0$, the remaining mechanical energy is the cause of such seismic events as rock bursts, unstable zones of low longitudinal wave velocities and seismic "nails".

Keywords: mantle-crust migrants, seismic events, rheological barriers, fluid-fracturing.

Citation: Vasiliev, V. I., and E. V. Vasilieva (2025), Modelling of Mantle-Crust Migrant Systems: A New Approach to Systems Analysis of Seismic Events, *Russian Journal of Earth Sciences*, 25, ES2011, EDN: FDEFUY, https://doi.org/10.2205/2025ES000970

1. Introduction

The fluid factor in seismic events has received attention not so long ago [*Hickman et al.*, 1995]. And currently, research in this area is most often limited to studying the properties of fluid-saturated rocks and hydrocarbon reservoirs of the upper crust [*Xuan et al.*, 2023]. Meanwhile, the presence of H_2O, CO_2 and other fluid components in the mantle, lithosphere and plastic zone of the crust is beyond doubt. These components have a great influence on tectonic processes. Studies of this influence are being carried out [*Levin et al.*, 2010; *Park et al.*, 2021], but are still relatively rare. In this paper, the term *"fluid"* refers not only to H_2O and CO_2, but to the entire mobile group of phases "magma + aqueous solution + gas", and if at least one of these components is present, the *fluid* exists. The aim of the work is to apply a systems analysis of a number of seismic events in plastic medium and at the plastic-brittle transition (PBT) from the standpoint of the theory of systems of mantle-crustal migrants (MCM), which was developed and experimentally tested by N. S. Zhatnuev with the participation of the authors [*Vasiliev et al.*, 2019; *Zhatnuev et al.*, 2009; 2013; *Zhatnuev*, 2005]. They are *fluid*-filled cavities that rise through the solid plastic mantle and lithospheric environment by means of *fluid* fracture. The latter occurs as a result of excess pressure arising in the cavities due to the difference in density between the *fluid* and the enclosing medium [*Zhatnuev*, 2005].

2. Conceptual model

In the first approximation, the formation of the MCM can be described as follows. At a depth H from the PBT, under a layer with tensile strength S (strength barrier), a *fluid* with a significantly reduced density ρ_F relative to the density of the medium ρ_R ($\rho_F \ll \rho_R$) accumulates. It forms a chamber with a thickness Δ_H increasing due to the *fluid* supply (Figure 1). The difference in densities ($\rho_F - \rho_R$) and the increase in Δ_H create excess pressure

Research Article

Received: 15 November 2024
Accepted: 15 April 2025
Published: 23 May 2025

in the roof of the chamber, which leads to the accumulation of normal stress σ_Z, causing deformation ε.

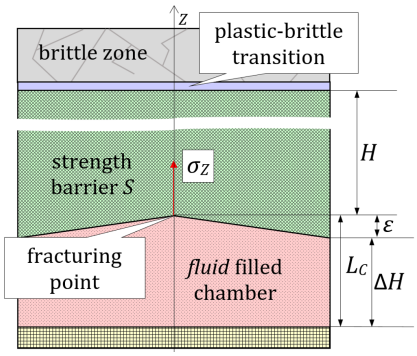

Figure 1. Schematic diagram of the initial chamber of the MCM under the strength barrier *S*. Explanations in the text.

When the chamber reaches the critical thickness L_C, the excess pressure in the chamber exceeds the strength of the overlying barrier *S*. In it, under the action of *fluid*-fracturing, an MCM is formed — a vertical cavity filled with the chamber material. Its formation is described by the condition [*Vasiliev et al.*, 2019]:

$$\int_0^{H+\Delta H} g\rho_R h\mathrm{d}h - \int_0^{H} g\rho_R h\mathrm{d}h - \int_0^{L_C} g\rho_F h\mathrm{d}h > S, \tag{1}$$

where g and h represent the acceleration of gravity and the variable of integration over depth, respectively. Note that the left-hand side of inequality (1) represents the excess pressure in the roof of the chamber (at the strength barrier).

3. Energy model

Let us consider, as a first approximation, the energy balance at the fracture point. It consists of accumulation (stress buildup) with increasing chamber height and discharging (relaxation) during the formation of the MCM. The accumulation consists of the potential energy of the lithostatic pressure of the overlying rocks W_P and the deformation energy of the strength barrier W_E. For the isotropic medium with a thickness H and a vertical density gradient $\nabla\rho_R$, located above a circular in plan *fluid* chamber with a diameter D and a thickness ΔH, the potential energy is described by the expression:

$$W_P = \frac{1}{4} H\pi D^2 g\Delta H \int_0^{H} \rho_R h\mathrm{d}h. \tag{2}$$

The deformation energy can be described in the simplest way [*Xuan et al.*, 2023]:

$$W_E = \frac{3\sigma_Z^2(1-2\mu)}{2E}, \tag{3}$$

where μ and E denote the Poisson's ratio and Young's modulus, respectively.

When estimating energy expenditure (without taking into account dissipation), it is necessary to take into account the expenditure for forming a cavity in the strength layer as a result of *fluid*-fracturing and of lifting the *fluid* into the cavity. The first process can be described as the energy of crack formation (including the energy of new surfaces formation). Previously, we conducted tectonophysics experiments to study the formation and evolution of *fluid*-filled cavities in a transparent plastic medium (gelatin matrices with different properties) [*Zhatnuev et al.*, 2009; 2013]. It was noted that most often the forming cavity has the shape of a subvertical close-to-rounded lens with a thickness of a few millimeters with a maximum thickness to diameter ratio of $\sim 1:k$, where the coefficient k is proportional

to the ratio of kinematic viscosities of the *fluid* and the medium with a maximum lens diameter of up to ~250 mm. The experimental conditions did not allow sizes larger than this due to the influence of edge effects. Within these limits, the average $k \approx 30$. This ratio, of course, cannot be directly applied to natural conditions, but the dependence on the viscosity ratio will be present. Taking this into account, the area of the resulting surface can be approximated by the doubled area of a circle with a radius of $l/2$. Then the energy of formation of the W_C cavity is:

$$W_C = \frac{\pi l^2 \sigma_Z^2}{4E}. \tag{4}$$

The energy of *fluid* ascent is calculated similarly to the potential energy of the rock massif. If we take the volume of a lens of the MCM as 2/3 of the volume of the its corresponding cylinder and assume that the volumes of the chamber and the MCM at the time of its formation are equal, then the height l is as follows:

$$l = \left(\frac{3kD^2\Delta H}{2}\right)^{\frac{1}{3}}. \tag{5}$$

Then the energy of *fluid* ascent W_F is described by the expression:

$$W_F = \frac{1}{8} H \pi l^2 g \Delta H \int_0^l \rho_F h \mathrm{d}h. \tag{6}$$

The accumulated deformation energy W_E can be almost completely spent on the formation of a crack with a small remainder of free energy, which can be neglected similarly to dissipation. But the potential energy W_P is physically much greater than the potential energy of *fluid* ascent W_F, therefore as a result of the formation of the MCM, a significant part of the energy will remain free and can be interpreted as mechanical (seismic) energy W_S:

$$W_S = W_P + W_E - (W_C + W_F). \tag{7}$$

4. Application to seismic events

After the formation of the MCM at $l \ll H$, the accelerated ascent of the migrant in the plastic medium begins. It continues when condition (1) is true until it connects with another MCM, or until the migrant reaches the brittle zone or the next strength barrier. The location and strength of such barriers depend on the rheological profile in a specific geodynamic setting. The most significant barrier is undoubtedly the PBT, which S. N. Ivanov [*Ivanov et al.*, 2018] called a "detachment fault" and estimated its strength for continents at 150 MPa, which is 5–15 times greater than the strength of the underlying rocks: at depths of ~8–15 km for granitoids, ~25–30 km for gabbroids, ~50–55 km for hyperbasites. Other barriers can appear due to viscosity and density abnormalities, as well as due to stress pressures, phase transitions of minerals, etc.

Relatively weak seismic events can occur not only on strength barriers, but also during the merging of the MCMs (Figure 2). The main factor of the rate of rise is the vertical length of the MCM, therefore the long cavity 1 will "catch up" with the short one 2 and "absorb" it. In this case, the length of the resulting cavity 3 will be the sum of the first and second ones, therefore its speed will increase sharply, which will cause additional energy release according to expressions (2)–(7). When calculating the energy, it is necessary to take into account two fundamentally possible variants of confluence of the MCMs: coaxial (Figure 2a) and angular (Figure 2b), and the latter requires simple mathematical transformations for σ_Z.

Thus, the formation and evolution of MCM is not a single phenomenon. The main mechanism of *fluid* transport from the core to the brittle crust are MCM systems. They are localized in column-form areas of significant vertical extension in rheologically weakened zones. At lower and upper mantle depths, such long-lived MCM systems can be interpreted

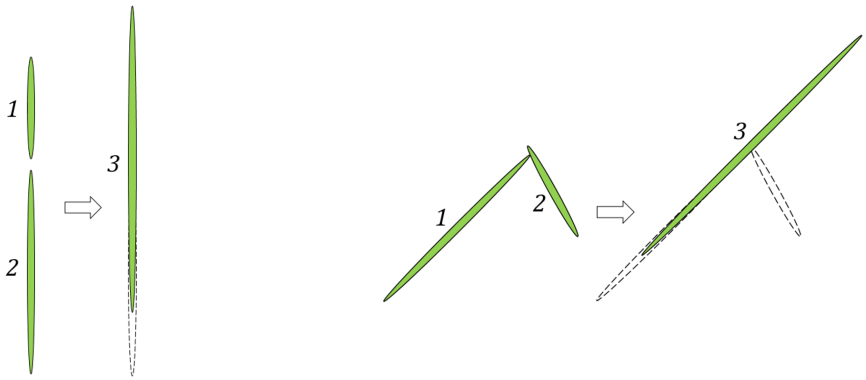

(a) **(b)**

Figure 2. Schemes of two basic types of MCM merging. Explanations in the text.

as mantle plumes. In lithospheric and crustal conditions, the formation and evolution of MCM systems can be the cause of difficult-to-explain and sometimes controversial seismic phenomena, among which we note the following.

1. Unstable thermodynamic zones of low velocities at depths of 9–16 km, "the nature of which has not been sufficiently studied" [*Korchin*, 2010]. They can be interpreted as areas of *fluid* accumulation under the PBT strength barrier, which is located precisely at these depths [*Ivanov et al.*, 2018; *Zhatnuev et al.*, 2009].
2. Rock-tectonic bursts that are practically not associated with anthropogenic processes, the problem of which "has been one of the most complex in world science and mining practice for many years" [*Marcak et al.*, 2013; *Rasskazov et al.*, 2023]. One of the factors causing such bursts is considered to be long-lived *deep faults*, which are possible with low probability in a plastic environment below the PBT. By the term "*deep faults*" we mean long-lived deeply propagated faults in a brittle environment, communicated with the surface, i.e. those in which the *fluid* is under its own hydrostatic pressure. In contrast, closed, non-communicating *fluid*-filled cavities in a plastic medium, which we consider in this paper as MCM, are under the lithostatic pressure of the surrounding rocks [*Zhatnuev*, 2005]. The mechanism described by equations (1)–(7) successfully explains such bursts, including in regions with weak seismicity.
3. Seismic "nails" [*Vadkovsky*, 2012; *Zakharov*, 2013], which are subvertical congestions of the earthquake hypocenters. They fit perfectly into the picture of systems with numerous MCMs localized in column-form areas. Seismic events in such systems occur not only and not so much on strength barriers as during numerous chaotic acts of MCM integration. This can explain the absence of a preferential direction of "nail" formation in time and the equally probable filling of the entire "nail" body with earthquake hypocenters during its formation. The best argument in favor of explaining seismic nails with the MCM theory is that the forming "nail" almost instantly (in less than a day) "grows" to a vertical length of 5–10 km or more [*Vadkovsky*, 2012]. This occurs due to jumps in the lengths of MCMs after their merging (Figure 2) and, as a consequence, a sharp increase in the velocity of their rise.

5. Conclusion

In connection with the systemic theme of the research, we connect the mantle, lithospheric and crustal processes of migrant evolution. They are, firstly, united by one mechanism for the formation of MCM (no matter in layer D'' or on some rheological barrier of the plastic crust), the same driving force (excess pressure), one method of migration (*fluid*-fracturing) and complete continuity: the initial MCM can originate at the core-lower mantle boundary as hydrogen-methane and rise, evolving and interacting with the host environment until unloading in the brittle crust [*Vasiliev et al.*, 2019; *Zhatnuev et al.*, 2013]. Another source of the initial substance for the migrant may be the dehydration of the plate

in the subduction zone, but even there it remains precisely mantle-crustal, since it is formed in the mantle wedge and rises to the brittle crust as a component of the fluid-mantle system. Hypothetically, there may be other ways for a sufficient amount of *fluid* to enter a plastic medium to form a migrant, but we have not considered them yet.

The authors consider modeling of MCM systems as a promising direction in the system analysis of seismic events: both those described in the work and those left outside its scope. Significant assumptions and approximations (idealized isotropic medium, consideration of only the main types of stresses, deformations and energy, etc.) do not detract from the achievement of the main aim of the work: determining the direction of further research of MCM systems as one of the main seismo-generating factors. Undoubtedly, the considerations presented in the article are mostly preliminary and only outline the direction of system research, which are going to be interesting and useful.

Acknowledgments. The authors express their deep gratitude, first of all, to holder of an Advanced Doctorate in Geology and Mineralogy N. S. Zhatnuev both for the idea of the article and for fruitful consultations during the work on it. The authors are also grateful to PhD of Geology and Mineralogy Ts. A. Tubanov and to G. D. Sanzhiev for their assistance and provided materials. The work was carried out within the framework of the state assignment (reg. No. AAAA-A21-121011390003-9).

References

Hickman S., *Sibson R.*, *Bruhn R.* Introduction to Special Section: Mechanical Involvement of Fluids in Faulting // Journal of Geophysical Research: Solid Earth. — 1995. — Vol. 100, B7. — P. 12831–12840. — DOI: 10.1029/95jb01121.

Ivanov S. N., *Ivanov K. S.* Rheological model of Earth's crust (model of third generation) // Litosfera. — 2018. — Vol. 18, no. 4. — P. 500–519. — DOI: 10.24930/1681-9004-2018-18-4-500-519. — (In Russian).

Korchin V. A. Thermobaric elastic heterogeneity of the earth's crust and the dynamics of its change // Vestnik Otdelenia nauk o Zemle RAN. — 2010. — Vol. 2, no. 6. — P. 141–148. — DOI: 10.2205/2010NZ000037. — (In Russian).

Levin B. V., *Rodkin M. V.*, *Sasorova E. V.* Specific features of the seismic regime in the lithosphere: Manifestations of the deep aqueous fluid action // Izvestiya, Physics of the Solid Earth. — 2010. — Vol. 46, no. 5. — P. 451–459. — DOI: 10.1134/s1069351310050113.

Marcak H., *Mutke G.* Seismic activation of tectonic stresses by mining // Journal of Seismology. — 2013. — Vol. 17, no. 4. — P. 1139–1148. — DOI: 10.1007/s10950-013-9382-3.

Park J.-O., *Tsuru T.*, *Fujie G.*, *et al.* Seismic Reflection Images of Possible Mantle-Fluid Conduits and Basal Erosion in the 2011 Tohoku Earthquake Rupture Area // Frontiers in Earth Science. — 2021. — Vol. 9. — DOI: 10.3389/feart.2021.687382.

Rasskazov I. Y., *Fedotova I. V.*, *Anikin P. A.*, *et al.* Improvement of methods and means of geomechanical monitoring based on digital technologies // Mining Industry Journal (Gornay Promishlennost). — 2023. — 5S/2023. — P. 18–24. — DOI: 10.30686/1609-9192-2023-5s-18-24. — (In Russian).

Vadkovsky V. N. Subvertical congestions of the earthquake hypocenters - Seismic "Nails" // Vestnik Otdelenia nauk o Zemle RAN. — 2012. — Vol. 4, no. 1. — P. 1–8. — DOI: 10.2205/2012nz000110. — (In Russian).

Vasiliev V. I., *Vasilieva E. V.*, *Zhatnuev N. S.* Parameters of Origin and Evolution of the Mantle-Crust Migrant // Geoinformatica. — 2019. — No. 2. — P. 34–42. — EDN: NNNRGI. (In Russian).

Xuan Z., *Cheng Z.*, *Li C.*, *et al.* Energy evolution mechanism during rockburst development in structures of surrounding rocks of deep rockburst-prone roadways in coal mines // Frontiers in Energy Research. — 2023. — Vol. 11. — DOI: 10.3389/fenrg.2023.1283079.

Zakharov V. S. On the mechanism of the generation of seismic "nails" // Moscow University Geology Bulletin. — 2013. — Vol. 68, no. 5. — P. 282–288. — DOI: 10.3103/S0145875213050086.

Zhatnuev N. S., *Tubanov T. A.*, *Vasilieva E. V.* Elastic-Plastic Transition as a Stress Concentrator in the Earth's Crust // Fault Formation and Seismicity in the Lithosphere: Tectonophysical Concepts and Consequences. Proceedings of the All-Russian Conference: in 2 volumes. Volume 2. — Irkutsk : IEC SB RAS, 2009. — P. 22–23. — EDN: TICFUF. (In Russian).

Zhatnuev N. S., *Vasiliev V. I.*, *Sanzhiev G. D.* The ascending migration of fluids in mantle, the conceptual, rated and analogous models // National geology. — 2013. — No. 3. — P. 24–30. — EDN: QBFNVD. (In Russian).

Zhatnuev N. S. Fissure fluid systems in the ductile deformation zone // Doklady Earth Sciences. — 2005. — Vol. 404, no. 7. — P. 1014–1017. — EDN: LJKSBF.

Russian Journal of Earth Sciences

Special Issue: "Data Science, Geoinformatics and Systems Analysis in Geosciences"

Remote Research of Archaeological Sites of the Southern Trans-Urals Using Geophysics and Machine Learning

A. V. Vokhmintsev[1], A. V. Melnikov[2,3], N. S. Batanina[1], E. V. Kupriyanova[1], L. A. Muravyev[4], M. A. Romanov[1]

[1]Chelyabinsk State University, Chelyabinsk, Russia
[2]Yugra Research Institute of Information Technologies, Khanty-Mansiysk, Russia
[3]Yugra State University, Khanty-Mansiysk, Russia
[4]Institute of Geophysics UB of RAS, Ekaterinburg, Russia
* **Correspondence to:** Vokhmintsev Alexander, vav2000@inbox.ru

Abstract: The so-called "Country of Cities" discovered in the second half of the 20th century in the Southern Trans-Urals — more than two dozen fortified settlements of the Middle Bronze Age belonging to the Sintashta culture (about 3–2 thousand years BC) is a unique object of interdisciplinary research. In this paper the study of the architecture of these settlements is carried out by interpreting aerial photographs, space photographs and geophysical methods: magnetometry and areal electromagnetic profiling with the AEMP-14 induction system. The construction of orthophotoplans and a digital relief model is made based on UAV survey data and ground surveys using GNSS and tacheometry. Fundamentally new opportunities are provided by applying modern methods of detection, classification and segmentation of objects based on the use of convolutional neural networks to the obtained data. This paper presents and discusses the results of applying neural networks based on graphs and transformer architecture to the problem of 3d archaeological sites segmentation and methods of their detection based on residual neural networks and networks with transformer architecture.

Keywords: Southern Trans-Urals, Bronze Age, Sintashta culture, fortified settlement, remote research methods, graph convolutional neural networks, data segmentation.

Citation: Vokhmintsev, A. V., A. V. Melnikov, N. S. Batanina, E. V. Kupriyanova, L. A. Muravyev, and M. A. Romanov (2025), Remote Research of Archaeological Sites of the Southern Trans-Urals Using Geophysics and Machine Learning, *Russian Journal of Earth Sciences*, 25, ES2012, EDN: ERYSGY, https://doi.org/10.2205/2025ES000971

1. Introduction

Natural scientific methods are currently widely used to study the material culture of mankind in the past — archaeological sites. Non-destructive mapping is a necessary part of archaeological site's study, allowing the selection of specific parts of interest for planning excavations. These are mainly geophysics and remote sensing methods – photographs obtained from satellites, manned and unmanned aerial vehicles, in optical range and multispectral cameras. UAV surveys allows obtaining accurate and detailed digital terrain models (Digital Terrain Model, DTM), which serve as a basis for research and reconstruction of the structure of an archaeological site, confirming the results of excavations, as well as finding relationships between "digital images" of various sites in geophysical fields, photographs and terrain models. In the last 10 years, machine learning (ML) methods have begun to be used in archaeology, which make it possible to increase the effectiveness of the above research methods. At the end of the 20th century, analysis of aerial photography revealed a number of fortified Bronze Age (21st–18th centuries BC) settlements in the Southern Urals – Sintashta archaeological culture. Each object is a unique architectural

Research Article

Received: 15 November 2024
Accepted: 15 April 2025
Published: 23 May 2025

ensemble, surrounded by massive fortifications. The largest and most famous settlement of this group is Arkaim, and the whole system was named as "Country of Cities". 23 such fortified settlements were discovered until recently and now it is a unique object for interdisciplinary research aimed at studying the material culture of the age of the ancient Egyptian pyramids, the way of life, technology and techniques that people possessed at that time. Geophysical methods for research of these settlements have been used since the 1990s to the present day. It is high-precision magnetometry, symmetrical electrical profiling, resistance method and with ground penetrating radar. Another two fortified settlements were discovered in 2023 in the northern parts of the territory. The finds are located in the area between the two northernmost settlements (Stepnoe and Chernorechye) and the other monuments.

2. Geophysical research

Currently, geophysical mapping covered more than a dozen fortified settlements, corresponding burial mounds and ancient mines [*Noskevich et al.*, 2022]. The main method is magnetometric survey, performed using Overhauser magnetometers [*Epimakhov et al.*, 2021; *Narkhov et al.*, 2017]. The second was the SIR-3000 ground penetrating radar for reconstructing the internal structure of individual parts of settlement (wells, furnaces, mines) and three-dimensional modeling [*Fedorova et al.*, 2020]. However, the study of the fortified settlement Stepnoye showed that magnetic survey is ineffective due to the intense magnetization of the soils. This created the prerequisites for using a new method of soil research — the dipole electromagnetic profiling device AEMP-14 [*Karin et al.*, 2018]. The efficiency of field work performed by the AEMP-14 induction system was comparable to the speed of magnetic survey in motion. Electromagnetic survey of the Stepnoye was completed in 2023 (Figure 1). The map revealed some details complementary to other studies. The walls and similar structural elements are characterized by increased resistivity, while the rows of housing depressions and ditches have reduced resistivity. The outer defensive wall is clearly visible in the western and eastern parts of the site. Overall, the complex structure of the site corresponds to the interpretations made earlier based on the aerialphotographs interpretation. New rectangular and sub-square structures were built and reconstructed in several stages on the early oval fortified settlement. The electrical resistivity map shows new elements — walls separating the rows of housing depressions. Future research will focus on the heterogeneous structure of the ash pit revealed in the map. The territory of the recently discovered fortified settlements of Nizhneuspenskoe and Verkhneuralskoe was also surveyed using the AEMP-14 and results allowed us to understand the structure of these sites.

3. Application of machine learning methods in archaeology

The authors of this study proposed a methodology for non-destructive research of archaeological sites [*Vokhmintcev et al.*, 2024b]. The data involved in its comprehensive study can be divided into two groups. This is 2D data as rasters: space images and aerial photographs, and 3D data as point clouds with an irregular structure (results of tacheometry, stereophotogrammetry from UAVs, LIDAR, geophysical methods - magnetometry, electrical survey). Each type of source data corresponds to groups of ML methods aimed at solving specific problems. On two-dimensional data, the problems of detecting objects and determining their contours are solved. On 3D data, ML methods we can solve problems of semantic segmentation, classification and segmentation of instances. For the detection task, based on the accumulated experience of studying Bronze Age sites in this region [*Zdanovich et al.*, 2003], 8 types of classes of objects of interest were selected: burial cult complexes with wall-shaped horseshoe or dumbbell-shaped structures (M-1), burial grounds with stone fences from the Middle Ages (M-2), fortified settlements of the Bronze Age (P-1), unfortified settlements of the Bronze Age (P-2), four types of stone barrows of the early Iron Age or the Middle Ages (K1, K2, K3, K4), a soil or stone barrow of the early Middle Ages with "whiskers" (K5). To study the internal structure and architecture of an archaeological site

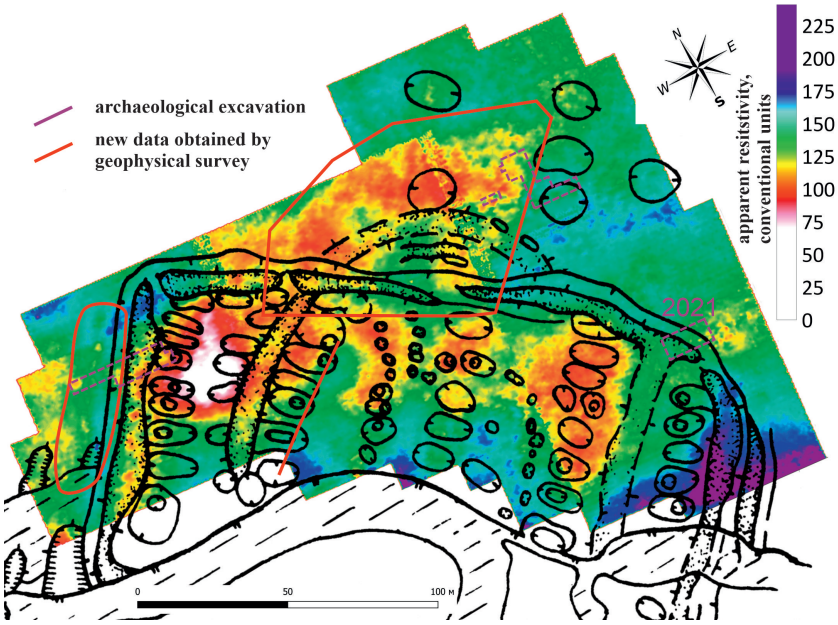

Figure 1. Electromagnetic survey of the Stepnoye settlement, combined with data from the interpretation of an aerial photograph from 1956.

using 3D data, the following set of classes was selected: dwelling (s1); ditch (s2); defensive wall (s3); burial ground (s4); internal wall (s5); well (s6); entrance to the settlement (s7). For object detection, two approaches were proposed: one based on residual neural networks ResNet 50 with a modified fully connected layer in the form of a radial basis network RBF, and another using the Pointview-GCN transformer architecture [*Mohammadi et al.*, 2021], which showed the following results: for classes K-1, K2, K3 average value of metric F1 0.93, precision 0.82, recall 0.88, for class P-1 F1 0.90, precision 0.96, recall 0.88, for P-2 F1 0.77, precision 0.84, recall 0.81. The detection results based on ResNet-50 showed [*Vokhmintcev et al.*, 2024b] the worst values for all metrics and classes.

For the semantic segmentation task, original models for 3D semantic segmentation based on a dynamic weighted graph convolutional neural network (DWG*CNN) were proposed, and for 3D segmentation of instances, an improved version based on the Mask3d [*Schult et al.*, 2023] transformer architecture was proposed. Using a combination of neural networks DWG*CNN+Mask3d* [*Vokhmintcev et al.*, 2024a], a set of geophysical data and DTM of two objects was analyzed: the fortified settlements of Stepnoye and Levoberezhnoye. Preliminary preparation of 3D data includes: division into semantic blocks; determination of special points and calculation of normals in the cloud; formation of a multimodal feature vector consisting of object coordinates, their normalized coordinates, normals and data on the color of the point in the cloud; upsampling or downsampling of the point cloud depending on the morphology of the 3D data. For example, the terrain data from UAV stereophotogrammetry or LIDAR may contain overly detailed data, so downsampling may be required. In contrast, the tacheometric terrain data of individual site in our collection contain sparse and uneven data, and for them, data upsampling is performed based on the RepKPU algorithm [*Rong et al.*, 2024]. The collection of geophysical data and elevation models of the Stepnoye and Levoberezhnoye sites included 116 original point clouds containing markers of the 7 classes indicated above. Augmentation of the original set of point clouds was performed using the Real3D-Aug algorithm [*Šebek et al.*, 2022]. As a result, 928 different point clouds were obtained, each with a uniformly dense structure. The input for DWG*CNN is a dense irregular point cloud $C = \{c_1, \ldots, c_n\}$ in $\mathbb{R}^3$, where $i = 1, \ldots, n$, each element of which is a point features vector the form of its coordinates and normals, for depth data obtained from LiDAR, the feature vector is extended with

color components in RGB format. The DWG*CNN model allows eliminating the main drawback of known graph convolutional networks — dependence on the dimensionality of the analyzed point clouds by approximating the convolution signal with a 3-order Chebyshev polynomial. For the Mask3d model, modification of the data preprocessing process in the feature map construction module, an adaptive scheme for dealing with outliers in the decoder module, and a modified scheme for concatenating local and global features of the neural network made it possible to significantly increase the efficiency of solving the problem of segmenting instances for sparse, noisy, and heterogeneous 3D data. Computer simulations made it possible to compare the efficiency of the proposed model based on DWG*CNN and models based on graph networks DGCNN [*Wang et al.*, 2019] and RGCNN [*Te et al.*, 2018]. A comparison of metrics shows the advantage of the DWG*CNN method for all metrics (Table 1).

Table 1. Results of 3d semantic classification for graph neural networks.

Metric	RGCNN	DGCNN	DWG*CNN
Accuracy	0.730	0.685	0.910
IoU	0.695	0.530	0.781
F1	0.734	0.695	0.934

Computer modeling for instances segmentation task show that according to the quality metric F1 (see Table 2), the proposed modified method Mask3d* allows to obtain better segmentation quality (Figure 2) for classes s1–s4 relative compared to state-of-the-art methods: Mask3d and OneFormer [*Kolodiazhnyi et al.*, 2023]. For classes s5–s7, all methods showed unsatisfactory results.

Table 2. Results of 3d instance segmentation.

Method	s1	s2	s3	s4	s5	s6	s7
OneFormer3d	0.680	0.582	0.470	0.568	0.522	—	—
Mask3d	0.730	0.593	0.602	0.635	0.478	—	—
Mask3d*	0.876	0.910	0.803	0.844	0.664	0.398	0.393

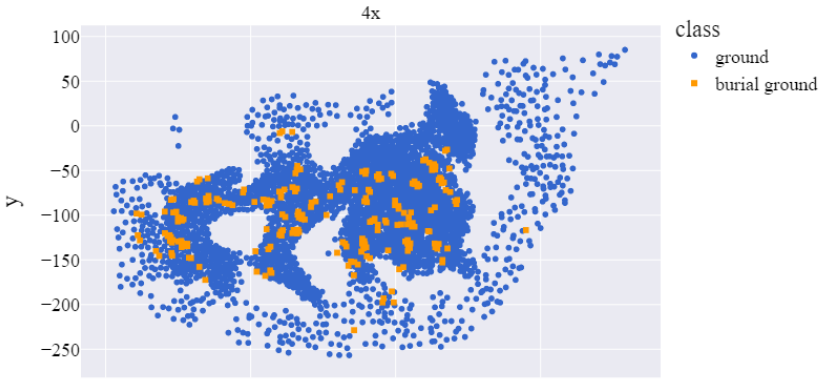

Figure 2. Results of 3d semantic segmentation for the burial ground Kamenka 2.

4. Conclusions

The integrated use of geophysical and remote sensing methods made it possible to create a digital model of the territory along the middle reaches of the Sintashta River, to provide a detailed description of the settlements and burial grounds of the Bronze Age, housing depressions and various types of burials. Analysis of the model of the largest

fortified settlement near the Sintashta river -Levoberezhnoye area made it possible to trace the dynamics of the number of housing depressions during different stages of the Bronze Age. It is shown that ML methods can help archaeologists in studying the structure of an archaeological site and its interpretation. Using the example of fortified settlements of the Bronze Age in the Southern Trans-Urals, we can conclude that the complex use of several non-destructive methods allows us to form an idea of the structure of a site that is in an unsatisfactory state of preservation or has even been completely leveled in the landscape as a result of human anthropogenic activity.

Acknowledgments. The study was supported by a grant of the Russian Science Foundation No. 23-11-20007, https://rscf.ru/project/23-11-20007/

References

Epimakhov A. V., Berseneva N. A., Fedorova N. V. Fortification lines of the Kamennyi Ambar settlement // The Bronze Age tn the Karagaily-Ayat Region (Trans-Urals, Russia). Culture, Environment and Economy. — Bonn : Verlag Dr. Rudolf Habelt GmbH, 2021. — P. 101–158. — EDN: ADHHQM.

Fedorova N. V., Noskevich V. V. Geophysical Researches at Belousovsky Copper Mine of the Bronze Age (Southern Urals) // Geoarchaeology and Archaeological Mineralogy. — Springer International Publishing, 2020. — P. 38–44. — DOI: 10.1007/978-3-030-48864-2_6.

Karin Y. G., Balkov E. V., Fadeev D. I., et al. Electromagnetic Profiling by Compact Apparatus: New Approach and Results of Application // Vestnik NSU. Series: Information Technologies. — 2018. — Vol. 16, no. 4. — P. 68–78. — DOI: 10.25205/1818-7900-2018-16-4-68-78. — In Russian.

Kolodiazhnyi M., Vorontsova A., Konushin A., et al. OneFormer3D: One Transformer for Unified Point Cloud Segmentation. — 2023. — DOI: 10.48550/ARXIV.2311.14405.

Mohammadi S. S., Wang Y., Bue A. D. Pointview-GCN: 3D Shape Classification With Multi-View Point Clouds // 2021 IEEE International Conference on Image Processing (ICIP). — IEEE, 2021. — P. 3103–3107. — DOI: 10.1109/icip42928.2021.9506426.

Narkhov E. D., Muravyev L. A., Sergeev A. V., et al. Applications of modern high-precision Overhauser magnetometers // Physics, Technologies and Innovation (PTI-2017): Proceedings of the IV International Young Researchers' Conference. Vol. 1886. — AIP Conference Proceedings, 2017. — DOI: 10.1063/1.5002972.

Noskevich V., Fedorova N. Geophysical Studies of Wells in the Settlements of Konoplyanka 1 and Konoplyanka 2 (Bronze Age) // Interdisciplinaria Archaeologica Natural Sciences in Archaeology. — 2022. — Vol. XIII, no. 1. — P. 19–28. — DOI: 10.24916/iansa.2022.1.2.

Rong Y., Zhou H., Xia K., et al. RepKPU: Point Cloud Upsampling with Kernel Point Representation and Deformation // 2024 IEEE/CVF Conference on Computer Vision and Pattern Recognition (CVPR). — IEEE, 2024. — P. 21050–21060. — DOI: 10.1109/cvpr52733.2024.01989.

Schult J., Engelmann F., Hermans A., et al. Mask3D: Mask Transformer for 3D Semantic Instance Segmentation // 2023 IEEE International Conference on Robotics and Automation (ICRA). — IEEE, 2023. — P. 8216–8223. — DOI: 10.1109/icra48891.2023.10160590.

Šebek P., Pokorný Š., Vacek P., et al. Real3D-Aug: Point Cloud Augmentation by Placing Real Objects with Occlusion Handling for 3D Detection and Segmentation. — 2022. — DOI: 10.48550/ARXIV.2206.07634.

Te G., Hu W., Zheng A., et al. RGCNN: Regularized Graph CNN for Point Cloud Segmentation // Proceedings of the 26th ACM international conference on Multimedia. — ACM, 2018. — P. 746–754. — DOI: 10.1145/3240508.3240621.

Vokhmintcev A., Khristodulo O., Melnikov A., et al. Application of Dynamic Graph CNN* and FICP for Detection and Research Archaeology Sites // Analysis of Images, Social Networks and Texts. — Springer Nature Switzerland, 2024a. — P. 294–308. — DOI: 10.1007/978-3-031-54534-4_21.

Vokhmintcev A. V., Melnikov A. V., Romanov M. A., et al. Remote Research System of Archaeological Sites Using Deep Learning // Pattern Recognition and Image Analysis. — 2024b. — Vol. 34, no. 3. — P. 574–582. — DOI: 10.1134/s105466182470038x.

Wang Y., Sun Y., Liu Z., et al. Dynamic Graph CNN for Learning on Point Clouds // ACM Transactions on Graphics. — 2019. — Vol. 38, no. 5. — P. 1–12. — DOI: 10.1145/3326362.

Zdanovich G. B., Batanina I. M., Levit N. V., et al. Archaeological atlas of the Chelyabinsk region. Issue 1. Steppe-forest-steppe. Kizilsky district. — South Ural Book Publishing House, 2003. — 256 p. — In Russian.

Russian Journal of Earth Sciences

Special Issue: "Data Science, Geoinformatics and Systems Analysis in Geosciences"

A Series of Strong Earthquakes in Chile at the Beginning of the 21st Century: Similarities, Differences, Relationship

I. S. Vladimirova[1], **Y. V. Gabsatarov**[1], **N. S. Shcheveva**[1]

[1]Shirshov Institute of Oceanology of Russian Academy of Sciences, Moscow, Russia
* **Correspondence to:** Irina Vladimirova, vladimirova.is@ocean.ru

Abstract: In less than six years, three devastating earthquakes with magnitude exceeding 8.0 have occurred over the Chilean subduction zone. These events were quite well recorded by permanent GNSS stations. We used finite element modeling for a spherically symmetric layered Earth and machine learning methods to investigate the geodynamic processes preceding and accompanying the Chilean earthquake sequence. We find that preseismic coupling before all events is strongly correlated with the coseismic slip distribution, while afterslip primarily located around the coseismic slip patches. We also found that large geologic structures of the oceanic plate have a decisive influence on the development of geodynamic processes in the rupture zones of large Chilean earthquakes.

Keywords: Chilean subduction zone, strong earthquakes, geodynamic processes, numerical modeling, machine learning.

Citation: Vladimirova, I. S., Y. V. Gabsatarov, and N. S. Shcheveva (2025), A Series of Strong Earthquakes in Chile at the Beginning of the 21st Century: Similarities, Differences, Relationship, *Russian Journal of Earth Sciences*, 25, ES2013, EDN: IEMQCL, https://doi.org/10.2205/2025ES000972

1. Introduction

The first two decades of the 21st century were marked by an alarming surge in strong earthquakes all over the world. During this period, great earthquakes with magnitudes exceeding 8 occurred in many seismically active regions of the Earth. Three such strong seismic events have occurred over the Chilean subduction zone in less than six years: the 2010 Maule earthquake (M_W = 8.8), the 2014 Iquique earthquake (M_W = 8.1) and the 2015 Illapel earthquake (M_W = 8.3).

All these earthquakes are the shallow-depth megathrust events that ruptured the long-lived seismic gaps. The main objective of our research is to study and compare the deformation processes preceding and accompanying each of the three $M \geq 8$ earthquakes in Chile, and to identify the factors controlling the accumulation and release of stress during strong earthquakes.

2. Data and methods

The dataset used in this study consists of three-component time series from 111 permanent GNSS stations over the 2007–2016 period provided by Nevada Geodetic Laboratory.

We constructed the finite-fault models to investigate the distribution of preseismic coupling along the fault zones as well as the distribution of coseismic slip and afterslip. The geometric design of the finite-fault models was based on the aftershock distribution. To estimate the interplate coupling, coseismic slip and afterslip distribution, we inverted preseismic velocities, coseismic offsets and postseismic displacements using the constrained damped least squares [*Gill et al.*, 1984] over a uniform rectangular grid.

Research Article

Received: 15 November 2024
Accepted: 15 April 2025
Published: 23 May 2025

The inversion minimizes the objective function:

$$F = \|w(Gm - d)\|_{L_2}^2 + \lambda \|m\|_{L_2}^2 .$$

The first term represents the misfit between modeled Gm and observed velocities/displacements d, and the second term provides a regularization of the solution. Here w is a weight vector inferred from observation uncertainties, G is a matrix consisting of convolutions of the corresponding Green's functions and unit displacements over the subfaults, m is a vector of estimated model parameters and λ is a positive damping factor [*Steblov et al.*, 2023]. We calculated Green's functions for a spherically layered Earth model using a method described in [*Pollitz*, 1996]. To evaluate the capability of the damped least squares method in reconstructing the spatial variation of the slip or coupling distribution, we perform the checkerboard tests as described in [*Steblov et al.*, 2023].

The modeling of postseimic processes is a challenging task since potential candidates for intense postseismic deformation after the megathrust events are afterslip, viscoelastic relaxation and poroelastic rebound. Distinguishing between these different mechanisms is nearly impossible based on only GNSS data. It is believed that vertical postseismic deformations may be an indicator of the dominant postseismic mechanism e.g., [*Nishimura et al.*, 2003]. However, the use of vertical observations is somewhat complicated due to their smaller amplitude compared to horizontal ones and, at the same time, larger observation errors, as well as due to the superposition of tectonic and non-tectonic signals (for example, surface loads) [*Wang et al.*, 2016]. Moreover, according to recent studies, vertical deformation during the seismic cycle shows significant spatiotemporal variations depending on the mechanical properties and fault kinematics [*Li et al.*, 2024]. Therefore, the vertical displacement pattern is difficult to interpret unambiguously.

To shed some light on the on the spatially and temporally dominant postseismic mechanism after the Chilean earthquakes we perform regression analysis of continuous GNSS time-series using machine learning methods. The solution for best regression model parameters was obtained by a minimization of an empirical risk functional $\min_{\theta\in\Theta} \left\|p(T)\theta - Y\right\|_{L_2}^2$, where $\theta \in \Theta = \mathbb{R}^M$ is a model parameter vector, $T \in \mathbb{R}$ is a set of time moments, $Y \in \mathbb{R}$ is a set of time series values,

$$p(t) = \begin{array}{c}(1, t, \sin(2\pi t), \cos(2\pi t), \sin(4\pi t), \cos(4\pi t), H(t > T_0), \dots, \\ H(t > T_l),\ H(t > T_0^{\text{post}}) \cdot \text{post}_0(t), \dots, H(t > T_k^{\text{post}}) \cdot \text{post}_k(t))\end{array}$$

is a feature vector, H is a Heaviside function, $\text{post}_i(t) = \left(\ln\left(1 + \frac{t}{\tau_a}\right), -\exp\left(-\frac{t}{\tau_b}\right)\right)$ is a postseismic features vector for i-th event [*Sobrero et al.*, 2020], τ is a decay time. Here we neglect the poroelastic rebound due to large distances from the sources to GNSS stations. Moments of earthquakes l and onsets of postseismic processes k (Figure 1) was determined using the Change Point Detection (CPD) approach [*Truong et al.*, 2020].

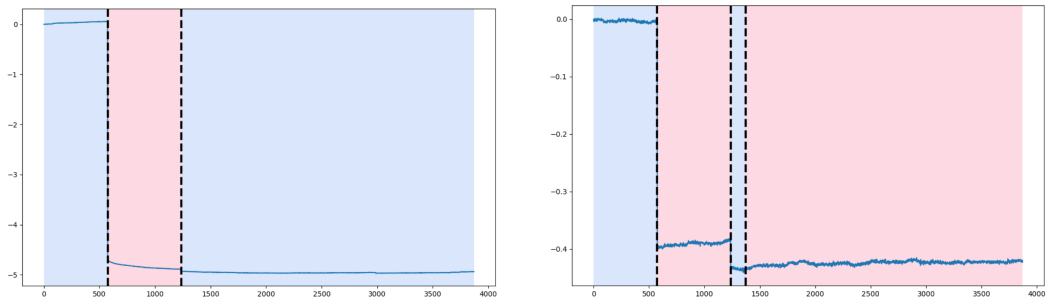

(a) **(b)**

Figure 1. Results of applying the CPD algorithm to the east (a) and north (b) components of time series of the GNSS-station CONT (Conception, Chile). Dashed lines denote the instantaneous shifts.

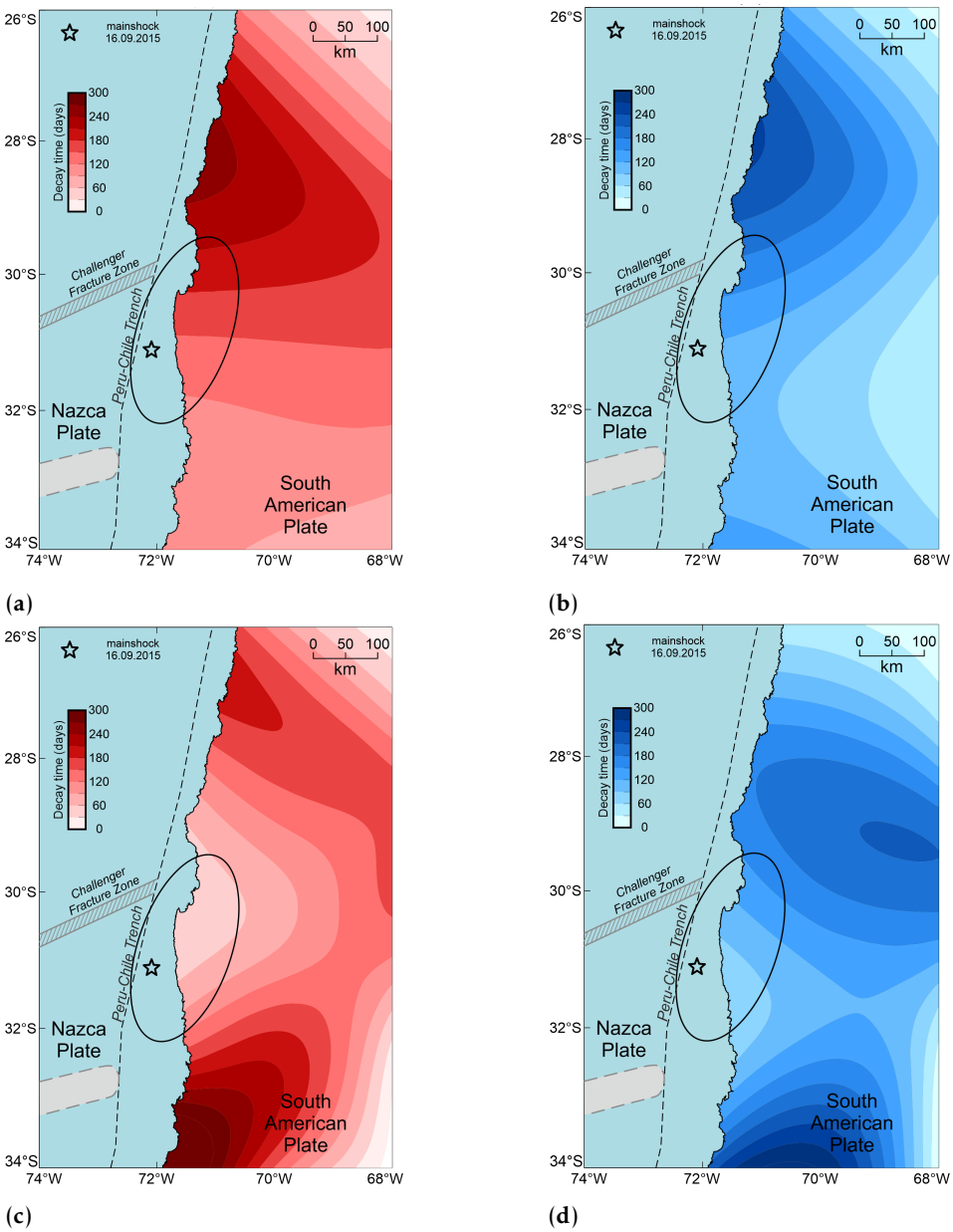

Figure 2. Geographical distribution of logarithmic (a, b) and exponential (c, d) decay times after the 2015 Illapel earthquake. Red and blue colors denote east and north components, respectively.

The estimated decay constants τ_a and τ_b show prominent domination of afterslip in the near-field and viscoelastic relaxation in the far-field towards the continent. An example of estimated decay fields for 2015 Illapel earthquake is shown on Figure 2.

3. Results

Our inverted preseismic coupling, coseismic slip and afterslip distributions for the 2010 Maule, 2014 Iquique and 2015 Illapel earthquakes are represented on Figure 3–5. These models agree in their main characteristics (location of areas of maximum displacements, size of earthquake sources, etc.) with similar models obtained from the inversion of teleseismic body waves (e.g., [*Lay et al.*, 2014; *Pulido et al.*, 2011]), joint inversion of tsunami waveforms and geodetic or teleseismic data (e.g., [*Gusman et al.*, 2015; *Heidarzadeh et al.*, 2016]) as well as joint inversion of GNSS and InSAR data (e.g., [*Klein et al.*, 2017; *Lin et al.*, 2013]).

The results of our modeling show good spatial agreement between location of locked patches (Figure 3a, 4a, 5a) and areas of stress release (Figure 3b, 4b, 5b) for all studied earthquakes.

The afterslip models (Figure 3c, 4c, 5c) show a predominantly dipping and along-strike development of rupture zones, which indicate the postseismic stress release in patches adjacent to areas of high coseismic slip.

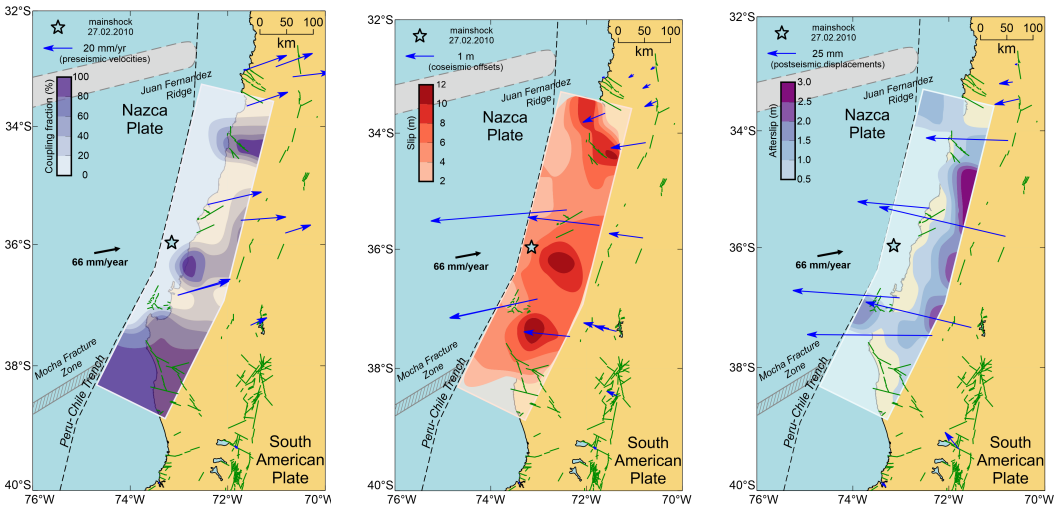

(a) **(b)** **(c)**

Figure 3. Models of preseismic coupling (a), coseismic slip (b) and 6-months afterslip (c) in the 2010 Maule rupture zone. The star is the mainshock (gCMT). Blue vectors indicate the GNSS data. Green lines show active regional faults [*Maldonado et al.*, 2021].

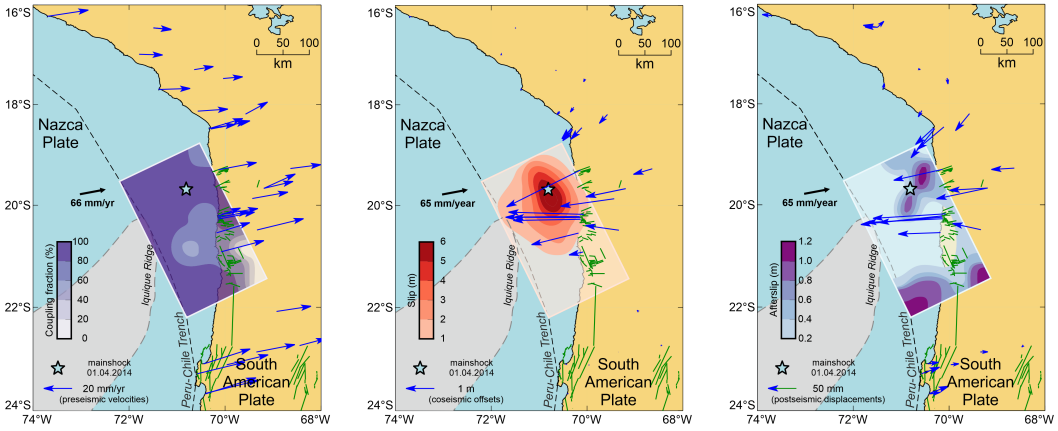

(a) **(b)** **(c)**

Figure 4. Models of preseismic coupling (a), coseismic slip (b) and 6-months afterslip (c) in the 2014 Iquique rupture zone. Designations according to Figure 3.

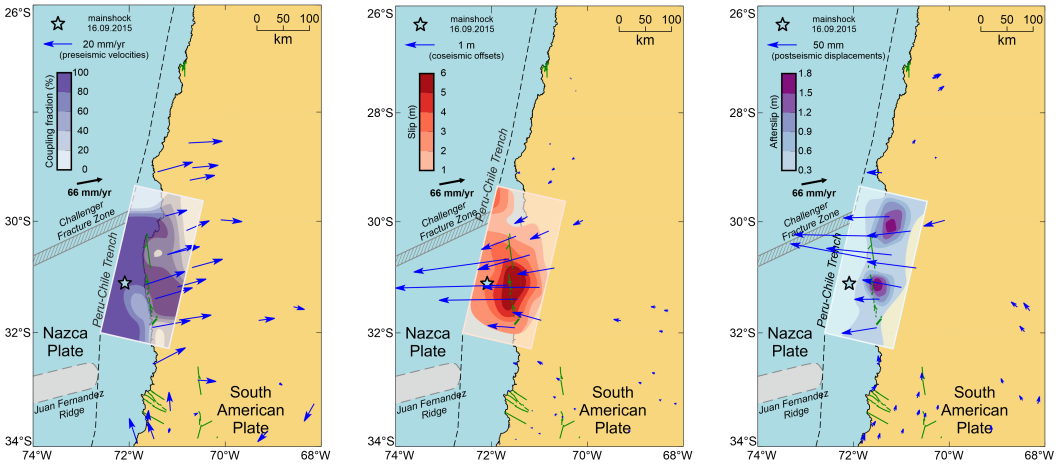

(a) **(b)** **(c)**

Figure 5. Models of preseismic coupling (a), coseismic slip (b) and 6-months afterslip (c) in the 2015 Illapel rupture zone. Designations according to Figure 3.

Comparison of our inverted models and regional morphostructures show that large geological features of the oceanic plate act as natural boundaries of rupture zones, while active tectonic structures of the continental margin have a local influence on the processes of stress accumulation and release.

4. Conclusion

We have modeled the preseismic coupling as well as coseismic slip and afterslip on three megathrust earthquakes rupture zones in Chile based on GNSS data.

We inferred thst postseismic deformations localized around the mainshock rupture zone are most likely explained by afterslip, whereas long-term diffuse deformations observed in the far field can be explained by viscoelastic relaxation of the lower crust or upper mantle.

We also found that large geologic structures of the oceanic plate have a decisive influence on the development of geodynamic processes in the rupture zone.

Acknowledgments. This research was supported by a grant from the Russian Science Foundation, No. 24-27-00176, https://rscf.ru/en/project/24-27-00176/.

References

Gill P. E., Murray W., Saunders M. A., et al. Procedures for optimization problems with a mixture of bounds and general linear constraints // ACM Transactions on Mathematical Software. — 1984. — Vol. 10, no. 3. — P. 282–298. — DOI: 10.1145/1271.1276.

Gusman A. R., Murotani S., Satake K., et al. Fault slip distribution of the 2014 Iquique, Chile, earthquake estimated from ocean-wide tsunami waveforms and GPS data // Geophysical Research Letters. — 2015. — Vol. 42, no. 4. — P. 1053–1060. — DOI: 10.1002/2014gl062604.

Heidarzadeh M., Murotani S., Satake K., et al. Source model of the 16 September 2015 Illapel, Chile, Mw 8.4 earthquake based on teleseismic and tsunami data // Geophysical Research Letters. — 2016. — Vol. 43, no. 2. — P. 643–650. — DOI: 10.1002/2015gl067297.

Klein E., Vigny C., Fleitout L., et al. A comprehensive analysis of the Illapel 2015 Mw 8.3 earthquake from GPS and InSAR data // Earth and Planetary Science Letters. — 2017. — Vol. 469. — P. 123–134. — DOI: 10.1016/j.epsl.2017.04.010.

Lay T., Yue H., Brodsky E. E., et al. The 1 April 2014 Iquique, Chile, Mw 8.1 earthquake rupture sequence: Lay et al.: April 1, 2014 Iquique Mw 8.1 earthquake // Geophysical Research Letters. — 2014. — Vol. 41, no. 11. — P. 3818–3825. — DOI: 10.1002/2014gl060238.

Li S., Chen L. Vertical Crustal Deformation Due To Viscoelastic Earthquake Cycles at Subduction Zones: Implications for Nankai and Cascadia // Journal of Geophysical Research: Solid Earth. — 2024. — Vol. 129, no. 8. — DOI: 10.1029/2024jb028817.

Lin Y.-n. N., *Sladen A.*, *Ortega-Culaciati F.*, *et al.* Coseismic and postseismic slip associated with the 2010 Maule Earthquake, Chile: Characterizing the Arauco Peninsula barrier effect // Journal of Geophysical Research: Solid Earth. — 2013. — Vol. 118, no. 6. — P. 3142–3159. — DOI: 10.1002/jgrb.50207.

Maldonado V., *Contreras M.*, *Melnick D.* A comprehensive database of active and potentially-active continental faults in Chile at 1:25,000 scale // Scientific Data. — 2021. — Vol. 8, no. 1. — DOI: 10.1038/s41597-021-00802-4.

Nishimura T., *Thatcher W.* Rheology of the lithosphere inferred from postseismic uplift following the 1959 Hebgen Lake earthquake // Journal of Geophysical Research: Solid Earth. — 2003. — Vol. 108, B8. — DOI: 10.1029/2002jb002191.

Pollitz F. F. Coseismic Deformation From Earthquake Faulting On A Layered Spherical Earth // Geophysical Journal International. — 1996. — Vol. 125, no. 1. — P. 1–14. — DOI: 10.1111/j.1365-246x.1996.tb06530.x.

Pulido N., *Yagi Y.*, *Kumagai H.*, *et al.* Rupture process and coseismic deformations of the 27 February 2010 Maule earthquake, Chile // Earth, Planets and Space. — 2011. — Vol. 63, no. 8. — P. 955–959. — DOI: 10.5047/eps.2011.04.008.

Sobrero F. S., *Bevis M.*, *Gómez D. D.*, *et al.* Logarithmic and exponential transients in GNSS trajectory models as indicators of dominant processes in postseismic deformation // Journal of Geodesy. — 2020. — Vol. 94, no. 9. — DOI: 10.1007/s00190-020-01413-4.

Steblov G., *Vladimirova I.* Geodetic Inversions and Applications in Geodynamics // Applications of Data Assimilation and Inverse Problems in the Earth Sciences. — Cambridge University Press, 2023. — P. 278–292. — DOI: 10.1017/9781009180412.019.

Truong C., *Oudre L.*, *Vayatis N.* Selective review of offline change point detection methods // Signal Processing. — 2020. — Vol. 167. — DOI: 10.1016/j.sigpro.2019.107299.

Wang K., *Tréhu A. M.* Invited review paper: Some outstanding issues in the study of great megathrust earthquakes - The Cascadia example // Journal of Geodynamics. — 2016. — Vol. 98. — P. 1–18. — DOI: 10.1016/j.jog.2016.03.010.

Russian Journal of Earth Sciences

Special Issue: "Data Science, Geoinformatics and Systems Analysis in Geosciences"

Problems of Implementing Web GIS Technologies for Processing, Analysis and Visualization of Geophysical Data

A. V. Vorobev[1,2], **G. R. Vorobeva**[2]

[1]Geophysical Center of the Russian Academy of Sciences, Moscow, Russia
[2]Ufa University of Science and Technology, Ufa, Russia
* **Correspondence to:** Vorobev A. V., geomagnet@list.ru

Abstract: The modern trend towards widespread use of software and tools for processing geospatial (including geophysical) data for a wide range of consumers contributes to the development of web-oriented solutions to the associated problems. A special complexity in the context of program implementation as well as the client computing capabilities is the visualization of geospatial information, which in the web environment is associated with the need to ensure acceptable rendering reactivity, on the one hand, and spatial image quality, on the other. Two main problems can be highlighted here: spatial image artifacts that appear as breaks in level lines, and the impossibility of technically combining heterogeneous spatial primitives into a single layer for retrospective dynamic visualization. The paper is concerned with the solutions to eliminate the above problems using geostatistical models and methods, as well as web design algorithms, patterns, and technologies. Using a web GIS for visualizing geophysical parameters as an example, the operability and effectiveness of the proposed software and algorithmic solutions are confirmed.

Keywords: geophysical data, geoinformatics, data visualization, spatial layers, spatial isolines.

Citation: Vorobev, A. V., and G. R. Vorobeva (2025), Problems of Implementing Web GIS Technologies for Processing, Analysis and Visualization of Geophysical Data, *Russian Journal of Earth Sciences*, 25, ES2014, EDN: PBHKJA, https://doi.org/10.2205/2025ES000973

1. Introduction

Modern geoinformation technologies provide solutions to a wide range of problems concerned with processing, analysis and visualization of geophysical data [*Gorokhov et al.*, 2021; *Papadakis et al.*, 2022]. However, the majority of GIS solutions are implemented as desktop applications, which significantly limits the possibilities of their use in development, especially for web-oriented applications.

One of the common approaches to visualizing spatial data in general and geophysical data in particular supposes generation of contour lines. There are libraries, services, and APIs that perform such a transformation of the spatial data for web applications, both on the client side and on the server side [*Kumari et al.*, 2022]. However, the increase in the volume and complexity of data lead to the fact that the formation of an array of isolines using known libraries is usually accompanied by visual artifacts, which complicate the analysis of the spatial distribution of the parameters, on the one hand, and reduce the quality of rendering the spatial image, on the other.

Another problem of programming visualization of geospatial data is the low efficiency and limitation of frame-by-frame change of spatial layers with a time reference. There can be outlined the impossibility of synchronous switching of a group of spatial layers by a time parameter, which negatively affects the results of assessing the temporal anisotropy of the spatial data [*Pakdil et al.*, 2021; *Podany et al.*, 2022].

In this regard, there is a need to develop algorithmic and programming solutions that provide highly responsive web-oriented visualization of geospatial (geophysical) data

Research Article

Received: 15 January 2025
Accepted: 15 April 2025
Published: 23 May 2025

in the format of spatial isolines, allowing retrospective frame-by-frame processing of the corresponding layers, on the one hand, and free of visual artifacts during rendering, on the other.

2. State of art

It is reasonable to consider the problem of visualizing geophysical data as a set of spatial isolines. When visualizing spatial isolines on a cartographic base, they may be accompanied by so-called artifacts – visual distortions of spatial lines that complicate their analysis and interpretation. They may be caused by both the imperfection of algorithms and programming libraries for constructing spatial contour lines, as well as the limited capabilities of visualization tools, taking into account the reactivity of applications, rendering speed, projection, etc. [*Kachanov et al.*, 2016; *Traxler et al.*, 2017]

So, the problem of eliminating these artifacts can be defined as the detecting of open contour lines by comparing the number of pairs of spatial points and the segments connecting them. It is necessary to complete the contour line connecting the corresponding extreme spatial points. Here two main approaches are possible: the missing points can be built by one of the interpolation methods, or an approximation function obtained analytically can be used. In the case of using the first of the mentioned approaches, it seems reasonable to analyze the spatial anisotropy of the original data to determine the interpolation method that best takes into account such variability.

Another highlighted artifact is the "noise" in spatial contour lines, which is largely determined by the insufficient number of initial spatial points, which attribute values are implemented with algorithm of contour lines generating. The spatial isoline is built along the basic regular grid, in the nodes of which the initial spatial points with the corresponding attribute values are placed. If the number of initial points does not coincide with the number of nodes of the spatial grid modeled for visualization, then an isoline is formed that fragmentarily repeats the lines of its rectangular cells, resulting in "kinks" characteristic of such an isoline. To solve the problem, it is necessary to apply a filter to the generated spatial isolines. In this case, the use of smoothing filters should be performed in accordance with the features of the spatial distribution of the processed data.

Another problem of geoinformation programming libraries in the visualization of geospatial data is the low efficiency and limitation of frame-by-frame changes of a group of spatial layers with a time reference. Among the most significant difficulties of visualization, there can be outlined the impossibility of synchronous switching of a group of spatial layers by a time parameter, which negatively affects the results of assessing the temporal anisotropy of the spatial data.

3. An approach to eliminating contour artifacts in geophysical data

To eliminate artifacts expressed by the gaps in spatial contour lines, it is proposed to connect them together. It is obvious that connecting spatial contour lines is possible only if they correspond to the same level value. Therefore, at the initial stage, it is necessary to combine the available spatial contour lines into groups based on the value corresponding to each of them [*Sun et al.*, 2019]. For each group of contour lines, a sequential search procedure is performed in order to identify open contour lines whose start and end points do not coincide. For each open contour lines, a search is performed for another open line in the same group, and from the set of available ones, the one with the shortest distance from the original is selected. A pair of selected open contour lines is connected, forming one closed spatial isoline. Similar actions are performed for all open contour lines in each group.

A formal distinction is made between two types of gaps in spatial contour lines. A gap of the first type occurs if the end point of an arbitrarily selected fragment of a polyline does not coincide with the start point of the nearest fragment following the fragment of the polyline under consideration (and vice versa). To eliminate a gap of this type, it is necessary to connect the start and end points of adjacent fragments in a sequence, supplementing the

contour line with synthesized fragments. In this case, intermediate points are introduced to avoid additional artifacts. A gap of the second type occurs if the start and end points of a contour line do not coincide. To eliminate this gap of break, two solutions are proposed: to close the open isoline on itself or to connect it with the nearest open contour line of the same level [*Prince Czarnecki et al.*, 2022].

It is necessary to introduce descriptions of the initial isoline:

$$(x_1y_1, x_2y_2, x_3y_3, \dots, x_{n-2}y_{n-2}, x_{n-1}y_{n-1}, x_ny_n),$$

and the spatial contour line closest to it:

$$(x'_1y'_1, x'_2y'_2, x'_3y'_3, \dots, x'_{n-2}y'_{n-2}, x'_{n-1}y'_{n-1}, x'_ny'_n).$$

Here there are possible options for connecting pairs of open isolines.

1. Connecting the initial point of the source and the initial point of the spatial isoline closest to it:

$$\begin{aligned}&(x_ny_n, x_{n-1}y_{n-1}, x_{n-2}y_{n-2}, \dots, x_3y_3, x_2y_2, x_1y_1),\\ &(x_ny_n, x_{n-1}y_{n-1}, x_{n-2}y_{n-2}, \dots, x_3y_3, x_2y_2, x_1y_1,\\ &x'_1y'_1, x'_2y'_2, x'_3y'_3, \dots, x'_{n-2}y'_{n-2}, x'_{n-1}y'_{n-1}, x'_ny'_n).\end{aligned}$$

2. Connecting the end point of the initial and the end point of the isoline closest to it:

$$\begin{aligned}&(x'_ny'_n, x'_{n-1}y'_{n-1}, x'_{n-2}y'_{n-2}, \dots, x'_3y'_3, x'_2y'_2, x'_1y'_1),\\ &(x_1y_1, x_2y_2, x_3y_3, \dots, x_{n-2}y_{n-2}, x_{n-1}y_{n-1}, x_ny_n,\\ &x'_ny'_n, x'_{n-1}y'_{n-1}, x'_{n-2}y'_{n-2}, \dots, x'_3y'_3, x'_2y'_2, x'_1y'_1).\end{aligned}$$

3. Connecting the starting point of the initial and ending points of the isoline closest to it:

$$\begin{aligned}&(x'_1y'_1, x'_2y'_2, x'_3y'_3, \dots, x'_{n-2}y'_{n-2}, x'_{n-1}y'_{n-1}, x'_ny'_n,\\ &x_1y_1, x_2y_2, x_3y_3, \dots, x_{n-2}y_{n-2}, x_{n-1}y_{n-1}, x_ny_n).\end{aligned}$$

4. The connection of the end point of the initial and the starting point of the isoline closest to it:

$$\begin{aligned}&(x_1y_1, x_2y_2, x_3y_3, \dots, x_{n-2}y_{n-2}, x_{n-1}y_{n-1}, x_ny_n,\\ &x'_1y'_1, x'_2y'_2, x'_3y'_3, \dots, x'_{n-2}y'_{n-2}, x'_{n-1}y'_{n-1}, x'_ny'_n).\end{aligned}$$

To maintain a balance of distance between points, it is necessary to determine the points in the middle of the segment connecting the points of the initial and the closest open contour lines:

$$\begin{aligned}B_x &= \cos\varphi_2 \cdot \cos\Delta\lambda,\\ B_y &= \cos\varphi_2 \cdot \sin\Delta\lambda,\\ \varphi_m &= \operatorname{atan2}\left(\sin\varphi_1 + \sin\varphi_2, \sqrt{(\cos\varphi_1 + B_x)^2 + B_y^2}\right);\\ \lambda_m &= \lambda_1 + \operatorname{atan2}(B_y, \cos\varphi_1 + B_x),\end{aligned}$$

where $\varphi_1, \lambda_1, \varphi_2, \lambda_2$ are latitude and longitude of the starting and ending points, m is the index of the midpoint on the line connecting the starting and ending points.

The proposed method and algorithm for eliminating spatial isoline artifacts were implemented for the web application "Aurora-forecast" (https://www.aurora-forecast.ru), developed to visualize geophysical parameters in the auroral oval area. The spatial isolines

array is generated on the server side using Python scripts [*Figueiredo et al.*, 2021; *Horbiński et al.*, 2020a]. For clarity, Figure 1 shows the results of visualizing the spatial isolines layer in two cases: generating an array of spatial contour lines based on the original data (Figure 1a) and visualizing isolines after detecting and eliminating artifacts [*Vorobev et al.*, 2020; 2021; *Vorobev et al.*, 2022a; *Vorobev et al.*, 2022b] (Figure 1b).

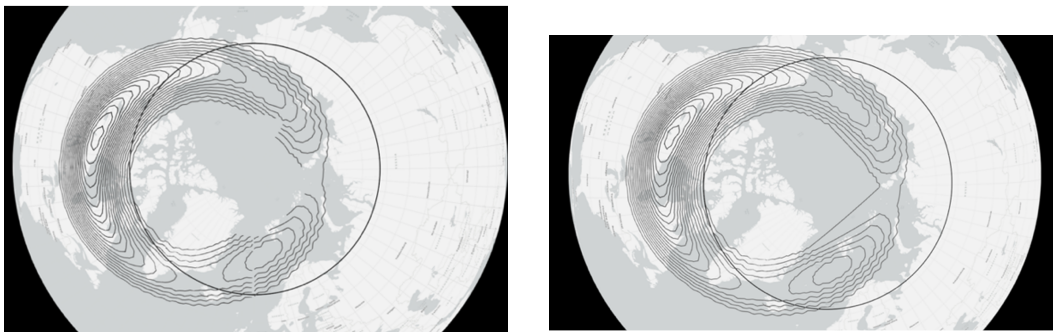

(a) **(b)**

Figure 1. An example of visualization of spatial isolines in the application "Aurora-Forecast".

4. An approach to constructing a retrospective spatial layer

The formation of a geospatial image from heterogeneous spatial data can be described as follows [*Breunig et al.*, 2020; *Chen et al.*, 2013; *Dintu et al.*, 2022; *Ma*, 2017; *Zhu et al.*, 2019]. First, it is necessary to bring data to a single discretization step, which requires defining the rules for converting the time intervals taking into account the units of measurement used, which, in turn, may differ. At the second (optional) stage, it is necessary to bring the processed spatial data to a single coordinate system, since data coming from different sources are not necessarily presented in the same coordinate system. If the coordinate systems used are the same, this stage is skipped. Then, all geospatial primitives used in the processed data are identified, the rules for their transformation and reduction to a single graphic primitive are determined to form an integrated spatial layer.

The most difficult problem here is concerned with transforming some geospatial primitives into others used in the target layer. The task of forming a target spatial layer from the obtained group of layers should be reduced to the use of a single geospatial primitive in each of the initial data, for example, a spatial point, where the transformation rule is generally specified by the function [*Alkaradaghi et al.*, 2022; *Yu et al.*, 2018; *Zhang et al.*, 2019]:

$$f_{lp} = l \to p = \{\text{lat}\} \to \{\text{pat}\} : p = \{x, y, (z)\};$$
$$l = \{\{x_1, y_1, (z_1)\}, \dots, \{x_n, y_n, (z_n)\}\}\ ,\ n \in \mathbb{N}.$$

Since in the initial version the attribute and time parameters were tied to the spatial polyline as a whole, when decomposing the polyline into points it is necessary to perform their redistribution [*Mohd Napi et al.*, 2021; *Peuquet et al.*, 1995]:

$$l_T = \{x_1, y_1, (z_1), a_1, t_1\}, \dots, \{x_n, y_n, (z_n), a_1, t_1\}, \dots, \{x_1, y_1, (z_1), a_D, t_D\}, \dots, \{x_n, y_n, (z_n), a_D, t_D\},$$

where l_T is the transformed polyline, $t_i (i = 1, \dots, D)$ is a generalized time parameter integrating the sampling steps for data sets X and Y with coefficients c and e respectively.

If the initial data X and Y are represented by spatial points and polygons, then the corresponding transformation of the layer group into the target layer is the following [*Oswald Beiler et al.*, 2021; *Rachmatullah et al.*, 2017; *Yu et al.*, 2018]:

$$r_T = \{x_1^1, y_1^1, (z_1^1), a_1, t_1\}, \dots, \{x_n^m, y_n^m, (z_n^m), a_1, t_1\}, \dots, \{x_1^1, y_1^1, (z_1^1), a_D, t_D\}, \dots, \{x_n^m, y_n^m, (z_n^m), a_D, t_D\},\ m, n \in \mathbb{N}.$$

Similarly, taking into account the spatio-temporal binding of the polygon, there can be defined a redistribution as follows [*Oswald Beiler et al.*, 2021; *Rachmatullah et al.*, 2017; *Yu et al.*, 2018]:

$$r_T = \{x_1^1, y_1^1, (z_1^1), a_1, t_1\}, \dots, \{x_n^m, y_n^m, (z_n^m), a_1, t_1\}, \dots, \{x_1^1, y_1^1, (z_1^1), a_D, t_D\}, \dots, \{x_n^m, y_n^m, (z_n^m), a_D, t_D\}, \ m, n \in \mathbb{N},$$

where $t_i (i = 1, \dots, D)$ is the a generalized time parameter integrating the sampling steps for data sets X and Y with coefficients c and e respectively.

A spatial polyline is a basic geospatial primitive and is widely implemented, including programming libraries. A spatial polyline typically has a "LineString" attribute in its metadata, as is seen, for example, in the GeoJSON format, which has become the de facto standard for representing geospatial information as spatial layers [*Moins et al.*, 2016]. Here it is appropriate to formalize the expressions [*Ding et al.*, 2021; *Horbiński et al.*, 2020b; *Moins et al.*, 2016; *Oswald Beiler et al.*, 2021; *Rachmatullah et al.*, 2017]:

$$f_{pl} = p \to l : p = \{x, y, z, a, t\}; l = \{p,\ p\} = \{\{x, y, z\}, \{x, y, z\}, a, t\};$$
$$f_{pr} = p \to r : p = \{x, y, z, a, t\}; r = \{p,\ p, p\} = \{\{x, y, z\}, \{x, y, z\}, \{x, y, z\}, a, t\}.$$

The quality assessment of the proposed solutions was performed at the level of its programming implementation. Within the framework of the developed research prototype of the web application, a variant of three-dimensional visualization of an integrated layer constructed from three sets of spatial data taking into account the specified timestamps was presented (Figure 2).

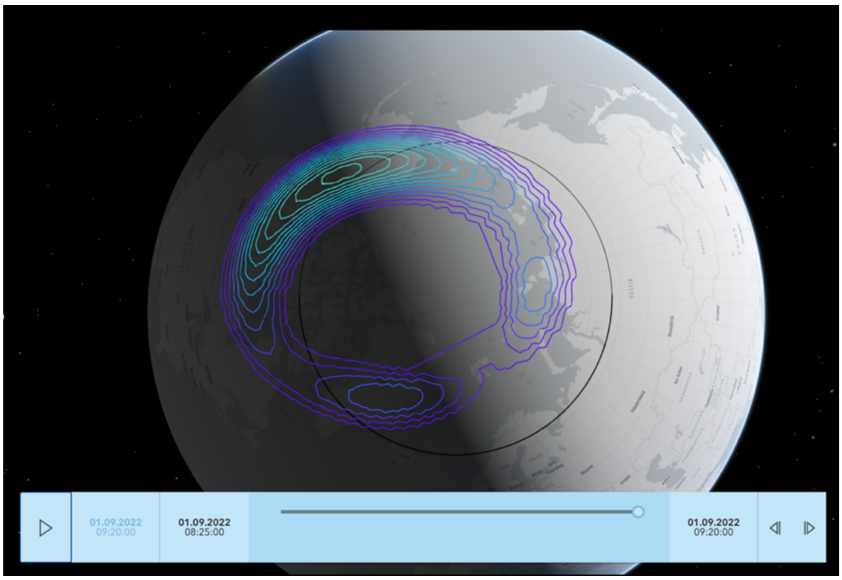

Figure 2. Screenshot of the application.

5. Conclusion

The problem of programming processing of spatial data in the context of modern technological development and exponential growth of volumes and complexity of such information is becoming especially relevant in the development of information systems for decision support in applied areas. Tendencies towards widespread distribution of relevant programming tools for a wide range of users contribute to the development of web-oriented solutions for such a problem. At the same time, developers face a number of problems in the implementation of relevant programming solutions that distort the visual representation of spatial data, on the one hand, and negatively affect the responsiveness of existing web applications, on the other.

The authors propose a method and algorithm for identifying and eliminating spatial isoline artifacts. It is based on the process of step-by-step detection of open isolines and determining the closest ones to them to form a closed contour line. In this case, various options for connecting polylines by starting and ending points are considered in such a way as to prevent new artifacts (by calculating and placing intermediate points).

In addition, an approach is proposed that involves the formation of a single integrated spatial layer based on a group of heterogeneous spatial layers. A method for mutual transformation of geospatial primitives is proposed, allowing spatial data to be converted to a given graphic object regardless of its original characteristics without losing attributive and temporal information. The novelty of the method lies in its universality in relation to vector graphic data, which will allow, after software implementation, to apply it in addition to known geoinformation libraries and tools.

Acknowledgments. The research was supported by the Russian Science Foundation grant No. 25-21-00143, https://rscf.ru/project/25-21-00143/.

References

Alkaradaghi K., *Hamamin D.*, *Karim H.*, *et al.* Geospatial Technique Integrated with MCDM Models for Selecting Potential Sites for Harvesting Rainwater in the Semi-arid Region // Water, Air, & Soil Pollution. — 2022. — Vol. 233, no. 8. — DOI: 10.1007/s11270-022-05796-2.

Breunig M., *Bradley P. E.*, *Jahn M.*, *et al.* Geospatial Data Management Research: Progress and Future Directions // ISPRS International Journal of Geo-Information. — 2020. — Vol. 9, no. 2. — P. 95. — DOI: 10.3390/ijgi9020095.

Chen F., *Ma X.*, *Ren H.* Progressive Transmission of Vector Spatial Data // Journal of Networks. — 2013. — Vol. 8, no. 5. — DOI: 10.4304/jnw.8.5.1065-1072.

Ding H., *Cai M.*, *Lin X.*, *et al.* RTVEMVS: Real-time modeling and visualization system for vehicle emissions on an urban road network // Journal of Cleaner Production. — 2021. — Vol. 309. — P. 127166. — DOI: 10.1016/j.jclepro.2021.127166.

Dintu S., *Suletea A.*, *Botez A.*, *et al.* The use of spatial modeling to teach engineering graphics // Journal of Social Sciences. — 2022. — Vol. 5, no. 2. — P. 104–112. — DOI: 10.52326/jss.utm.2022.5(2).09.

Figueiredo L. J. A. S., *Santos G. B. dos*, *Souza R. P. P. M.*, *et al.* MoreData: A Geospatial Data Enrichment Framework // Proceedings of the 29th International Conference on Advances in Geographic Information Systems. — ACM, 2021. — P. 419–422. — DOI: 10.1145/3474717.3484210.

Gorokhov S. N., *Shcherbakova T. F.*, *Sedov S. S.* Elimination of Isoline Drift when Analysis of the Electrocardiosignal of the Vehicle Driver // 2021 Intelligent Technologies and Electronic Devices in Vehicle and Road Transport Complex (TIRVED). — IEEE, 2021. — P. 1–5. — DOI: 10.1109/tirved53476.2021.9639163.

Horbiński T., *Lorek D.* The use of Leaflet and GeoJSON files for creating the interactive web map of the preindustrial state of the natural environment // Journal of Spatial Science. — 2020a. — Vol. 67, no. 1. — P. 61–77. — DOI: 10.1080/14498596.2020.1713237.

Horbiński T., *Lorek D.* The use of Leaflet and GeoJSON files for creating the interactive web map of the preindustrial state of the natural environment // Journal of Spatial Science. — 2020b. — Vol. 67, no. 1. — P. 61–77. — DOI: 10.1080/14498596.2020.1713237.

Kachanov P., *Zuev A.*, *Yatsenko K.* Method of overlapping geospatial data // Bulletin of the National Technical University «KhPI» Series: New solutions in modern technologies. — 2016. — 12 (1184). — P. 119. — DOI: 10.20998/2413-4295.2016.12.17.

Kumari S., *Parmar V.* GeoWebCln: An Intensive Cleaning Architecture for Geospatial Metadata // Quaestiones Geographicae. — 2022. — Vol. 41, no. 1. — P. 51–62. — DOI: 10.2478/quageo-2022-0004.

Ma X. Linked Geoscience Data in practice: where W3C standards meet domain knowledge, data visualization and OGC standards // Earth Science Informatics. — 2017. — Vol. 10, no. 4. — P. 429–441. — DOI: 10.1007/s12145-017-0304-8.

Moins I., *Boggio D.* SIRS Digues 2.0: A Cooperative Software For Levees Management // 3rd European Conference on Flood Risk Management (FLOODrisk 2016). — EDP Sciences, 2016. — DOI: 10.1051/e3sconf/20160704018.

Mohd Napi N. N. L., *Zainal M. H.*, *Abdullah S.*, *et al.* Spatio-Temporal Modelling of Noise Pollution // International Journal of Integrated Engineering. — 2021. — Vol. 13, no. 3. — DOI: 10.30880/ijie.2021.13.03.015.

Oswald Beiler M. R., *Filion E.* Amtrak Rail Trespasser Analysis using a GIS Space-Time Approach // Public Works Management & Policy. — 2021. — Vol. 26, no. 4. — DOI: 10.1177/1087724X211003249.

Pakdil M. E., *Çelik R. N.* Serverless Geospatial Data Processing Workflow System Design // ISPRS International Journal of Geo-Information. — 2021. — Vol. 11, no. 1. — P. 20. — DOI: 10.3390/ijgi11010020.

Papadakis G., *Mandilaras G.*, *Mamoulis N.*, *et al.* Static and Dynamic Progressive Geospatial Interlinking // ACM Transactions on Spatial Algorithms and Systems. — 2022. — Vol. 8, no. 2. — P. 1–41. — DOI: 10.1145/3510025.

Peuquet D. J., *Duan N.* An event-based spatiotemporal data model (ESTDM) for temporal analysis of geographical data // International journal of geographical information systems. — 1995. — Vol. 9, no. 1. — P. 7–24. — DOI: 10.1080/02693799508902022.

Podany J., *Stary V.*, *Tomicek J.* 3D surface roughness characteristics for biological applications // Manufacturing Technology. — 2022. — Vol. 21, no. 6. — P. 836–841. — DOI: 10.21062/mft.2021.096.

Prince Czarnecki J. M., *Jones M. A.* The problem with open geospatial data for on-farm research // Agricultural & Environmental Letters. — 2022. — Vol. 7, no. 1. — DOI: 10.1002/ael2.20062.

Rachmatullah R. S., *Azizah F. N.* A Conceptual Data Model for Flood Based on Cellular Automata Using Moving Object Data Model // Journal of Physics: Conference Series. — 2017. — Vol. 801. — DOI: 10.1088/1742-6596/801/1/012037.

Sun K., *Zhu Y.*, *Pan P.*, *et al.* Geospatial data ontology: the semantic foundation of geospatial data integration and sharing // Big Earth Data. — 2019. — Vol. 3, no. 3. — P. 269–296. — DOI: 10.1080/20964471.2019.1661662.

Traxler C., *Hesina G.* Interacting with big geospatial data // GIM International. — 2017. — Vol. 31. — P. 19–21.

Vorobev A. V., *Pilipenko V. A.*, *Krasnoperov R. I.*, *et al.* Short-term forecast of the auroral oval position on the basis of the "virtual globe" technology // Russian Journal of Earth Sciences. — 2020. — Vol. 20, no. 6. — DOI: 10.2205/2020es000721.

Vorobev A. V., *Vorobeva G. R.*, *Khristodulo O. I.* An information system for spatial visualization of prognostic and retrospective data on the probability of observing auroras // Scientific and Technical Journal of Information Technologies, Mechanics and Optics. — 2021. — Vol. 21, no. 2. — P. 225–233. — DOI: 10.17586/2226-1494-2021-21-2-225-233.

Vorobev A., *Soloviev A.*, *Pilipenko V.*, *et al.* An Approach to Diagnostics of Geomagnetically Induced Currents Based on Ground Magnetometers Data // Applied Sciences. — 2022a. — Vol. 12, no. 3. — P. 1522. — DOI: 10.3390/app12031522.

Vorobev A., *Soloviev A.*, *Pilipenko V.*, *et al.* Interactive computer model for aurora forecast and analysis // Solar-Terrestrial Physics. — 2022b. — Vol. 8, no. 2. — P. 84–90. — DOI: 10.12737/stp-82202213.

Yu B., *Zhang C.*, *Sun J.*, *et al.* Massive GIS Spatio-temporal Data Storage Method in Cloud Environment // Proceedings of the 2018 2nd International Conference on Computer Science and Artificial Intelligence. — ACM, 2018. — P. 105–109. — DOI: 10.1145/3297156.3297193.

Zhang H., *Gao P.*, *Li Z.* Improvements to Information Entropy for Raster Spatial Data: A Thermodynamic-based Evaluation // Abstracts of the ICA. — 2019. — Vol. 1. — DOI: 10.5194/ica-abs-1-426-2019.

Zhu X., *Hu T.*, *Ye X.*, *et al.* Development and implementation of a dynamic and 4D GIS based on semantic location model // Geo-spatial Information Science. — 2019. — Vol. 22, no. 3. — P. 193–213. — DOI: 10.1080/10095020.2019.1649192.

Russian Journal of Earth Sciences

Special Issue: "Data Science, Geoinformatics and Systems Analysis in Geosciences"

Semi-Analytical Refinement of Submicron Droplet Growth by Condensation

D. N. Gabyshev[1]

[1]Geophysical Center, Russian Academy of Sciences, Moscow, Russia
* **Correspondence to:** Dmitrii N. Gabyshev, d.n.gabyshev@gcras.ru

Abstract: Understanding the growth dynamics of water droplets is crucial for accurate modelling of cloud formation and climate processes. This paper delves into the theoretical aspects of condensational growth of tiny water droplets in humid environments, such as warm clouds. The effect of droplet size on growth is examined using a semi-analytical model based on established kinetic principles, including the effects of diffusion and the medium discontinuity. While it was previously understood that smaller sizes are followed by slower growth rates, the refined model predicts that submicron droplets should grow even more slowly than anticipated. The model is consistent with previous conclusions and encompasses the growth of larger droplets as a limiting case. This model is expected to be applicable across a broad range of settings, from near-freezing conditions in clouds to elevated temperatures in technical applications involving hot steam-droplet mixtures, where Stefan flows are significant.

Keywords: condensational growth, droplet, kinetic theory, Knudsen layer, precipitation formation, cloud physics.

Citation: Gabyshev D. N. (2025), Semi-Analytical Refinement of Submicron Droplet Growth by Condensation, *Russian Journal of Earth Sciences*, 25, ES2015, EDN: ZEHDKS, https://doi.org/10.2205/2025ES000974

1. Introduction

The primary process responsible for the formation of atmospheric clouds is the condensation of water vapour. The total mass of water vapours in the atmosphere is roughly 10^{16} kg, which is equivalent to ten thousand cubic kilometres of bulk water, with an average annual variation of this value of around 10% [*Trenberth et al.*, 2005]. Despite it comprises only 1% of the atmosphere's mass, clouds and fogs constantly cover about two-thirds of the Earth's surface, significantly affecting its radiation exchange with outer space.

The process of condensation has garnered considerable interest from researchers for both fundamental exploration and practical applications such as the development of systems for extracting moisture from the atmospheric air and artificial influencing weather patterns [*Kasparian et al.*, 2012; *Kozlov*, 2013; *Wilderer et al.*, 2017]. Today, numerous studies in cloud microphysics address various issues, though, a few approaches have been employed to study condensation. Direct computer modelling techniques have gained prominence in recent years [*Wang et al.*, 2019; *Wang et al.*, 2022; *Wang et al.*, 2024], but thermodynamic [*Gabyshev*, 2025; *Quan et al.*, 2014; *Wang et al.*, 2023a,b] and kinetic approaches [*Gabyshev et al.*, 2020; *Guerrini et al.*, 1990; *Seaver*, 1984] remain fundamental. This study applies the kinetic approach, which is based on classic molecular and mechanical concepts of the structure of gases and condensed matter [*Eucken*, 1930; *Fuchs*, 1959; *Shuleikin*, 1968].

The present study focuses on the initial droplet sizes ranging from several tens of nanometres (close to the molecular diffusion regime) to single tens of micrometres (when

Research Article

Received: 15 November 2024
Accepted: 15 April 2025
Published: 23 May 2025

near-surface layer effects become negligible and growth rate asymptotes to the radius-square-law [*Jakubczyk et al.*, 2012; *Kolwas et al.*, 2019]). Thereby, our paper aims to provide better insights into the very initial precipitation stages in clouds before gravitational coagulation becomes prominent (prevailing at diameters $\gtrapprox 30$ μm).

The main objective is to advance the analytical theory of stationary condensational growth of small droplets at scales comparable to the mean free path in air, assuming the absence of heat release by the condensed phase. Our semi-analytical approach elucidates the formal relationship between smaller droplet sizes and slower growth rates. Although this behaviour is generally understood, our calculation articulates and implements a specific concept underpinning it, which, despite being intuitively grasped, has not been expressed explicitly until now. While the literature may have implicitly acknowledged this concept, explicit discussion may have been avoided due to its perceived self-evidence. Nonetheless, a thorough review of the literature did not uncover any solution presented in precisely the same form as ours.

Exploration within the transition range of scales between kinetic molecular diffusion and diffusion in the developed Knudsen layer regime will show us that the growth rate of the droplets on Aitken nuclei (approximately 0.1 μm and smaller) not only deviates significantly from the radius-squared law limit but is also considerably slower than previously thought. Aitken nuclei fall within the so-called Greenfield gap [*Poydenot et al.*, 2024], a size range where particles are inefficiently removed from the atmosphere through scavenging by raindrops. This results in these particles remaining suspended for extended periods, ranging from weeks to months. The reduced growth rate of droplets on such nuclei, coupled with Brownian motion of theirs, may therefore contribute to their prolonged residence time in the atmosphere.

2. Basic assumptions and equations

Let a spherical droplet of radius r be in an infinite air space of constant temperature and humidity. The ordinary diffusion coefficient D of water vapour from the ambient air towards the droplet surface is affected by kinetic effects within the Knudsen layer, which surrounds the droplet and has a thickness approximately equal to the mean free path $\langle\lambda\rangle$ [*Fuchs*, 1959; *Jakubczyk et al.*, 2012]:

$$D_{\text{eff}} = \frac{D}{\frac{r}{r+\beta\langle\lambda\rangle} + \frac{D}{r\langle v\rangle\alpha_c}},$$

where β is a dimensionless coefficient that measures the thickness of the Knudsen layer in units of $\langle\lambda\rangle$ and for simplicity assumed to be taken as $\beta = 1$, noting that it is implied to follow $\langle\lambda\rangle$ in all subsequent equations; α_c is the condensation coefficient, representing the probability that the molecule transitioning to the condensed phase surface will not be reflected from it. A review of formulae for estimating the value of α_c has been provided by [*Golubkov et al.*, 2018]. The investigation of the contribution of this factor falls outside the scope of the present study. For simplicity, we therefore assume α_c to be constant, typically around 0.04 for water [*Kozyrev et al.*, 2001; *Mozurkewich*, 1986]. Above, $\langle v\rangle = \sqrt{\frac{kT}{2\pi m}}$ represents *one quarter* of the mean molecular speed of a water vapour molecule (with mass m). The mass flux (the increase of the droplet mass per unit time) towards the droplet surface should be determined taking into account the Stefan flow, which is responsible for hydrodynamic entrainment of air with the vapour flow [*Fuchs*, 1959]:

$$I_0 = -4\pi r^2 D_{\text{eff}} \frac{c_s}{c_s - \frac{c}{M}} \frac{dc}{dr},$$

where $c_s = \frac{c}{M} + \frac{c'}{M'}$ is the total molar concentration of the medium equal to the sum of the molar concentration c/M of water vapour (with an absolute humidity c and a molar mass M) and the molar concentration of the remaining components c'/M' (as dry air with the mass

concentration c' and molar mass M'), respectively. The value of c_s differs negligibly near and far from the droplet, therefore it can be considered constant. The concentration field is assumed to be steady, i.e. only the stationary growth is considered. Readers interested in the temperature decrease associated with condensation may refer to equations (3) in [*Jakubczyk et al.*, 2012] and (6.4) in [*Fuchs*, 1959] for a simplified treatment. In our analysis, we neglect it and consider exclusively the isothermal case.

After transformation, integration, and substitution of the integration limits as prescribed in [*Fuchs*, 1959], we obtain the following expression:

$$\frac{1}{r}\ln\left[\left(1+\frac{\langle\lambda\rangle}{r}\right)^{\frac{r}{\langle\lambda\rangle}}\right]+\frac{D}{2r^2\langle v\rangle\alpha_c}=\frac{4\pi D\Delta c}{I_0} \tag{1}$$

with the definition introduced

$$\Delta c \stackrel{\text{def}}{=} M\left[c_{s\infty}\ln\left(1-\frac{c_\infty}{Mc_{s\infty}}\right)-c_{s0}\ln\left(1-\frac{c_0}{Mc_{s0}}\right)\right],$$

where c_0 is the absolute humidity over the droplet surface and c_∞ is that of ambient air. The following form is convenient for numerical use:

$$\begin{aligned}&\Delta c \equiv c_\infty x_\infty \ln\left(1-\frac{1}{x_\infty}\right)-c_0 x_0\ln\left(1-\frac{1}{x_0}\right),\\ &x_i \stackrel{\text{def}}{=} 1+\frac{M}{M'\chi_i},\quad i=0,\infty,\end{aligned}$$

where $\chi=\frac{c}{c'}$ is the water vapour mixing ratio (ratio of the water vapour density c to that of dry air c). The ratio χ characterizes the intensity of the Stefan flow. It is small at or below room temperature, but not negligible at high temperatures (see [*Gabyshev et al.*, 2020] for all necessary material expressions). The flux of vapour condensed on the droplet is as from the equation (1). On the other hand, the flux is as follows:

$$I_0=4\pi r^2\frac{dr}{dt}\rho,$$

where ρ is the bulk water density. After transformation, separation of variables, and integration, we obtain the implicit function of the droplet radius r:

$$F(r)-F(r_0)+A(r-r_0)=\tau-\tau_0, \tag{2}$$

with the following definitions introduced

$$\begin{aligned}&F(r)\stackrel{\text{def}}{=}\frac{r^2}{3}\ln\left[\left(1+\frac{\langle\lambda\rangle}{r}\right)^{\frac{r}{\langle\lambda\rangle}}\right]+\frac{r\langle\lambda\rangle}{3}\ln\left[\left(1+\frac{r}{\langle\lambda\rangle}\right)^{\frac{\langle\lambda\rangle}{r}}\right]+\frac{r^2}{6}-\frac{r\langle\lambda\rangle}{3},\\ &A\stackrel{\text{def}}{=}\frac{D}{2\langle v\rangle\alpha_c},\quad \tau\stackrel{\text{def}}{=}\frac{t}{\frac{\rho}{D\Delta c}}.\end{aligned} \tag{3}$$

where r_0 is the initial radius of the droplet at time t_0. This can correspond to the radius of the condensation nucleus in heterogeneous nucleation, or the scale of inhomogeneity in homogeneous nucleation (1–20 nm). We posit that this expression is valid when the initial radius exceeds $\langle\lambda\rangle$ or is comparable to that. Otherwise, not kinetic but molecular diffusion regime takes place.

3. Micrometric droplets

If the droplet is quite large $r \gg \langle\lambda\rangle$, then the thickness of the near-surface layer can be neglected, resulting in $F(r) = r^2/2$. Substituting it to (2) yields the equation describing r as a function of time t:

$$\frac{1}{2}\left[(r+A)^2 - (r_0+A)^2\right] = \tau - \tau_0. \tag{4}$$

The droplet radius can be expressed explicitly from the equation (4). Thence, the surface area growth rate per unit time is the following:

$$\frac{dS}{d\tau} = 8\pi - 8\pi A\left[2(\tau-\tau_0) + (r_0+A)^2\right]^{-\frac{1}{2}}. \tag{5}$$

It is worth noting that hints for deriving the expression (5) can be found in the famous monograph [*Fuchs*, 1959]. While the author of that reasons in terms of mass increase rather than area increase per unit time, the line of reasoning is not carried through to its logical conclusion, which would have resulted in an expression (5). Nonetheless, as we see, this derivation is straightforward. A minor modification of (5) can be made, noting that (in our notation $\langle v\rangle$ is *a quarter* of the mean speed!):

$$D = \frac{4}{3}\langle\lambda\rangle\langle v\rangle.$$

Within the temperature range of 0 °C to 100 °C at atmospheric pressure, the ratio $A = \frac{2}{3}\frac{\langle\lambda\rangle}{\alpha_c}$ varies monotonously and falls between 1.9 µm and 2.9 µm based on the material expressions provided by [*Gabyshev et al.*, 2020]. When $r \gg A$, or when the time is sufficiently large $\left(t - t_0 \gg \frac{A\rho}{4\alpha_c\langle v\rangle\Delta c}\right)$, the growth rate asymptotically approaches the well-known value (below, the infinity symbol in the index indicates unlimited time and the dot above denotes differentiation with respect to ordinary time t):

$$\left.\frac{dS}{d\tau}\right|_{\tau\to\infty} = 8\pi, \text{ or } \dot{S}_\infty = \frac{8\pi D}{\rho}\Delta c. \tag{6}$$

Furthermore, in the limit where $\chi \ll M/M'$, we have $\Delta c = c_0 - c_\infty$, and the equation (6) reduces to the classical 'Maxwellian' form [*Fuchs*, 1959; *Jakubczyk et al.*, 2012]. It is this expression is commonly referred to as the radius-square-law, as the square of the radius, representing the surface area, increases linearly with time. And the constant value (6) for large droplets leads to the common use of the derivative of the area as a measure of the rate of condensational growth.

In the temperature range where Stefan flow is weak, the expression for Δc can be expanded in a series. Then the droplet growth rate $\dot{S}$ differs from that calculated by formula (6) by the following factor [*Fuchs*, 1959]

$$f_s = 1 + \frac{c_0 + c_\infty}{2c_s M},$$

which at room temperature gives a correction of just over 1%. This means that it can be neglected even for warm clouds, however must be taken into account for industrial applications involving hot steam-droplet mixtures [*Strizhak et al.*, 2017].

For a moving microdroplet, the effect of the surrounding medium can be accounted for by introducing a ventilation coefficient, which depends on relevant similarity criteria. For droplets with radii less than 60 µm in laminar flow, this coefficient can be described, for example, by the formula [*Pruppacher et al.*, 2010]:

$$f_v = 1 + 0.108 \cdot \mathrm{Sc}^{\frac{2}{3}} \cdot \mathrm{Re},$$

where Re is the Reynolds number and Sc is the Schmidt number. Specifically, for a 20 µm diameter droplet moving at 0.1 m/s through saturated steam, the correction f_v is only a

fraction of a percent. Therefore, this correction can be neglected when analysing cloud conditions.

It is noteworthy that the exact laws governing droplet growth or evaporation remain of particular interest to many modern researchers, due to their practical applications at the nano- and micro-scales [*Dalla Barba et al.*, 2021; *Rana et al.*, 2019]. Therefore, we will now consider the calculation of the growth rate in the presence of significant kinetic effects, where the thickness of the Knudsen layer cannot be neglected.

4. Submicrometric droplets

Combining equations (2) and (3) and employing the apparatus of inverse derivatives, we readily obtain the following expression:

$$\frac{dr}{d\tau} = \left\{ A + r \ln \left[\left(1 + \frac{\langle \lambda \rangle}{r} \right)^{\frac{r}{\langle \lambda \rangle}} \right] \right\}^{-1}. \tag{7}$$

For large radii $r \gg A, \langle \lambda \rangle$, it yields a simplified expression:

$$\frac{dr}{d\tau} \approx \frac{1}{r}.$$

Recognising that $8\pi r \frac{dr}{d\tau} = \frac{dS}{d\tau}$, from (7) we obtain an expression for the growth rate:

$$\frac{dS}{d\tau} = \frac{8\pi r}{A + r \ln \left[\left(1 + \frac{\langle \lambda \rangle}{r} \right)^{\frac{r}{\langle \lambda \rangle}} \right]}. \tag{8}$$

When the droplet radius is large $r \gg A, \langle \lambda \rangle$, expression (8) approaches the constant value 8π. This effectively recovers the well-known classical expression (6) as a limiting case. We also could similarly derive an expression for the rate of mass increase. It mirrors expression (8), but the numerator becomes $4\pi r^2 \rho$ instead of $8\pi r$.

Together with equation (2), expressions (7) and (8) form a closed system for the precise numerical calculation of the rate of change of radius and area at any given time. When considering the inverse functions $t(r)$ and $\dot{S}(r)$, the dependence $t\left(\dot{S}\right)$ is fully analytical with r serving as a connecting parameter. Therefore, this approach can be termed semi-analytical (fully analytical in one direction and numerical in the other).

5. Calculations and discussion

For the calculations, the following values were adopted at 10°C [*Gabyshev et al.*, 2020]: $\langle \lambda \rangle = 6.2 \times 10^{-8}$ m, $D = 2.3 \times 10^{-5}$ m^2/s, $\langle v \rangle = 140$ m/s, $\alpha = 0.04$. Generally speaking, $A = \frac{D}{2\alpha \langle v \rangle} = 2.1 \times 10^{-6}$ m $\approx 33 \langle \lambda \rangle$ represents a characteristic length scale above which a droplet can be considered quite large.

Let the initial radius be equal to $r_0 = 0.1 \langle \lambda \rangle$ in a moment $\tau_0 = 0$. Since the ultimate rate (equation 6) is constant, we normalise the rates to it. Thus, we denote the ratio of the growth rate (8) to (6) for the submicron case as ξ_λ, and the ratio of the rate (5) to (6) for the micrometric case as ξ_m. Both of these functions are plotted in Figures 1, 2: ξ_λ is calculated numerically (solid line) and ξ_m analytically (dashed line). It was imperative to meticulously adhere to the proper chain of calculations. The first stage involved setting the radius for the submicron model r_λ at discrete steps, for example, $0.1 \langle \lambda \rangle$ apart. Subsequently, the value of ξ_λ was computed simultaneously using (8), and the corresponding time τ_λ was determined using (2). Following this, the radius r_m in the microscopic model was calculated at the same time τ_λ using equation (4), providing insight into the size that the radius would reach within the same timeframe as the droplet from the submicron model. It was only after completing these calculations that the rate in the submicron model ξ_m was derived using the time τ_λ and the radius r_m. Only this order of calculation is strictly proper, and in Figures 1, 2, the

graphs of $\xi_\lambda\,(r_\lambda)$ and $\xi_m\,(r_m)$ are actually displayed. Note that the graphs largely coincide, except in the submicrometric range, where they exhibit a substantial divergence.

The graphs indicate that the droplet growth rate approaches the asymptotic Maxwell's value (6) rather slowly. Notably, growth rate increases significantly slower in the submicrometric size range, and this finding was not previously reported in the literature. For instance, when the droplet radius equals the mean free path $\langle\lambda\rangle$, the growth rate is approximately half that previously anticipated (Figures 1 and 2, enlarged graphs). Similarly, when the droplet radius is $10\langle\lambda\rangle$, the actual growth rate may be 3% lower than previously assumed. Specifically, a droplet forming on a condensation nucleus with a size of $0.1\langle\lambda\rangle$ (the Aitken nucleus) would require a dimensionless time of $\tau = 0.005$ according to the normal model, and $\tau = 0.006$ according to our refined model, to achieve a dimensionless growth rate of $\xi = 0.12$.

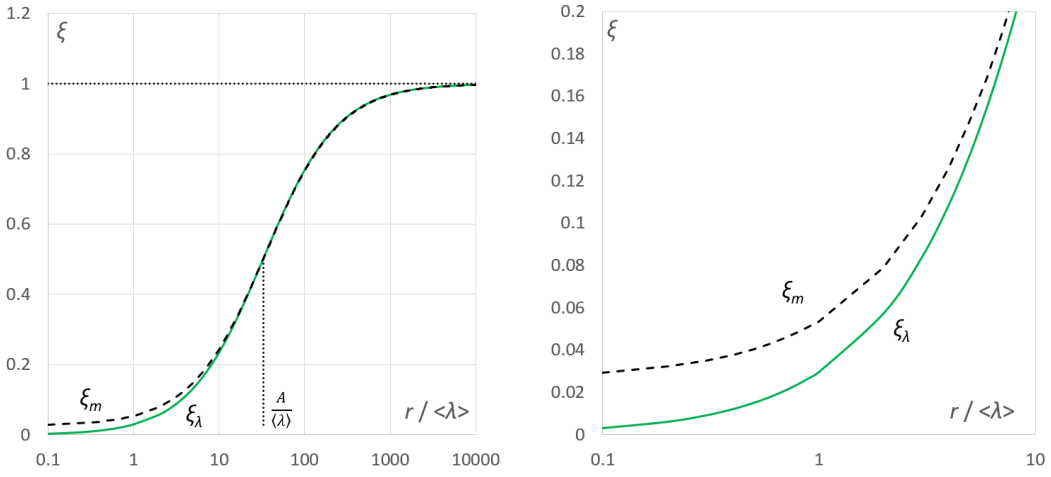

(a) **(b)**

Figure 1. Droplet growth rate ξ versus radius r for the submicron model (solid line) and the microscopic model (dashed line). Enlarged graph shown right.

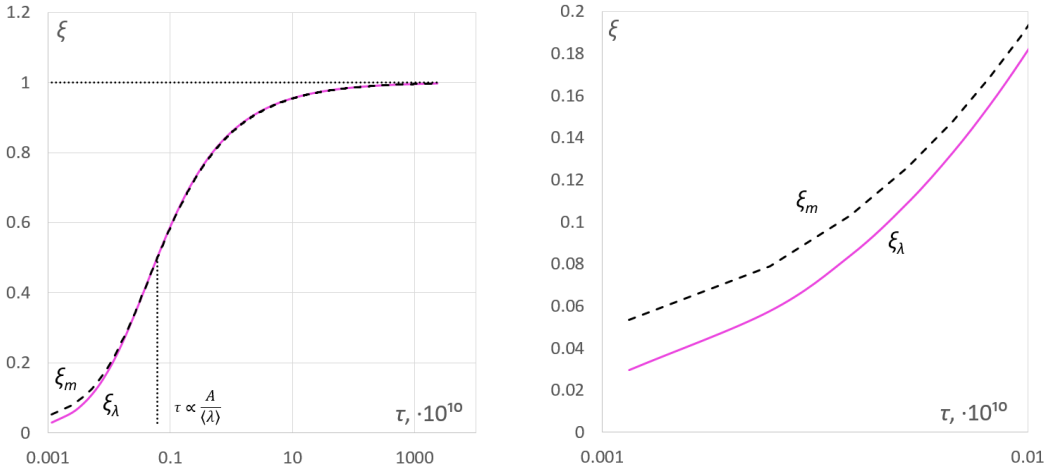

(a) **(b)**

Figure 2. Droplet growth rate ξ versus time τ: submicron model (solid line), microscopic model (dashed line). Enlarged graph shown right.

6. Conclusions

Accurate assessment of droplet mass exchange is essential for understanding droplet lifetime and influencing the feasibility of airborne processes, such as atmospheric precipitation formation. This study focused on the impact of droplet size on condensation rate, motivated by the fact that cloud droplets grow by condensation to a radius of approximately 15–20 μm, beyond which coagulation prevails.

While prior research established that smaller droplets grow slower than larger ones, a definitive model that considers the transfer of molecules within the Knudsen layer and provides a clear derivation of the radius-square law, with Maxwell's growth rate as the asymptotic limit, was lacking. This investigation addressed this gap by developing a semi-analytical model based on the kinetic approach with terms that vanish at large droplet sizes. Our results demonstrate a significant impact on the growth rate, especially for submicrometric droplets. We estimated that the growth rate is roughly half of what was previously expected when the droplet radius equals the thickness of the Knudsen layer (or the mean free path, if $\beta = 1$).

It appears that other researchers might want to validate this finding using molecular dynamics simulations, and we suggest that readers consider this for future research endeavors. It is also noteworthy that our model treats concentration as a time-independent multiplier in (3) due to the steady-state approximation assumed at the outset. This enables our model to be applied even at high temperatures where Stefan flow significantly modifies the concentration factor.

Acknowledgments. The work was carried out within the framework of the state assignment for the GC RAS, approved by the Ministry of Science and Higher Education of the Russian Federation.

References

Dalla Barba F., Wang J., Picano F. Revisiting D2-law for the evaporation of dilute droplets // Physics of Fluids. — 2021. — Vol. 33, no. 5. — DOI: 10.1063/5.0051078.

Eucken A. Lehrbuch der Chemischen Physik. Vol. 126. — Leipzig, 1930. — 988 p. — DOI: 10.1038/126988b0. — (In German).

Fuchs N. A. Evaporation and droplet growth in gaseous medium. — Elsevier, 1959. — DOI: 10.1016/C2013-0-08145-5.

Gabyshev D. N., Fedorets A. A., Klemm O. Condensational growth of water droplets in an external electric field at different temperatures // Aerosol Science and Technology. — 2020. — Vol. 54, no. 12. — P. 1556–1566. — DOI: 10.1080/02786826.2020.1804522.

Gabyshev D. N. Condensational growth of spherical water droplets altered under external electric fields // Journal of Aerosol Science. — 2025. — Vol. 186. — DOI: 10.1016/j.jaerosci.2025.106554.

Golubkov G. V., Manzhelii M. I., Berlin A. A., et al. Effects of the Interaction of Microwave Radiation with the Atmosphere on the Passive Remote Sensing of the Earth's Surface: Problems and Solutions (Review) // Russian Journal of Physical Chemistry B. — 2018. — Vol. 12, no. 4. — P. 725–748. — DOI: 10.1134/s1990793118040061.

Guerrini A., Murino G. Electric forces and physics of clouds // Il Nuovo Cimento C. — 1990. — Vol. 13, no. 3. — P. 663–668. — DOI: 10.1007/bf02507630.

Jakubczyk D., Kolwas M., Derkachov G., et al. Evaporation of Micro-Droplets: the "Radius-Square-Law" Revisited // Acta Physica Polonica A. — 2012. — Vol. 122, no. 4. — P. 709–716. — DOI: 10.12693/aphyspola.122.709.

Kasparian J., Rohwetter P., Wöste L., et al. Laser-assisted water condensation in the atmosphere: a step towards modulating precipitation? // Journal of Physics D: Applied Physics. — 2012. — Vol. 45, no. 29. — DOI: 10.1088/0022-3727/45/29/293001.

Kolwas M., Jakubczyk D., Do Duc T., et al. Evaporation of a free microdroplet of a binary mixture of liquids with different volatilities // Soft Matter. — 2019. — Vol. 15, no. 8. — P. 1825–1832. — DOI: 10.1039/c8sm02220h.

Kozlov V. N. Electrical methods for artificial precipitation regulation: Doctor thesis. — St. Petersburg : The Voeikov Main Geophysical Observatory, 2013. — (In Russian).

Kozyrev A. V., Sitnikov A. G. Evaporation of a spherical droplet in a moderate-pressure gas // Physics-Uspekhi. — 2001. — Vol. 44, no. 7. — P. 725–733. — DOI: 10.1070/pu2001v044n07abeh000953.

Mozurkewich M. Aerosol Growth and the Condensation Coefficient for Water: A Review // Aerosol Science and Technology. — 1986. — Vol. 5, no. 2. — P. 223–236. — DOI: 10.1080/02786828608959089.

Poydenot F., Andreotti B. Gap in drop collision rate between diffusive and inertial regimes explains the stability of fogs and non-precipitating clouds // Journal of Fluid Mechanics. — 2024. — Vol. 987. — DOI: 10.1017/jfm.2024.413.

Pruppacher H. R., Klett J. D. Microphysics of Clouds and Precipitation. — Springer Netherlands, 2010. — DOI: 10.1007/978-0-306-48100-0.

Quan X., Yang L., Cheng P. Effects of electric fields on onset of dropwise condensation based on Gibbs free energy and availability analyses // International Communications in Heat and Mass Transfer. — 2014. — Vol. 58. — P. 105–110. — DOI: 10.1016/j.icheatmasstransfer.2014.08.026.

Rana A. S., Lockerby D. A., Sprittles J. E. Lifetime of a Nanodroplet: Kinetic Effects and Regime Transitions // Physical Review Letters. — 2019. — Vol. 123, no. 15. — DOI: 10.1103/physrevlett.123.154501.

Seaver A. E. Closed Form Equations for the Evaporation Rate and Droplet Size of Knudsen Droplets // Aerosol Science and Technology. — 1984. — Vol. 3, no. 2. — P. 177–185. — DOI: 10.1080/02786828408959006.

Shuleikin V. V. Physics of Sea. — Moscow : Nauka, 1968. — 1090 p. — (In Russian).

Strizhak P. A., Piskunov M. V., Volkov R. S., et al. Evaporation, boiling and explosive breakup of oil–water emulsion drops under intense radiant heating // Chemical Engineering Research and Design. — 2017. — Vol. 127. — P. 72–80. — DOI: 10.1016/j.cherd.2017.09.008.

Trenberth K. E., Smith L. The Mass of the Atmosphere: A Constraint on Global Analyses // Journal of Climate. — 2005. — Vol. 18, no. 6. — P. 864–875. — DOI: 10.1175/jcli-3299.1.

Wang Q., Xie H., Hu Z., et al. The Impact of the Electric Field on Surface Condensation of Water Vapor: Insight from Molecular Dynamics Simulation // Nanomaterials. — 2019. — Vol. 9, no. 1. — P. 64. — DOI: 10.3390/nano9010064.

Wang P., Chen Z. Vapor Condensation Under Electric Field: A Study Using Molecular Dynamics Simulation // Supercomputing Frontiers. — Springer International Publishing, 2022. — P. 20–30. — DOI: 10.1007/978-3-031-10419-0_2.

Wang Y., Rastogi D., Malek K., et al. Electric Field-Induced Water Condensation Visualized by Vapor-Phase Transmission Electron Microscopy // The Journal of Physical Chemistry A. — 2023a. — Vol. 127, no. 11. — P. 2545–2553. — DOI: 10.1021/acs.jpca.2c08187.

Wang Y., Rastogi D., Malek K., et al. Electric Field-Induced Water Condensation Visualized by Vapor-Phase Transmission Electron Microscopy // The Journal of Physical Chemistry A. — 2023b. — Vol. 127, no. 11. — P. 2545–2553. — DOI: 10.1021/acs.jpca.2c08187.

Wang Z.-J., Wang S.-Y., Wang D.-Q., et al. The growth of condensed nanodroplets in electric fields: A molecular dynamics study // International Journal of Heat and Mass Transfer. — 2024. — Vol. 226. — DOI: 10.1016/j.ijheatmasstransfer.2024.125511.

Wilderer P. A., Fluher H., Davydova E. Risking Weather Engineering: Fiction or Contribution to Conflict Prevention? // Sustainable Risk Management. — Springer International Publishing, 2017. — P. 103–126. — DOI: 10.1007/978-3-319-66233-6_8.

Russian Journal of Earth Sciences

Special Issue: "Data Science, Geoinformatics and Systems Analysis in Geosciences"

Satellite Gravimetry as a Tool for Forecasting Oil and Gas Potential

I. N. Ognev[1], G. S. Khamidullina[1], D. K. Nurgaliev[1], F. N. Garaev[1], D. I. Ikhsanova[1], D. I. Mulikova[1]

[1]Kazan Federal University, Kazan, Russia
* **Correspondence to:** Igor Ognev, IgNOgnev@kpfu.ru

Abstract: This study explores the use of satellite gravity data and derived crustal models for predicting oil and gas potential in the east of the Russian platform. The research utilizes structural data (including GOCE satellite gravity-derived Moho depth), thermal data, and hydrocarbon potential data. The methodology involves three steps: 1) statistical analysis using Student's *t*-test to identify significant parameters distinguishing areas with and without hydrocarbon fields; 2) classification of the study area into three zones based on their hydrocarbon potential; and 3) application of a logistic regression machine learning model to forecast hydrocarbon potential in uncertain areas. The results show that most analyzed parameters have statistically significant differences between areas with and without hydrocarbon fields. The logistic regression model achieves 83% accuracy in predicting hydrocarbon potential. The study concludes that satellite gravity data and derived crustal models can be effectively used to forecast oil and gas potential in sedimentary basins, with the Precaspian basin, Cis-Ural trough, parts of the Central-Russia and Mezen rift systems, and the Timan-Pechora basin identified as the most promising areas in the east of the Russian platform.

Keywords: satellite gravimetry, oil and gas content, hydrocarbon deposits, gravity field, hydrocarbon exploration, heat flow, machine learning, logistic regression.

Citation: Ognev, I. N., G. S. Khamidullina, D. K. Nurgaliev, F. N. Garaev, D. I. Ikhsanova, and D. I. Mulikova (2025), Satellite Gravimetry as a Tool for Forecasting Oil and Gas Potential, *Russian Journal of Earth Sciences*, 25, ES2016, EDN: JGHKBN, https://doi.org/10.2205/2025ES000975

1. Introduction

Gravity measurements have long been used for hydrocarbon (HC) exploration and historically it was one of the initial geophysical techniques aimed at locating oil and gas fields [*Constantino et al.*, 2017; *Nabighian et al.*, 2005]. Nevertheless, exploring for HCs in remote and expansive territories often requires extensive land, marine, or airborne gravity surveys, yet combining these different ground-based measurements over large areas remains challenging [*Förste et al.*, 2016]. The solution is to measure the gravity field components from space using satellites. Modern satellite gravity missions have reached unprecedented spatial resolution of ~80 km which was achieved by Gravity Field and Steady-State Ocean Circulation Explorer (GOCE) satellite [*Bouman et al.*, 2013; *Zheng et al.*, 2014].

The resolution of GOCE gravity data and its particular sensitivity to the Moho boundary has made it essential in the regional and global scale solid Earth research [*Bouman et al.*, 2015]. Therefore, a large number of crustal models was built based on the GOCE gravity field using inverse and forward gravity modelling techniques, e.g. [*Haas et al.*, 2020; *Ognev et al.*, 2022a; *Sobh et al.*, 2019]. Considering a direct link between the crustal and geothermal structure of any geological province [*Fowler*, 2004], such crustal models gain utmost importance for studying the geothermal heat flow and temperature distribution within the crust. Given that the thermal maturity of HC-generating source rocks is closely tied to sediment temperatures, these models are becoming valuable tools for predicting geothermal properties and assessing oil and gas potential [*Beardsmore et al.*, 2001].

Research Article

Received: 15 November 2024
Accepted: 15 April 2025
Published: 23 May 2025

In our study we show how satellite gravity data and its derivatives can be used for forecasting oil and gas potential in the east of the Russian platform.

2. Data and methods

The dataset used in the present study can be subdivided into three categories: structural data, thermal data, and the data on HC-bearing potential. The data are summarized in Table 1.

As the structural data, the depth of lithosphere-asthenosphere boundary (LAB) from the thermal isostasy model of Europe [*Artemieva*, 2019], sedimentary cover thickness from EUNAseis model [*Artemieva et al.*, 2013], and the Moho depth of Volgo-Uralian subcraton derived from the inversion of GOCE gravity data and subsequent forward gravity modelling [*Ognev et al.*, 2022a] were used. The thermal data included the surface heat flux (HF) distribution obtained from the Thermoglobe database [*Jennings et al.*, 2021], the maps of lateral distribution of crustal thermal conductivity and radiogenic heat production (RHP), upper mantle thermal conductivity, and mantle HF derived from [*Ognev et al.*, 2022b]. Assessment of HC-bearing potential was based on polygons of the oil and gas fields [*Paraskun et al.*, 2011] and the zones of HC prospectivity from [*Avrov et al.*, 1969].

The workflow of the study consisted of the following 3 steps. Firstly, it was necessary to consider whether the areas with existing HC fields differ statistically from the areas without HC fields in terms of crustal and geothermal structure. We addressed this problem using the Student's *t*-test to assess the significance of the difference in means for the available thermal and structural parameters. Here, we considered only the Volgo-Ural HC province since it is the most studied province and it lies fully within the study area. The analyzed parameters were subdivided into two sampling groups based on the spatial location: (1) areas with HC fields, (2) areas without HC fields (Figure 1a). The *t*-test analysis allowed us to see which parameters have significant differences in means between these zones and thus can be used in the further analysis.

Table 1. Dataset used in the study.

Data	Reference
Structural data	
LAB depth	[*Artemieva*, 2019]
Moho depth derived from satellite gravity data	[*Ognev et al.*, 2022a]
Sedimentary cover thickness	[*Artemieva et al.*, 2013]
Thermal data	
Surface HF	[*Jennings et al.*, 2021]
Crustal thermal conductivity and RHP	[*Ognev et al.*, 2022b]
Upper mantle thermal conductivity and HF	[*Ognev et al.*, 2022b]
HC-bearing potential data	
Polygons of the oil and gas fields	[*Paraskun et al.*, 2011]
Zones of HC prospectivity	[*Avrov et al.*, 1969]

Secondly, the study area was subdivided into three zones in terms of its HC potential: (1) no HC-bearing potential, (2) high HC-bearing potential, (3) uncertain HC-bearing potential. The subdivision was done based on the map of HC prospectivity zones of the USSR [*Avrov et al.*, 1969]. Here in the zone 1 we incorporated only the regions which objectively hold minimal potential for HC exploration due to either thin or absent sedimentary cover (Voronezh massif, Fennoscandia, part of Ukrainian shield) or due to orogens with low preservation potential for oil or gas (Ural mountains). The rest of the territory was subdivided into zones 2 and 3 by the relative area of the grid pixel that was covered by HC fields. If more than 1% of the pixel was covered by HC fields, it was considered

as zone 2 with existing HC fields. If less than 1% of a pixel's area was covered, it was considered as zone 3 with uncertain HC-bearing potential (Figure 1b). The size of the pixel is ~ 50 km × 50 km.

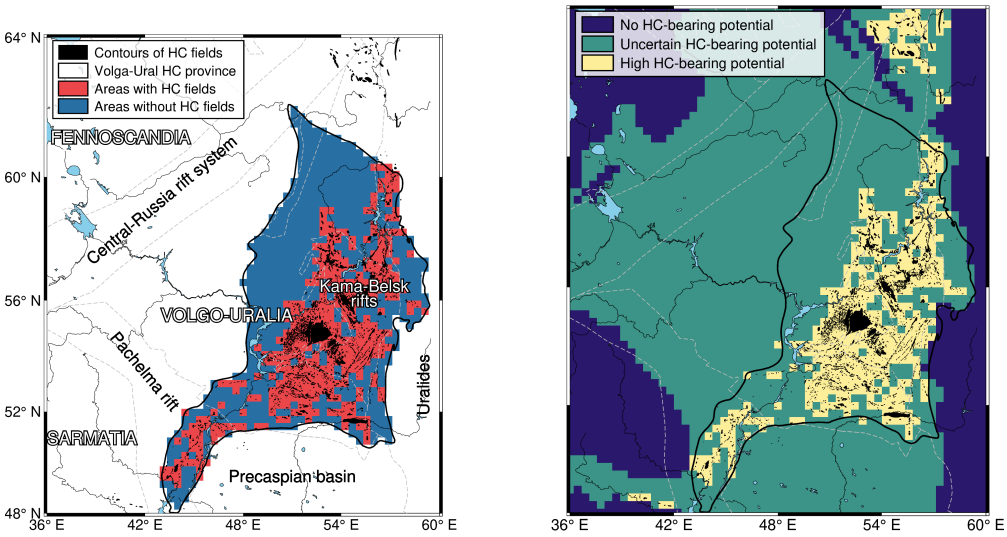

(a) (b)

Figure 1. Study area classification for the Student's *t*-test (a) and for the logistic regression ML algorithm (b).

Thirdly, the selected parameters from step 1 were used to train the machine learning (ML) model based on logistic regression scheme. Here the 1st and 2nd zones from the step 2 were taken to train the model, and zone 3 was used to forecast the HC potential. Before the training was commenced, the values of input parameters were standardized to have 0 mean and standard deviation of 1.

3. Results and discussion

Student's *t*-test was performed with a threshold p-value of 0.001 for the available parameters (Table 2). It can be seen that only the upper mantle thermal conductivity has a *p*-value > 0.001. The rest of the analyzed parameters can be considered to have statistically significant difference in means, so they can be used further in logistic regression model.

Table 2. Student's *t*-test results.

Parameter	Mean value in areas without HC fields	Mean value in areas with HC fields	*P*-value of Student's *t*-test
Sedimentary cover thickness (km)	4.33	5.68	2.53×10^{-10}
Moho depth (km)	43.33	41.54	6.77×10^{-22}
Lithosphere-asthenosphere boundary depth (km)	190.8	179.29	2.54×10^{-15}
Crustal thermal conductivity ($W\,m^{-1}\,K^{-1}$)	2.06	2.12	5.77×10^{-4}
Upper mantle thermal conductivity ($W\,m^{-1}\,K^{-1}$)	3.73	3.76	4.01×10^{-3}
Crustal radiogenic heat production ($\mu W\,m^{-3}$)	0.56	0.62	1.22×10^{-5}
Surface HF ($mW\,m^{-2}$)	43.03	46.18	6.79×10^{-8}
Mantle HF ($mW\,m^{-2}$)	19.04	20.42	2.37×10^{-16}

The results of logistic regression performance are shown on Figure 2. The accuracy of the model was calculated to be 83%. Here 62% of territories with existing HC fields and 92% of barren territories were predicted correctly (Figure 2a). Receiver operating characteristics (ROC) curve shows high value of area under the curve (AUC) of 0.83 (Figure 2b).

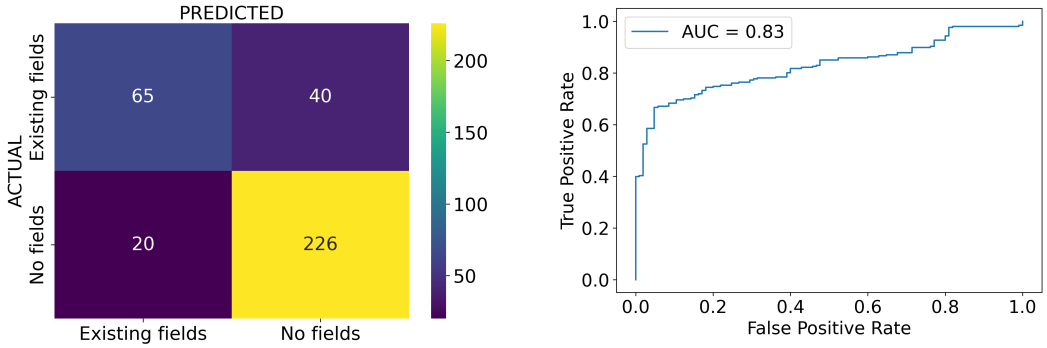

(a) **(b)**

Figure 2. Confusion matrix (a) and ROC curve (b) of the trained logistic regression model.

To forecast the HC potential in the east of the Russian platform predicted probability of HC fields' occurrence from the logistic regression model was visualized (Figure 3). As it can be seen, Precaspian basin, Cis-Ural trough, some parts of Central-Russia Rift System, Mezen rifts, and Timan-Pechora basin are the areas with the highest predicted probability of HC occurrence. These areas coincide with the thickest sedimentary column and higher values of geothermal parameters. The lowest predicted probability corresponds to the central-western part of Volgo-Uralia, which has the thickest crust, the deepest LAB, and the lowest HF.

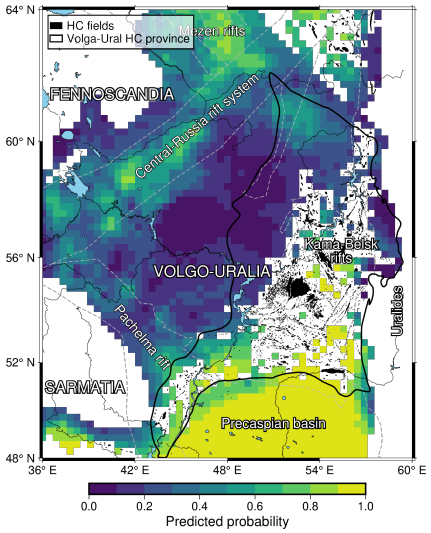

Figure 3. Predicted probability of HC fields' occurrence in the east of the Russian platform.

The performed analysis in case of the east of the Russian platform has its own limitations. As it is seen on Figure 2a, the model performs moderately better for defining barren territories rather than spotting the existing fields. Therefore, extra caution must be taken with the decision-making process for new areas of oil exploration and the areas with the highest probability must be evaluated first. To improve the presented model, several strategies might be undertaken: (1) use data with a finer spatial resolution, (2) incorporate spatial data sets with source-rocks' characteristics to account for the petroleum charge, (3) utilize other ML algorithms.

4. Conclusion

The described approach uses a satellite-gravity-derived structural model of the Earth's crust along with thermal parameters to forecast the oil and gas potential of sedimentary basins using a logistic regression ML algorithm. It has been shown in the case of the east of the Russian platform that the most perspective territories are located in the Precaspian

depression, Cis-Ural trough, parts of the Central-Russia and Mezen rift systems, and Timan-Pechora basin. The presented logistic regression approach demonstrated a considerable accuracy with 62% of true positive and 92% of true negative predictions. Nevertheless, other ML methods, additional source-rocks' related data and overall finer spatial resolution must be examined to improve the predictability of the forecast.

Acknowledgments. This work has been supported by the Ministry of Science and Higher Education of the Russian Federation under agreement No. 075–15-2022-299 within the framework of the development program for a world-class Research Centre "Efficient development of the global liquid hydrocarbon reserves".

References

Artemieva I. M., Thybo H. EUNAseis: A seismic model for Moho and crustal structure in Europe, Greenland, and the North Atlantic region // Tectonophysics. — 2013. — Vol. 609. — P. 97–153. — DOI: 10.1016/j.tecto.2013.08.004.

Artemieva I. M. Lithosphere structure in Europe from thermal isostasy // Earth-Science Reviews. — 2019. — Vol. 188. — P. 454–468. — DOI: 10.1016/j.earscirev.2018.11.004.

Avrov V. Y., Buyalov N. I., Vasiliev V. G. Map of oil and gas potential of the USSR as of January 1 1967. — Moscow : Main Directorate of Geodesy, Cartography, 1969. — (In Russian).

Beardsmore G. R., Cull J. P. Crustal Heat Flow: A Guide to Measurement and Modelling. — Cambridge University Press, 2001. — DOI: 10.1017/cbo9780511606021.

Bouman J., Floberghagen R., Rummel R. More Than 50 Years of Progress in Satellite Gravimetry // Eos, Transactions American Geophysical Union. — 2013. — Vol. 94, no. 31. — P. 269–270. — DOI: 10.1002/2013eo310001.

Bouman J., Ebbing J., Meekes S., et al. GOCE gravity gradient data for lithospheric modeling // International Journal of Applied Earth Observation and Geoinformation. — 2015. — Vol. 35. — P. 16–30. — DOI: 10.1016/j.jag.2013.11.001.

Constantino R. R., Hackspacher P. C., Souza I. A. de, et al. Basement structures over Rio Grande Rise from gravity inversion // Journal of South American Earth Sciences. — 2017. — Vol. 75. — P. 85–91. — DOI: 10.1016/j.jsames.2017.02.005.

Förste C., König R., Bruinsma S., et al. On the principles of satellite-based Gravity Field Determination with special focus on the Satellite Laser Ranging technique // 20th International Workshop on Laser Ranging. — Potsdam : Helmholtz Centre, 2016.

Fowler C. M. R. The Solid Earth: An Introduction to Global Geophysics (2nd ed.) — Cambridge : Cambridge University Press, 2004.

Haas P., Ebbing J., Szwillus W. Sensitivity analysis of gravity gradient inversion of the Moho depth—a case example for the Amazonian Craton // Geophysical Journal International. — 2020. — Vol. 221, no. 3. — P. 1896–1912. — DOI: 10.1093/gji/ggaa122.

Jennings S. S., Hasterok D., Lucazeau F. ThermoGlobe: Extending the global heat flow database // Journal TBD. — 2021.

Nabighian M. N., Ander M. E., Grauch V. J. S., et al. Historical development of the gravity method in exploration // Geophysics. — 2005. — Vol. 70, no. 6. — P. 63–89. — DOI: 10.1190/1.2133785.

Ognev I., Ebbing J., Haas P. Crustal structure of the Volgo-Uralian subcraton revealed by inverse and forward gravity modelling // Solid Earth. — 2022a. — Vol. 13, no. 2. — P. 431–448. — DOI: 10.5194/se-13-431-2022.

Ognev I., Ebbing J., Lösing M., et al. The thermal state of Volgo–Uralia from Bayesian inversion of surface heat flow and temperature // Geophysical Journal International. — 2022b. — Vol. 232, no. 1. — P. 322–342. — DOI: 10.1093/gji/ggac338.

Paraskun V. I., Rozhetskiy B. Y. Database of Oil and gas fields of FSUE "VNIGNI". — Rosgeolfond, 2011. — (In Russian).

Sobh M., Ebbing J., Mansi A. H., et al. Inverse and 3D forward gravity modelling for the estimation of the crustal thickness of Egypt // Tectonophysics. — 2019. — Vol. 752. — P. 52–67. — DOI: 10.1016/j.tecto.2018.12.002.

Zheng W., Hsu H., Zhong M., et al. Requirements Analysis for Future Satellite Gravity Mission Improved-GRACE // Surveys in Geophysics. — 2014. — Vol. 36, no. 1. — P. 87–109. — DOI: 10.1007/s10712-014-9306-y.

Russian Journal of Earth Sciences

Special Issue: "Data Science, Geoinformatics and Systems Analysis in Geosciences"

Identification of Icings Spreading Patterns in Selenga Middle Mountains by Methods of Geoinformation Analysis

V. N. Chernykh, B. Z. Tsydypov, A. A. Ayurzhanaev, M. A. Zharnikova, B. V. Sodnomov, Zh. B. Alymbaeva

Baikal Institute of Nature Management SB RAS, Ulan-Ude, Russia
* **Correspondence to:** Tsydypov Bair Z., bz61@mail.ru

Abstract: The purpose of this work is to determine the main regularities of icing distribution in the Selenga middle mountains. The objectives of the study included mapping of icings using Landsat imagery and geoinformation analysis of their spatial differentiation. The geoinformation analysis of the distribution of icings in the Selenga mid-mountain depending on various environmental factors (tectonics, relief, permafrost, meteorological indicators) revealed the main regularities of their formation. The relation of the glaciers to different categories according to the main classification features was determined. Icings of the Selenga mid-mountain are divided into 4 size classes (medium, large, very large and giant), 2 main genetic types are identified according to the prevailing sources of supply (groundwater and spring icings), the number of slope and valley icings is determined. The role of relief and snow cover influence on the distribution of icings in the territory was assessed. It has been established that in the current climatic conditions in the Selenga middle mountains 7.7 thousand icings are formed, most of which (70%) belong to groundwater icings. The maximum number of glaciers is observed in areas with a transitional type of permafrost distribution, while valley glaciers prevail in mountainous areas at altitudes from 850 to 1000 m. They are formed along watercourses in intermountain hollows and in the spurs of mountain ranges.

Keywords: icing, permafrost, groundwater, terrain, Selenga mid-mountains, snow cover, tectonic faults, geoinformation analysis.

Citation: Chernykh, V. N., B. Z. Tsydypov, A. A. Ayurzhanaev, M. A. Zharnikova, B. V. Sodnomov, and Zh. B. Alymbaeva (2025), Identification of Icings Spreading Patterns in Selenga Middle Mountains by Methods of Geoinformation Analysis, *Russian Journal of Earth Sciences*, 25, ES2017, EDN: PTTSVB, https://doi.org/10.2205/2025ES000976

1. Introduction

Geoinformation analysis is an effective method for studying the state and dynamics of various landscape components. In this study, we examine icing formations as the research objects. Icings are layered ice masses or crusts on the surface of the ground, ice, or engineering structures formed when periodically discharged natural or man-made water freezes [*Alekseev*, 1976; *Glaciological…*, 1984]. The cold, sharply continental climate of the Selenga mid-mountains leads to seasonal and widespread permafrost, making cryogenic processes, including the formation of icings, quite active. The complex tectonic structure, mountainous terrain, predominance of island permafrost, and the presence of water-saturated gravel deposits in river valleys all contribute to a high number of icings. Depending on the climatic conditions, between 3.3 and 7.7 thousand icings form in this area [*Chernykh et al.*, 2024].

Despite many years of research on icings in Transbaikalia, those in the Selenga mid-mountains are still insufficiently studied. Previous research on icings in the region has focused on areas near the Baikal-Amur Mainline (BAM) [*Chmutov*, 1982; *Markov et al.*, 2016;

Research Article

Received: 15 November 2024
Accepted: 15 April 2025
Published: 23 May 2025

Vasekhina, 1980], mountainous regions (Eastern Sayan range, Khamar-Daban, etc.) [*Alekseev*, 1974; 1975; *Glaciological…*, 1984], with some publications on Eastern Transbaikalia [*Alekseev*, 2016; *Shesternev et al.*, 2006; *Zvyagintseva et al.*, 2022].

Therefore, questions about determining the genesis and distribution features of icings, their morphometric characteristics, spatial-temporal dynamics, and the intensity of icing formation in response to global and regional natural and climatic changes are relevant for the Selenga mid-mountains. This study aimed to identify these formation characteristics using geoinformation methods.

2. Materials and Methods

The study area is the Selenga mid-mountains, an orographic region within Western Transbaikalia with a total area of more than 60000 km^2.

Vector polygons of icings (2022) derived from Landsat satellite image decoding, digital elevation models (DEMs) SRTM [*Farr et al.*, 2000] and HydroSHEDS (Void-filled DEM 3s product) [*Lehner et al.*, 2008], tectonic data from [*GIS-packages…*, 2024], refined using 1:200000 scale digital geological maps in SASPlanet software (version 200606), were used as baseline data. Materials from [*Brown et al.*, 2002] were used to assess the role of permafrost in the spatial differentiation of icings, and snow cover data from [*Ecological Atlas…*, 2015].

Icing distribution in the Selenga mid-mountains was mapped based on Landsat-8 satellite imagery (spatial resolution of 30 m) with dates from April 2 to April 22, 2022. Automated image data processing was conducted by analyzing threshold values of the NDSI (Normalized Difference Snow Index) [*Hall et al.*, 1995] according to the technique described in [*Alekseev et al.*, 2022], coupled with visual decoding and manual digitization. The threshold value of NDSI to identify snow and ice surfaces is taken to be equal to 0.4 [*Alekseev et al.*, 2022].

The resulting polygons were compared using vector data on tectonic faults to identify potential sources of icing formation. The distribution of icings based on terrain elevation and slope steepness was analyzed using the void-filled DEM from Hydrological data and maps based on Shuttle Elevation Derivatives at multiple Scales (HydroSHEDS), based on DEM from the Shuttle Radar Topography Mission (SRTM) with a spatial resolution of 90 m (3 arc seconds). HydroSHEDS was chosen because, unlike the original SRTM model, it includes hydrological corrections, improving watershed and talweg delineation accuracy.

The distribution of icings was compared with vector maps of permafrost types and snow cover thickness to clarify their roles. Data processing was conducted in ArcGIS, QGIS, and SASPlanet software.

Results

Figure 1 shows the current distribution of icings in the Selenga mid-mountains compared with permafrost distribution. Currently, in the cold season, 7747 icings form in the Selenga mid-mountains with a total area of 206.4 km^2. According to N. I. Tolstikhin classification [*Tolstikhin*, 1941], this includes 2 giant icings (area more than 1 km^2), 267 large ones (0.1 to 1 km^2), 4827 medium-sized ones (0.01 to 0.1 km^2), and 2651 small ones (less than 0.01 km^2). Smaller icings were not included in mapping based on satellite images, as recommended in [*Alekseev et al.*, 2022].

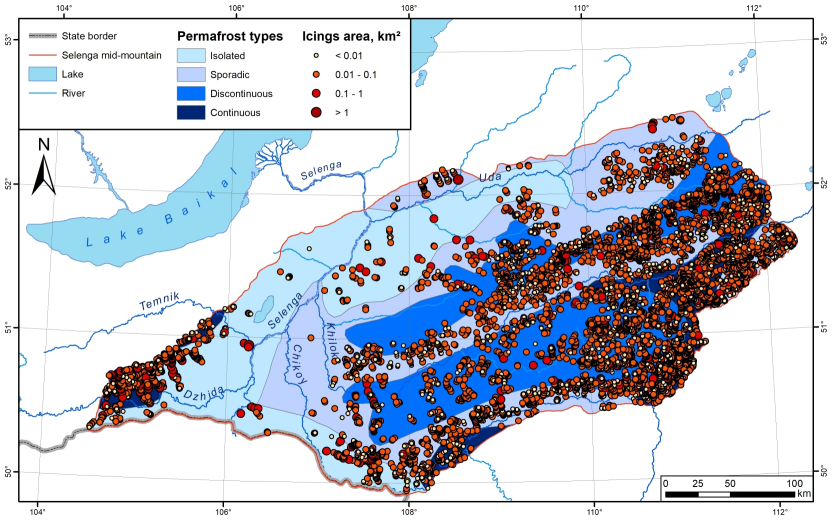

Figure 1. Current distribution of icings in the Selenga mid-mountains (permafrost distribution types by [*Brown et al.*, 2002]).

Figure 2 shows a map of icings located in fault zones. These areas are often associated with hydrogeogenic taliks [*Romanovsky*, 1973], where groundwater from deep aquifers discharges to the surface as non-freezing springs that feed the icings during the cold season.

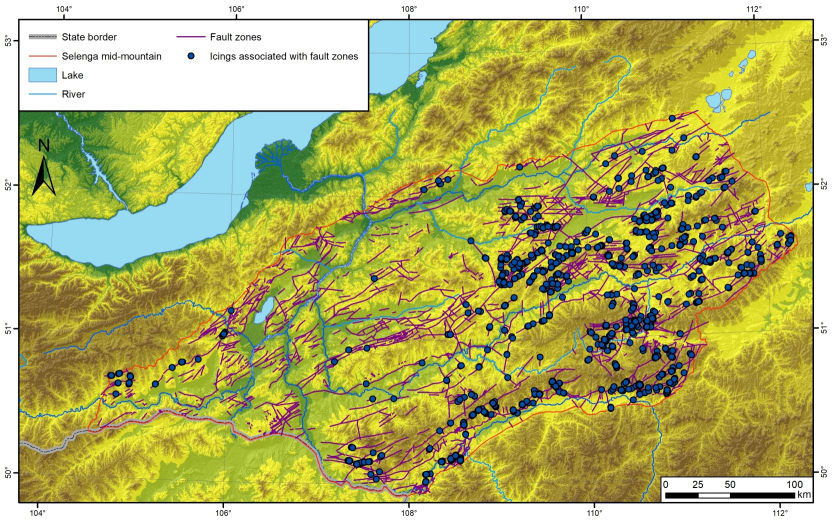

Figure 2. Icings associated with fault zones.

Figure 3a shows the analysis of icing distribution by elevation. The largest number of icings (3400) forms at elevations of 850 to 1000 meters. In the Selenga mid-mountains, these elevations correspond to the foothills of mountain ridges and river valleys in their spurs. Figure 3b presents a diagram of icing distribution by slope steepness.

The largest number of icings (4300) forms in the gently sloping valleys of small rivers. However, there are also a significant number of slope icings forming in mountainous areas with slopes greater than 8°.

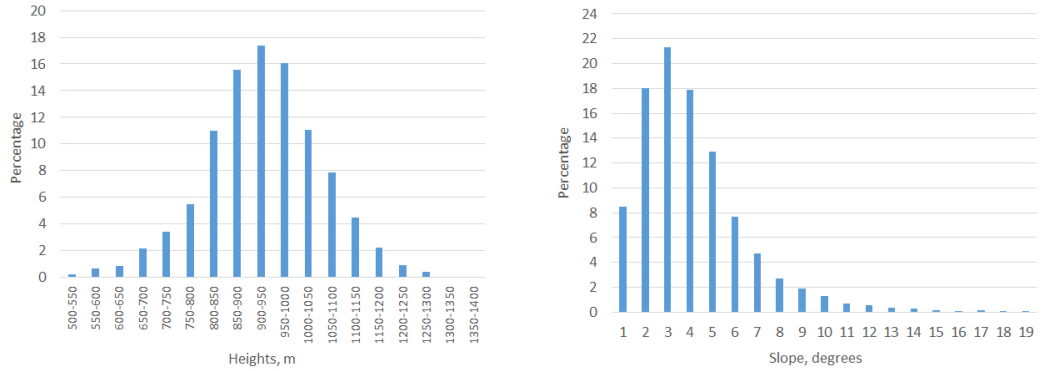

(a) **(b)**

Figure 3. Icing distribution in the terrain by elevation (a) and slope steepness (b).

Among meteorological factors influencing icing distribution, air temperature during the cold season and snow cover thickness are the most important. These two characteristics determine the freezing depth of rock, thus affecting groundwater circulation and cryogenic pressure. The results of analyzing the relationship between icing distribution and these parameters are shown in Table 1.

Table 1. Distribution of icings in the Selenga Middle mountains depending on the thickness of the snow cover.

Thickness of the snow cover, cm	Number of icings	Area of the territory, %	Amount of icings, %
<20	1224	49.2	15.7
20–40	5712	45.2	71.5
40–60	776	4.5	10.2
60–80	35	1.1	2.6

Note: snow cover thickness according [*Ecological Atlas…*, 2015].

3. Discussion of Results

In areas where icings have not been studied in detail, identifying general patterns of their formation is relevant. The most important aspects include determining the genesis of icing-forming water, clarifying their size and location in the landscape, and examining how various environmental factors influence their development intensity. Geoinformation analysis methods are well-suited for these purposes, as they enable assessment across large areas. Some data, such as the relationship between icings and fault zones, are challenging to establish without specific field investigations. GIS technologies, albeit with some conditionality, allow for such analysis.

Figure 1 shows that most icings form in mountainous areas with discontinuous or continuous permafrost coverage, where they are notably abundant. In regions with a continuous, thick cryolithozone (such as Northeast Russia), the density of icings per area is considerably lower, although their sizes are larger due to limited groundwater discharge on the surface because of permafrost. Here, icings form near large springs located in talik zones [*Alekseev et al.*, 2022; *Romanovsky*, 1973]. The high number of icings confirms that in the Selenga mid-mountains, even in areas marked as continuous permafrost on maps, numerous taliks exist.

The predominance of icings with areas up to 100,000 m^2 indicates that their primary water source is groundwater, which surfaces under cryogenic pressure arising from the seasonal freezing of rocks. For example, a spring with a constant flow rate of 5 liters per second (as described in [*Velmina*, 1970]) produces over 30,000 m^3 of water, or 32,000 m^3 of ice per season. According to [*Hydrogeology…*, 1970], the spring discharge rate in the Selenga

mid-mountains rarely exceeds 10 liters per second. Given that the average thickness of icings in the Selenga mid-mountains is 0.7–1.5 meters [*Chernykh et al.*, 2024], the area of icings with a constant supply from deep groundwater sources at this rate should range from 25000 to 45,000 m^2. Of the mapped icings, 5100 (65%) are under 45,000 m^2.

The groundwater sources nourishing most icings in the region are buried alluvial gravel deposits, which are widespread in river valleys of the Selenga mid-mountains, lying at depths of 1.5 meters or more, with significant water reserves [*Kibanov et al.*, 1980]. There are also river water icings in riverbeds and floodplains of medium rivers, though these are few.

Meanwhile, in Figure 2, 1850 icings (about 24%) are shown to intersect with known and suspected tectonic fault zones, where icing areas mostly exceed 50000 m^2. This indirectly suggests that icings are fed not only by groundwater but also by springs discharging groundwater through hydrogeogenic taliks in fault zones. Such icings are classified as spring-fed icings.

Thus, around 65% of icings in the Selenga mid-mountains are groundwater-fed, while 24% are spring-fed. The genesis of 11% of icings could not be precisely determined via geoinformation analysis. It should be understood that these figures are somewhat conditional; often, icings are fed by groundwater from various aquifer horizons. Accurate data would require chemical analysis of icing-forming water sources, though this is challenging given the number of icings.

The dissected terrain of the Selenga mid-mountains results in an uneven distribution of icings. About 12% form in areas with an absolute elevation below 850 meters, i.e., in intermountain basins, while 49% form at elevations of 850 to 1000 meters (Figure 3). These heights correspond to foothills of ridges, and icings located between 900 and 1000 meters are generally found in the valleys of watercourses in ridge spurs, typically on terrain slopes of 2 to 4°, where 57.2% of all regional icings form. About 8.5% form on terrain with slopes around 1°.

Thus, the analysis of icing distribution in the landscape shows that about 66% (5100) are valley icings, 32% (2400) are slope icings, and slightly over 2% can be classified as watershed icings. Some of these are located above 1100 meters, as shown in Figure 3.

Cryogenic pressure, which depends on rock freezing depth, is a crucial condition for icing formation. Factors influencing freezing depth include cold-season air temperature and snow cover thickness [*Verkhoturov*, 2010]. A comparative analysis of air temperature and icing distribution for one year would not reveal patterns, as a dynamic approach is more suitable. Therefore, this question was not addressed in this study. Since a direct correlation between icing formation intensity and snow cover thickness has been established for Transbaikalia [*Verkhoturov*, 2010], this relationship was analyzed for the Selenga mid-mountains as well.

The speed and depth of freezing of rocks depend on the thickness of the snow cover. The deeper the seasonal freezing, the higher the cryogenic pressure. In the Selenga middle mountains, the greatest number of icings are formed in areas with thickness of the snow cover less than 40 cm (Table 1). These are mountainous areas covered with forest vegetation. At the same time, in intermountain basins with snow depth less than 20 cm total number of icings is less, but their area is larger. This fact indicates a significant influence of the snow cover on the intensity of icings processes, but additional research is required due to local differences.

This pattern is related to the absence of permafrost in many intermountain basins (see Figure 1) or the presence of a permafrost layer at depths far beyond the seasonal freezing layer (5–7 meters and deeper [*Hydrogeology…*, 1970]). Hydraulic connections within aquifers allow groundwater circulation without surfacing to form icings. At the foot of slopes, groundwater volume increases due to ridge runoff. Additionally, in these areas, permafrost and crystalline bedrock often act as aquicludes. Therefore, even with thicker snow cover leading to shallower rock freezing, icings are more numerous than where snow cover is minimal.

Thus, while snow cover influences icing formation intensity, in the Selenga mid-mountains, its role is less significant than the impact of terrain or permafrost-hydrogeological conditions.

4. Conclusion

Geoinformation analysis using a comprehensive data set identified key spatial distribution patterns of icings in the Selenga mid-mountains. Based on Landsat satellite imagery, over 7700 icings form in the study area under current natural and climatic conditions, with most being large and medium-sized.

Morphometric analysis and comparison of icing locations with tectonic fault distribution revealed that over 60% of icings are groundwater-fed, about 30% are spring-fed, sourced from deep aquifers through springs. River-fed icings are rare in the Selenga mid-mountains.

The terrain analysis showed that most icings (66%) are valley icings, forming at elevations of 850 to 1000 meters in intermountain basins and river valleys with slopes up to 4°. About 32% are slope icings.

Snow cover thickness in the Selenga mid-mountains has less influence on icing formation than factors like terrain and permafrost-hydrogeological conditions.

The obtained data reflect the general spatial distribution characteristics of icings in the Selenga mid-mountains and serve as a basis for further research.

Acknowledgments. The work was financially supported by the Russian Science Foundation, project No. 23-27-00402 "Icings of the northern (Russian) part of the Selenga River basin".

References

Alekseev V. R., Makarieva O. M., Shikhov A. N., et al. Atlas of giant taryns of the North-East of Russia. — Novosibirsk : SB RAS, 2022. — 302 p. — (In Russian).

Alekseev V. R. Icings of Siberia and the Far East // Siberian Geographical Collection. Vol. 8. — Novosibirsk : Nauka, 1974. — P. 5–68. — (In Russian).

Alekseev V. R. Icings of the Lena-Amur Interfluve // Siberian Geographical Collection. Vol. 10. — Novosibirsk : Nauka, 1975. — P. 46–127. — (In Russian).

Alekseev V. R. Icings of the Sayano-Baikal Plateau // Notes of the Transbaikal branch of the Geographical Society of the USSR. Vol. 101. Glaciers and ice processes of Eastern Siberia. — Irkutsk : Transbaikal branch of the Geographical Society of the USSR, 1976. — P. 22–87. — (In Russian).

Alekseev V. R. Long-term variability of the spring taryns-aufeises // Ice and Snow. — 2016. — Vol. 56, no. 1. — P. 73–92. — (In Russian).

Brown J., Ferrians O., Heginbottom J., et al. Circum-Arctic Map of Permafrost and Ground-Ice Conditions, Version 2. — Boulder, Colorado USA, 2002. — DOI: 10.7265/SKBG-KF16.

Chernykh V. N., Tsydypov B. Z., Sodnomov B. V., et al. Icings in the Uda river basin (Western Transbaikalia): peculiarities of modern distribution and possibilities of use // Bulletin of the Tomsk Polytechnic University. Geo Assets Engineering. — 2024. — Vol. 335, no. 8. — P. 161–173. — DOI: 10.18799/24131830/2024/8/4432. — (In Russian).

Chmutov A. M. Catalog of icings of the BAM zone. Icings of the Upper Angara River basin. — Leningrad : Gidrometeoizdat, 1982. — 95 p. — (In Russian).

Ecological Atlas of the Lake Baikal Basin / ed. by V. M. Plusnin, D. Dorzhgotov, A. R. Batuev, *et al.* — Irkutsk : Institute of Geography named after V. B. Sochava SB RAS, 2015. — 145 p. — (In Russian).

Farr T. G., Kobrick M. Shuttle radar topography mission produces a wealth of data // Eos, Transactions American Geophysical Union. — 2000. — Vol. 81, no. 48. — P. 583–585. — DOI: 10.1029/eo081i048p00583.

GIS-packages of operative geological information. — URL: http://atlaspacket.vsegei.ru (visited on 10/25/2024). — (In Russian).

Glaciological dictionary / ed. by V. M. Kotlyakov. — Leningrad : Gidrometeoizdat, 1984. — 528 p. — (In Russian).

Hall D. K., Riggs G. A., Salomonson V. V. Development of methods for mapping global snow cover using moderate resolution imaging spectroradiometer data // Remote Sensing of Environment. — 1995. — Vol. 54, no. 2. — P. 127–140. — DOI: 10.1016/0034-4257(95)00137-p.

Hydrogeology of the USSR. Vol. XXII. Buryat ASSR / ed. by A. I. Efimov. — Moscow : Nedra, 1970. — 432 p. — (In Russian).

Kibanov G. A., *Khandalov V. I.*, *Kharaev P. K.* Groundwater utilization in Buryatia agriculture and problems of construction industry. — Ulan-Ude : Buryat Statistical Department, 1980. — 40 p. — (In Russian).

Lehner B., *Verdin K.*, *Jarvis A.* New Global Hydrography Derived From Spaceborne Elevation Data // Eos, Transactions American Geophysical Union. — 2008. — Vol. 89, no. 10. — P. 93–94. — DOI: 10.1029/2008EO100001.

Markov M. L., *Vasilenko N. G.*, *Gurevich E. V.* Icings of the BAM zone: Expeditionary studies. — SPb. : Nestor-Istoria, 2016. — 320 p. — (In Russian).

Romanovsky N. N. On the geologic activity of icings // Merzlotnyye issledovaniya. — 1973. — Vol. XIII. — P. 66–89. — (In Russian).

Shesternev D. M., *Verkhoturov A. G.* Iced areas of Transbaikalia. — Chita : ChitSU, 2006. — 212 p. — (In Russian).

Tolstikhin N. I. Groundwater of the frozen zone of the lithosphere. — Moscow-Leningrad : State Publishing House of Geological Literature of the Committee for Geological Affairs under the Council of People's Commissars of the USSR, 1941. — 210 p. — (In Russian).

Vasekhina N. A. Catalog of icings of the BAM zone. Icings of the upper part of the Chara River basin. — Leningrad : Gidrometeoizdat, 1980. — 62 p. — (In Russian).

Velmina N. A. Peculiarities of hydrogeology of the frozen zone of the lithosphere (cryohydrogeology). — Moscow : Nedra, 1970. — 326 p. — (In Russian).

Verkhoturov A. G. Icings formation and assessment of its impact on engineering structures (on the example of Transbaikalia) : PhD thesis / Verkhoturov A. G. — Chita, 2010. — 24 p. — (In Russian).

Zvyagintseva V. V., *Yu. Z. O.* Dynamics of icings formation in the conditions of Eastern Transbaikalia: a study using Earth remote sensing data // Bulletin of ZabGU. — 2022. — Vol. 28, no. 7. — P. 17–25. — DOI: 10.21209/2227-9245-2022-28-7-17-25. — (In Russian).

Russian Journal of Earth Sciences

Special Issue: "Data Science, Geoinformatics and Systems Analysis in Geosciences"

The Use of Climatic and Geospatial Data in Assessing the Potential of "Green Energy" and Designing Energy Systems with Renewable Energy Sources in the Republic of Adygea

M. K. Bedanokov[1], P. Y. Buchatskiy[2], S. V. Teploukhov[2], S. V. Onishchenko[2]

[1]Maykop State Technological University, Maykop, Russia
[2]Adyghe State University, Maykop, Russia
* **Correspondence to:** Teploukhov Semen Vasilyevich, tepl_sv@adygnet.ru

Abstract: The integration of green energy sources has many advantages, but their variable nature of generation introduces additional difficulties in organizing a stable supply of end-users. To solve this problem, it is necessary to use renewable energy sources (RES) assessment and forecasting models that allow not only to identify the most suitable locations for such energy systems, but also to determine the potential volumes of energy generation, taking into account seasonal features that determine the amount of incoming energy in the mountainous areas of the Republic of Adygea. However, the construction of such models requires the availability of large sets of climatic data that allow to fully assess the behavior of a particular resource in the area under consideration. The article considers the characteristics of renewable energy sources that can be obtained from open data sources and geographic information systems, the use of which will allow not only to preliminarily assess the potential of renewable energy sources, but also to manage distributed energy systems by realizing short-term forecasts, and also considers examples of such data sources, interaction with which allows to assess the potential of the selected energy resource in the study area.

Keywords: renewable energy sources, data, energy potential assessment, geographic information systems.

Citation: Bedanokov, M. K., P. Y. Buchatskiy, S. V. Teploukhov, and S. V. Onishchenko (2025), The Use of Climatic and Geospatial Data in Assessing the Potential of "Green Energy" and Designing Energy Systems with Renewable Energy Sources in the Republic of Adygea, *Russian Journal of Earth Sciences*, 25, ES2018, EDN: ZLJXTG, https://doi.org/10.2205/2025ES000977

1. Introduction

Active integration of renewable energy sources into existing energy systems is becoming a relevant trend in recent years in many countries of the world [*Awogbemi et al.*, 2023; *Sher et al.*, 2024]. Such an increase in the share of "green" energy in the energy systems of states leads to the emergence of hybrid distributed systems that include various energy sources that are subject to climate impacts [*Ahmed et al.*, 2024; *Simankov et al.*, 2023a]. This problem can be solved by organizing complex distributed systems that combine several types of renewable energy sources, traditional carbon carriers and energy storage systems, allowing to achieve absolute stability in the generation of the required amounts of energy [*Arabzadeh et al.*, 2024]. However, in order to effectively manage such systems, monitoring systems and predictive analytics are needed to estimate, at least in the short term, the future generation volumes when using a particular type of resources [*Simankov et al.*, 2023b; *Simankov et al.*, 2024]. In such a case, one of the most important issues is the question of obtaining all necessary parameters from various available sources. In this paper we propose to consider the key parameters of RES and other characteristics that are important in assessing the potential of "green energy" and ways to obtain them.

Research Article

Received: 15 November 2024
Accepted: 15 April 2025
Published: 23 May 2025

2. Materials and methods

Data is one of the key elements necessary for further analysis of the subject area, making informed decisions and final recommendations in the field of renewable energy. Geospatial datasets [*Buchatskiy et al.*, 2024] are the most widely used in the assessment of renewable energy resources to provide the necessary basis for effective decision-making, as they contain, in addition to information on renewable energy resources, information on existing infrastructure, regional and district boundaries, terrain and current land use, and some of the parameters have temporal characteristics, which is an important factor in building an assessment of the resource potential that changes over time.

Renewable energy datasets provide information on the availability and intensity of available energy: solar, wind, geothermal, hydropower, wave, tidal and biomass energy in a particular geographic location under study. The availability of most renewable energy sources is directly related to their location, and for variable sources such as solar and wind power an additional component appears — time dependence. Next, consider what data can be generated to estimate major sources of renewable energy through the use of GIS.

3. Solar energy

Solar irradiance data are most commonly reported as one of three components (or various combinations thereof):

- direct normal radiation coming directly from the sun;
- scattered horizontal radiation (diffuse) — radiation that comes in scattered (reflected) form from different directions;
- global horizontal radiation, which is the amount of energy arriving on a flat surface during the day.

In terms of time scale, the considered characteristics can have different ranges, from several minutes to hours or days, but the most popular and convenient is the representation in the form of average monthly or average annual radiation for a particular territory. Figure 1 shows the result of displaying solar radiation characteristics in the PVGIS tool [*PVGIS*, 2024], which allows us to obtain sets of raw data in the form of time series for certain coordinates and conveniently visualize them for better clarity.

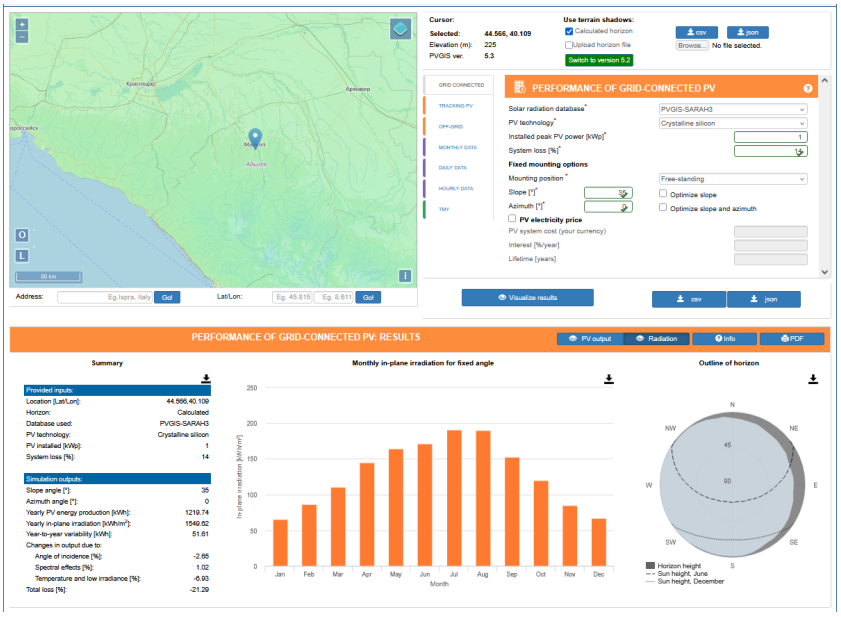

Figure 1. Solar radiation data in the PVGIS tool for the territory of the city of Maykop (Republic of Adygea) [*PVGIS*, 2024].

3.1. Wind energy

Typically, wind resource data are more complex than solar irradiance data, and their use requires high spatial resolution data. A second important aspect is the need to obtain information on wind speeds at different heights, sometimes called hub heights. These values are typically 30, 60, 80, 100 and 120 meters, representing the most common heights for installing wind turbines. Similarly, wind speed data can have different time scales, from a few minutes to annual averages. Figure 2 shows the values of annual average wind speed for 10- and 150-meters altitude obtained with the Global Wind Atlas tool [*Global Wind Atlas*, 2024].

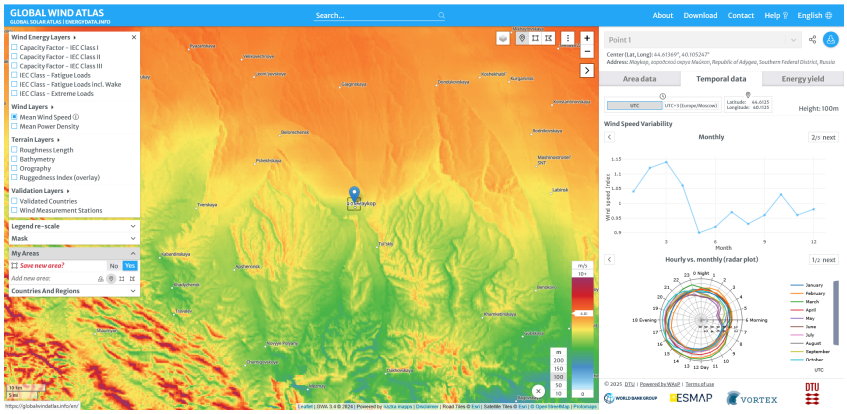

Figure 2. Map of mean wind speed distribution and monthly mean wind speed values for the city of Maykop (Republic of Adygea).

3.2. Geothermal energy

Geothermal energy has one of the highest efficiency factors among all renewable energy sources, reaching 70-80% [*Nkinyam et al.*, 2025], but its distribution is very limited and requires serious investments for the creation of energy systems, therefore it is most often used precisely for heating various premises [*Buchatskiy et al.*, 2023], rather than for the production of electricity. Data on geothermal deposits do not contain a large number of indicators, and the basic information includes the location of such wells, their depth, and the temperature of the water or steam coming out. As a rule, such maps show those sources that are already in use, and the area of use of this type of energy is very limited due to the strict connection to the areas with the presence of such deposits. Not for all sources of geothermal energy can be determined their potential, so, recently to geothermal energy include the energy of heat pumps [*Gaur et al.*, 2021], which convert the natural heat of the earth at a certain depth, but the energy potential when using such technology can not be calculated analytically for each case because of a large number of factors, and it can be determined only for a specific area. Various approaches can be used for assessment [*Zhang et al.*, 2023], including the use of GIS, for which data from open sources can be transferred to a tool for further processing and utilization. Open source energy distribution atlases such as the energy atlas (Geothermal Potential) can be used as open sources [*Geothermal Potential*, 2024] or Open Geoscience Computing Repository [*Open Geoscience…*, 2024].

3.3. Biomass energy

When it comes to assessing the potential of bioenergy resources, an important factor is the use of GIS to extract additional attributes: agricultural land area, forest area, number of livestock facilities and livestock population [*Okedu et al.*, 2024; *Ukoba et al.*, 2023]. Let us consider the characteristics needed to assess the renewable energy potential at different levels:

- meteorological data — an example of such meteorological datasets is the typical meteorological year (TMY) [*Fan*, 2022], which can be used to identify key seasonal dependencies in energy inputs;
- land use and land ownership — using these parameters it is possible to determine the areas actually available for RES implementation and those areas where it is not possible to locate any generation facilities;
- population and density data — such information allows to determine in which of the locations it is more convenient to locate generation facilities and what shares of energy they can cover in real conditions;
- data on energy and transmission infrastructure.

For example, tools such as Bioenergy Simulator [*IRENA*, 2025] can be used to assess bioenergy resources to determine the primary potential of bioenergy resources for a selected area.

3.4. Small hydropower

When assessing small hydropower potential, there is a lack of baseline datasets, so either hydropower distribution atlases have to be used or measurements have to be made independently. There are therefore two approaches to data collection:

- data modeling — obtaining sets of parameters to be studied using various models (empirical, semi-empirical);
- data measurement — obtaining the necessary parameters to assess the potential at a particular location using meteorological equipment and other measuring tools [*Buchatskiy et al.*, 2020].

The second approach is a more accurate tool for obtaining data, although it requires certain costs and time to accumulate the necessary data set. In order to collect data, metering equipment must be installed directly on the generation system being operated, and the configuration of the metering equipment will be highly dependent on the type of hydroelectric plant used. For power generation on small streams, small plants are most suitable, but off-the-shelf solutions often use a large elevation difference [*Berrada et al.*, 2019] to provide the necessary pressure level, which is not always feasible in the field and available terrain conditions, so the best solution was the realization of an in-house prototype generating device that can be used to study the flow patterns of small mountain streams. To be able to assess the potential of small hydropower, the authors developed an autonomous complex for collecting the parameters of microhydropower plant operation for use in the conditions of mountainous regions [*Onishchenko et al.*, 2024]. As a result, the complex allows for the offline collection of microhydropower plant operation characteristics:

- the flow rate of the river;
- the generated voltage at the generator and the solar panel used;
- the current consumed by the load (generator and solar panel);
- ambient air temperature and humidity.

A view of the parameter acquisition device for microhydropower estimation is shown in Figure 3.

Figure 3. Autonomous installation for collecting microhydropower parameters.

4. Conclusion

The paper considers aspects of applying data from various sources in renewable energy assessment and decision-making, considers the main parameters for the main types of RES and identifies tools that allow to extract these data. As a result, it is possible to form the following approach, presented in Figure 4 [*Cox et al.*, 2018], describing the main stages of data utilization in the field of green energy.

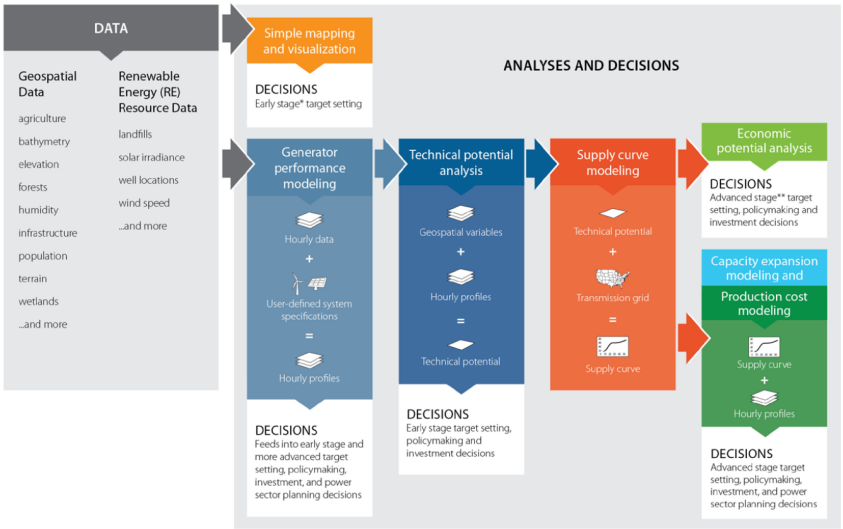

Figure 4. The relationship between geospatial data, analysis, and decision-making in renewable energy generation [*Cox et al.*, 2018].

Aspects of data acquisition in case of their absence in open sources are also considered, and an example of a complex for collecting microhydropower parameters developed by the authors is given. Extracted data from open sources, or synthetic data obtained with the help of various models can be successfully used to assess the theoretical and technical potential of the studied type of "green" energy, while the data obtained from real measurement complexes can be used to build forecast values of energy generation volumes.

References

Ahmed S., Ali A., D'Angola A. A Review of Renewable Energy Communities: Concepts, Scope, Progress, Challenges, and Recommendations // Sustainability. — 2024. — Vol. 16, no. 5. — P. 174–179. — DOI: 10.3390/su16051749.

Arabzadeh V., Frank R. Creating a renewable energy-powered energy system: Extreme scenarios and novel solutions for large-scale renewable power integration // Applied Energy. — 2024. — Vol. 374. — DOI: 10.1016/j.apenergy.2024.124088.

Awogbemi O., Kallon D. V. V. Towards the development of underutilized renewable energy resources in achieving carbon neutrality // Fuel Communications. — 2023. — Vol. 17. — DOI: 10.1016/j.jfueco.2023.100099.

Berrada A., Bouhssine Z., Arechkik A. Optimisation and economic modeling of micro hydropower plant integrated in water distribution system // Journal of Cleaner Production. — 2019. — Vol. 232. — P. 877–887. — DOI: 10.1016/j.jclepro.2019.06.036.

Buchatskiy P. Y., Teploukhov S. V., Onishchenko S. V. Software and Hardware Complex for Evaluating the Potential of Wind and Solar Energy // 2020 International Conference on Industrial Engineering, Applications and Manufacturing (ICIEAM). — IEEE, 2020. — P. 1–5. — DOI: 10.1109/icieam48468.2020.9112028.

Buchatskiy P. Y., Onishchenko S. V., Teploukhov S. V., et al. Modeling of Geothermal Heating System for an Individual Heating Station // 2023 7th International Conference on Information, Control, and Communication Technologies (ICCT). — IEEE, 2023. — P. 1–5. — DOI: 10.1109/icct58878.2023.10347126.

Buchatskiy P. Y., Teploukhov S. V., Onishchenko S. V. Geospatial Data in the Design of an Intelligent Information and Analytics System for Renewable Energy // 2024 International Conference on Information Processes and Systems Development and Quality Assurance (IPS). — IEEE, 2024. — P. 7–11. — DOI: 10.1109/ips62349.2024.10499552.

Cox S. L., Lopez A. J., Watson A. C., et al. Renewable Energy Data, Analysis, and Decisions: A Guide for Practitioners. — National Renewable Energy Laboratory, United States Agency for International Development, 2018.

Fan X. A method for the generation of typical meteorological year data using ensemble empirical mode decomposition for different climates of China and performance comparison analysis // Energy. — 2022. — Vol. 240. — DOI: 10.1016/j.energy.2021.122822.

Gaur A. S., Fitiwi D. Z., Curtis J. Heat pumps and our low-carbon future: A comprehensive review // Energy Research & Social Science. — 2021. — Vol. 71. — DOI: 10.1016/j.erss.2020.101764.

Geothermal Potential. — U.S. Energy Atlas. — URL: https://atlas.eia.gov/datasets/6515281935cc4cc1afdd585358d0aee3_0/explore?location=27.522590%2C-76.423938%2C4.76 (visited on 09/17/2024).

Global Wind Atlas. — WAsP, 2024. — URL: https://globalwindatlas.info/en (visited on 09/17/2024).

IRENA. Bioenergy Simulator. — 2025. — URL: https://biosimulator.irena.org/ (visited on 03/14/2025).

Nkinyam C. M., Ujah C. O., Asadu C. O., et al. Exploring geothermal energy as a sustainable source of energy: A systemic review // Unconventional Resources. — 2025. — Vol. 6. — DOI: 10.1016/j.uncres.2025.100149.

Okedu K. E., Oyinna B. C., Diemuodeke E. O., et al. Multicriteria GIS-based assessment of biomass energy and hydropower potentials in Nigeria // Measurement: Sensors. — 2024. — Vol. 33. — DOI: 10.1016/j.measen.2024.101243.

Onishchenko S. V., Mamiy A. R., Yurkaev K. A. Development of Hardware Module for Collecting Parameters of Micro-hydroelectric Power Plant Operation in Mountainous Conditions // 2024 International Conference on Industrial Engineering, Applications and Manufacturing (ICIEAM). — IEEE, 2024. — P. 245–249. — DOI: 10.1109/icieam60818.2024.10553856.

Open Geoscience Computing Repository. — URL: https://github.com/yohanesnuwara/open-geoscience-repository#google-drive-public-geoscience-data (visited on 09/17/2024).

Photovoltaic Geographical Information System (PVGIS). — European Commission. — URL: https://re.jrc.ec.europa.eu/pvg_tools/en (visited on 09/15/2024).

Sher F., Smječanin N., Hrnjić H., et al. Prospects of renewable energy potentials and development in Bosnia and Herzegovina – A review // Renewable and Sustainable Energy Reviews. — 2024. — Vol. 189. — DOI: 10.1016/j.rser.2023.113929.

Simankov V. S., Buchatskiy P. Y., Teploukhov S. V., et al. Designing an Intelligent Information and Analytical System for Evaluating Solutions in Renewable Energy Based on Digital Twins // 2023 Seminar on Information Systems Theory and Practice (ISTP). — IEEE, 2023a. — P. 85–88. — DOI: 10.1109/istp60767.2023.10426987.

Simankov V., Buchatskiy P., Onishchenko S., et al. Review of Models for Estimating and Predicting the Amount of Energy Produced by Solar Energy Systems // Russian Journal of Earth Sciences. — 2023b. — P. 1–17. — DOI: 10.2205/2023es02si01.

Simankov V., Buchatskiy P., Kazak A., et al. A Solar and Wind Energy Evaluation Methodology Using Artificial Intelligence Technologies // Energies. — 2024. — Vol. 17, no. 2. — DOI: 10.3390/en17020416.

Ukoba M., *Diemuodeke E.*, *Briggs T.*, *et al.* Geographic information systems (GIS) approach for assessing the biomass energy potential and identification of appropriate biomass conversion technologies in Nigeria // Biomass and Bioenergy. — 2023. — Vol. 170. — DOI: 10.1016/j.biombioe.2023.106726.

Zhang X., *Zhang Y.*, *Li Y.*, *et al.* Geothermal Spatial Potential and Distribution Assessment Using a Hierarchical Structure Model Combining GIS, Remote Sensing, and Geophysical Techniques—A Case Study of Dali's Eryuan Area // Energies. — 2023. — Vol. 16, no. 18. — DOI: 10.3390/en16186530.

Russian Journal of Earth Sciences

Special Issue: "Data Science, Geoinformatics and Systems Analysis in Geosciences"

Method for Detection of Forbush Effects in Cosmic Ray Flux According to Neutron Monitors Data Using Wavelet Transform

O. V. Mandrikova[1], **B. S. Mandrikova**[1]

[1]Institute of Cosmophysical Research and Radio Wave Propagation, FEB RAS, Paratunka, Kamchatka, Russia
* **Correspondence to:** Oksana Mandrikova, oksanam1@mail.ru

Abstract: The method developed by the authors for detection of Forbush effects in cosmic ray variations based on ground data of neutron monitors is presented. The method is based on the synthesis of the classical theory of risks with nonlinear approximating schemes in wavelet bases. The basis of the method are the rules composed by the authors. Numerical realization of the developed rules makes it possible to obtain a solution close to optimal without pre-training in near real-time mode. On the example of periods of extreme magnetic storms in 2024, method results confirming its efficiency are illustrated. General anomalous dynamics of the cosmic ray flux is distinguished. Anomalous changes, preceding the beginnings of the events under analysis, were discovered. The observed correlation with the changes of interplanetary environment parameters indicates the reliability of the obrained results.

Keywords: data analysis method, cosmic rays, neutron monitor data, Forbush effects, magnetic storms.

Citation: Mandrikova, O. V., and B. S. Mandrikova (2025), Method for Detection of Forbush Effects in Cosmic Ray Flux According to Neutron Monitors Data Using Wavelet Transform, *Russian Journal of Earth Sciences*, 25, ES2019, EDN: MSLQEP, https://doi.org/10.2205/2025ES000978

1. Introduction

To this date, investigations of cosmic rays are of interest both for astrophysical researches and for applied fields associated with space weather problems [*Kuznetsov*, 2014; *Rycroft*, 2007]. Solar activity and its sporadic manifestations (flares, coronal mass ejections, shock waves) are the main sources of space weather, which determine power outage, radio communication noise, failures in satellite, aviation and navigation systems up to catastrophic faults [*Kuznetsov*, 2014; *Rycroft*, 2007]. As advanced technical systems develop, methods and tools capable of analyzing cosmic ray variations in real-time and with the required accuracy and preventing their negative consequences are becoming increasingly relevant and in demand [*Rycroft*, 2007].

At present time, cosmic ray variations are analyzed by the scientists of different countries in related disciplines. Mew methods are created and current methods are developed for obtaining the main characteristics of cosmic ray variations [*Getmanov et al.*, 2023; 2024; *Kovylyaeva et al.*, 2019; *Krymsky et al.*, 1966; *Lukovenkova et al.*, 2018]. The known Global Survey Method (GSM), which was suggested by the Russian scientists in 60-s of the last century for the first time [*Krymsky et al.*, 1966], has been successfully developed by the research group [*Belov et al.*, 2018] up to the present. The GSM is applied to estimate the anisotropy of galactic cosmic rays and, as a sequence, to predict geomagnetic disturbances. However, this method is efficient not for all kinds of anomalies in cosmic rays (for example, proton increase beginning), and it does not provide real-time results due to the complexity of estimations. The applied threshold algorithms [*Real-Time Database…*, 2024] are insensitive to small-amplitude anomalies that significantly decreases their efficiency. It was illustrated in a number of papers [*Kalashev et al.*, 2020; *Mandrikova et al.*, 2015] that

Research Article

Received: 15 November 2024
Accepted: 15 April 2025
Published: 23 May 2025

application of current methods of artificial intelligence, based on neural networks, makes it possible to detect anomalies in cosmic rays in near real-time mode and with adequate accuracy. However, the efficiency of this approach depend on data training samplings and decreases significantly when natural process properties change that is inevitable. The investigations [*Borog et al.*, 2011; *Mallat*, 1999; *Mandrikova et al.*, 2024; *Mandrikova*, 2024; *Zhu et al.*, 2015] showed that the wavelet transform apparatus allows one to solve the problem of significant nonsationarity of data in a number of cases. For example, in the paper [*Zhu et al.*, 2015], successful application of wavelet analysis of cosmic ray flux for geomagnetic storm prediction was shown. The paper [*Borog et al.*, 2011] presents application of spectral-singular decomposition and wavelet transform for identification of galactic cosmic ray flux variations associated with interplanetary magnetic field disturbances.

This paper presents the automated method developed by the authors for detection of Forbush effects in cosmic ray variations. The method is based on the synthesis of the classical theory of risks with nonlinear approximating schemes in wavelet bases. Numerical realization of the method allows us to obtain a solution close to optimal one in near real-time mode. The advantage of the proposed method, in contrast to its analogues, is the absence of a training procedure. This allows the method to be used with limited data sets. In addition, the built-in adaptation mechanism, according to the developed rules, does not require periodic adjustment of the method parameters due to the continuous variability of natural data (changes associated with the level of solar activity, seasonal variations, etc.). Another important advantage of the method is its ability to suppress interference based on the construction of a tree of wavelet packets and the use of threshold functions. This advantage allows us not to use a preliminary data processing procedure, which reduces the methodological and computational complexity of the calculations performed. In order to be able to detect different types of structures in neutron monitor data, the paper proposes to use a superposition of discrete wavelet transform and nonlinear adaptive schemes in the dictionary of wavelet packets. It is known [*Mallat*, 1999] that wavelet packets have the best frequency-time resolution. On the example of extreme magnetic storms in 2024, the method results are presented. They confirm its efficiency.

2. Method description

The recorded time series of data can be represented as

$$f(t) = \sum_{m,n} p_{m,n}\Psi_{m,n}(t) + R(t) + \epsilon(t) = A(t) + e(t), \tag{1}$$

where the component $A(t) = \sum_m \sum_n p_{m,n}\Psi_{m,n}(t)$ describes anomalous changes in data and is the informative component, the component $R(t)$ describes regular variations in data, the component $\epsilon(t)$ is noise; among the agreed notations, the component $e(t) = R(t)+\epsilon(t)$ is noise, the informative component $A(t)$ is determined by the basic functions: $\Psi = \{\Psi_{m,n}\}_{(m,n)\epsilon Z^2}$ is the wavelet basis, $\Psi_{m,n}(t) = 2^{\frac{m}{2}}\Psi(2^m t - n)$, $p_{m,n} = \langle f, \Psi_{m,n}\rangle$ are the coefficients, m is the scale parameter, n is the time parameter.

The problem of detection of anomalous changes, according to representation (1), is reduced to the problem of estimation of the component $\hat{A}(t)$ in the model. The recorded data are considered as the ones generated by time-changing random process. Due to the variety of anomalies, distribution of the component $A(t)$ probabilities is evidently typical. Then, as it was shown in the papers [*Mallat*, 1999; *Mandrikova*, 2024], to estimate $\hat{A}(t)$, nonlinear approximation is effective. Here the approximating vectors are determined adaptively to the structure of recorded input data. From the results of the papers [*Mandrikova et al.*, 2021; 2024], in this case, *nonlinear approximating schemes* in orthonormal wavelet basis are effective that agrees well with representation (1).

Considering wavelets as Ψ functions according to (1), we obtain a nonlinear approximating scheme of the following form from the results [*Mandrikova*, 2024] to estimate $\hat{A}(t)$

$$\hat{A}(t) = \sum_{(m,n)\in I_B} p_{m,n}\Psi_{m,n}, \tag{2}$$

where I_B is the set of indexes $p_{m,n}$, having the highest amplitudes $\left|\left\langle f, \Psi_{m,n}\right\rangle\right|$. The error of such an estimate is

$$\varepsilon\left[I_B\right] = \left\|f(t) - \tilde{f}_{I_B}(t)\right\|^2 = \sum_{(m,n)\notin I_B} \left|\left\langle f, \Psi_{m,n}\right\rangle\right|^2. \tag{3}$$

From the other side, as long as the nonlinear approximating scheme is expressed through the threshold function $\Pi_{T_{m,n}}(\cdot)$ [*Mandrikova et al.*, 2024], we have

$$\hat{A}(t) = \sum_m \sum_n \Pi_{T_{m,n}}\left(\left\langle f, \Psi_{m,n}\right\rangle\right)\Psi_{m,n}(t), \Pi_{T_{m,n}}\left(\left\langle f, \Psi_{m,n}\right\rangle\right) = \begin{cases} \left\langle f, \Psi_{m,n}\right\rangle, if \left|\left\langle f, \Psi_{m,n}\right\rangle\right| \geq T_{m,n} \\ 0, if \left|\left\langle f, \Psi_{m,n}\right\rangle\right| < T_{m,n} \end{cases}. \tag{4}$$

Based on the accepted ratio (4), we introduce the following *rule 1: we will consider that the data $f(t)$ contain anomalous changes on the scale m at the time moment $t = n$, if amplitudes of the coefficients $p_{m,n} = \left|\left\langle f(t), \Psi_{m,n}(t)\right\rangle\right|$ exceed the threshold $T_{m,n}$ on the scale m at the time moment $t = n$.*

We should note that the guarantee of the presence of anomalous changes in data, according to (4) is provided by the amplitude $\left|\left\langle f, \Psi_{m,n}\right\rangle\right|$ limitation by the lower boundary (the thresholds $T_{m,n}$). To optimize the estimates of $\hat{A}(t)$, following the paper [*Mandrikova et al.*, 2024], when determining the thresholds, we use the *likelihood ratio* [*Levin*, 1989] and introduce the following *rule 2: anomalous changes on the scale m at the time moment $t = n$, if*

$$\frac{\Pi\left(\left|p_{m,n}\right| \left|\Gamma_1\right.\right)}{\Pi\left(\left|p_{m,n}\right| \left|\Gamma_0\right.\right)} \geq T_{\alpha,m,n},$$

where $\Pi\left(\left|p_{m,n}\right| \left|\Gamma_0\right.\right)$ and $\Pi\left(\left|p_{m,n}\right| \left|\Gamma_1\right.\right)$ are the probability densities $\left|p_{m,n}\right|$, Γ_0 is the zero hypothesis, Γ_1 is the alternative, the threshold $T_{\alpha,m,n} = h_\alpha * \hat{\sigma}_{m,n}$ is estimated in the vicinity of (m, n) with respect to Neumann-Pearson criterion from the condition $\int_A W\left(\left|p_{m,n}\right| \left|\Gamma_0\right.\right) d\left|p_{m,n}\right| = \alpha$, α is the first-kind error.

Using the *rule 2*, we detect anomalous changes in data according to the following *rule 3:*

Step 1. Basis $B_{l,m} = \{\Psi^l_{m,n}\}_{n\in N}$ of wavelet packet space B^l_m: $B_{l,m} = B^{2l}_{m+1} \oplus B^{2l+1}_{m+1}$ is the basis

$$B_{l,m} = \begin{cases} \Psi^l_{m,n}, if\, O\left(c^l_{m,n}\right) + O\left(c^{2l}_{m+1,n}\right) \geq O\left(c^{2l+1}_{m+1,n}\right), \\ \Psi^{2l}_{m+1,n} \cup \Psi^{2l+1}_{m+1,n}, if\, O\left(c^l_{m,n}\right) + O\left(c^{2l}_{m+1,n}\right) < O\left(c^{2l+1}_{m+1,n}\right), \end{cases}$$

where $O\left(c^{cl+k}_{m+k,n}\right) = \sum_{n\in I^{cl+1}} \left|c^{cl+1}_{m+k,n}\right|^2$, $c^l_{m,n} \in I^{cl} : \left|c^l_{m,n}\right| \geq T^l_{m,n}$, $T^l_{m,n} = k_\alpha * \sigma^l_{m,n}$.

Step 2. Error $B_{l,m}$ is $\varepsilon_{B_{l,m}} = \left\|f(t) - \tilde{f}_{I_B}(t)\right\|^2$ (see (3)).

Step 3. The best basis for $\hat{A}(t)$ is $R_{B_{best}} = \min_{B_{l,m}\in \mathrm{B}} \varepsilon_{B_{l,m}}$, B is the set of wavelet bases.

A fragment of the wavelet packet tree and *rule 3* elements are illustrated in Figure 1.

As an example, Figure 2 shows the numerical results of Step 1 and Step 2, performed according to the proposed rule 2. The wavelet packet tree was constructed for the data of the Inuvik st. neutron monitor. The numbers in the tree nodes show the estimated values of the function $B_{l,m}$. The nodes determined on the basis of rule 2 are marked in green.

As an example, Figure 3 shows the results of the proposed Forbush effect detection method performed for different threshold values (formula (4)). The calculations were performed using Oulu st. data for the period containing the geomagnetic storm (October 10, 2024). According to the proposed rule 1, the best threshold is determined, which

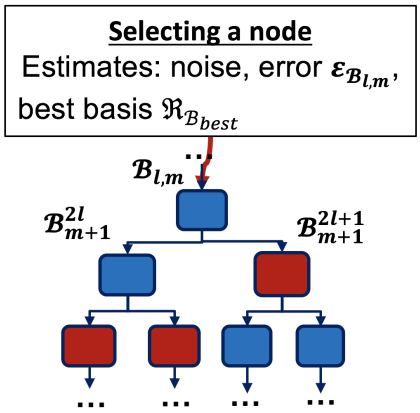

Figure 1. Fragment of the wavelet packet tree and the rule elements.

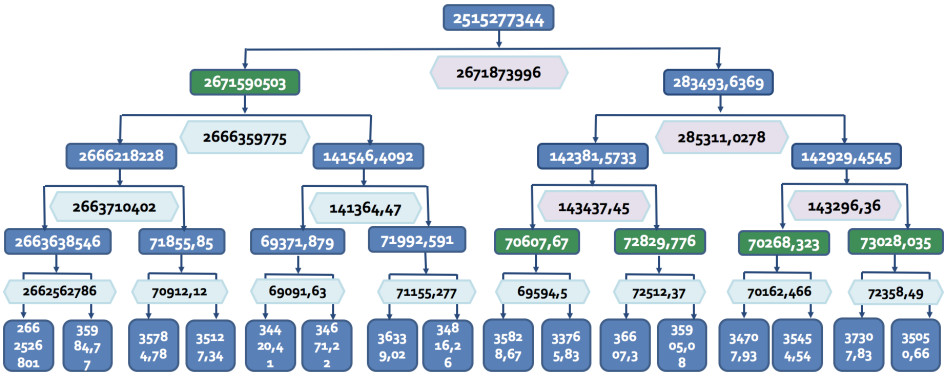

Figure 2. Wavelet packet tree.

minimizes the error in detecting Forbush effects shown in Figure 3d. The results with the best thresholds for the data from different stations are shown in Figure 5. Analysis of the results in Figure 3 shows that the best threshold allows suppressing the correlated noise associated with the daily variation of neutron monitor data. The results obtained confirm the importance of determining the best threshold in the process of implementing the method calculations and indicate the effectiveness of rule 1.

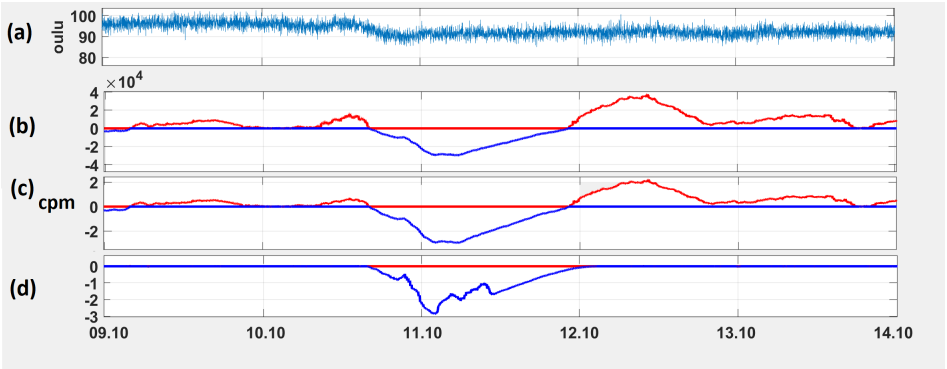

Figure 3. Neutron monitor data processing results.

3. Results and discussion

Neutron monitor data (www.nmdb.eu) and information on the parameters of the interplanetary environment and magnetosphere (ckp.gcras.ru, ipg.geospace.ru, spaceweather.izmiran.ru) was used in the investigation. Figure 4 shows the results of the developed method during the extreme magnetic storm on 10–11 May 2024. The near-Earth space state was calm before the magnetic storm on 8–9 May (ipg.geospace.ru). Based on the method results

(Figure 4 (c), (d)), cosmic ray (CR) intensity was within the background during the second half of the day on 9 May. Then, from the beginning of the day on 10 May, sudden anomalous increase of CR intensity occurred according to the data of all the stations under analysis. It lasted for about a day (indicated with red in Figure 4 (c), (d)). During the anomalous increase on 10 May, inhomogeneous accelerated fluxes from coronal mass ejection arrived at 16:00 UT and 22:00 UT, IMF fluctuations increased to Bz = −50 nT, solar wind velocity (SWV) grew to 790 km/s (ipg.geospace.ru). At the end of the day on 10 May, an extreme magnetic storm occurred. The time of the storm commencement is indicated by a vertical red line in Figure 4. The storm initial phase was accompanied by anomalous decrease in CR intensity. Deep Forbush decrease appeared (indicated with blue in Figure 3 (c), (d)). The next day, on 11 May, an inhomogeneous accelerated flux from a coronal whole and coronal mass ejection arrived at 10:00 UT, the SWV reached 1000 km/s (ipg.geospace.ru). CR variation intensity during that period decreased again. Based on the data of the stations under analysis, it took more than two days for the characteristic level of CR variations to recover (Figure 4 (d)). The distinguished general dynamics of CR confirms the reliability of the method results. Anomalous changes in CR flux variations agree with the results of other researchers [*Badruddin et al.*, 2019; *Belov et al.*, 2018; *Dorman*, 2005], confirm the importance of CR investigation and indicate the necessity of development of the methods for their analysis and extension of the observation network.

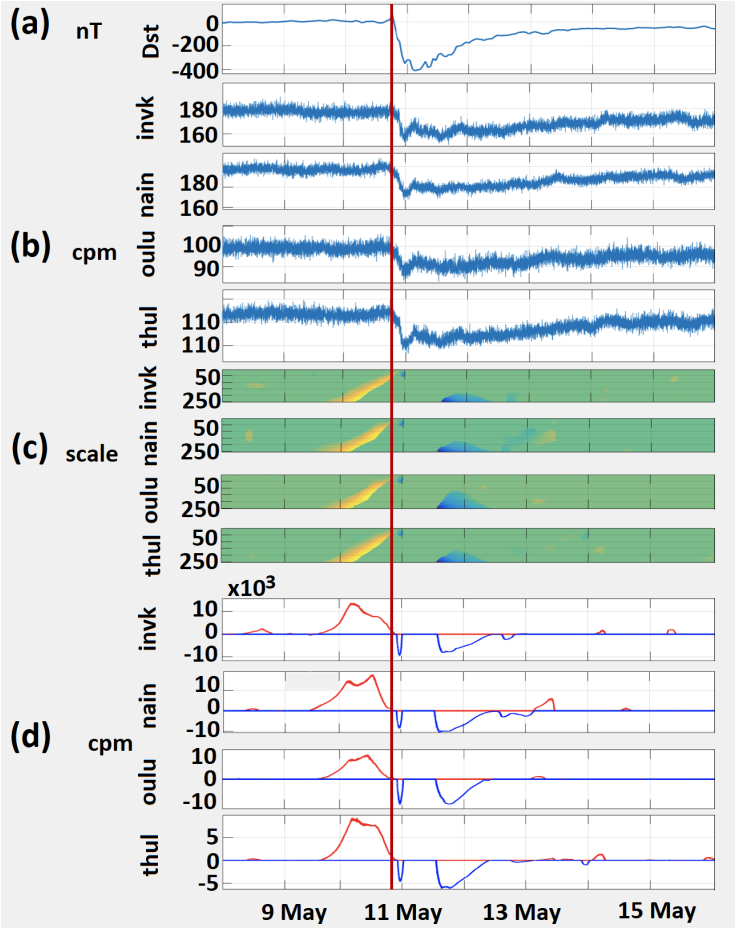

Figure 4. Neutron monitor data processing results.

Figure 5 illustrates the method results during the extreme magnetic storm on 10–11 October 2024. The magnetic field was unstable before the event. At the beginning of the day on 9 October, a moderate magnetic storm occurred (ipg.geospace.ru). The inhomogeneous accelerated flux from a coronal whole and coronal mass ejection (CME on 9 October) arrived at 14:00 UT on 10 October, IMF fluctuations were intensified to Bz = −46 nT, the SWV

reached 760 km/s by 16:00 UT (ipg.geospace.ru). Based on the results of Sopo and Tule stations, a short-term weak increase of CR variation intensity occurred during the flux arrival (indicated with red in Figure 5 (l), (m)). During the initial phase of the storm, CR variation intensity decreased (Figure 5 (f)–(m)) and remained anomalously decreased during the main and the recovery phases. The Forbush decrease reached the maximum amplitude during the strongest geomagnetic disturbances (Figure 5 (j)–(m)). Then the SWV was within 760–650 km/s, IMF component fluctuated from Bz = −30 nT to Bz = +19 nT (ipg.geospace.ru). At the end of the day on 12 October, the SWV began to decrease and by the end of the period it reached 400 km/s. During this period, the CR variation level recovered (Figure 5 (f)–(m)).

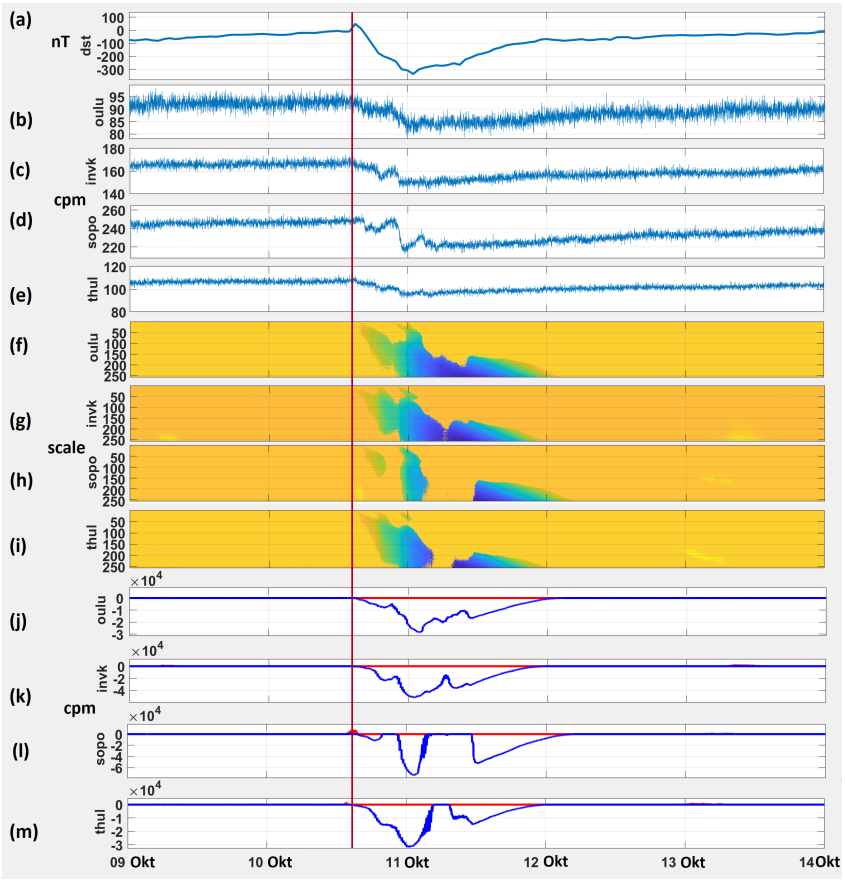

Figure 5. Neutron monitor data processing results.

The results of the method evaluation, performed using real data from neutron monitors (www.nmdb.eu), are presented in Table 1.

Table 1. Results of the effectiveness of the method.

Period	Number of Forbush effects	Results of algorithms (probability of detecting Forbush effects)
2013–2015 (high Solar activity)	285	Detected: 0.86 Not detected: 0.14 (probability of missing target) False alarm: 0.13
2019–2020 (low Solar activity)	174	Detected: 0.88 Not detected: 0.12 (probability of missing target) False alarm: 0.11
2023–2025 (high Solar activity)	127	Detected: 0.89 Not detected: 0.11 (probability of missing target) False alarm: 0.14

4. Conclusions

The results of the work confirmed the efficiency of the proposed method for the task of detecting Forbush effects based on neutron monitor data. Estimates based on real data showed:

- the probability of detecting Forbush effects for periods of high solar activity is ~0.87, with a target miss probability of ~0.12;
- the probability of detecting Forbush effects for periods of low solar activity is ~0.88, with a target miss probability of ~0.12.

Due to the absence of a training procedure, the method can be applied to limited data sets. The built-in adaptation mechanism, according to the developed rules, also does not require the procedure for periodic adjustment of the method parameters due to the continuous variability of natural data (changes associated with the level of solar activity, seasonal variations, etc.). In addition, the use of adaptive thresholds, when constructing a nonlinear approximating scheme, makes it possible to suppress interference and avoid the procedure of preliminary data processing.

The presented results show the necessity of taking into account the cosmic ray data when predicting space weather. On the example of the event on 10–11 October 2024, we have confirmed the impotence of development of real-time methods for data analysis, providing timely alarm notification on the beginning of a magnetic storm, and extension of observation network. The detected general dynamics in CR flux and the correlation with the parameter changes in interplanetary environment and magnetosphere as well as correspondence of the results to the data of other investigations [*Badruddin et al.*, 2019; *Belov et al.*, 2018; *Dorman*, 2005] indicate the reliability of the obtained results and confirm the suggested method efficiency.

Acknowledgments. The work was supported by the State Task of IKIR FEB RAS (No. 124012300245-2).

References

Badruddin B., Aslam O. P. M., Derouich M., et al. Forbush Decreases and Geomagnetic Storms During a Highly Disturbed Solar and Interplanetary Period, 4–10 September 2017 // Space Weather. — 2019. — Vol. 17, no. 3. — P. 487–496. — DOI: 10.1029/2018sw001941.

Belov A. V., Eroshenko E. A., Yanke V. G., et al. Global Survey Method for the World Network of Neutron Monitors // Geomagnetism and Aeronomy. — 2018. — Vol. 58, no. 3. — P. 356–372. — DOI: 10.1134/S0016793218030039.

Borog V. V., *Kryanev A. V.*, *Udumyan D. K.* Combined method for detecting hidden anomalies in galactic cosmic ray variations // Geomagnetism and Aeronomy. — 2011. — Vol. 51, no. 4. — P. 475–482. — DOI: 10.1134/s0016793211040086.

Dorman L. I. Space weather and dangerous phenomena on the Earth: principles of great geomagnetic storms forcasting by online cosmic ray data // Annales Geophysicae. — 2005. — Vol. 23, no. 9. — P. 2997–3002. — DOI: 10.5194/angeo-23-2997-2005.

Getmanov V. G., *Gvishiani A. D.*, *Soloviev A. A.* Methods of digital processing of matrix time series of observations of muon fluxes for geophysical research. — Moscow : RAS, 2023. — 184 p. — (In Russian).

Getmanov V. G., *Gvishiani A. D.*, *Soloviev A. A.*, *et al.* Recognition of geomagnetic storms from time series of matrix observations with the muon hodoscope URAGAN using neural networks of deep learning // Solar-Terrestrial Physics. — 2024. — Vol. 10, issue 1, no. 1. — P. 76–83. — DOI: 10.12737/stp-101202411.

Kalashev O., *Pshirkov M.*, *Zotov M.* Identifying nearby sources of ultra-high-energy cosmic rays with deep learning // Journal of Cosmology and Astroparticle Physics. — 2020. — No. 11. — DOI: 10.1088/1475-7516/2020/11/005.

Kovylyaeva A. A., *Astapov I. I.*, *Barbashina N. S.*, *et al.* Investigating Characteristics of Forbush Effects Recorded by the URAGAN Muon Hodoscope in the Period 2012–2017 // Bulletin of the Russian Academy of Sciences: Physics. — 2019. — Vol. 83, no. 5. — P. 563–565. — DOI: 10.3103/s1062873819050174. — (In Russian).

Krymsky G. F., *Altukhov A. M.*, *Kuzmin A. I.* — Moscow : New method for studying the anisotropy of cosmic rays. Research on geomagnetism, aeronomy, 1966. — 105 p. — (In Russian).

Kuznetsov V. D. Space weather and risks of space activity // Space technique and technologies. — 2014. — Vol. 3. — P. 3–13. — EDN: TEMDOH. (In Russian).

Levin B. R. Theoretical Foundations of Statistical Radio Engineering. — Moscow, Russia : Radio i Svyaz', 1989. — (In Russian).

Lukovenkova O. O., *V. M. Y.*, *Tristanov A. B.*, *et al.* Optimization of adaptive matching pursuit method to analyze geoacoustic emission signals // Vestnik KRAUNC. Fiziko-matematiceskie nauki. — 2018. — Vol. 24, no. 4. — P. 197–207. — DOI: 10.18454/2079-6641-2018-24-4-197-207.

Mallat S. A Wavelet Tour of Signal Processing. — London, UK : Academic Press, 1999. — 620 p.

Mandrikova O., *Zalyaev T.* Modeling of cosmic ray variations based on combining multiscale wavelet decompositions and variable structure neural networks // Digital signal processing. — 2015. — Vol. 1. — P. 11–16. — EDN: TSNQIP. (In Russian).

Mandrikova O., *Mandrikova B.* Method of Wavelet-Decomposition to Research Cosmic Ray Variations: Application in Space Weather // Symmetry. — 2021. — Vol. 13, no. 12. — DOI: 10.3390/sym13122313.

Mandrikova O., *Mandrikova B.* Hybrid Model of Natural Time Series with Neural Network Component and Adaptive Nonlinear Scheme: Application for Anomaly Detection // Mathematics. — 2024. — Vol. 12, no. 7. — P. 1079. — DOI: 10.3390/math12071079.

Mandrikova O. Intelligent methods for natural data analysis: application to space weather // Computer Optics. — 2024. — Vol. 48, no. 1. — P. 139–148. — DOI: 10.18287/2412-6179-CO-1367.

Real-Time Database for high-resolution Neutron Monitor measurements / NMDB: the Neutron Monitor Database. — URL: https://www.nmdb.eu (visited on 11/11/2024).

Rycroft M. J. J.Lilensten (ed.), Space weather: research towards applications in Europe, Astrophysics and space science library. Book Review // Surveys in Geophysics. — 2007. — Vol. 28, no. 1. — P. 115–116. — DOI: 10.1007/s10712-007-9015-x.

Zhu X.-L., *Xue B.-S.*, *Cheng G.-S.*, *et al.* Application of wavelet analysis of cosmic ray in prediction of great geomagnetic storms // Chinese Journal of Geophysics (Acta Geophysica Sinica). — 2015. — Vol. 58. — P. 2242–2249. — DOI: 10.6038/cjg20150703.

Russian Journal of Earth Sciences

Special Issue: "Data Science, Geoinformatics and Systems Analysis in Geosciences"

Estimation of Parameters of Non-stationary Geophysical Signals Based on Two-Stage Approximations Using Local Models

V. G. Getmanov[1,2], A. D. Gvishiani[1,2], V. A. Pilipenko[1,2], D. A. Stukov[2]

[1]Geophysical Center of the Russian Academy of Sciences, Moscow, Russia
[2]Schmidt Institute of Physics of the Earth, Moscow, Russia
* **Correspondence to:** Victor Getmanov, vgetm2015@yandex.ru

Abstract: The authors have developed a technology for estimating the parameters of non-stationary geophysical signals, using a two-stage approximation with local approximation models at the first stage and weighted averaging at the second stage. This article considered an example of estimating the amplitude, frequency and trend parametric functions for geomagnetic pulsations Pc1.

Keywords: geophysical signals, geomagnetic pulsations, estimation, non-stationary parameters, two-stage approximation.

Citation: Getmanov, V. G., A. D. Gvishiani, V. A. Pilipenko, and D. A. Stukov (2025), Estimation of Parameters of Non-stationary Geophysical Signals Based on Two-Stage Approximations Using Local Models, *Russian Journal of Earth Sciences*, 25, ES2020, EDN: ZWLDSR, https://doi.org/10.2205/2025ES000979

1. Introduction

Geophysical signals (geomagnetic pulsations, seismic waves, wave processes in the atmosphere, etc.) in some cases have pronounced non-stationarity. The geomagnetic pulsations considered here are quasi-periodic oscillations, characterized by non-stationary parameters. Such pulsations occupy frequency ranges from thousandths to several Hz and amplitudes from hundredths to hundreds of nT [*Klejmyonova*, 2007]. Pulsations arise due to the resonant interaction of magnetospheric plasma and the geomagnetic field.

Estimates of non-stationary parameters of geomagnetic pulsations are used for diagnostics of the magnetosphere [*Guglielmi et al.*, 1973], can be used to determine the frequencies and amplitudes of "serpentine emission" signals [*Guglielmi et al.*, 2015], to find the parameters of Alfvén signals [*Potapov et al.*, 2021], etc.

The most widely used method of signal analysis is the discrete Fourier transform (DFT) [*Le'j*, 2007], which, however, is poorly suited for non-stationary signals due to its limited resolution. The fairly common spectral-temporal analysis using the Wigner transform [*Time-Frequency Analysis: Concepts and Methods*, 2008], which is actually based on the DFT, has errors in parameter estimates of approximately the same level as the errors of the DFT. When implementing these methods, important information about the properties and characteristics of signals may be lost.

The purpose of this work is to describe the developed technology for estimating parametric functions of geomagnetic pulsations based on two-stage approximations [*Getmanov*, 2021] using local approximation models [*Katkovnik et al.*, 2006]. The proposed technology is an alternative to the DFT, due to a more accurate fit of the approximation models used, and is largely universal and suitable for non-stationary signals of many subject areas.

Research Article

Received: 15 November 2024
Accepted: 15 April 2025
Published: 23 May 2025

Functional models of non-stationary signals with parametric functions, including geomagnetic pulsation signals, are represented by the following relation

$$Y(T_i) = Y_0(p(T_i), T_i) + W(T_i) = \sum_{l=1}^{L} A_l(T_i)\cos\varphi_{0l}(T_i) + E(T_i) + W(T_i), \quad (1)$$

where $A_l(T_i)$, $f_{0l}(T_i) = \dot{\varphi}_{0l}(T_i)$, $E(T_i)$ are amplitude, frequency and trend functions, $W(T_i)$ is model noise, L is the number of possible frequency components, T is a sampling step. $Y_0(p(T_i), T_i)$ for (1) depends on the vector of parametric functions $p(T_i)$, composed of $p_j(T_i)$, $j = 1, \dots, j_0$, where j_0 is the number of components in the model

$$p(T_i)^T = (p_1(T_i), p_2(T_i), \dots, p_{j_0}(T_i)). \quad (2)$$

In particular, if the components are the amplitude, frequency and trend functions, then $j_0 = 3$. Expressions (1), (2) serve as the basis for constructing local approximation models.

2. The problem of two-stage approximation estimation of non-stationary signal parameters based on local models

At the first stage of the approximation, we represent the observations as $Y(T_i)$, $1 \le i \le N_f$. Let us introduce local intervals $N_{1s} \le i \le N_{2s}$ dimensions N, $N \ll N_f$ with the boundaries $N_{1s} = 1N(s-1)$, $N_{2s} = Ns$, $s = 1, \dots, s_0$, where $s_0 = \mathrm{ent}(N_f/N)$, $1 \le i \le N_{f1}$ and $N_{f1} = N_{s0}$, $N_{f1} \le N_f$. Let $Y_s(T_i)$ be observations for $Y(T_i)$ on local intervals. We define local approximation models [*Getmanov et al.*, 2016; 2018] by known functions $y_M(c_s, T_i)$, that depend on the parameter vectors c_s, $s = 1, \dots, s_0$, and local functionals $F(c_s, Y_s)$, and formulate the problems of local approximation of estimation c_s^0

$$F(c_s, Y_s) = \sum_{i=N_{1s}}^{N_{2s}} (Y_s(T_i) - y_M(c_s, T_i))^2,\ c_s^0 = \arg\{\min_{c_s}(F(c_s, Y_s))\},\ s = 1, \dots, s_0. \quad (3)$$

We obtain local functions on local intervals based on c_s^0 (3) local functions $p_{j,s}^0(c_s^0, T_i)$ taking into account (1), (2) for $i < N_{1s}, N_{2s>i}$ and $p_{j,s}^0(c_s^0, T_i) = 0$, $j = 1, \dots, j_0$. Let us estimate the parametric function with number j

$$p_j^0(c^0, T_i) = \sum_{s=1}^{s_0} p_{j,s}^0(c_s^0, T_i),\ j = 1, \dots, j_0. \quad (4)$$

We take the functions $p_j^0(c^0, T_i)$, $j = 1, \dots, j_0$ from (4) as the first approximations to the parametric functions $p_j(T_i)$.

At the second stage of approximation, we introduce local intervals of size equal to N_0 , sliding with a step N_d, with the boundaries $N_{1r} \le i \le N_{2r}$, where $N_{1r} = 1 + N_d(r-1)$, $N_{2r} = N_{1r} + N_0 - 1$, $r = 1, \dots, r_0$, $r_0 = \mathrm{ent}((N_{f1} - N_0)/N_d)$ and $N_{f2} = N_d(r_0 - 1) + N_0$, $N_{f2 \le N_{f1}}$. Let us define sliding models $y_M(d_{j,r}, T_i)$, and parameter vectors $d_{j,r}$. Let us form local functionals $G(d_{j,r}, p_j^0(c^0, T_i))$ and calculate estimates $d_{j,r}^0$

$$G(c^0, d_{jr}, p_j^0) = \sum_{i=N_{1r}}^{N_{2r}} (p_j^0(c^0, T_i) - y_M(d_{j,r}, T_i))^2,\ d_{j,r}^0 = \arg\{\min_{d_{j,r}}(G(d_{j,r}, p_j^0))\}. \quad (5)$$

Using $d_{j,r}^0$ (5) we find the sliding models $p_{j,r}^0(c^0, d_r^0, T_i)$, $N_{1r \le i \le N_{2r}}$, $p_{j,r}^0(c^0, d_r^0, T_i) = 0$, $i < N_{1r}, N_{2r} > i$, $r = 1, \dots, r_0$, $j = 1, \dots, j_0$ and sum them up

$$p_{0j}^0(c^0, d_j^0, T_i) = \sum_{r=1}^{r_0} p_j^0(c^0, d_{r,j}^0, T_i),\ j = 1, \dots, j_0. \quad (6)$$

The function $p^0_{0j}(c^0, d^0_j, T_i)$ is implemented as a sum with overlaps from sliding, the result (6) is averaged with weighting, as proposed in [*Getmanov et al.*, 2015]. Let us introduce unit functions, find their sum, calculate the weight function $W(T_i)$ and estimates of parametric functions

$$\begin{aligned} &W_{0r}(T_i) = 1,\ N_{1r} \le i \le N_{2r}, \\ &W_{0r}(T_i) = 0,\ 1 \le i \le N_{1r} - 1,\ N_{2r} + 1 \le i \le N_{f2}, \\ &W_{0r}(T_i) = \sum_{r=1}^{r_0} W_{0r}(T_i),\ W(T_i) = 1/W_0(T_i). \end{aligned} \tag{7}$$

$$p^0_j(c^0, d^0, T_i) = W(T_i) p^0_{0j}(c^0, d^0, T_i),\ j = 1,\ ldots, j_0. \tag{8}$$

We accept functions $p^0_j(c^0, d^0, T_i)$ based on (7), (8) as second approximations to $p_j(T_i)$ (2).

Let us make a choice of parameters N, N_0, N_d for approximation procedures. We write down the funtional $S_0(N, N_0, N_d, Y)$ and implement its optimization

$$\begin{aligned} &S_0(N, N_0, N_d, Y) = (1/N_{f2}) \sum_{i=1}^{N_{f2}} (Y(T_i) - Y(p^0(c^0(N), d^0(N, N_0, N_d), T_i))^2) \\ &(N^0, N^0_0, N^0_d) = \arg\{\min_{N, N_0, N_d} S_0(N, N_0, N_d, Y)\}. \end{aligned}$$

3. Application of local approximation piecewise sinusoidal models with piecewise linear additive trends for estimating non-stationary parameters of geomagnetic pulsations

In practice, geomagnetic pulsations can be adequately represented by local approximate piecewise sinusoidal models with linear additive trends.

For the first stage, we adopted local models $y_M(c_s, T_i)$ and functionals $F(c_s, Y_s)$

$$y_M(c_s, T_i) = a_s \cos \omega_s T_i + b_s \sin \omega_s T_i + g_{1s} + g_{2s} T_i,\ c^T_s = (a_s, b_s, g_{1s}, g_{2s}, \omega_s), \tag{9}$$

$$F(c_s, Y_s) = \sum_{i=N_{1s}}^{N_{2s}} (Y_s(T_i) - y_M(c_s, T_i))^2,\ s = 1, \ldots, s_0. \tag{10}$$

For model (9) frequency boundaries were fixed ω_n, $\omega_{\min} \le \omega_n \le \omega_{\max}$, $\omega_{\min}$, $\omega_{\max}$ partially optimal parameters were calculated $a^0_s(\omega_n)$, $b^0_s(\omega_n)$, $g^0_{1s}(\omega_n)$, $g^0_{2s}(\omega_n)$ and partially optimal sums $F(c^0_s(\omega_n), Y_s)$ (10), minimization was performed by enumeration for $\omega_n = \omega_{\min} + \Delta\omega(n-1)$, $n = 1, \ldots, n_f$, $\Delta\omega = (\omega_{\max} - \omega_{\min})/n_f$.

$$\omega^0 = \arg\{\min_{\omega_{\min} \le \omega_n \le \omega_{\max}} F(c^0_s(\omega_n), Y_s)\}. \tag{11}$$

We calculated optimal local parameters $\omega^0_s = \omega^0$, $a^0_s = a^0_s(\omega^0)$, $b^0_s = b^0_s(\omega^0)$, $g^0_{1s}(\omega^0)$, $g^0_{2s}(\omega^0)$ for (11) and evaluation of parameter functions $p^0_1(c^0, T_i) = A^0_L(T_i)$, $p^0_2(c^0, T_i) = f^0_{0L}(T_i)$, $p^0_3(c^0, T_i) = E^0_L(T_i)$, $1 \le i \le N_{f1}$,

$$\begin{aligned} &A^0_L(c^0, T_i) = \sum_{s=1}^{s_0} A^0_s(c^0_s, T_i),\ A^0_s(c^0_s, T_i) = (a^{0^2}_s + b^{0^2}_s)^{1/2},\ A^0_s(c^0_s, T_i) = 0,\ i < N_{1s},\ i > N_{2s}, \\ &f^0_{0L}(c^0, T_i) = \sum_{s=1}^{s_0} f^0_{0s}(c^0_s, T_i),\ f^0_{0s}(c^0_s, T_i) = \omega^0_{0s}/2\pi,\ f^0_{0s}(c^0_s, T_i) = 0,\ i < N_{1s},\ i > N_{2s}, \\ &E^0_L(c^0, T_i) = \sum_{s=1}^{s_0} E^0_s(c^0_s, T_i),\ E^0_s(c^0_s, T_i) = (d^0_{1s} + d^0_{2s} T_i),\ E^0_s(c^0_s, T_i) = 0,\ i < N_{1s},\ i > N_{2s}. \end{aligned} \tag{12}$$

At the second stage we used local models $y_{Mj}(d_{r,j}, T_i)$ and functionals $G_j(d_r, Y_r)$ and calculated weighted parameter estimations $p_j^0(c^0, d^0, T_i)$, $j = 1, \dots, j_0$

$$
\begin{aligned}
&y_{Mj}(d_{r,j}, T_i) = d_{1r,j} + d_{2r,j}T_i,\ d_{r,j}^T = (d_{1r,j}, d_{2r,j}),\\
&G_j(d_{r,j}, p_j^0(c^0)) = \sum_{i=N_{1r}}^{N_{2r}} (p_j^0(c^0, T_i) - d_{1r,j} - d_{2r,jT_i})^2,\ r = 1, \dots, r_0,\ d_{r,j}^0 = \arg\{\min_{d_{r,j}} G(d_{r,j}, Y_r)\},\\
&p_{0j}^0(c^0, d^0, T_i) = \sum_{r=1}^{r_0} p_j(c^0, d_{r,j}^0, T_i),\ p_j^0(c^0, d^0, T_i) = W(T_i) p_{0j}^0(c^0, d_{r,j}^0, T_i),\\
&p_1^0(c^0, d^0, T_i) = A_W^0(T_i),\ A_W^0(T_i),\ p_2^0(c^0, d^0, T_i) = f_{0W}^0(T_i),\ p_3^0(c^0, d^0, T_i) = E_W^0(T_i).
\end{aligned}
\tag{13}
$$

4. Estimation of non-stationary parameters for an experimental signal with geomagnetic pulsations

We received the observations $Y(T_i)$ nT, $i = 1, \dots, N_f$ of the experimental signal with pulsations Pc1, station PG4 (Antarctica), 17.12.2016, 14.00–16.00, $N_f = 69144$, $T = 0.1$c, $N_f T = 1.920$ h. Figure 1 shows an image $Y(T_i)$, its non-stationarity for amplitude, trend and frequency is obvious.

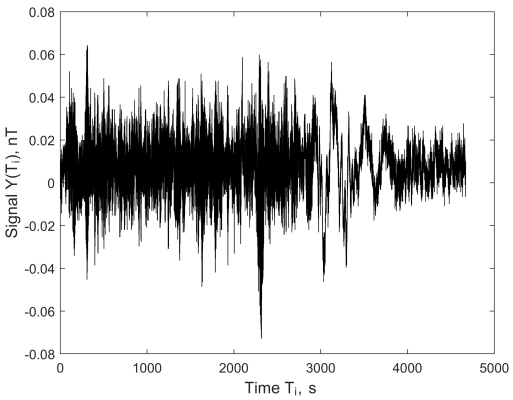

Figure 1. Experimental signal $Y(T_i)$ with pulsations Pc1; station PG4 (Antarctica), 17.12.2016, 14.00–16.00 UT.

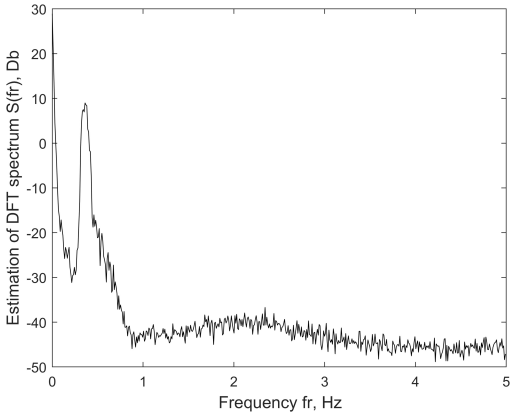

Figure 2. DFT-spectrum $S(f_k)$ for $Y(T_i)$, average frequency $\bar{f}_0 \approx 0.3$ Hz.

Figure 2 shows the DFT-spectrum graph $S(f_k) = \Delta f(k-1)$, $k = 1, \dots, N_S/2$, $N_S = 512$ is the dimension of the DFT. The average frequency of the signal and the trend are $\bar{f}_0 \approx 0.3$ Hz $\bar{f}_E \approx 0.05$ Hz.

We used the local models (9) and functionals (10). The boundaries $\bar{f}_{\min} = 0.005$, $\bar{f}_{\max} = 0.605$ Hz, $n_f = 200$ were established taking into account the DFT spectrum (Figure 2), and the model parameters were found using formulas (12), (13). The optimal parameters of the approximation procedures with ranges $N_0^0 = 2048 \div 4096$, $N_d^0 = 64 \div 128$ were determined using formulas (9), (10).

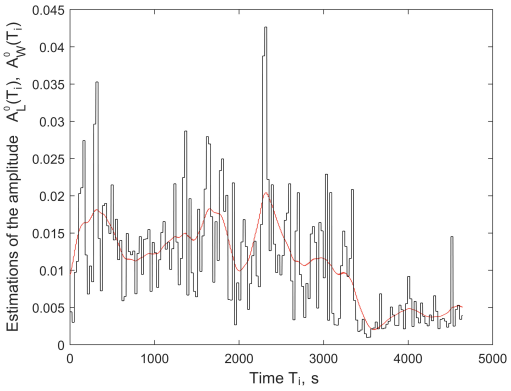

Figure 3. Amplitude estimates for the 1st and 2nd approximation stages.

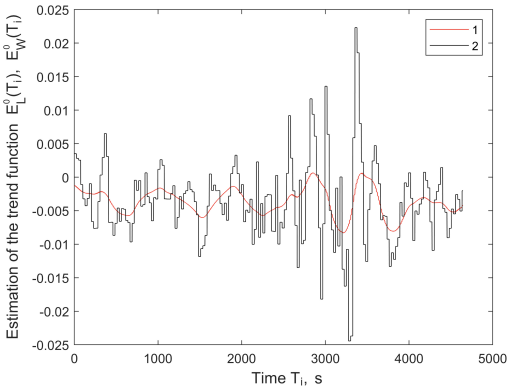

Figure 4. Trend estimates for the 1st and 2nd approximation stages.

Estimates of parametric functions were calculated for $N = 512$, $N_0 = N * 8$, $N_d = N_0/32$. Figure 3 shows amplitude estimations: 1 — $A^0_L(T_i)$, 2 — $A^0_W(T_i)$; Figure 4 shows trend estimates: 1 — $E^0_L(T_i)$, 2 — $E^0_W(T_i)$. Estimates of frequency functions were calculated. Figure 5 (for $N = 512$, $N_0 = N * 8$, $N_d = N_0/32$) and Figure 6 (for $N = 512/2$, $N_0 = N * 16$, $N_d = N_0/8$) show graphs: 1 — $f^0_{0L}(T_i)$, 2 — $f^0_{0W}(T_i)$.

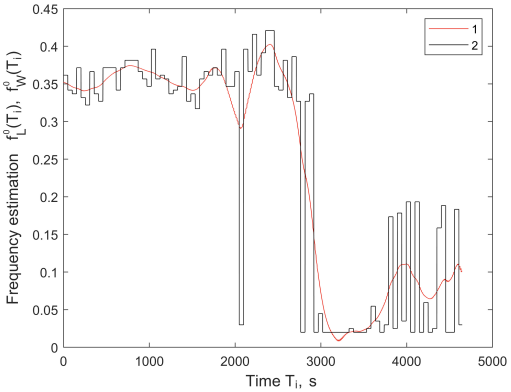

Figure 5. Frequency function estimates for the 1st and 2nd approximation stages, $N = 512$, $N_0 = N * 8$, $N_d = N_0/32$.

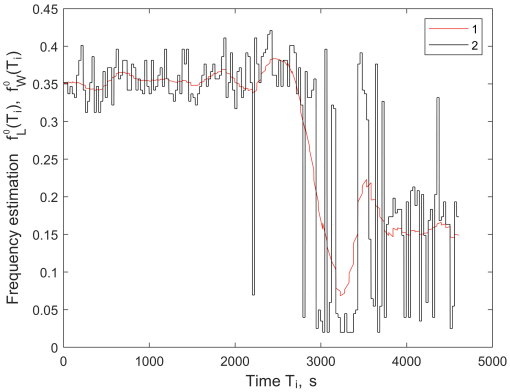

Figure 6. Frequency function estimates for the 1st and 2nd approximation stages, $N = 512/2$, $N_0 = N * 16$, $N_d = N_0/8$.

The results of the calculations in Figure 3–6 showed that the developed technology for estimating non-stationary parameters of geomagnetic pulsations turned out to be efficient and effective.

The mathematical modeling of pulsations and the implemented statistical testing method [*Mixajlov et al.*, 2018] allowed us to conclude that the relative errors in parameter estimates were (3÷4)% for amplitude and trend functions and (4÷5)% for frequency functions. The results obtained made it possible to consider that similar estimations using the proposed technology should also be implemented for experimental signals with pulsations.

The residual sum functional is a multi-extremal function of frequency and the position of its global and local minima depends on the noise in the observations. For large noises, their positions changed places, which led to large errors. The use of weighted averaging significantly reduced the errors in frequency estimates, as can be seen in Figure 5, 6.

5. Conclusion

1. The developed technology for estimating non-stationary parameters of geomagnetic pulsations based on two-stage approximations turned out to be efficient and effective.

2. Mathematical modeling of signals with pulsations allowed us to conclude that the relative errors in parameter estimates were (3÷4)% for amplitude and trend functions and (4÷5)% for frequency functions; the results obtained made it possible to consider that similar estimations using the proposed technology should also be realized for experimental signals with pulsations.
3. It was found that the use of weighted averaging significantly reduced the errors in frequency estimations.
4. The proposed estimation of non-stationary parameters of geomagnetic pulsations based on two-stage approximations has large reserves for improvement and a favorable prospect for use in information problems of geophysics.

Acknowledgments. The work was carried out within the framework of the state assignment for the GC RAS and the IPE RAS, approved by the Ministry of Science and Higher Education of the Russian Federation.

References

Getmanov V. G., *Sidorov R. V.*, *Dabagyan R. A.* A Method of Filtering Signals Using Local Models and Weighted Averaging Functions // Measurement Techniques. — 2015. — Vol. 58, no. 9. — P. 1029–1036. — DOI: 10.1007/s11018-015-0837-5.

Getmanov V. G., *Dabagyan R. A.*, *Sidorov R. V.* Studying geomagnetic pulsation characteristics with the local approximation method // Geomagnetism and Aeronomy. — 2016. — Vol. 56, no. 2. — P. 195–202. — DOI: 10.1134/S0016793216020055.

Getmanov V. G., *Dovbnya B. V.*, *Kornilov A. S.* Estimating the Frequency and Amplitude Parameters of the Serpentine-Emission Type of Geomagnetic Pulsations // Geomagnetism and Aeronomy. — 2018. — Vol. 58, no. 4. — P. 523–532. — DOI: 10.1134/s0016793218040060.

Getmanov V. G. Digital Signal Processing With Applications for Geophysics and Experimental Mechanics. — Moscow : Texnosfera, 2021. — 354 p. — (In Russian).

Guglielmi A. V., *Troiczkaya V. A.* Geomagnetic Pulsations and Diagnosis of the Magnetosphere. — Moscow : Nauka, 1973. — 208 p. — (In Russian).

Guglielmi A. V., *Potapov A. S.*, *Dovbnya B. V.* On the origin of frequency modulation of serpentine emission // Solnechno-Zemnaya Fizika. — 2015. — Vol. 1, no. 2. — P. 85–90. — DOI: 10.12737/9617. — (In Russian).

Katkovnik V., *Egiazarian K.*, *Astola J.* Local Approximation Techniques in Signal and Image Processing. — SPIE, 2006. — 576 p. — DOI: 10.1117/3.660178.

Klejmyonova N. G. Geomagnetic Pulsations // Models of the Space / ed. by M. I. Panasyuk. — Moscow : MGU, 2007. — P. 511–627. — (In Russian).

Le'j E. Digital Signal Processing for Engineers and Technical Specialists. — Moscow : Gruppa IDT, 2007. — 336 p. — (In Russian).

Mixajlov G. A., *Vojtishek A. V.* Numerical Statistical Modeling. Monte Carlo Method. — 2018. — (In Russian).

Potapov A. S., *Polyushkina T. N.*, *Tsegmed B.* Morphology and diagnostic potential of the ionospheric Alfvén resonator // Solar-Terrestrial Physics. — 2021. — Vol. 7, no. 3. — P. 36–52. — DOI: 10.12737/stp-73202104.

Time-Frequency Analysis: Concepts and Methods / ed. by F. Hlawatsch, F. Auger. — Wiley, 2008. — 434 p. — DOI: 10.1002/9780470611203.

Russian Journal of Earth Sciences

Special Issue: "Data Science, Geoinformatics and Systems Analysis in Geosciences"

Analysis of Changes in the Seismic Regime at Engineering Facilities Under the Influence of Natural and Man-made Factors

B. A. Trifonov[1], **S. Yu. Milanovskiy**[1,2]

[1]Sergeev Institute of Geoecology of the RAS, Moscow, Russia
[2]Schmidt Institute of Physics of the Earth of the RAS, Moscow, Russia
* **Correspondence to:** Svyatoslav Yurievich Milanovskiy, svetmil@mail.ru

Abstract: The experience of studying the consequences of strong earthquakes indicates that intensity and type of seismic effects are determined by local features of the geological environment, which can change over time under the influence of natural and man-made factors. The results of long-term systematic experimental studies on the study of changes in seismic conditions over time in the soil complexes of the Imereti lowland and the site of the Balakovo NPP are presented. This made it possible to carry out long-term forecasting of changes in seismic conditions during economic development of territories.

Keywords: seismic microzonation, seismic properties, seismic forecast, calculated accelerograms, man-made changes.

Citation: Trifonov, B. A., and S. Yu. Milanovskiy (2025), Analysis of Changes in the Seismic Regime at Engineering Facilities Under the Influence of Natural and Man-made Factors, *Russian Journal of Earth Sciences*, 25, ES2021, EDN: CNSORY, https://doi.org/10.2205/2025ES000980

1. Introduction

In the seventies, the problem facing engineering geology was formulated — the need to take into account the role of exogenous processes and engineering and economic activities in space and time [*Sergeev et al.*, 1974]. In particular, it was noted the need to develop methods for forecasting and combating the disturbance of the natural balance in the Earth's crust under the influence of anthropogenesis. This task has been given attention by many seismological researchers when considering the problem of seismic microzonation (SMZ) [*Aleshin*, 2010; *Dzhurik et al.*, 1988; *Krieger et al.*, 1994; *Wight*, 1974; *Zaalishvili*, 2009] and others]. In [*Dif et al.*, 2018; *Johnson et al.*, 2020; *Mindel et al.*, 2003; *Prasad*, 2011] the features of the seismic properties of dispersed soils and the manifestation of the seismic effect on them were studied. In [*Kapustyan et al.*, 2007; *Mindel et al.*, 2005; *Pavlenko*, 2005], the consequences of man-made impacts on changes in seismic conditions at a number of nuclear power plants and urban areas were considered in details. Let us note the work [*Ozmidov*, 2014] devoted to the influence of ground conditions on the characteristics of vibrations on the surface using the example of Sochi. The study and assessment of the risk of seismic liquefaction of the geological base of the Olympic facilities sites in Sochi was carried out in the paper [*Bardet et al.*, 2001].

The purpose of this article is to show how the seismic properties of dispersed soils at the base of buildings and structures have changed over time under the influence of engineering activity. And as a result of these changes, to investigate and evaluate the magnitude of the seismic effect on them. The possibility of improving seismic conditions using engineering training methods was also considered. These studies are illustrated by the example of the Imereti lowland (Sochi area) during the construction and operation of

Research Article

Received: 15 November 2024
Accepted: 15 April 2025
Published: 23 May 2025

Olympic facilities, as well as by the example of the Balakovo NPP for more than 35 years of its existence.

2. Materials and methods

The author's analysis was based on the results of engineering, geological and seismic studies conducted during different observation periods. The research results served as the basis for the construction of seismic models. Accelerograms, amplification factor graphs $\beta(T)$, and amplitude-frequency response characteristics were calculated using these models using the well-known programs NERA [*Ratnikova et al.*, 1967] and COEF-9 [*Aleshin*, 2015; *Ratnikova*, 1984]. Methods of engineering and geological analogies and seismic rigidities were used to build maps of seismic microzoning (SMZ) [*Aleshin*, 2010; *Detailed seismic zoning…*, 2019; *Ulomov et al.*, 1999].

3. Results and discussion

3.1. Analysis of changes in seismic conditions in the Imereti lowland (Sochi)

Based on the GSZ-97(OCP-97) database for the Sochi region, V. I. Ulomov [*Balabanov*, 2010; *Ulomov*, 2005] performed a probabilistic analysis of seismic hazard in the parameters of seismic intensity (I) in the MSK-64 scale and peak acceleration values (in cm/s^2) for various periods of earthquake recurrence on soils of category II according to seismic properties. The results of earlier tectonic and seismological studies conducted in 1998–2000 by a team of PNIIIS[1] specialists (V. N. Averyanova, I. I. Barkhatov, S. A. Nesmeyanov, A. I. Lutikov, L. S. Shumilina et al.), potential earthquake foci (PEF) zone scheme was drawn up for the Sochi area on a scale of 1:1,000,000 with the Sochi and Sukhumi PEF zones most dangerous for the territory under consideration. They correspond to the two lineaments that are most dangerous for the Sochi region from the OSR-97 database according to [*Ulomov*, 2005]. Based on these studies, the authors synthesized initial accelerograms for the near "Sochi" and remote "Sukhumi" PEF zones for calculations. At sites where Olympic facilities are located, it is necessary to take into account the features of the geological structure not only of the upper 30-meter soil layer, but also of the entire low-velocity Quaternary sediments [*Averyanova*, 1985; *Balabanov et al.*, 2011]. The geological structure of the Imereti lowland, with its thickness (up to 100 m) and horizontal stratification, have a major impact on the amplitude level and frequency composition during seismic vibrations on the daytime surface.

In the late 80th, the territory of the Imereti lowland (the site of the future Olympic facilities) was an artificially irrigated state farm fields. The soils of the territory under consideration were classified as category III in terms of seismic properties [*Averyanova*, 1985; *Balabanov et al.*, 2011]. The maximum acceleration values calculated by authors according to COEF-9 program were: from close dangerous zones of potential earthquake foci (PEF) (Sochi) Amax = 450 cm/s^2; from the far Sukhumi PEF zone Amax = 465 cm/s^2 [*Balabanov*, 2010; *Ozmidov*, 2014]. Based on the results of geophysical research in 1986–1996 SMZ map was constructed (1996), where most of the territory of the Imereti lowland was assigned to areas with seismic intensity I = 9 points.

11 years after the engineering preparation of the territory for construction (removal of swampy lagoon sediments), according to the results of research for the purpose of placing Olympic facilities, the SMZ map (2007) was compiled. The SMZ map of 2007 has changed compared to 1996. Compared with 1996, areas with soils of category II–III with seismicity I were allocated = 8.5 points and with Amax = 305–330 cm/s^2 from the PEF close zones and Amax = 300–335 cm/s^2 from the PEF Sukhumi zone. After 4–5 years, studies have shown a deterioration in soil properties under the influence of man-made factors as a result of intensive construction and operation of constructed structures. The studied soils of the II–III categories have become closer to the soils of the III category in terms of their seismic properties. According to calculations, the maximum acceleration values increased

[1] Industrial and Scientific Research Institute for Engineering Research in Construction in the USSR.

to Amax = 380 cm/s^2 (from close PEF zones) and Amax = 380–390 cm/s^2 (from the far PEF Sukhumi zone). On the 2014 SMZ schematic map (Figure 1), after the construction and operation of Olympic facilities, compared with the 2007 map, there was an increase in the territory with soils of category III and seismicity I = 9(9*) points.

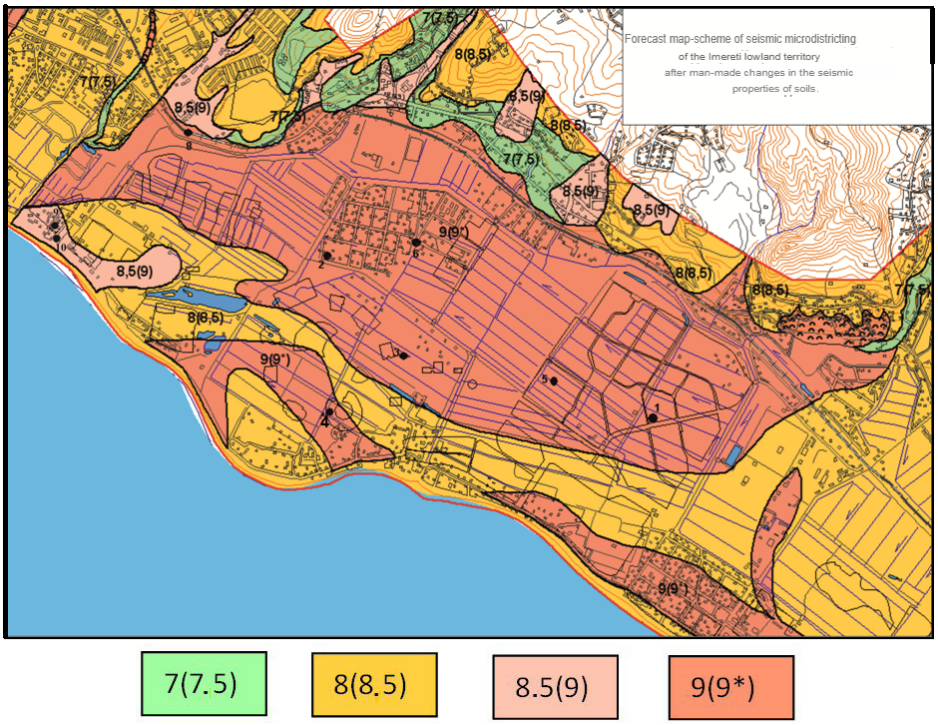

Figure 1. A schematic map of the seismic microzoning (SMZ) of the Imereti lowland territory after man-made changes in the seismic properties of soils (after research in 2010–2014) with bold dots indicating the locations of experimental engineering and geophysical research, indicating their numbers. Earthquake intensity values (I) in color zones with a recurrence of earthquakes 1 time in 500 years and intensity values in brackets with a recurrence of 1 time in 1000 years.

The results of studies of the seismic properties of soil complexes in various construction sites of Olympic facilities in the Imereti lowland, conducted before the start of construction in 2007 and after 4–5 years, showed changes in the initial seismic conditions due to the deterioration of the seismic properties of soils in the upper part of the section as a result of intensive construction and long-term operation of the constructed Olympic facilities.

For possible construction on soils of the III category of the Imereti lowland, experimental studies were conducted to assess the improvement of seismic conditions of the soils of the base under the foundations of structures by creating a pile field. The artificial massif created by a field of reinforced concrete piles on a grid of 2 × 2 m and 1.5 × 1.5 m increased the seismic rigidity of the massif and improved the seismic conditions of construction. Results of calculation of accelerograms on typical soil complexes composing most of the Imereti lowland, according to the COEF-9 program show a tendency to decrease the Amax values and improve the seismic properties of the base soils when pile fields are created in them (research sites No. 1, 2, 3, 5, 6 and No. 4, where the risk of seismic soil liquefaction is possible). Similar results we obtained when calculating using the NERA code. The values of Amax accelerations decreased by 25–30% from close PEF zones and by 10–14% from earthquakes from the far PEF Sukhumi zone.

3.2. Analysis of changes in seismic conditions on the territory of the Balakovo NPP over more than 35 years of its operation

The Balakovo NPP was built on the left bank of the Saratov reservoir in the area of the junction of large geostructures of the East European Platform: Caspian Depres-

sion, Volga-Ural and Voronezh anteclises, Pachelma aulacogen, and Volga dislocation system [*Ogadzhanov et al.*, 2009]. The base of the NPP is Cenozoic (Q, N, Pg), sandy-clay strata underlain by Cretaceous carbonate deposits.

The engineering-geological and seismic situation as a result of the manifestation of man-made human activity at the NPP site has been changing since 1980. (the beginning of the design) for 2004–2010 (construction of power units) and in 2019 (after 9 years of NPP operation). After leveling the construction site to the planning mark of 34 m, the natural dense soils were replaced with man-made backfilling (tQIV) of the III category according to seismic properties. The initial seismic conditions of the territory deteriorated (Figure 2A and B). When calculating using the NERA program, an accelerogram (horizontal VS component) borrowed from the materials of OJSC "Atomenergoproekt" in 2010 for the Balakovo NPP with Amax = 0.057 g was set as the input signal at the boundary of the elastic half-space (Cretaceous limestone roof at a depth of about 140 m). Four our calculations of the accelerogram set on a conditional rock base on the surface (calculations A, B, C, D) were performed.

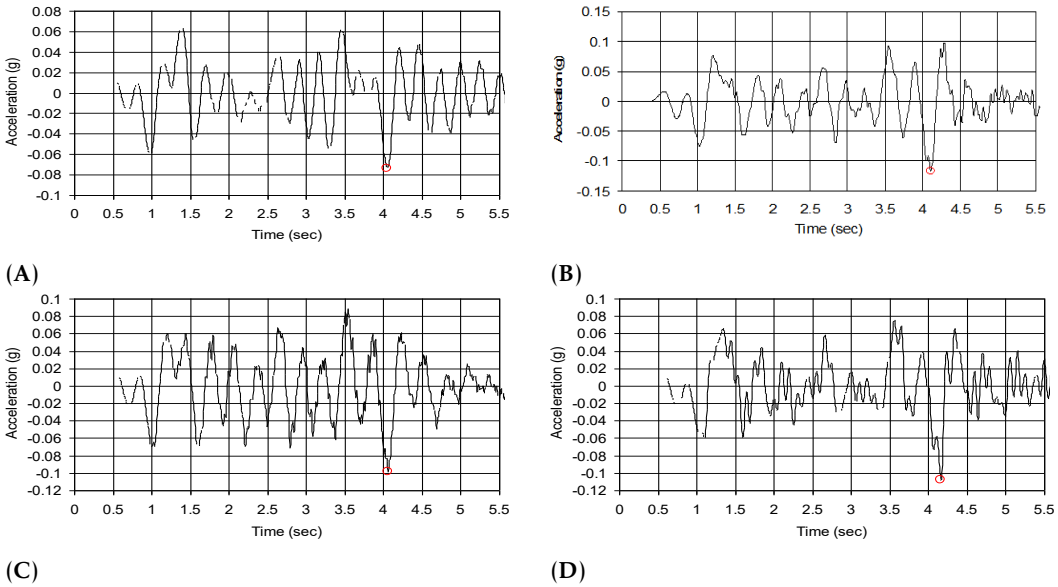

Figure 2. The results of our calculation of accelerograms for Balakovo NPP site using NERA code [*Bardet et al.*, 2001]: model A — before the start of construction in 1978–1980 on the surface of the site at the initial natural state of the soil, Amax = 0.073 g; model B — after the engineering preparation of the territory in 2004–2010 on the surface at the planning mark of 34 m, Amax = 0.116 g.; model C — on a free surface next to power unit No. 5, a section with waterproofing side clay locks and a crushed stone cushion on which the foundation rests in 2012, Amax = 0.098 g; model D — in the same place in 2019, Amax = 0.108 g.

The deterioration of the initial seismic conditions (Figure 2A) after the preparation of the construction site (Figure 2C) caused the need to lay slabs with a 4-meter rubble cushion of compacted soils (dolomite rubble) at the base of the foundations of the Main Building with the engine room and reactor compartment (RC). Together with the water reduction and the device of clay locks, this made it possible to reduce the Amax value to 0.098 g (Figure 2C). There was a decrease in the values of accelerations relative to the surface by 16% (observations in 2012). 7 years after the start of operation of the RC power unit No. 5 of the study in 2019 showed a deterioration in the properties of the crushed stone cushion, which manifested itself in a change in the Amax values over seven years, respectively, from 0.098 g (Figure 2C) in 2012 to 0.108 g (Figure 2D) in 2019 (decrease in Amax relative to the surface was reduced to 7%).

The calculated accelerograms shown in Figure 2 for models describing the condition of the soil mass at different time periods illustrate the changes that have occurred not

only in the Amax values, but also in their shape. At the same time, the calculated spectral characteristics have also changed — frequency response and amplification factor graphs $\beta(T)$ (Figure 3). The technogenic rise of groundwater level (GWL) and the destruction of clay locks affected the partial dissolution and swelling of the gravelly soils of the foundation cushion under the slab, which led to a deterioration of seismic conditions and further disruption of the stability of the bearing capacity of the foundation slab. Figure 3 below shows the change in the frequency response and the amplification factor graphs $\beta(T)$ for different stages of research at the NPP site (models A, B, C and D).

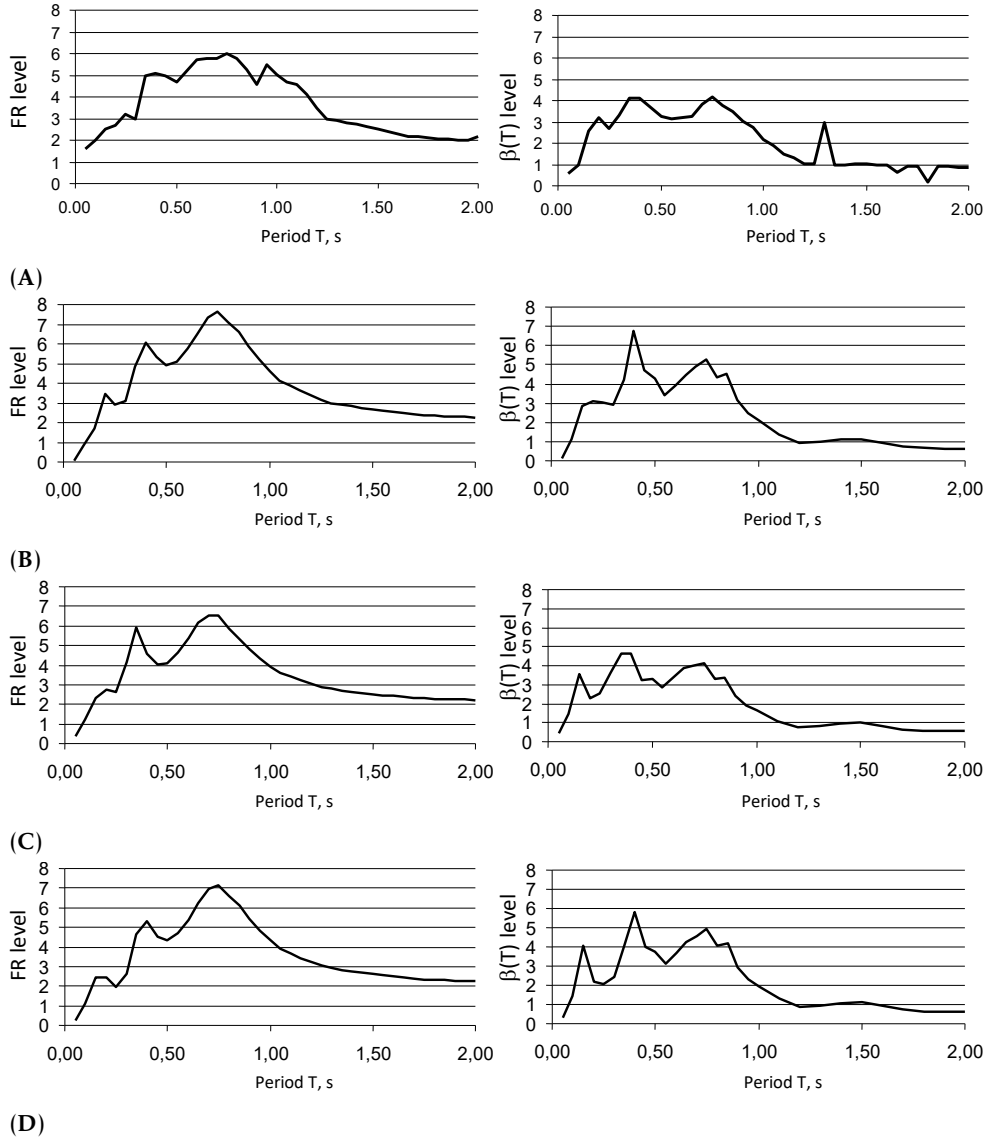

Figure 3. Calculated amplitude-frequency characteristics: FR-frequency response (left), according to COEF-9 and amplification factor graphs $\beta(T)$ (right), according to NERA on the surface site for different stages of research (see Figure 2).

The analysis allows us to assume a possible change in the engineering-geological and seismic conditions in the coming years, which may lead to a violation of the stability of the bearing capacity of the foundation plate, as well as to further deterioration of seismic conditions.

4. Conclusion

Systematic long-term studies of the seismic properties of soil complexes in territories affected by natural and man-made factors, such as the construction and operation of

Olympic facilities and Balakovo NPP, have shown how the seismic conditions of these territories has changed over time.

Based on the results of long-term research:

- a forecast map of the SMZ has been built on the territory of the Imereti lowland. It allows for long-term seismic forecasting during further urbanization of the territory of Sochi. It is shown that artificially creating an array of foundation soils using pile fields can significantly improve the seismic conditions of engineering and geological sections composed of category III soils in terms of seismic properties.
- changes in the seismic properties of soils have been shown at the Balakovo NPP site over more than 35 years of operation of previously built NPP power units and the construction of new ones, which make it possible to predict changes in seismic ground conditions.

Acknowledgments. The work was performed within the framework of the state assignments of the Schmidt Institute of Physics of the Earth of the Russian Academy of Sciences (scientific topic FMWU-2022-0006) and Sergeev Institute of Environmental Geoscience of the Russian Academy of Sciences (scientific topic FMWU-2022-0010). The authors will be grateful to the reviewers who will take the trouble to critically read the article and make a comments necessary to finalize and improve the text.

References

Aleshin A. S. Seismic microzonation of especially responsible objects. — Moscow : Svetoch Plus, 2010. — 303 p. — (In Russian).

Aleshin A. S. Fundamentals of Continuum Theory of Seismic Microzonation // Earthquake engineering. Constructions safety. — 2015. — No. 5. — P. 18–26. — (In Russian).

Averyanova V. N. Energy-spectral method of seismic hazard assessment. — Moscow : Nauka, 1985. — 192 p. — (In Russian).

Balabanov I. P. and. Gay N. A. The history of the development of the Imereti lagoon in the mesopotamia of Mzynta-Psou // Collection of the Black Sea region and conditions of global climate change: patterns of development of the natural environment over the past 20 thousand years and forecast for the current century. — Moscow : Moscow State University, 2010. — P. 25–41. — (In Russian).

Balabanov I. P., *Nikiforov S. P.*, *Pashkovsky I. S.* Imereti lowland. Natural and geological conditions, problems of development. — Moscow : Nedra, 2011. — 281 p. — (In Russian).

Bardet J. P., *Tobita T.* NERA. A computer program for nonlinear earthquake site response analyses of layered soil deposits. — USA : Department of Civil Engineering, University of Southern California, 2001. — 44 p.

Detailed seismic zoning and seismic microzoning for territorial planning SP 408.1325800.2018. — Standartinform, 2019. — 16 p. — (In Russian).

Dif H., *Zendagui D.*, *Bard P.-Y.* Implementing effects of site conditions in damage estimated at urban scale // Bulletin of Earthquake Engineering. — 2018. — Vol. 17, issue 3, no. 3. — P. 1185–1219. — DOI: 10.1007/s10518-018-0512-8.

Dzhurik V. I., *V. V. Sevastyanov V. A. P.* Assessment of the influence of groundwater conditions on seismic hazard: A methodological guide to seismic microzonation. — Moscow : Nauka, 1988. — 224 p. — (In Russian).

Johnson C. W., *Kilb D.*, *Baltay A.*, *et al.* Peak Ground Velocity Spatial Variability Revealed by Dense Seismic Array in Southern California // Journal of Geophysical Research: Solid Earth. — 2020. — Vol. 125, no. 6. — DOI: 10.1029/2019jb019157.

Kapustyan N. K., *Yudakhin F. N.* Seismic studies of anthropogenic impacts on the Earth's crust and their consequences. — Ekaterinburg : Ural Branch of the Russian Academy of Sciences, 2007. — 415 p. — (In Russian).

Krieger N. I., *Kozhevnikov A. D.*, *Mindel I. G.* Seismic properties of dispersed soils (a seismolithoecological approach). — Moscow : INZHEKO, 1994. — 195 p. — (In Russian).

Mindel I. G., *Trifonov B. A.* Changes in the seismic properties of soils at the base of buildings and structures over time, as well as after their improvement by engineering training methods // Industrial and Civil engineering. — 2003. — No. 10. — P. 35–37. — (In Russian).

Mindel I. G., *Trifonov B. A.*, *Ragozin N. A.* Seismic exploration methods for studying soil properties at the base of buildings and structures, including after their improvement by engineering training methods // Proceedings of the international geotechnical conference. Soil-structure interaction: calculation methods and engineering practice. Volume 2. — Saint Petersburg : ASV Publishers, 2005. — P. 307–311. — (In Russian).

Ogadzhanov V. A., *Maslova M. Y.*, *Ogadzhanov A. V.* Saratov geodynamic polygon // Earthquakes of Northern Eurasia in 2003. — Obninsk : GS RAS, 2009. — P. 222–226. — (In Russian).

Ozmidov O. R. The assessment of risk of seismic liquefaction of a soil deposit at Olympic construction at Sochi city // Bulletin of the Russian Academy of Natural Sciences. — 2014. — No. 1. — P. 48–54. — (In Russian).

Pavlenko O. V. Influence of soil conditions on the characteristics of vibrations on the surface on the example of Sochi // Earthquake-resistant construction. Structure safety . VI Russian National Conference on earthquake-resistant construction and seismic zoning, September 19–24, 2005, Sochi. — 2005. — No. 5. — P. 53–56. — (In Russian).

Prasad B. B. Fundamentals of Soil Dynamics and Earthquake Engineering. — New Delhi : PHI Learning Private Limited, 2011. — 567 p.

Ratnikova L. I., *Levshin A. L.* Calculation of spectral characteristics of thin-layered media // Izvestiya AN SSSR. Physics of the Earth. — 1967. — No. 2. — P. 41–53. — (In Russian).

Ratnikova L. I. Calculation of vibrations on a free surface and at internal points of a horizontally layered absorbing soil. Seismic microzoning. — Nauka, 1984. — (In Russian).

Sergeev E. M., *Osipov V. I.* The Problems and ways of further development of Engineering Geology after International Geological Congress, XXIV Session // Problems of geology and mineral deposits at the XXIV Session of the International Geological Congress. — Moscow : Nauka, 1974. — P. 111–117. — (In Russian).

Ulomov V. I., *Shumilina L. S.* A set of maps of the general seismic zoning of the territory of the Russian Federation — GSZ-97. Scale 1 : 8,000,000. Explanatory note and list of cities and settlements located in earthquake-prone areas. — Moscow : Schmidt Joint Institute of Physics of the Earth of the Russian Academy of Sciences, 1999. — 57 p. — (In Russian).

Ulomov V. I. Probabilistic-deterministic assessment of seismic impacts based on maps of GSZ-97 (OCP-97) and scenario earthquakes // Earthquake-resistant construction. Structure safety. — 2005. — No. 4. — P. 60–68. — (In Russian).

Wight L. H. A geological and seismological investigation of the Lawrence Livermore laboratory site. Prepared for US. Atomic Energy Commission under contract No. W-7405-Eng-48 Lawrence Livermore Laboratory University of California/Livermore May 17. — 1974. — 38 p.

Zaalishvili V. B. Seismic microzonation of urban territories, settlements and large building sites. — Moscow : Nauka, 2009. — 349 p. — (In Russian).

Russian Journal of Earth Sciences

Special Issue: "Data Science, Geoinformatics and Systems Analysis in Geosciences"

Problems of Processing of Raw Data from Magnetic Observatories: Will Modern Mathematical Technologies Help?

S. Yu. Khomutov[1]

[1]Institute of Cosmophysical Research and Radio Wave Propagation, FEB RAS, Paratunka, Kamchatka, Russia
* **Correspondence to:** Sergey Y. Khomutov, khomutov@ikir.ru

Abstract: Various aspects of the measurements and processing of raw magnetic data obtained at observatories are considered. It is noteworthy that the processing can be executed through simple mathematical methods and algorithms at almost all stages. Nevertheless, there are a number of tasks, for example, related to the mass recognition of noise in raw data and the need to fill in gaps, for the effective solution of which it is necessary to involve more powerful mathematical technologies.

Keywords: magnetic observatory, raw data, noise, modern mathematical methods.

Citation: Khomutov, S. Yu. (2025), Problems of Processing of Raw Data from Magnetic Observatories: Will Modern Mathematical Technologies Help?, *Russian Journal of Earth Sciences*, 25, ES2022, EDN: VTMATG, https://doi.org/10.2205/2025ES000994

1. Introduction

There are several problems that magnetic observatories currently face in their daily practice:

- Modern magnetometers allow measurements to be performed with greater frequency and greater sensitivity. This leads both to a simple increase in the volume of data received by orders of magnitude and to an expansion of the semantic content of this data, which was previously unavailable;
- The enhancement of magnetometer parameters and the increase in man-made load on magnetic measurements lead to the fact that noise is recorded, which previously had not been dealt with;
- Previously gained experience of the observatory staff becomes irrelevant.

On the other hand, the rapid growth of the volume and content of information in modern society leads to the development of new mathematical technologies aimed at solving emerging problems. In one way or another, these technologies can and are beginning to be used in magnetic monitoring at observatories.

Some steps of the work of standard INTERMAGNET observatory will be considered here, and an assessment of the need and possibility of using modern mathematical methods in this work will be given.

2. Absolute Observations and the Calculation of the Baselines Values for Variational Magnetometers

Absolute magnetic observations are an essential requirement for INTERMAGNET observatories [*INTERMAGNET*, 2020; *Jankowski et al.*, 1996]. As standard, they include manual observations of magnetic declination D and inclination I, the results of which are usually manually recorded in the protocol. After the observations, the observer types the data into a file. This procedure is one of the most common sources of possible errors that cannot always be detected. Modern text recognition methods, in principle, can avoid the manual procedure of typing data into a computer. However, it seems inefficient to use

Research Article

Received: 15 November 2024
Accepted: 15 April 2025
Published: 23 May 2025

this approach in the real practice of observatories since the protocols are handwritten and the records look very complex (a fragment of a typical record is shown in Figure 1). Even modern text recognition methods would have a hard time dealing with this text.

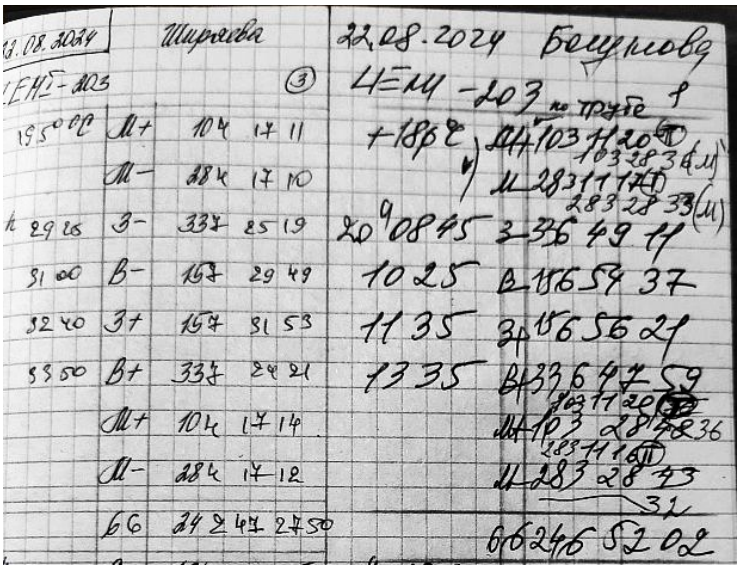

Figure 1. A fragment of the protocol with the absolute observations results (Observatory Paratunka PET).

The obtained baseline values are estimates of certain points in time. According to the absolute observation schedule established at the observatory, such estimates can range from a few values per day to several values per week. At the same time, it is necessary to know the behavior of the baselines as reliably as possible during each variometer measurement. Therefore, it is necessary to approximate the irregularly distributed data on a uniform grid. Various methods of approximation are employed in the practice of observatories, both formal and taking into account the physical features of the baseline's behavior.

To illustrate, you can take the information about the methods used during the preparation of the Definitive data of the INTERMAGNET observatories, which are usually reported in blv-files with baseline values. For example, in 2021, such information was presented in the data sets of 108 observatories:

- The use of polynomial and piecewise polynomial functions was 29%;
- The use of linear and piecewise linear functions was 34%;
- The use of cubic splines, including smoothing ones was 29%;
- The use of filters with various weight functions, visual approximation, etc. was 8%;

As you can see, traditional methods are used, which are often implemented in various standard software packages. This can be explained by the small volume of the processed baseline values, the absence of "hidden" uncertainties, and the effective control of the results by the observatory specialist. However, in extremely difficult cases, such as a long gaps between absolute observations or rapidly and irregularly changing baselines, the methods used remain rather traditional [*Gonsette et al.*, 2017; *Soloviev et al.*, 2018].

3. Daily Processing of Raw Data

The main task of the magnetic observatory is to obtain and provide users with data as complete as possible and, at the same time, as free as possible from any signals of artificial origin (noise). A significant, if not the main, amount of work of a observatory specialist is associated precisely with the analysis of raw magnetic data and the recognition of noise results of hardware failures. The identification problem is often solved if:

- The noise has an amplitude significantly exceeding the amplitude of natural signals;
- The structure (shape) of the signal obviously indicates its artificial origin;

- The signal has a regular repeatability over time and/or if information about its source is available;
- The signal recorded by spatially spaced magnetometers,

and in some other cases. Figure 2 shows an example of a regular noise with an amplitude of up to 4–5 nT in the data from the fluxgate variometer at the Paratunka observatory with deleted points marked with ×. The noise occurs during ionospheric soundings every 15 minutes.

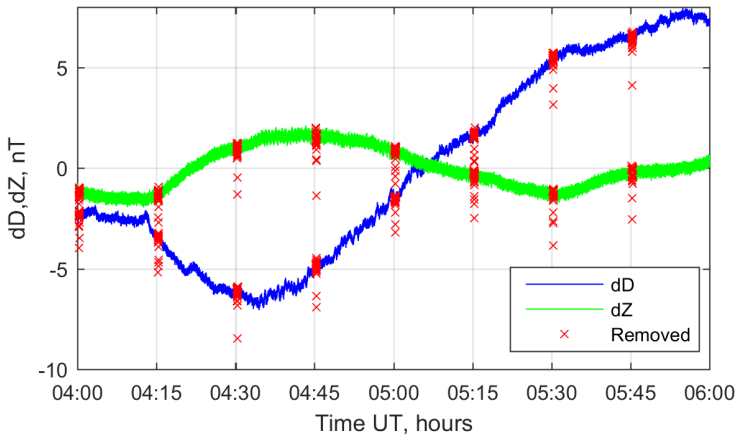

Figure 2. A sample of the records of the variations in the magnetic declination dD and vertical component dZ, in which there is a regular noise from the ionosonde, marked with the symbols ×. This noise was removed automatically.

Simple processing methods become ineffective if, for example, the noise has a small amplitude, morphologically differs little from natural magnetic variations, or there are many of them. Moreover, an artificial signal is more difficult to recognize when online or archived data is being processed. Data processing using modern mathematical technologies that take into account the more detailed and non-obvious characteristics of noise may prove be more effective in this case.

An example of the results of this approach is shown in Figure 3 (see [*Khomutov et al.*, 2017]). The daily recording in Figure 3a shows that in the vertical component Z at the observatory Hyderabad (HYB, CSIR-NGRI, India) there are frequent quasi-spikes with an amplitude of up to 5 nT, which are presumably associated with a branch of the skytrain passing near the observatory. Figure 3c shows a more detailed form of such spike. The result of noise recognition and clearing by the simplest method (by the spike amplitude taking into account its structural features) is shown in Figure 3d. A method for noise recognition based on continuous wavelet transform and threshold functions was also used, the results are shown in Figure 3b, e. It can be seen that a more complex method made it possible to remove spikes with an amplitude of up to 0.5 nT, in contrast to the simple method, which remained the noise with an amplitude of up to 1 nT. This technology has progressed further (see, [*Papsheva et al.*, 2019]), but it remained unclaimed in real practice at magnetic observatories.

In 2009–2012, a few articles were published with algorithms for the recognition of various types of the noise in minute and second magnetic data which were being developed at the Geophysical Center of the Russian Academy of Sciences (see [*Soloviev et al.*, 2009; 2012], [*Sidorov et al.*, 2012]). Algorithms based on the theory of discrete analysis and fuzzy logic methods have demonstrated their efficacy. Unfortunately, there are no details regarding the development of this technology. It is not known if it is actually used at most Russian observatories.

Machine learning methods were used in [*McCuen et al.*, 2023] to identify a noise of various types and origins in the measurement results at observatories in northeastern Canada over several years. To train the system, the expert (manual) processing of annual

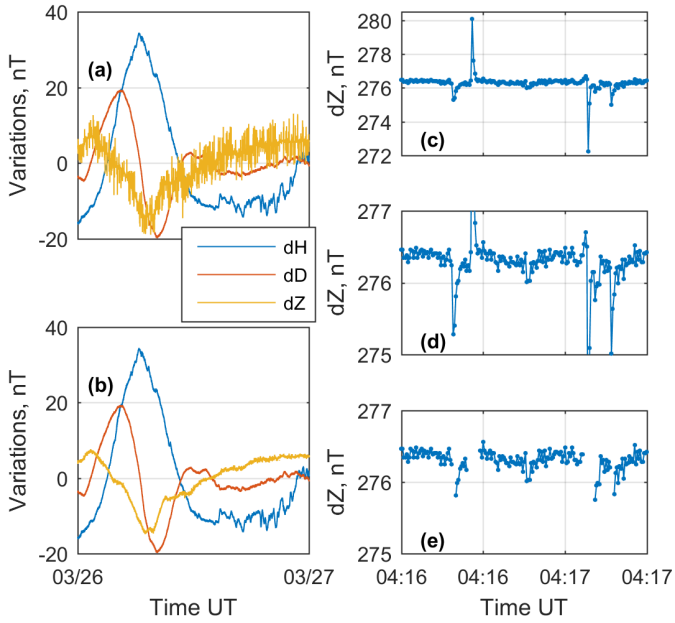

Figure 3. Frequent spikes in the vertical component Z at the Hyderabad Observatory (HYB): (a) Daily records of the variations dH, dD, dZ. (b) as (a), but the recognized spikes are removed. (c) The detailed form of some spikes. (d) Result of recognition and clearing by the simplest method. (e) as (d) but a more complex method was used.

raw data was performed, so a huge volume of magnetic measurement results was analyzed. The article perfectly illustrates the problem that raw data that is not processed promptly significantly increases costs and reduces the quality of the results obtained.

4. Conclusions

The experience of most Russian and many foreign observatories shows that at almost all steps of magnetic measurements, the processing of raw data is quite simple, and when performed every day and directly at observatories, modern high-tech mathematical methods are not required. The most critical points in this process are related to the recognition and correct cleaning of noise in the raw data, especially if there is a lot of noise, archived data is being processed, or the level of qualification of the observatory staff is low. Modern mathematical technologies with elements of artificial intelligence could be relevant.

Acknowledgments. The work was supported by the IKIR FEB RAS State Task (subject registration No. 124012300245-2; Russian Federation). The results presented in this paper rely on data collected at magnetic observatories. I thank the national institutes that support them and INTERMAGNET for promoting high standards of magnetic observatory practice (www.intermagnet.org). I also thank the reviewer, whose comments and suggestions undoubtedly allowed us to correct annoying errors and improve the article as a whole.

References

Gonsette A., Rasson J., Humbled F. In situ vector calibration of magnetic observatories // Geoscientific Instrumentation, Methods and Data Systems. — 2017. — Vol. 6, no. 2. — P. 361–366. — DOI: 10.5194/gi-6-361-2017.

INTERMAGNET Technical Reference Manual, Version 5.1.0 / ed. by B. V. St-Louis. — INTERMAGNET Operations Committee, Executive Council, 2020. — 146 p.

Jankowski J., Sucksdorff C. Guide for magnetic measurements and observatory practice. — Warshaw : International Association of Geomagnetism, Aeronomy, 1996. — 236 p.

Khomutov S. Y., Mandrikova O. V., Budilova E. A., et al. Noise in raw data from magnetic observatories // Geoscientific Instrumentation, Methods and Data Systems. — 2017. — Vol. 6, no. 2. — P. 329–343. — DOI: 10.5194/gi-6-329-2017.

McCuen B. A., *Moldwin M. B.*, *Steinmetz E. S.*, *et al.* Automated high-frequency geomagnetic disturbance classifier: A machine learning approach to identifying noise while retaining high-frequency components of the geomagnetic field // Journal of Geophysical Research: Space Physics. — 2023. — Vol. 128, no. 2. — P. 1–22. — DOI: 10.1029/2022JA030842.

Papsheva S. Y., *Mandrikova O. V.*, *Khomutov S. Y.* Method of noise detection in magnetic data // Vestnik KRAUNC. Fiziko-matematicheskie nauki. — 2019. — Vol. 29, no. 4. — P. 87–97. — DOI: 10.26117/2079-6641-2019-29-4-87-97. — (In Russian).

Sidorov R. V., *Soloviev A. A.*, *Bogoutdinov S. R.* Application of the SP algorithm to the INTERMAGNET magnetograms of the disturbed geomagnetic field // Izvestiya, Physics of the Solid Earth. — 2012. — Vol. 48. — P. 410–414. — DOI: 10.1134/S1069351312040088.

Soloviev A. A., *Bogoutdinov S. R.*, *Agayan S. M.*, *et al.* Detection of hardware failures at INTERMAGNET observatories: application of artificial intelligence techniques to geomagnetic records study // Russian Journal of Earth Sciences. — 2009. — Vol. 11, no. 2. — ES2006. — DOI: 10.2205/2009ES000387.

Soloviev A. A., *Chulliat A.*, *Bogoutdinov S. R.*, *et al.* Automated recognition of spikes in 1 Hz data recorded at the Easter Island magnetic observatory // Earth, Planets and Space. — 2012. — Vol. 64. — P. 743–752. — DOI: 10.5047/eps.2012.03.004.

Soloviev A. A., *Lesur V.*, *Kudin D. V.* On the feasibility of routine baseline improvement in processing of geomagnetic observatory data // Earth, Planets and Space. — 2018. — Vol. 70. — P. 1–14. — DOI: 10.1186/s40623-018-0786-8.

Russian Journal of Earth Sciences

Special Issue: "Data Science, Geoinformatics and Systems Analysis in Geosciences"

Instrumental Support for Ionospheric, Magnetic and Heliogeophysical Observations

V. T. Minligareev[1], **E. N. Khotenko**[1]

[1]Institute of applied geophysics named after Academician E. K. Fedorov (FSBI "IPG"), Moscow, Russia
* **Correspondence to:** V. T. Minligareev, vns32@yandex.ru

Abstract: During the period of maximum solar activity, extreme space weather events increasingly affect technical means and systems. The article considers the ground-based heliogeophysical observation platform, as well as on-board heliogeophysical hardware complexes (GGAK), which conduct operational monitoring of space weather from space crafts.

Keywords: ionospheric, magnetic, heliogeophysical observations, space weather, instruments, metrology.

Citation: Minligareev, V. T., and E. N. Khotenko (2025), Instrumental Support for Ionospheric, Magnetic and Heliogeophysical Observations, *Russian Journal of Earth Sciences*, 25, ES2023, EDN: DDLVIR, https://doi.org/10.2205/2025ES000995

1. Introduction

At the peak of the 25th cycle of solar activity instrumentation support, reliability and accuracy of ground-based ionospheric, magnetic, and heliogeophysical observations and space grouping are becoming increasingly relevant, due to the increasing dangerous phenomena of space weather [*Mayorova et al.*, 2024a] (Figure 1).

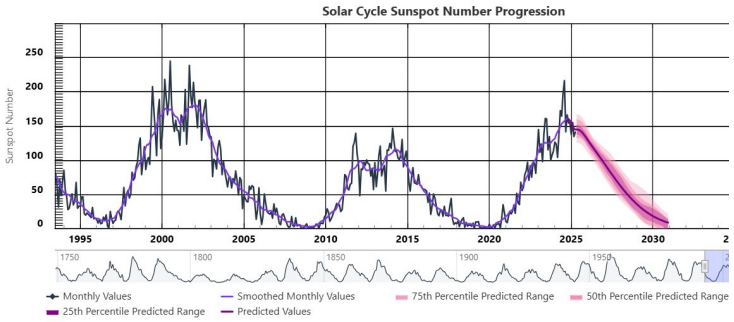

Figure 1. Graph of sunspots and solar cycles (https://www.swpc.noaa.gov/products/solar-cycle-progression).

In Russian Federation, Roshydromet is responsible for operational monitoring of the quality and reliability of ionospheric, magnetic and heliogeophysical observations in accordance with federal regulations. The leading scientific and methodological organizations are FGBI "IPG" (http://ipg.geospace.ru/?view=desktop) and FGBI "AANI" (https://www.aari.ru).

Ionospheric, magnetic and heliogeophysical observations are carried out to monitor space weather and identify dangerous heliogeophysical phenomena. Space weather and storms affect a wide range of human activities: they create a radiation hazard for astronauts, can destroy or damage power lines, cause corrosion of oil and gas pipelines, affect radio communications and navigation of terrestrial and satellite systems, absorb radio waves in the

Research Article

Received: 15 November 2024
Accepted: 15 April 2025
Published: 23 May 2025

polar cap, causing failures in radio communications and radar. Irradiation of spacecraft with high-energy particles can cause anomalies in operation, destroy electronics, degradation of solar panels and "blindness" of optical systems of telescopes and stellar orientation sensors [*Minligareev et al.*, 2023b].

Taking into account the factors of space weather, forecasting their negative impact and operational information support are important elements of national security, including the Arctic zone of the Russian Federation [*Minligareev et al.*, 2023a]. The instrumental support of ionospheric, magnetic and heliogeophysical observations plays a key role in this process. The last modernization of the instrument bases for geophysical monitoring was carried out more than 12 years ago, therefore, a planned replacement of equipment is necessary, taking into account modern realities.

2. Instrumental observations of space weather

Russia has established a system for monitoring the geophysical situation (which dates back to 1973 with the ionospheric magnetic service), which is part of the observation network of Roshydromet. Geophysical information is received from ground-based (ionospheric stations, magnetic observatories, GNSS receivers, solar and radio telescopes) and space platforms (spacecraft of the Meteor-M, Electro-L, Arktika-M, Ionosphere-M series), as well as through international information exchange channels.

The main structure of the ground-based ionospheric and magnetic observation network includes: the Parus-A ionosonde (10), the CADI ionosonde (7), the LFM ionosonde (6), the riometer (8), the hardware and software complex of high-orbit radiotomography (120), magnetometers (14).

In addition, ground-based observation instruments of the Russian Academy of Sciences are used, including solar observatories (ISTF RAS (https://badary.iszf.irk.ru/ssrt.php), GAS GAO (https://observatories.ru/gas-gao/), Special Astrophysical Observatory (https://www.sao.ru/), etc. Measurement information is transmitted and processed in the analytical centers of Roshydromet, including the Heliogeophysical Service, the Federal Information and Analytical Center, the International Space Weather Center for Air Navigation CRC (https://space-weather.ru/) and the Polar Geophysical Center (https://geophys.aari.ru/main.php). Mailing and warnings about dangerous geophysical phenomena are carried out in 200 organizations of the Federal executive power, international organizations, including WMO, ISES and ICAO.

2.1. Ground observation network

The ground segment is represented by ionospheric stations, magnetic observatories, GNSS receivers, solar and radio telescopes. The main part consists of Roshydromet's own observation points, some of them are instruments and observation points of the Russian Academy of Sciences and the Ministry of Education and Science.

Ionospheric observations are the most demand part. The ionospheric network is represented by ionosondes of vertical and inclined sensing, software and hardware complexes of high-orbit radiotomography. Ionosondes measure the delay time of a 1–20 MHz radio pulse, which is recorded and presented in the form of ionograms. The network ionosonde and its characteristics are shown in Figure 2 and in Table 1.

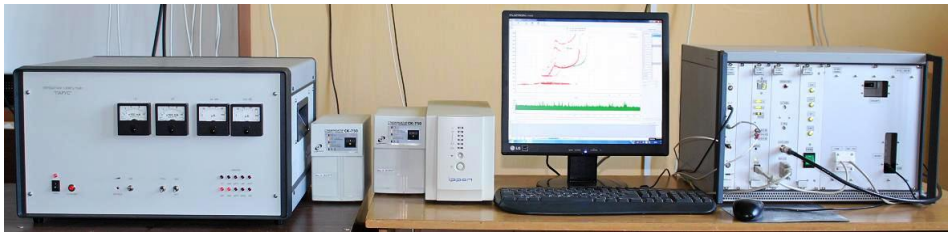

Figure 2. General view of the ionosonde "Parus-A".

Table 1. Technical and metrological characteristics of the ionosonde "Parus-A".

Characteristics	Value
The measurement range of the delay time of the radio pulse	0.5–10 ms
The limits of the permissible absolute error in measuring the delay time of the radio pulse	±12 μs
The range of reproducible radio pulse filling frequencies	1–20 MHz
The limits of the permissible absolute error in measuring the frequency of filling the radio pulse	±5 kHz
Limits of permissible error of setting GPS second pulses	±1 μs
The number in the State Register of Measuring Instruments	51425-12

2.2. Space grouping

The space segment of the heliogeophysical observation network is represented by a grouping of hydrometeorological and heliogeophysical spacecraft of the Meteor-M, Electro-L and Arktika-M series with GGAK hardware heliogeophysical complexes (Figure 3).

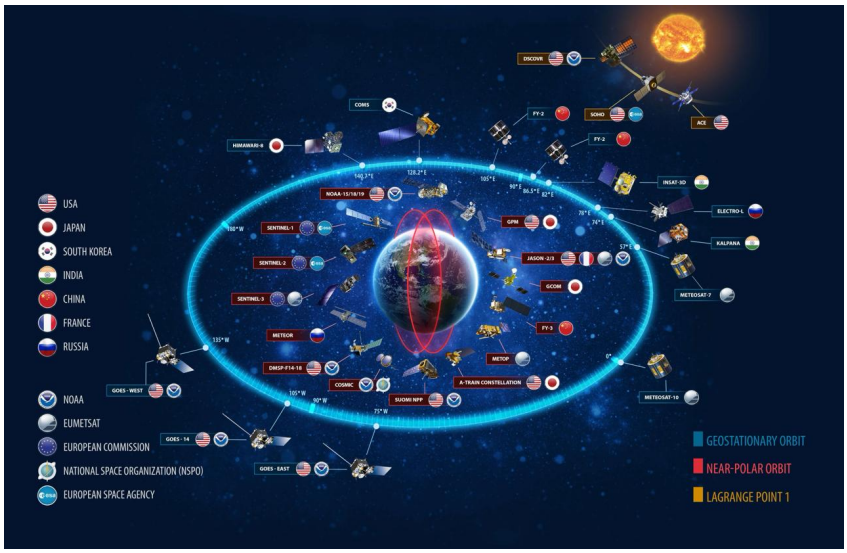

Figure 3. International grouping of hydrometeorological and heliogeophysical satellites with Russian satellites (https://www.nesdis.noaa.gov/news/what-satellite?page=5).

GGAK heliogeophysical hardware complexes (modifications E, VE, M) are designed for global monitoring of heliogeophysical parameters in order to [*Avdyushin et al.*, 2014]:

- monitoring and forecasting of solar flare activity;
- monitoring of the radiation situation in the OKP;
- diagnostics and monitoring of the state of the geomagnetic field.

The integrated target heliogeophysical equipment (CCA) on the Electro-L spacecraft is shown in Figure 4.

Typical composition of GGAK-VE on the Electro-L spacecraft:

- SKIF-VE spectrometer for measuring the flux density of protons (up to 160 MeV) and electrons (up to 10 MeV);
- GALS-VE spectrometer for measuring galactic cosmic rays (proton flux densities of more than 600 MeV and electrons);
- ISP-2M solar constant meter (1360–1365 W/m^2);
- VUSS-E solar extreme ultraviolet radiation flux meter in the HLa range (121.6 nm);
- DIR-E Solar X-ray flux density meter in the range of 3–8 keV;

Figure 4. KCA GGAK-VE on the Electro-L spacecraft.

- FM-E magnetometer for measuring the components of the Earth's magnetic field in the range of +65,000 NT.

3. Promising developments

As noted, the ground equipment on the observation network has been in operation for more than 12 years and needs to be replaced. FSBI IPG is developing a program for the replacement of devices and equipment, which includes several key positions.

3.1. Development of a three-component ferrosonde magnetometer

Figure 5 shows the magnetometer MAG GEO-3 and its tests with leading domestic and foreign analogues. The main characteristics are given in the Table 2. The device is used for retrofitting networks, placement on spacecraft and small spacecraft of the CubSate type.

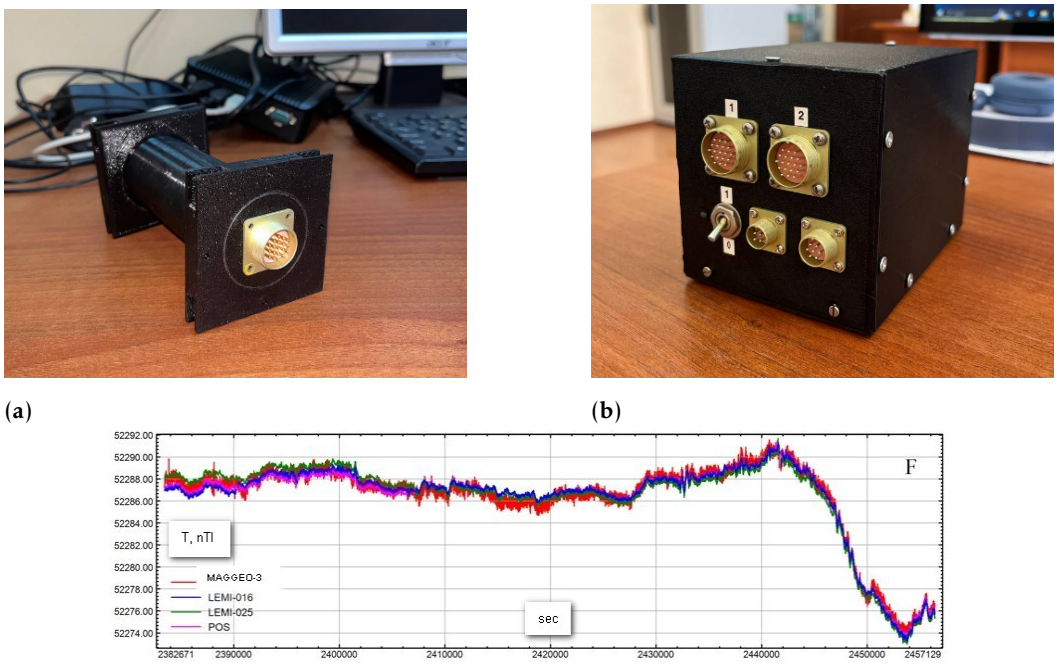

Figure 5. External view of the magnetic sensor, control unit and test results (comparison of the full magnetic field vector).

Table 2. The main characteristics of the magnetometer MAGGEO-3.

Characteristics	Value
Limits of relative measurement error, not more than	±0.5%
The standard deviation according to second measurements in one minute	±0.3 nT
The absolute error	±1 nT
Operating temperature range of the control unit, ranging	from −40 °C to 80 °C
The supply voltage from a DC source, within	12 V
Power consumption, no more than	5.0 W
Sensor weight	300 g

3.2. Development of an ionosonde for vertical sensing of the ionosphere

To replace the network ionosonde "Parus-A", a new generation of complex with automatic ionogram processing, remote access for maintenance via telemetry, a new compact antenna-feeder complex (AFC) 60×60 m, domestic software and ECB is being developed (Figure 6).

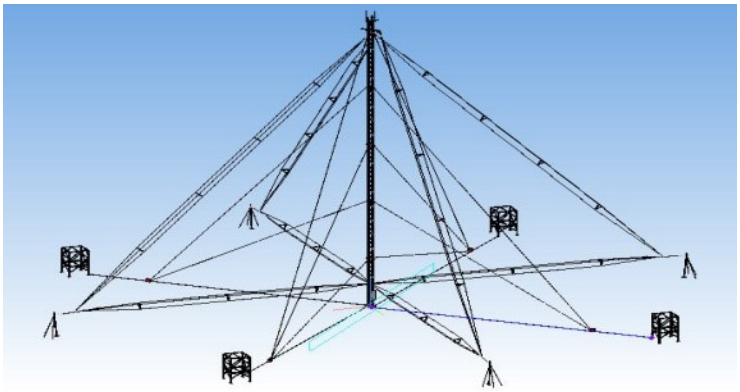

Figure 6. Antenna-feeder complex of the new ionosonde.

Ionosondes are designed to determine the heights of reflection of radio waves of various frequencies from the ionosphere, the critical frequencies of the ionosphere and the altitude distribution of electron concentrations for consumers and research.

3.3. Development of hardware and software complex of high-orbit radiotomography

Ionospheric radiotomography methods are used to determine radiotomographic sections of the ionosphere and three-dimensional distributions of the ionospheric electron concentration (TEC). This method is implemented in the of hardware and software complex of high-orbit radiotomography. The technical and metrological characteristics of the "Venus" package being developed (Figure 7) are shown in Table 3. The hardware and software complex of high-orbit radiotomography allows you to build electronic maps of the critical frequency f0F2; PES, flicker indices (scintillation) RoTi and other characteristics of the ionosphere in real time.

Table 3. The main characteristics of the of hardware and software complex of high-orbit radiotomography "Venus".

Characteristics	Value
Operating frequency range	1–20 MHz
Average radiation power, no more than	60 W
Pulse duration	100–200 μs
The error in measuring the amplitudes of reflected signals	1 dB
The error of linking time to the time scale	1 μs

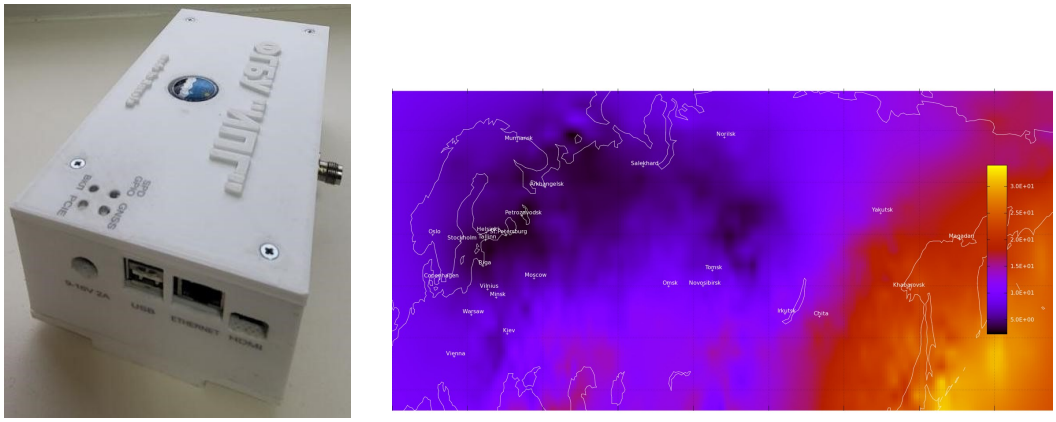

(a) **(b)**

Figure 7. PAK VORT "Venus" and TEC map.

3.4. Development of target equipment for small spacecraft of the CubSate type

The development of small spacecraft is rapidly gaining momentum [*Bragina et al.*, 2023; *Melnikova et al.*, 2021]. Targeted equipment for small spacecraft of the CubSate heliogeophysical type is being developed. The FSBI IPG has developed the GAMVEKI-GM charged particle detectors, which have passed flight qualification on the Khors No. 1 and No. 2 spacecraft (launched and successfully operating in a 550 km circular polar orbit since June 2023) [*Mayorova et al.*, 2024b]. These devices monitor space weather by measuring the density of electron and proton fluxes in the Earth's radiation belts using Geiger-Muller counters. (Figure 8). In the future, small spacecraft with magnetometric systems are being prepared for development [*Bragina et al.*, 2022].

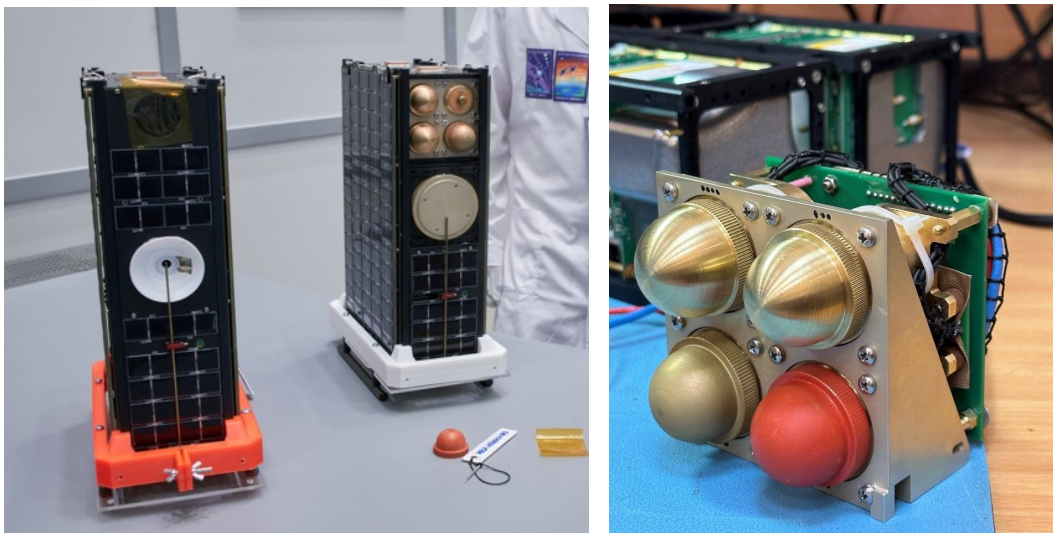

(**a**) (**b**)

Figure 8. 6U-XL CubSate "Khors" MCA No. 1, 2 with GAMVEKI detectors.

All the above developments are technologically innovative and are performed mainly on domestic ECBs and software. An important direction in ensuring the accuracy and reliability of measurements is the metrological support of geophysical observations. FSBI IPG, as the basic organization of Roshydromet for metrology in its field, ensures the unity of measurements on the ionospheric, magnetic and heliogeophysical observation network [*Minligareev et al.*, 2016; 2021].

4. Conclusion

Thus, the instrumental provision of ionospheric, magnetic and heliogeophysical observations on the state observation network is important for monitoring the geophysical situation in Russia. This is especially true during periods of peak solar activity. The above-ground part needs to be upgraded with outdated equipment.

FSBI "IPG" has developed and is preparing for production fluxgate magnetometers for magnetic observatories (with an error of ±0.5%), which are not mass-produced in Russia, as well as vertical sounding ionosondes in the range of 1–20 MHz, the production and scientific development of which are currently absent in our country. Together with the leading universities of the country (Bauman Moscow State Technical University, Lomonosov Moscow State University), a new unique direction has been mastered — the development of devices for heliogeophysical spacecraft of the CubeSat format, which have both a scientific basis and new technological solutions (based on the results of measurements, it is possible to install a sensor inside the device instead of an external rod) [*Bragina et al.*, 2025].

Based on previous and current developments shown in the publication in the Federal State Budgetary Institution "IPG", by decision of ICAO and the International Commission on Space Weather, one of the four global world centers of space weather for ensuring the safety of air navigation CRC has been operating since 2021. The CRC center carries out duty around the planet once every 2–2.5 months, based on high international standards for dangerous space weather phenomena (solar flares, magnetic storms affecting communications and positioning, the danger of radiation load during air travel) and issues warnings on dangerous heliogeophysical phenomena to automated air traffic control centers in real time.

References

Avdyushin S. I., Vazhenin A. A., Ginzburg E. A., et al. Measurements of fluxes of ionizing radiation characteristics in near-space on hydro-meteorological satellite "Meteor-3M" // Spetsial'naya Tekhnika. — 2014. — No. 2. — P. 45–54. — (In Russian).

Bragina A. A., Arutyunyan D. A., Minligareev V. T. Review of heliogeophysical space system with magnetometric equipment // Heliogeophysical research. — 2022. — No. 34. — P. 40–48. — DOI: 10.5425/2304-7380_2022_34_40. — (In Russian).

Bragina A. A., Minligareev V. T., Bogodyazh S. D. Prospects for the Development of Heliogeophysical Satellite Observations on Small Satellites // Cosmic Research. — 2025. — Vol. 63, no. 1. — P. 94–102. — DOI: 10.1134/S0010952524601488.

Bragina A. A., Minligareev V. T., Bogodyazh S. D. Prospects for the development of small spacecraft constellations for space weather monitoring // Eleventh International Scientific and Technical Conference "Current Problems of Creating Space Systems for Remote Sensing of the Earth". — Moscow : VNIIEM Corporation, 2023. — P. 38–39. — (In Russian).

Mayorova V., Minligareev V., Akhmedshin R., et al. Flight Experience in Space Weather Monitoring Using CubeSats // 31st IAA Symposium on Small Satellite Missions. — International Astronautical Federation (IAF), 2024a. — P. 174–179. — DOI: 10.52202/078365-0020.

Mayorova V., Minligareev V., Akhmedshin R., et al. Flight Experience in Space Weather Monitoring Using CubeSats // 31st IAA Symposium on Small Satellite Missions. — International Astronautical Federation (IAF), 2024b. — P. 174–179.

Melnikova V., Mayorova V., Tenenbaum S., et al. Experience in the Development and Operation of the Nanosatellites for Space Weather Monitoring // 72nd International Astronautical Congress 2021. — United Arab Emirates : IAF, 2021.

Minligareev V. T., Kachanovsky Y. M., Panshin E. A., et al. Creation of a distributed reference base for radiometric equipment of heliogeophysical complexes of hydrometeorological spacecraft // Measurements World. — 2016. — No. 1. — P. 51–59. — (In Russian).

Minligareev V. T., Kachanovskii Y. M., Kravchenok V. L., et al. Metrological support for the roshydromet ionospheric and magnetic observation network // Meteorologiya i Gidrologiya. — 2021. — No. 4. — P. 43–52. — DOI: 10.52002/0130-2906-2021-4-43-52. — (In Russian).

Minligareev V. T., Kalishin A. S. Monitoring geophysical condition in the Arctic zone of Russian Federation // Proceedings of the scientific and practical conference "Prevention and elimination of emergency situations in the Arctic zone of the Russian Federation". — Murmansk : MASU, 2023a. — P. 224–226. — (In Russian).

Minligareev V. T., Vishnyakov D. D., Kalishin A. S. Space weather hazards impact on technical means and systems // Tekhnologii grazhdanskoy bezopasnosti. — 2023b. — Vol. 20, 3(77). — P. 30–34. — (In Russian).

Russian Journal of Earth Sciences

Special Issue: "Data Science, Geoinformatics and Systems Analysis in Geosciences"

Artificial Neural Network for Downward Continuation of Anomalous Magnetic Fields

R. A. Rytov[1]

[1]Pushkov Institute of Terrestrial Magnetism, Ionosphere and Radio Wave Propagation of the Russian Academy of Sciences (IZMIRAN), Moscow, Troitsk, Russia

* **Correspondence to:** Rytov Ruslan Alekseevich, morozovalexey@yandex.ru

Abstract: The downward continuation of an anomalous magnetic field is used for many applications in geophysics. However, such a problem is ill-posed, so it does not have a unique and stable solution. In this paper, we propose an artificial neural network architecture for the downward continuation of the vertical component of an anomalous geomagnetic field measured in a plane at a given height. The inverse problem is solved here by a direct method: the neural network is trained to reconstruct such a distribution of the magnetic field B_{down}, which after a stable upward continuation corresponds to the measured field B_{up}. The performance of the neural network was demonstrated using the example of an anomalous geomagnetic field obtained using the Enhanced Magnetic Model.

Keywords: stray magnetic field, magnetic anomaly, untrained neural networks, inverse modeling, downward continuation.

Citation: Rytov, R. A. (2025), Artificial Neural Network for Downward Continuation of Anomalous Magnetic Fields, *Russian Journal of Earth Sciences*, 25, ES2024, EDN: BUDHDY, https://doi.org/10.2205/2025ES000996

1. Introduction

The downward continuation of the magnetic field is an important applied task, primarily for general navigation and for directional drilling [*Buchanan et al.*, 2013; *Kaji et al.*, 2019]. For example, during aeromagnetic surveying, the magnetic field is measured at a given height above the Earth's surface, but for technical applications the magnetic field must be known at the ground level and several kilometers deeper.

The geometry of the problem is schematically illustrated in Figure 1. Magnetized bodies create an anomalous magnetic field B_{up} in the plane (x, y) at a certain height above the ground level. The problem is to calculate, from the measured magnetic field B_{up}, the magnetic field B_{down} at a depth ΔZ, closer to the magnetized sources.

The magnetic fields in the upper and lower planes are related through the well-known integral equation [*Blakely*, 1995]

$$B_{\text{up}}(x,y) = \frac{\Delta z}{2\pi}\int_{-\infty}^{\infty}\int_{-\infty}^{\infty}\frac{B_{\text{down}}(x',y')}{\left[(x-x')^2+(y-y')^2+\Delta z^2\right]^{3/2}}\mathrm{d}x'\mathrm{d}y' = A\left[B_{\text{down}}\right],\ \Delta z > 0. \quad (1)$$

Here, if the magnetic field below is known, B_{down}, then the calculation of the field in the upper plane, B_{up}, is performed directly using the operator of upward continuation, $B_{\text{up}} = A[B_{\text{down}}]$. However, in order to calculate the magnetic field in the lower plane B_{down} from the known distribution in the upper plane B_{up}, it is necessary to construct the inverse operator of downward continuation, $B_{\text{down}} = A^{-1}[B_{\text{up}}]$.

An equation of type (1) is a Fredholm integral equation of the first kind. If the magnetic field B_{down} is unknown, then this is a linear inverse problem, which, generally speaking, does not have a unique and stable solution [*Blakely*, 1995; *Tikhonov et al.*, 1977].

Research Article

Received: 15 November 2024
Accepted: 15 April 2025
Published: 23 May 2025

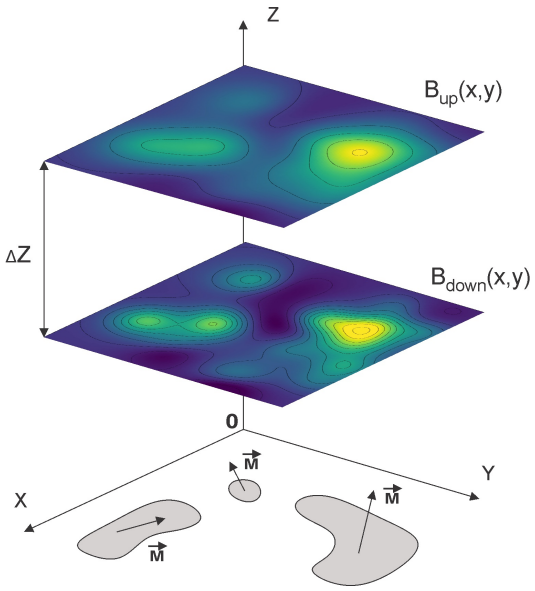

Figure 1. Schematic representation of the magnetic field downward continuation problem.

Although it is possible to obtain an analytical solution specifically for an equation of type (1) using the Fourier transform, however, recalculating the magnetic field downwards using such a solution is unstable [*Blakely*, 1995]. Therefore, to find an approximate solution to equation (1), some numerical methods are usually used.

2. Neural network architecture

One way to find an approximate solution is to construct a downward continuation operator A^{-1} using a stable solution of the forward problem. Artificial neural networks, which are universal approximators, may be well suited for this purpose [*Nielsen*, 2015]. Neural network models have already been successfully applied to solve a number of inverse problems in magnetism and stray magnetic field modeling [*Coskun et al.*, 2022; *Dubois et al.*, 2022; *Pollok et al.*, 2021; 2023].

In this paper, we propose for the scalar magnetic field downward continuation the neural network architecture schematically shown in Figure 2. Here, the neural network is trained to act as a downward continuation operator A^{-1}. In the first step, the neural network calculates a trial magnetic field in the lower plane, B_{down}, using the known magnetic field distribution B_{up}. After the calculation, the trial field B_{down} is used to directly calculate the field in the upper plane, B_{trial}, at a height of ΔZ using the stable upward continuation operator A. Finally, the loss between the known field B_{up} and the calculated trial B_{trial} is calculated, which is then used to train the neural network using the backpropagation method. The neural network is trained until the error becomes less than a certain small value.

It is worth noting that a computationally efficient way to calculate convolution-type integrals (1) is to use the Fourier transform [*Blakely*, 1995]

$$F[B_{\text{up}}] = F[B_{\text{down}}]\mathrm{e}^{-\Delta Z|k|}, \tag{2}$$

where $F[B]$ denotes the Fourier transform of the magnetic field B, and the modulus of the wave number $|k| = \sqrt{k_x^2 + k_y^2}$. The calculation of the field in the upper plane B_{up}, in the developed neural network training scheme, was carried out using the fast Fourier transform.

Numerical tests have shown that the neural network structure can be quite simple to implement the scheme in Figure 2, and its structure can be more or less arbitrary. Here, a convolutional neural network was created to work with 512×512 pixel images. It contains an input layer, three Conv2D layers with a 2×2 pixel kernel, 32 filters, and linear activation functions. Each convolutional layer is followed by an AveragePooling layer with a 2×2 pixel

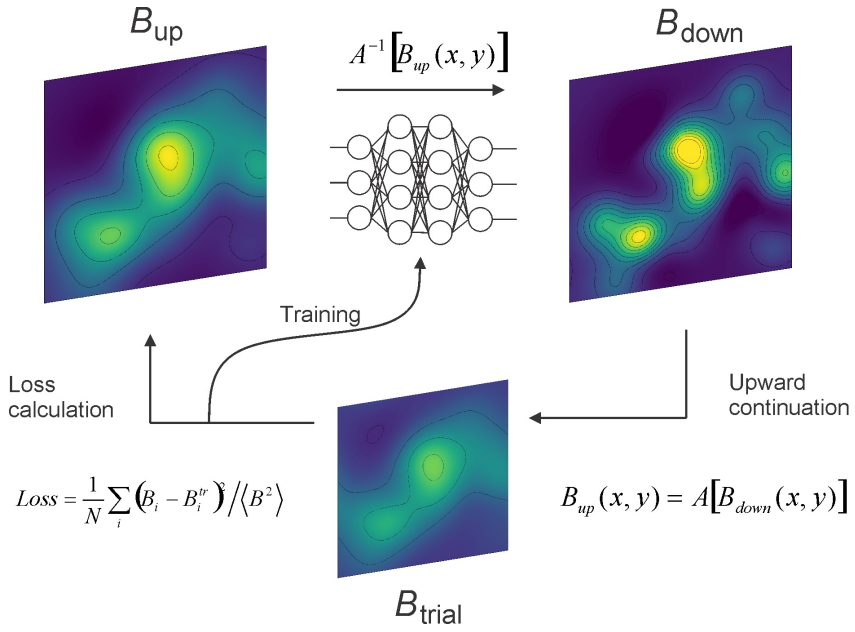

Figure 2. Architecture of a neural network for magnetic field downward continuation using stable upward continuation operator.

kernel, and an output layer. The standard normalized mean squared error function was used to calculate the loss Loss = $\frac{1}{N}\sum_i (B_i - B_i^{\text{tr}})^2 / \langle B^2 \rangle$, where B_i is the known field at point i, B_i^{tr} is the trial field at point i, $\langle B^2 \rangle$ is the mean square of the known anomalous field, N is the total number of measurement points.

The neural network was implemented using the tensorflow library [*Abadi et al.*, 2016] and the model was trained using the Adam stochastic optimization algorithm [*Kingma et al.*, 2014]. The training was carried out on a simple personal computer with an Intel processor Core i7-9700 and NVIDIA graphics card GeForce GTX 950.

This type of neural networks called untrained neural network in opposite to traditional trained on large datasets models [*Dubois et al.*, 2022]. Untrained neural network does not require a database for training, which is its advantage. Also, the accuracy of the magnetic field downward continuation is controlled while training.

This method assumes that magnetized bodies are located under the plane of magnetic field calculation. If the plane of the calculation field is located in the magnetized bodies area, this method may not work correctly.

3. Synthetic example

The performance of the neural network was tested on the anomalous magnetic field of the EMM model [*The National Centers…*, 2018]. The EMM model is compiled from satellite, marine, aeromagnetic and ground-based data. It represents both the main and anomalous magnetic fields of the Earth using the Gaussian model with 790 spherical harmonics, which corresponds to a spatial resolution of about 50 km. In order to isolate the anomalous magnetic field, the coefficients of the first 16 harmonics in the EMM model were set to zero. The model anomalous magnetic field was calculated at sea level on an equidistant grid in of 512×512 points with a step of 2 km. Then, using (2), the magnetic field was extended upward to a height of ΔZ = 4–24 km, and then extended downward using the developed method.

In Figure 3a, the region in which the vertical component of the anomalous magnetic field was calculated is highlighted. The dynamics of the loss function during neural network training is shown in Figure 3b for heights ΔZ = 4–24 km. The series Figure 3c–3e show the distribution of the anomalous magnetic field at heights of 12, 8, 4 km, the results of the downward continuation of the vertical component of the magnetic field, and the error

distribution between true and estimated magnetic fields. For a height of ΔZ = 4 km the average error is 15 nT, for a height of ΔZ = 8 km the average error is 30 nT, for a height of ΔZ = 12 km the average error is 45 nT.

Figure 3b shows that the loss here quickly reaches values below 0.4, followed by a smooth decrease in the loss to values of 0.2 and below. The total calculation time of 5000 training iterations on a personal computer does not exceed 10 minutes.

In Figure 3c–3e it is evident that with increasing altitude the efficiency of the downward continuation of the field decreases. This is easily explained by equation (2), which shows that the decrease in the intensity of the magnetic anomaly exponentially depends on the product of the wave number of its constituent harmonics k and the altitude ΔZ.

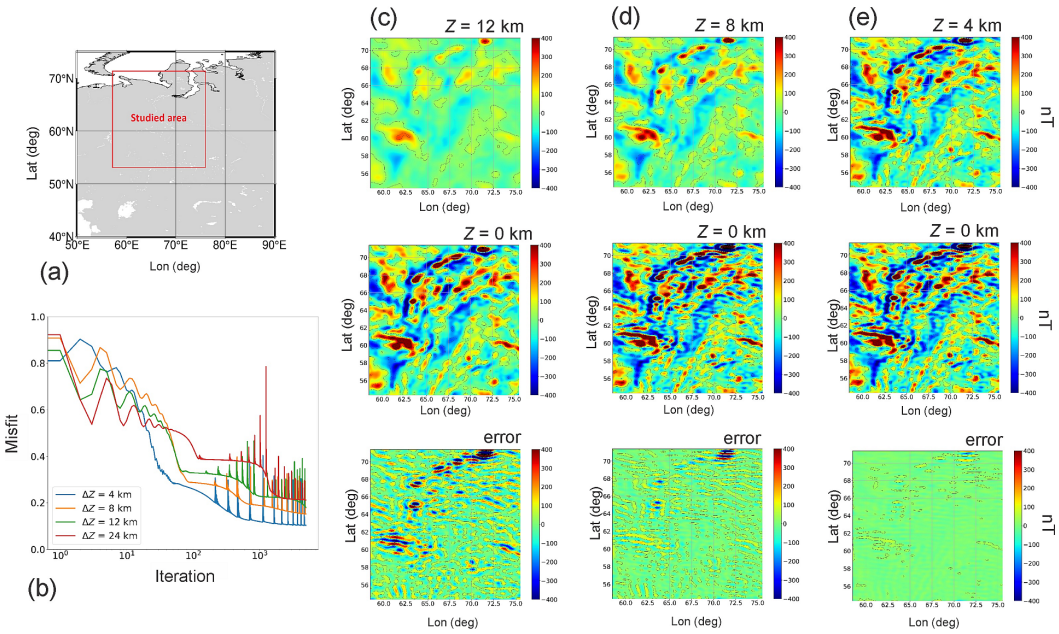

Figure 3. (a) The region in which the vertical component of the anomalous magnetic field was calculated; (b) The dynamics of the loss function during the training of the neural network for heights ΔZ = 4–24 km; the distribution of the anomalous magnetic field at a given height, the result of magnetic field downward continuation and the error for ΔZ = 12 km (c), ΔZ = 8 km (d), ΔZ = 4 km (e).

For example, the intensity of harmonics with a wavelength l = 50 km decreases by a factor of e at an altitude $\Delta Z \approx 8$ km. The high-frequency contribution to the anomalous field decreases first with increasing altitude ΔZ, which is reflected in the efficiency of the downward continuation of the anomalous magnetic field.

4. Conclusions

In this paper, a neural network model was developed for downward continuation of the anomalous magnetic field towards the location of magnetic sources. The performance of the neural network was demonstrated using a synthetic example. The accuracy of magnetic field reconstruction depends on the distance ΔZ, for the demonstrated examples the error did not exceed 45 nT for ΔZ = 4–12 km. Further improvement of the algorithm is planned.

Acknowledgments. The study was supported by the Russian Science Foundation grant No. 24-27-00250.

References

Abadi M., Agarwal A., Barham P., et al. TensorFlow: Large-Scale Machine Learning on Heterogeneous Distributed Systems. — 2016. — DOI: 10.48550/arXiv.1603.04467.

Blakely R. J. Potential Theory in Gravity and Magnetic Applications. — Cambridge University Press, 1995. — DOI: 10.1017/cbo9780511549816.

Buchanan A., Finn C. A., Love J. J. Geomagnetic referencing the real-time compass for directional drillers // Oilfield Review. — 2013. — Vol. 25, no. 3. — P. 32–47.

Coskun U. H., Sel B., Plaster B. Magnetic field mapping of inaccessible regions using physics-informed neural networks // Scientific Reports. — 2022. — Vol. 12, no. 1. — DOI: 10.1038/s41598-022-15777-4.

Dubois A. E. E., Broadway D. A., Stark A., et al. Untrained Physically Informed Neural Network for Image Reconstruction of Magnetic Field Sources // Physical Review Applied. — 2022. — Vol. 18, no. 6. — DOI: 10.1103/physrevapplied.18.064076.

Kaji C. V., Hoover R. C., Ragi S. Underwater Navigation using Geomagnetic Field Variations // 2019 IEEE International Conference on Electro Information Technology (EIT). — IEEE, 2019. — P. 1–6. — DOI: 10.1109/eit.2019.8834192.

Kingma D. P., Ba J. A. Adam: A Method for Stochastic Optimization. — 2014. — DOI: 10.48550/ARXIV.1412.6980.

Nielsen M. A. Neural networks and deep learning. — San Francisco, CA, USA : Determination press, 2015. — P. 15–24.

Pollok S., Bjørk R., Jørgensen P. S. Inverse Design of Magnetic Fields Using Deep Learning // IEEE Transactions on Magnetics. — 2021. — Vol. 57, no. 7. — P. 1–4. — DOI: 10.1109/tmag.2021.3082431.

Pollok S., Olden-Jørgensen N., Jørgensen P. S., et al. Magnetic field prediction using generative adversarial networks // Journal of Magnetism and Magnetic Materials. — 2023. — Vol. 571. — DOI: 10.1016/j.jmmm.2023.170556.

The National Centers for Environmental Information. — 2018. — URL: https://www.ngdc.noaa.gov/geomag/geomag.shtml (visited on 10/14/2024).

Tikhonov A. N., Arsenin V. Y. Solutions of ill-posed problems. — New York : Winston, 1977.

Russian Journal of Earth Sciences

Special Issue: "Data Science, Geoinformatics and Systems Analysis in Geosciences"

70 Years of the Geophysical Center of the Russian Academy of Sciences: History and Current State

Anatoly Soloviev[1,2,*], **Alexei Gvishiani**[1,2]

[1] Geophysical Center of the Russian Academy of Sciences, Moscow, Russian Federation
[2] Schmidt Institute of Physics of the Earth of the Russian Academy of Sciences, Moscow, Russian Federation
* **Correspondence to:** Anatoly Soloviev, a.soloviev@gcras.ru

Abstract: This paper outlines the main milestones in the evolution of the Geophysical Center of the Russian Academy of Sciences (GC RAS) over its 70-year history. It covers the period from the establishment of the Interdepartmental Committee for the Preparation and Conducting the International Geophysical Year under the Presidium of the USSR Academy of Sciences to the formation of a progressive academic institute. Particular attention is paid to the individuals who contributed to the development of the scientific potential of the institute. We discuss the modern directions of fundamental research of the GC RAS and emphasize those, which are highly demanded in solving crucial applied problems.

Keywords: International Geophysical Year, Russian Academy of Sciences, geophysical observatories, magnetic survey, geoinformatics, geomagnetism, space weather, radioactive waste disposal, Russian Arctic, artificial intelligence.

Citation: Soloviev A. and Gvishiani A. (2025), 70 Years of the Geophysical Center of the Russian Academy of Sciences: History and Current State, *Russian Journal of Earth Sciences*, 25, ES2025, EDN: FNTQZM, https://doi.org/10.2205/2025ES000999

Background

The first steps in coordinating worldwide research in geosciences were taken in the first half of the 19th century, including the discovery of new lands and the expedition of Alexander von Humboldt. However, the real onset of the international cooperation in geophysics dates back to August 1, 1882 when the First International Polar Year (IPY) started. This scientific program united 12 countries and coordinated 15 polar expeditions. Its research areas included studying the processes in the high latitudes of the Northern Hemisphere, weather, climate, ice drift and geomagnetic phenomena. Over 1882–1883, the President of the International Polar Commission was Heinrich von Wild, the Academician of the Saint Petersburg Academy of Sciences. 50 years later, the Second IPY started on August 1, 1932. It was aimed mainly at studying magnetic storms, ionosphere, cosmic rays and relationships with solar activity. Forty-four countries participated in the implementation of the Second IPY. During one year, more than 100 stations were deployed both in the Northern and Southern polar regions. Despite the general success of the two IPYs, some failures were also revealed. For instance, the neglect of providing the centralized, secure and reliable storage for the collected data led to their significant loss during World War II. Thus, both the achievements of the Second IPY and its faults confirmed the need for coordinated efforts by geophysicists around the world.

Research Article

Received: 15 November 2024
Accepted: 15 April 2025
Published: 23 May 2025

In 1952, the International Union of Geodesy and Geophysics (IUGG), International Union of Radio Science (URSI) and International Council of Scientific Unions (ICSU) put forward an initiative to conduct the International Geophysical Year (IGY) in 1957–1958. By the decision of the Council of Ministers of the USSR, the Interdepartmental Committee for the Preparation and Conducting the IGY under the Presidium of the USSR Academy of Sciences (IGY Committee) was created on July 19, 1954 (Figure 1). Academician Grigory Gamburtsev, a prominent geophysicist and Director of the Geophysical Institute of the USSR Academy of Sciences, was appointed Head of the IGY Committee. On July 5, 1955, the Council of Ministers of the USSR issued a decree defining the principles of geophysical data exchange with foreign partners, and also obliging industry to manufacture equipment for conducting IGY observations. Another important resolution on organizing and supporting research in Antarctica by the USSR conducted by international community in the course of IGY preparation was issued by the Council of Ministers of the USSR on July 13, 1955.

In 1955, Academician Ivan Bardin, Vice President of the USSR Academy of Sciences, became the Chairman of the IGY Committee. By that time, Academician Bardin had vast experience in managing the entire metallurgical industry of the country. Therefore, he was a worthy candidate for the position of the IGY Committee Chairman, which he held during the IGY (1957–1958) and until 1961. Four distinguished scientists were appointed Deputy Chairmen: Corresponding Member Vladimir Belousov (geotectonist), Corresponding Member Yuri Boulanger (gravimetrist), Professor Nikolay Pushkov (geomagnetist) and Doctor of Science Feophan Davitaya (climatologist). Professor Valeria Troitskaya (space physicist) was appointed Scientific Secretary of the IGY Committee.

The main goals of the IGY Committee were planning and coordination of complex geophysical research conducted under international projects and programs, and a comprehensive scientific approach to the objects under study. Another important task was establishing reliable and long-term data storage and free exchange of the data collected in the course of the IGY. More than 100 scientific organizations of the USSR took part in the IGY implementation. The IGY was the largest international scientific event of the mid-twentieth century. It united scientists from 67 countries, which at that time constituted 2/3 of the countries in the world.

Among the most outstanding results of the IGY, the following should be mentioned. Apparently, the pivotal outcome was the launch of the first artificial Earth satellite "Sputnik-1" on October 4, 1957, which marked the beginning of the space era (Figure 2a). Despite the absence of specific scientific equipment, the basic radio beacon installed onboard made it possible to obtain new knowledge about the ionosphere properties, including the density, distribution of electron density and its influence on the propagation of radio waves. Another important goal accomplished in the course of the IGY was the deployment of the unprecedented observational network of scientific stations in the Soviet Union (Figure 2b). These stations provided measurements covering all the thematic sections within the IGY Committee: Meteorology and Atmospheric Physics, Geomagnetism, Auroras, Solar Activity, Cosmic Rays, Ionosphere, Meteors, Longitudes and Latitudes, Oceanology, Glaciology, Seismology, Gravimetry, Rockets and Artificial Earth Satellites. For handling the vast volume of the observation results collected worldwide from all sections of the IGY program, the World Data Centers (WDCs) were established in the USA (WDC A) and USSR (WDC B) by the National Governments. The WDCs provided the unprecedented mechanism for ensuring data preservation and free access for researchers worldwide. Other important scientific results of the IGY included the empirical support of the radiation belts in the magnetosphere by Academician Sergei Vernov (USSR) and Prof. James Van Allen (USA).

The absolute success of the IGY encouraged the world community to extend the IGY to 1959. The Decree of Presidium of the USSR Academy of Science on October 21, 1958 obliged the Ministry of the Maritime Fleet, Main Directorate of the Hydrometeorological Service under the Council of Ministers of the USSR and other organizations and academies of sciences of the Soviet Union republics to ensure in 1959 the implementation of scientific research according to the plan approved by the IGY Committee. The studies of Antarctica in

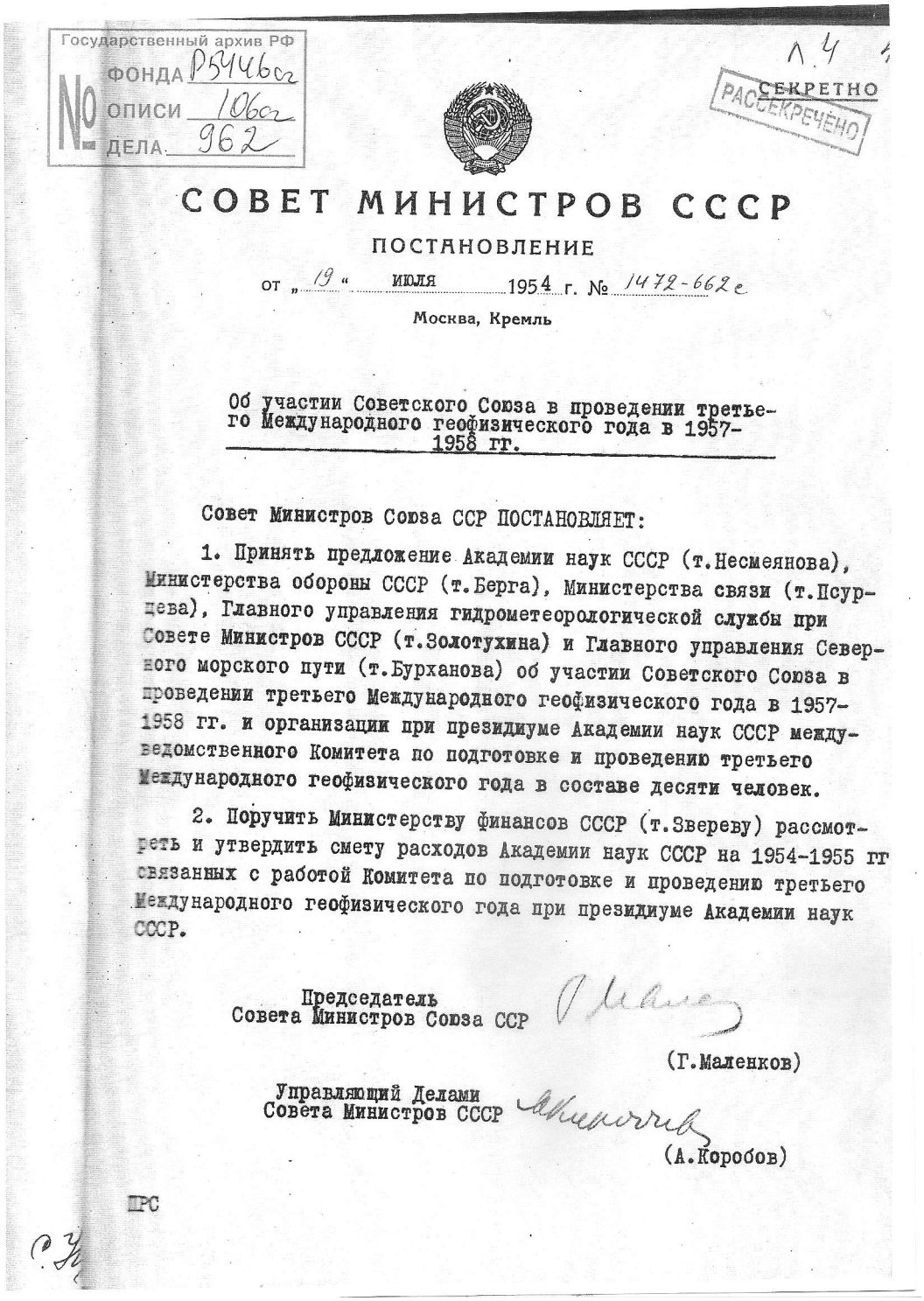

Государственный архив РФ
ФОНДА Р5446сг
ОПИСИ 106сг
ДЕЛА 962

СЕКРЕТНО
РАССЕКРЕЧЕНО

СОВЕТ МИНИСТРОВ СССР

ПОСТАНОВЛЕНИЕ

от „19" июля 1954 г. № 1472-662с

Москва, Кремль

Об участии Советского Союза в проведении третьего Международного геофизического года в 1957-1958 гг.

Совет Министров Союза ССР ПОСТАНОВЛЯЕТ:

1. Принять предложение Академии наук СССР (т.Несмеянова), Министерства обороны СССР (т.Берга), Министерства связи (т.Псурцева), Главного управления гидрометеорологической службы при Совете Министров СССР (т.Золотухина) и Главного управления Северного морского пути (т.Бурханова) об участии Советского Союза в проведении третьего Международного геофизического года в 1957-1958 гг. и организации при президиуме Академии наук СССР междуведомственного Комитета по подготовке и проведению третьего Международного геофизического года в составе десяти человек.

2. Поручить Министерству финансов СССР (т.Звереву) рассмотреть и утвердить смету расходов Академии наук СССР на 1954-1955 гг связанных с работой Комитета по подготовке и проведению третьего Международного геофизического года при президиуме Академии наук СССР.

Председатель
Совета Министров Союза ССР
(Г.Маленков)

Управляющий Делами
Совета Министров СССР
(А.Коробов)

ПРС

Figure 1. Decree of the Council of Ministers of the USSR on creation of the IPY Committee signed by Prime Minister Georgy Malenkov.

the fields of geophysics, geology and nature, as well as special measures for the processing of materials from Antarctic expeditions and the publication of scientific papers were especially valuable for the scientific community. The Computing Center of the USSR Academy of Sciences was assigned the task of processing the results of observations submitted by the IGY Committee [*Lyubovtseva et al.*, 2020].

(**a**) (**b**)

Figure 2. The first artificial Earth Satellite "Sputnik-1" launched on October 4, 1957 (a) and the map of Soviet scientific stations deployed in the course of the IGY, 1957–1958 (b).

To preserve and enhance the legacy of the IGY, the Interdepartmental Geophysical Committee (IGC) under the Presidium of the USSR Academy of Science was created in January 1961. The prescribed goals of the IGC were as follows:

- Coordination and planning of complex geophysical research under international projects and programs;
- Operation of WDC for Solar-Terrestrial Physics and WDC for Solid Earth Physics (since 1971) within the structure of the IGC;
- Ensuring the participation of the USSR in the relevant international organizations of the International Council of Scientific Unions (ICSU) and International Union of Geodesy and Geophysics (IUGG);
- International data exchange on planetary geophysics.

In 1961–1990, the Director of the IGC was Corresponding Member Vladimir Belousov, a well-known geologist and IUGG President (1960–1963). Over 1975–1985, the number of employees increased up to 91 people mainly due to new scientific workers of the WDCs. In 1980, 28 employees were under 30 years of age. An important organizational enhancement of that time was the creation of the temporary laboratory "Atomic and Subatomic Data Center". The Committee gradually became a full-fledged research institute.

In 1990, a well-known seismologist, Corresponding Member Gennady Sobolev became the Director of the IGC; he held this position until 2005. In June 1992, the IGC was renamed and transformed into the Geophysical Center of the Russian Academy of Sciences (GC RAS) within the structure of the Geoscience Department of the RAS and the name of the institution remains until now. All functions of the IGC were transferred to GC RAS. Additionally, GC RAS became responsible for data collection and exchange between World Data Centers worldwide and became a host for the National Geophysical Committee of IUGG. The research directions of the institute expanded towards seismology, earthquake prediction, geoecology and altimetry.

Geophysical Center RAS in its current status

A new era of the GC RAS development started when Academician Alexey Gvishiani became its Director in July 2005. He merged the Center of Geophysical Data Studies and Telematics Applications (CGDS, a department of the Schmidt Institute of Physics of the Earth RAS), which he headed at that time, with GC RAS. The CGDS included a powerful shared computing center, which became a part of the GC RAS facilities. Immediately after that, GC RAS was appointed a National coordinator of the Electronic Geophysical Year (eGY) Programme (2007–2008) initiated by IUGG on the 50th Anniversary of the IGY. Among other initiatives, eGY stimulated creation of international virtual laboratories.

GC RAS significantly expanded cooperation with many foreign institutions and increased its visibility and recognition in Russia and worldwide. The involvement of GC RAS in IUGG, ICSU, CODATA and the International Institute of Applied Systems Analysis (IIASA) was notably strengthened. Being CODATA Vice President (2002–2006), in 2005 Academician Gvishiani became the Chair of the CODATA National Committee in Russia. In 2014, he was elected as Vice Chairman of the IIASA Scientific Council. Later on he became an Acting Chair of the IIASA Council [*Gvishiani et al.*, 2018a,b, 2019a,b].

Under the leadership of Academician Gvishiani and his team, GC RAS became a full-scale multifunctional and multipurpose geophysical institute. The scope of the scientific research areas at the institute became even broader by developing fundamental and applied studies in the field of geophysics, geodynamics, geodesy, geoinformatics, system analysis and related Earth sciences and their information support. GC RAS has intensified field works including geophysical observations using ground based and airborne equipment for both fundamental and applied research. GC RAS has revived and coordinates high-precision geomagnetic observations in Russia. Since 2010, the network of geomagnetic observatories in Russia and near-abroad countries has been significantly expanded. The institute management pays much attention to intensive recruitment of young scientists. Because of the efficient management, GC RAS was classified as a first category institution by the Ministry of Science and Higher Education. Academician Gvishiani's directorship lasted until 2018. Figure 3 depicts portraits of all Chairs and Directors from 1954 to 2018 [*Gvishiani et al.*, 2021, 2020a,b; *Lyubovtseva et al.*, 2019, 2022].

Full member of the AS of the USSR Grigory Gamburtsev

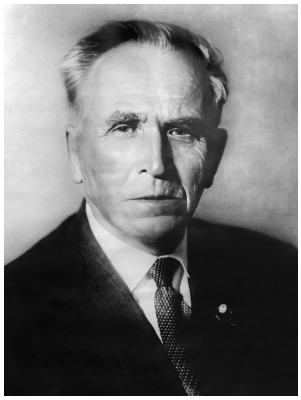

Vice President and Full member of the AS of the USSR Ivan Bardin

Correspondent member of the AS of the USSR Vladimir Belousov

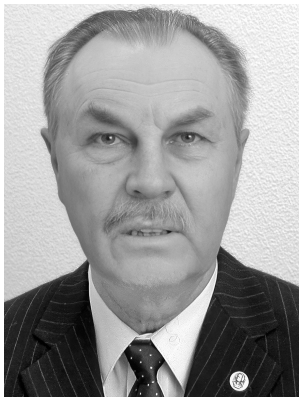

Correspondent member of the RAS Gennady Sobolev

Full member of the RAS Alexei Gvishiani

Figure 3. Chairs of IGY Committee, IGC and Directors of GC RAS over 1954–2018.

GC RAS has become a key scientific organization in solving a number of important applied problems for industries. Below we mention some of them. In particular, GC RAS provides the full range of services ensuring the geomagnetic support of high-tech directional drilling process, which is now an essential part of oil and gas production. It includes ground and airborne high-precision geomagnetic surveys, deployment of magnetic observatories, a complete description of static and time-varying magnetic fields in a three-dimensional environment, and a forecast of geomagnetic disturbances. In also involves artificial intelligence methods for real-time multi-criteria recognition of magnetic activity and specific IT infrastructure for handling Big Data, which together form the MAGNUS (Monitoring and Analysis of Geomagnetic aNomalies in Unified System) software-hardware system. This approach provides precision navigation of the drill string, which achieves hitting the target with an error of 3 m at a distance of 15 km from the wellhead. This science-driven result significantly contributes to increasing the efficiency of mineral deposit development. The expansion of GC RAS applications for the oil and gas industry triggered the creation of a new Geophysical Monitoring Sector in 2023, headed by Dr. Dmitry Kudin since that time. Figure 4 shows a map of the oil and gas fields where the relevant GC RAS services are being introduced. The map also shows the network of magnetic observatories maintained by GC RAS and regional research institutions.

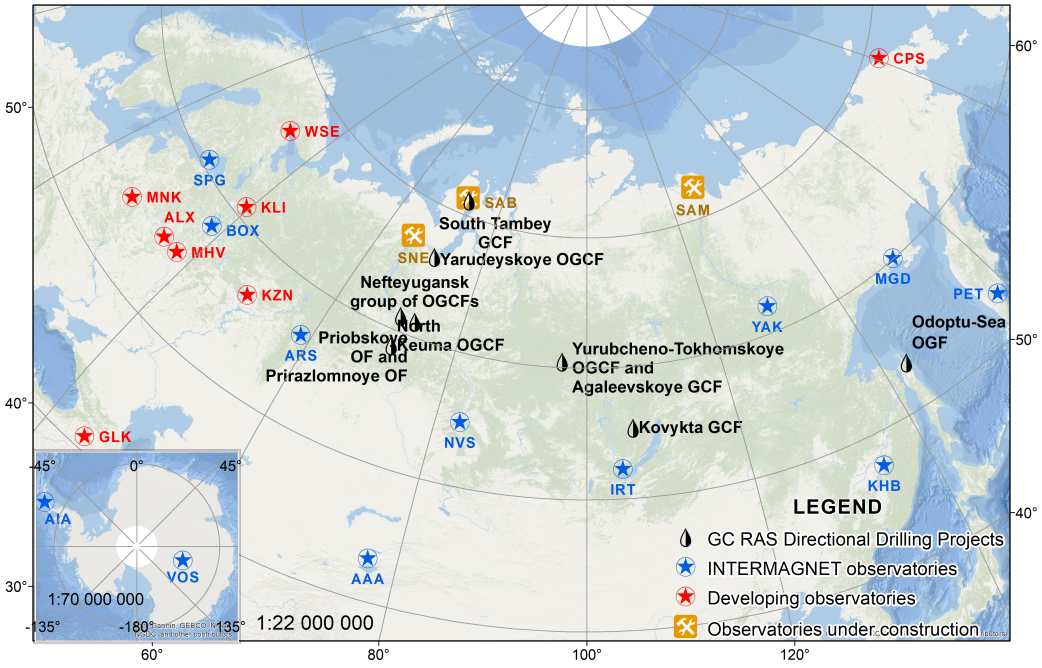

Figure 4. Map of oil and gas fields where GC RAS provides geomagnetic support technology for directional drilling, and magnetic observatories in Russia and neighboring countries, which transmit data to Analytical Geomagnetic Data Center at GC RAS.

The applied geodynamics researches of GC RAS are highly demanded by the nuclear industry. The results obtained in the field of studying the modern movements and modeling the stress-strain state of the Earth's crust as well as seismic hazard assessment are used for justification of geoecological safety of highly radioactive waste disposal. In particular, GC RAS is responsible for estimating the stability of the geological environment in the area of construction of the underground research lab in the Nizhnekansky massif for monitoring the disposal of highly radioactive waste (Figure 5). GC RAS does the full package of works, including both field and office research to summarize experimental and theoretical materials.

Figure 5. Construction of the underground research lab in the Nizhnekansky massif for monitoring the disposal of highly radioactive waste (https://strana-rosatom.ru/).

A number of geoinformatics products have been developed for the transport and energy industries. They include electronic atlas on climate change in the Russian Arctic since 1950 and its forecast up to 2100 for the Russian Railways. This atlas contains more than 1000 maps and provides information on spatiotemporal variability of the following hydrometeorological parameters both for vast regions and along railway mainlines: air temperature at the surface, atmospheric precipitation, wind speed at the surface, soil temperature, soil moisture content, air humidity, and snow thickness (Figure 6a). Another product is the online system for the short-term forecast of aurora intensity and auroral oval position (Figure 6b). It allows to predict the locations of excitation of the intense geomagnetically induced currents harmful for railways, power transmission grids and gas pipelines.

GC RAS is the only manufacturer in Russia of the hardware-software system ORBUS for interactive spherical visualizations. It enables visualizing various dynamic global processes of the stars, planets and Earth (natural and anthropogenic) on a sphere up to 1 m radius. This system has been manufactured and installed in several museums, universities, space agencies and other organizations as well as at many exhibitions in Russia and abroad (Figure 7). All the above-mentioned activities stimulated the significant expansion of the fleet of scientific instrumentation.

Since 1998, GC RAS publishes a peer-reviewed "Russian Journal of Earth Sciences" (RJES), which covers all areas of the Earth sciences and interdisciplinary results integrating the achievements of relevant scientific disciplines (https://rjes.ru/). Dr. Andrey Grachev (DSc) and Dr. Vitaly Nechitailenko (PhD) greatly contributed to the development of the journal in its infancy. Starting from 2018, the RJES Editor-in-Chief is Academician Alexey Gvishiani. The languages of this fully online journal are English and Russian. For today, authors from more than 10 countries have published more than 800 papers in it (Figure 8). Over the last 10 years, RJES has attracted more than 20,000 readers. The journal is indexed in the following main bibliographic databases: Scopus (Q3), Web Of Science (Q4), "White List" (Q2) and RSCI (Q1). It publishes special issues on request and admits urgent publications, exceeded size and translation service for fee. In his capacity of the head of the GC RAS Electronic Publications Laboratory Dr. Ernest Kedrov is a prominent driving force of the RJES "engine".

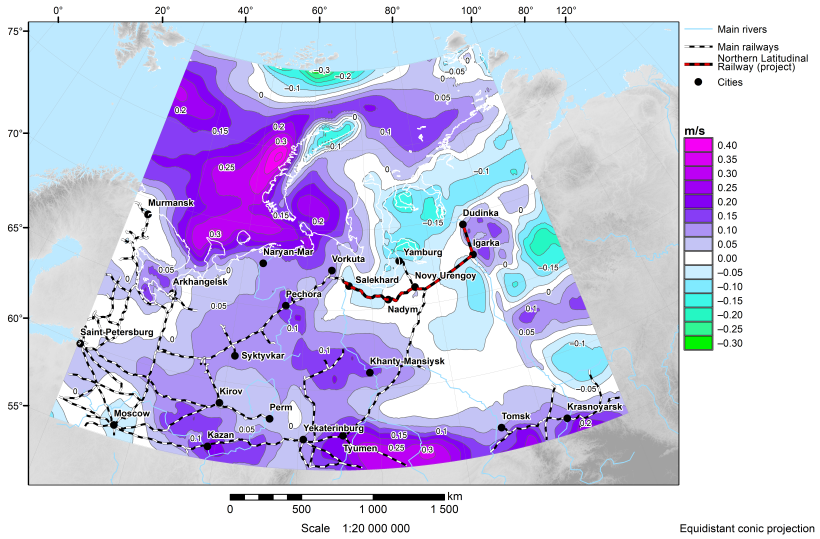

(**a**)

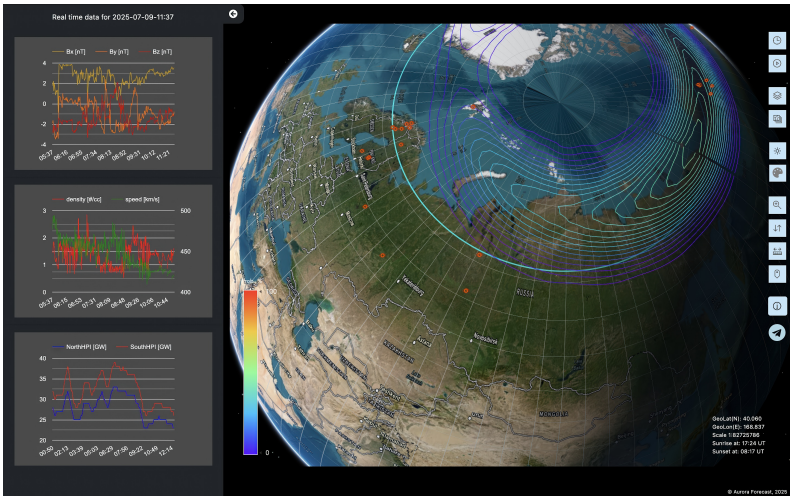

(**b**)

Figure 6. Map of the wind speed change between 2010–2021 and 1980–1989 from the Electronic Atlas on Climate for the Russian Arctic [*Gvishiani et al.*, 2023] (a) and short-term forecast of aurora intensity and auroral oval position using the online system https://aurora-forecast.ru/ (b).

Scientific achievements of GC RAS are regularly highlighted by the President of RAS and Head of RAS Geoscience Division and reported to the Russian Government on a yearly basis. In 2017–2024, these achievements were:

1. Recognition of the secular acceleration pulses of the core geomagnetic field at the core-mantle boundary using magnetic observatory data (2017);
2. Algorithm for sequential recognition of the earthquake prone areas (2017);
3. Creation of the stochastic seismicity model with exponential distribution of the earthquake productivity (2019);
4. Studying the fine structure of geomagnetic disturbances and geomagnetically induced currents in power grids (2019);
5. A new model of the geothermal heat flow for the Arctic (2022);
6. The most complete and representative catalog of earthquakes in the Russian Arctic with a unified magnitude scale (2023);
7. Discovery that the boundary between the North American and Eurasian lithospheric plates represents a broad diffuse zone in Siberia (2024).

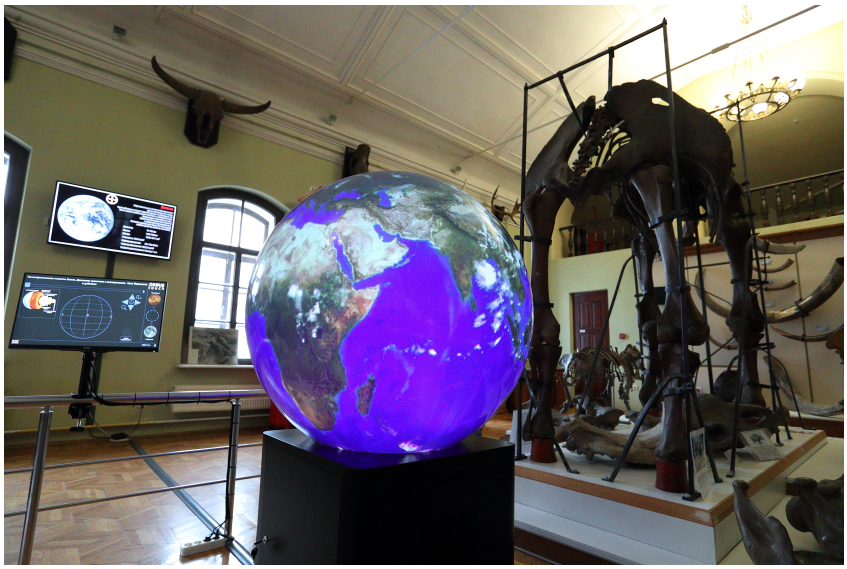

(**a**) (Photo by M. Zakharov)

(**b**)

Figure 7. Hardware-software system ORBUS installed at the museum of Kazan Federal University (a) and exhibition "Russia" in Moscow (b).

Since 2016, GC RAS organizes annual International and All-Russian Schools of Young Scientists. So far, more than 700 eminent lecturers and young researchers attended these events from more than 14 regions of Russia and abroad (Armenia, France, Germany, Italy, UK, Uzbekistan, …). Since 2021, a particular emphasis is placed on the study of natural processes in the Arctic (Figure 9).

For the intense knowledge exchange in geosciences, the institute organizes GC RAS Online Scientific Seminar on a biweekly basis since 2016. Prominent Professor Alexey Lushnikov chaired the Seminar in 2016–2021, and afterwards Academician Alexey Gvishiani took over. More than 100 seminar's online meetings have been held so far where more than 120 reports from Russia and abroad have been made. In total, the Seminar has attracted more than 300 participants, which makes it all-Russian event. A particular attention is paid to involving young scientists. The GC RAS researchers quite often appear in mass media reports and broadcasts. Some screen shots over the last several years along with media sources are given in Figure 10.

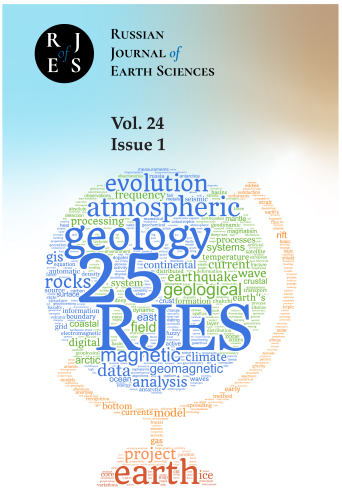

Figure 8. Cover of the 25th Anniversary issue of the RJES.

(**a**) (Photo by M. Zakharov)

(**b**)

Figure 9. Attendees of the All-Russian School of Young Scientists "System Analysis of the Natural Process Dynamics in the Russian Arctic" organized by the GC RAS in 2022 (a) and 2023 (b).

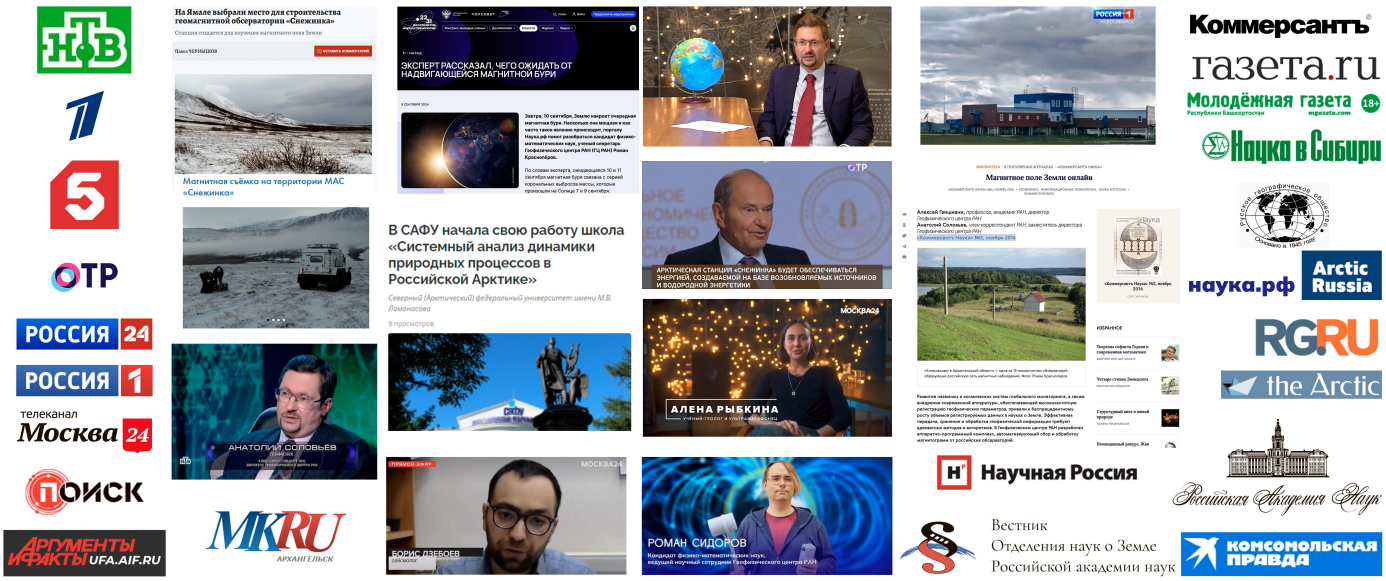

Figure 10. Screen shots of mass media reports and broadcasts featuring the GC RAS staff and media sources.

In 2018, the GC RAS management was renewed [*Solovieva and Gvishiani*, 2022; *Solovieva and Nikitina*, 2025]. Anatoly Soloviev, Corresponding Member of RAS, successfully headed the institute during his first term in 2018–2024. In September 2024, he was re-elected and appointed for the second 5-year term. Since 2017, Academician Alexei Gvishiani serves as Chief Scientist and Scientific Council Chair [*Kedrov*, 2023]. Dr. Boris Dzeboev (DSc) is Deputy Director for Science, Maxim Pasishnichenko is Deputy Director for General Issues and Dr. Roman Krasnoperov (PhD) is Scientific Secretary. The GC RAS management team is shown in Figure 11. The present day organizational structure of the institute is shown in Figure 12. GC RAS possesses a large fleet of modern world-class scientific equipment, which is essential in the activities of all structural divisions.

Figure 11. GC RAS management team as of 2024: Anatoly Soloviev, RAS Corr. Member, Director (2018–2024, re-elected 2024); Alexei Gvishiani, RAS full member, Chief Scientist, Scientific Council Chair; Boris Dzeboev, DSc, Deputy Director for Science; Maxim Pasishnichenko, Deputy Director for General Issues; and Roman Krasnoperov, PhD, Scientific Secretary.

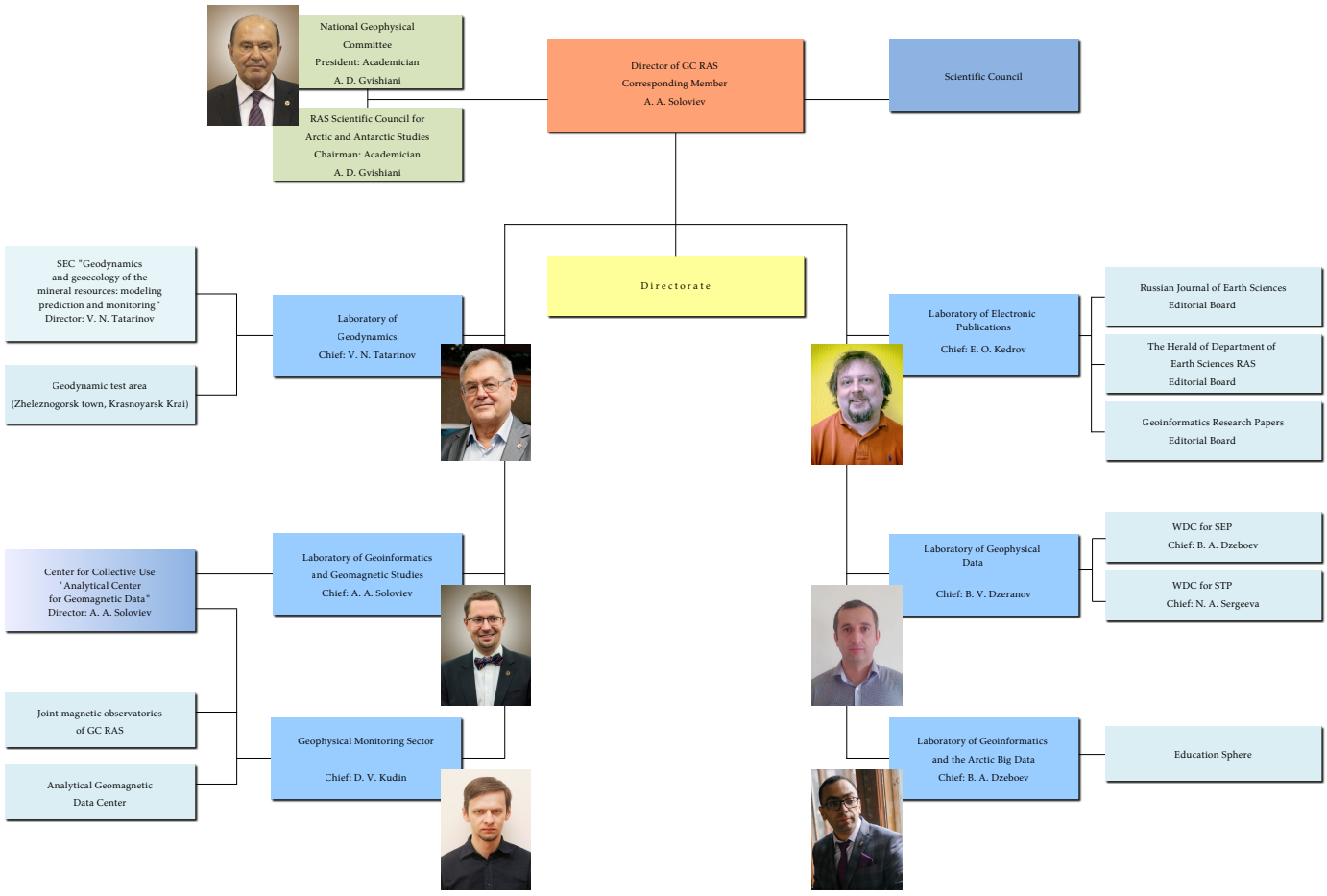

Figure 12. The GC RAS structure and heads of departments.

As of 2024, the GC RAS staff consists of 110 employees including 6 RAS members, 21 DSc's, 27 PhD's and 38 young researchers (up to age 39). Some staff member photos including those taken during field works are given in Figure 13. GC RAS representatives hold important positions in such international organizations as IIASA, IUGG, IAGA and CODATA. A special attention is paid to strengthening cooperation in geophysics and remote sensing with research institutions from the BRICS countries, including those under the China Earthquake Administration and the Ministry of Natural Resources of China, the South African National Space Agency and others. Today, the Geophysical Center of RAS is a new type of prominent research institute that efficiently combines fundamental research with high-priority applied projects.

Figure 13. The GC RAS staff.

Acknowledgments. This work has employed services and data provided by the Shared Research Facility "Analytical Geomagnetic Data Center" of the Geophysical Center of RAS (http://ckp.gcras.ru/). This work was conducted in the framework of budgetary funding of the Geophysical Center of RAS and the Schmidt Institute of Physics of the Earth of RAS, adopted by the Ministry of Science and Higher Education of the Russian Federation.

References

Gvishiani A., Rozenberg I., Soloviev A., et al. Study of the Impact of Climatic Changes in 1980–2021 on Railway Infrastructure in the Central and Western Russian Arctic Based on Advanced Electronic Atlas of Hydrometeorological Parameters (Version 2, 2023) // Russian Journal of Earth Sciences. — 2023. — P. 1–21. — https://doi.org/10.2205/2023es000882.

Gvishiani A. D., Kedrov E. O., Lyubovtseva Y. S., et al. The history of the research of the Geophysical Center of the Russian Academy of Sciences, 2010 // Vestnik Otdeleniya nauk o Zemle RAN. — 2018a. — Vol. 10, no. 6. — https://doi.org/10.2205/2018nz000356.

Gvishiani A. D., Kedrov E. O., Lyubovtseva Y. S., et al. The history of the research of the Geophysical Center of the Russian Academy of Sciences, 2011 // Vestnik Otdeleniya nauk o Zemle RAN. — 2018b. — Vol. 10, no. 4. — https://doi.org/10.2205/2018nz000352.

Gvishiani A. D., Kedrov E. O., Lyubovtseva Y. S., et al. The history of the research of the Geophysical Center of the Russian Academy of Sciences, 2009 // Vestnik Otdeleniya nauk o Zemle RAN. — 2019a. — Vol. 11, no. 1. — https://doi.org/10.2205/2018nz000358.

Gvishiani A. D., Kedrov E. O., Lyubovtseva Y. S., et al. The history of the research of the Geophysical Center of the Russian Academy of Sciences, 2012 // Vestnik Otdeleniya nauk o Zemle RAN. — 2019b. — Vol. 11, no. 1. — https://doi.org/10.2205/2019NZ000359.

Gvishiani A. D., Kedrov E. O., Lyubovtseva Y. S., et al. The history of the research of the Geophysical Center of the Russian Academy of Sciences, 2016 // Vestnik Otdeleniya nauk o Zemle RAN. — 2021. — Vol. 13, no. 1. — https://doi.org/10.2205/2021NZ000368.

Gvishiani A. D., Lyubovtseva Y. S., Kedrov E. O., et al. The history of the research of the Geophysical Center of the Russian Academy of Sciences, 2014 // Vestnik Otdeleniya nauk o Zemle RAN. — 2020a. — Vol. 12, no. 1. — https://doi.org/10.2205/2020nz000363.

Gvishiani A. D., Lyubovtseva Y. S., Kedrov E. O., et al. The history of the research of the Geophysical Center of the Russian Academy of Sciences, 2015 // Vestnik Otdeleniya nauk o Zemle RAN. — 2020b. — Vol. 12, no. 4. — https://doi.org/10.2205/2020NZ000367.

Kedrov E. Congratulations on the 75th Anniversary of Alexei Gvishiani // Russian Journal of Earth Sciences. — 2023. — Vol. 23, no. 4. — https://doi.org/10.2205/2023es0004.

Lyubovtseva Y. S., Gvishiani A. D., Kedrov E. O., et al. The history of the research of the Geophysical Center of the Russian Academy of Sciences, 2013 // Vestnik Otdeleniya nauk o Zemle RAN. — 2019. — Vol. 11, no. 1. — https://doi.org/10.2205/2019NZ000360.

Lyubovtseva Y. S., Gvishiani A. D., Kedrov E. O., et al. The history of the research of the Geophysical Center of the Russian Academy of Sciences, 2017 // Vestnik Otdeleniya nauk o Zemle RAN. — 2022. — Vol. 13, no. 1. — https://doi.org/10.2205/2022NZ000375.

Lyubovtseva Y. S., Gvishiani A. D., Soloviev A. A., et al. Sixtieth anniversary of the International Geophysical Year (1957-2017) - contribution of the Soviet Union // History of Geo- and Space Sciences. — 2020. — Vol. 11, no. 2. — P. 157–171. — https://doi.org/10.5194/hgss-11-157-2020.

Solovieva E. N. and Gvishiani A. D. The history of the research of the Geophysical Center of the Russian Academy of Sciences, 2019 // Vestnik Otdeleniya nauk o Zemle RAN. — 2022. — Vol. 14, no. 1. — https://doi.org/10.2205/2022NZ000374.

Solovieva E. N. and Nikitina I. M. History of Research of the Geophysical Center of the Russian Academy of Sciences. 2018. Change of the Director // Vestnik Otdeleniya nauk o Zemle RAN. — 2025. — Vol. 17, no. 1. — https://doi.org/10.2205/2025nz000377.